Analytical Sizing Models to Assess the Performances of High Specific Power Electric Motors for Hybrid Aircraft

Sarah Touhami

THÈSE

En vue de l'obtention du

DOCTORAT DE L'UNIVERSITÉ DE TOULOUSE

Délivré par :

Institut National Polytechnique de Toulouse (Toulouse INP)

Discipline ou spécialité :

Génie Electrique

Présentée et soutenue par :

Mme SARAH TOUHAMI

le mardi 15 septembre 2020

Titre :

Analytical Sizing Models to Assess the Performances of High Specific Power Electric Motors for Hybrid Aircraft

---

Ecole doctorale :

Génie Electrique, Electronique, Télécommunications (GEET)

Unité de recherche :

Laboratoire Plasma et Conversion d'Energie (LAPLACE)

Directeur(s) de Thèse :

M. YVAN LEFEVRE

M. JEAN-FRANCOIS LLIBRE

Rapporteurs :

M. ABDELMOUNAIM TOUNZI, UNIVERSITE LILLE 1

M. JEAN-FREDERIC CHARPENTIER, ECOLE NAVALE

Membre(s) du jury :

M. NOUREDDINE TAKORABET, INP LORRAINE, Président

M. JEAN-FRANCOIS LLIBRE, UNIVERSITE TOULOUSE 2, Membre

Mme NATHALIE RAVEU, TOULOUSE INP, Membre

M. YVAN LEFEVRE, TOULOUSE INP, Membre

Acknowledgment

The presented works have been carried out in Grem3 "Electrodynamic research group" at LAPLACE Laboratory "Laboratory on Plasma and Conversion of Energy", National Polytechnic Institute of Toulouse, between December 2016 and July 2020 in the framework of the European research project "HASTECS" of Clean Sky 2 European research program.

First of all, I would like to express my grateful to my supervisors, M. Yvan Lefevre, CNRS research fellow and M. Jean François Llibre, Associate Professor for their guidance and knowledge and constructive criticism throughout the journey that was this thesis. I would also like to express my deepest thanks for their kindness, patience, help and encouragement.

I would like to thank the examiners Professor Abdelmounaïm Tounzi and HDR Assistant Professor Jean-Frédéric Charpentier, for having read and evaluated this thesis. I would like to express my gratitude to Professor Noureddine Takorabet for chairing the jury of this thesis. I am also thankful to Professor Nathalie RAVEU for reading and exanimating my thesis. I am very thankful to M. M. Matthieu Fénot, Xavier Roboam and M. Jean-François Allias for accepting to participate as guests of this jury.

I would like to thanks Associate Professors Ms. Carole Henaux and M. François Pigache, for giving me the teaching opportunity. I would like also thanks Clement Nadal Associate Professor, Youness Rtimi and Linda Serairi to share with me these teaching classes.

I would like also to express my special thankful to M. Dominique Harribey, Research Engineer CNRS for his huge kindness and for his sharing with me his technical knowledge. I am also grateful others Grem3 permanent members: Professor Frédéric Messine, Professor Jean-François Rouchon and Associate Professor Thomas Huguet for their kindness, their help and their good environment inside the research group Grem3.

I am very grateful to the IT Managers M. Jacques Benaioun and M. Patrick Ferre for their great helping with big smile every time when I have a IT problem. I am also very grateful to the laboratory secretary staff Ms. Valerie Schwartz, Ms. Carine Alibert, Ms. Catherine Moll Mozella, Ms. Ariane Arnaud and Ms. Jessica Toscano for their administrative help of my thesis management.

I would now like to specially thank Thao Le Luong to for sharing with me the desk, its friendship, its support and its delicious Vietnamese food that she sometimes cooked specially for me.

I would like to specially thank Amal Zeaiter, PhD student at P'prim laboratory for its thesis interactions, its friendship and its huge support. I am grateful also to Phillippe Collin for its helps and its well thesis interactions. I would like also express my grateful to others HASTCES project colleagues Najoua Erroui, Matthieu Pettes-Duler, Flavio Accorinti for their all constructive discussions.

I thank Maxime Bonnet and Theo Capri for their thesis contributions and for their constructive discussions. I thank also all PhD students: André Mrad, Jessica Neumann, Carvalho Costa Mateus.

Finally, I would like to express my deeping thankful to my lovely parents Omar and Rachida, my sister Yasmine and my brothers chiefly my younger brother Mustapha for their all patience and their always support me, hoping that they are proud of me.

Thank you all.
Sarah Touhami

Abstract

After the industrial and the environmental successes of hybridization railways transport, the hybridization of aviation transport is acquiring more and more consideration. In this context, the European Union in partnership with the aerospace manufacturers, has launched in 2014 a largest research program Clean Sky 2 aiming to reduce aircraft fuel consumptions and noise levels. Clean Sky 2 research program includes several projects among of them: Academic reSearch on Thermal & Electric Components & Systems "HASTECS project" which aims to identify and to develop the most promising technologies for decreasing the weight and increasing efficiency of hybrid propulsion chain. "HASTECS project" is organized around six Work Packages (WPs) dedicated to the components of hybrid propulsion chain, for instance, the WP1 is dedicated to electric motors and the WP3 is dedicated to their cooling systems.

Indeed, the estimated reduction fuel consumptions for a short range flight would be 3.5% if the specific power of electric machines and power converters with their cooling systems is respectively increased to 5kW/kg and 15kW/kg for 2025, and also increased to 10kW/kg and 25kW/kg for 2035.
The targets are significantly higher than those of today. Specific power planned of the industrial electric machines and power converters is higher than the currently one. However, these specific powers present some limitations which depend on the involved material properties and by environment conditions such as: thermal limitations and partial discharges risk.

For reaching targeted specific powers for instance in electric machines, the mechanical, electrical and the magnetic loads linked to the materials and cooling technologies must be increased. However, considering the limitations and the environment constraints, choice of loads should be adequate. Therefore, it is important to develop models and tools allowing assessing the actual and the future technologies which allow achieving the HASTECS targets.

The present thesis focuses to the development of models and tools for satisfying the HASTECS targets about the electric machines and their cooling systems. There are several different electric machine topologies, namely: radial flux machines, axial flux machines, permanent magnet synchronous machines, wound rotor synchronous machines, asynchronous machines, etc. Performing for each electric machine topology a model for identifying the most promising technologies is a very complex and laborious task. Nevertheless, an analytical model of non-salient sine wave electric machines associated to load ability concepts characterizes a quite lot of electric machine topologies. Based on it, a Target Setting Tool is developed for assessing electric motor technologies considering limits and constraints while without specifying the electric motor topology. Therefore, very few input data are required to make quick trade-offs on electric motor performances as specific power and efficiency whereas Target Setting is based on huge assumptions. For assessing cooling system weight, sizing specified structure of electric motor is unavoidable. Moreover, studies of others work packages are strongly linked to the electric motor structure. Surface Mounted Permanent Magnet Synchronous Motor topology is one of electric motor topology which satisfies the analytical model of Target Setting Tool. A sizing tool called "SM-PMSM" has been carried out based on Surface Mounted Permanent Magnet topology helpful for others packages for providing more details and for checking the Target Setting Tool validity.

Two sizing of electric motors with their cooling systems were carried out using Target Setting Tool, SM-PMSM and others tools performed by WP3 to identify the required technologies for the term medium (2025) and long (2035) term HASTECS targets. The sizing using these tools was checked by finite element analysis.

Keywords— Hybrid Aircraft Propulsion, HASTECS Project, Clean sky 2 European Research Program, High Specific Power, Electric Motors, Cooling Systems, Technological Levels, Load concepts, High Speed, Thermal Constraints, Mechanical Constraints, Target Setting Tool, Sizing Tool, Analytical Model, Finite Element Analysis.

Résumé

Après les succès industriels et environnementaux de l'hybridation du transport ferroviaire, l'hybridation du transport aérien est de plus en plus envisagée. Dans ce contexte, l'Union européenne, en partenariat avec les constructeurs aéronautiques, a lancé en 2014 un vaste programme de recherche, Clean Sky 2, visant à réduire la consommation de carburant et le niveau sonore des avions. Le programme de recherche Clean Sky 2 comprend plusieurs projets parmi lesquels : Academic reSearch on Thermal & Electric Components & Systems "HASTECS project" qui vise à identifier et à développer les technologies les plus prometteuses pour réduire le poids et augmenter l'efficacité de la chaîne de propulsion hybride. Le "projet HASTECS" est organisé autour de six lot de travail (noté par WPs) dédiés aux différents composants de la chaîne de propulsion hybride, par exemple, le WP1 est dédié aux moteurs électriques et le WP3 à leurs systèmes de refroidissement. En effet, la réduction estimée des consommations de carburant pour un vol à courte distance serait de 3,5% si la puissance spécifique des machines électriques et des convertisseurs de puissance avec leurs systèmes de refroidissement est respectivement portée à 5kW/kg et 15kW/kg pour 2025, et également portée à 10kW/kg et 25kW/kg pour 2035. Les objectifs sont nettement plus élevés que ceux d'aujourd'hui. La puissance spécifique prévue des machines électriques industrielles et des convertisseurs de puissance est supérieure à celle d'aujourd'hui. Toutefois, ces puissances spécifiques présentent certaines limites qui dépendent des propriétés des matériaux concernés et des conditions environnementales, telles que les limitations thermiques et le risque de décharges partielles. Pour atteindre les puissances spécifiques visées, par exemple dans les machines électriques, les charges mécaniques, électriques et magnétiques liées aux matériaux et aux technologies de refroidissement doivent être augmentées. Toutefois, compte tenu des limitations et des contraintes environnementales, le choix des charges doit être adéquat. Par conséquent, il est important de développer des modèles et des outils permettant d'évaluer les technologies actuelles et futures qui permettent d'atteindre les objectifs d'HASTECS. La présente thèse se concentre sur le développement de modèles et d'outils permettant de satisfaire les objectifs d'HASTECS concernant les machines électriques et leurs systèmes de refroidissement. Il existe plusieurs topologies différentes de machines électriques, à savoir : les machines à flux radial, les machines à flux axial, les machines synchrones à aimants permanents, les machines synchrones à rotor bobiné, les machines asynchrones, etc. Réaliser pour chaque topologie de machine électrique un modèle permettant d'identifier les technologies les plus prometteuses est une tâche très complexe et laborieuse. Néanmoins, un modèle analytique de machines électriques sinusoïdales à pôles lisses basé sur le concept de charges peut satisfaire un grand nombre de topologies de machines électriques. Sur cette base, un outil "Target Setting Tool TST" est développé pour évaluer les technologies de moteurs électriques en tenant compte des limites et des contraintes sans spécifier la topologie des moteurs électriques. Par conséquent, très peu de données d'entrées sont nécessaires pour faire des compromis rapides sur les performances des moteurs électriques comme la puissance spécifique et l'efficacité, alors que l'atteinte d'objectifs ciblés nécessitent d'établir de nombreuse hypothèses. Pour évaluer le poids du système de refroidissement, le dimensionnement de la structure spécifique du moteur électrique est inévitable. De plus, les études des autres lots de travail sont fortement liées à la structure du moteur électrique. La topologie du moteur synchrone à aimants permanents montés en surface est une topologie de moteur électrique qui satisfait le modèle analytique de Target Setting Tool. Un outil de dimensionnement appelé "SM-PMSM" a été réalisé sur la base de la topologie des aimants permanents montés en surface, utile pour les autres lots ainsi pour vérifier la validité du TST. Deux dimensionnements de moteurs électriques avec leurs systèmes de refroidissement ont été effectués à l'aide du Target Setting Tool, SM-PMSM et d'autres outils réalisés par le WP3 pour identifier les technologies requises pour les cibles HASTECS à moyen (2025) et long (2035) termes. Le dimensionnement à l'aide de ces outils a été vérifié par analyse par éléments finis.

Mots-clés —Avion à Propulsion Hybride, Projet HASTECS, Programme de Recherche Européen Clean Sky2, Haute Puissance Spécifique, Moteurs Electriques, Systèmes de Refroidissement, Niveaux Technologiques, Concepts de Charge, Haute Vitesse, Contraintes Thermiques, Contraintes Mécaniques, Target Setting Tool, Outil de Dimensionnement, Model Analytique, Analyse par Eléments Finis.

Contents

List of Figures

List of Tables

Glossary

- $\boldsymbol{B}$ magnetic induction
- $\boldsymbol{H}$ magnetic field intensity
- $\boldsymbol{J}$ magnetic polarization
- μ_o the magnetic vacuum permeability
- μ_r relative magnetic permeability
- μ_{pm} PM permeability
- $\boldsymbol{B_r}$ remanence
- $\boldsymbol{H_c}$ coercive field
- $\boldsymbol{T}$ temperature
- $\boldsymbol{B_{r20°}}$ remanence at 20°C
- $\boldsymbol{H_{c20°}}$ coercivity at 20°C
- $\boldsymbol{\alpha_B}$ temperature coefficient of the remanence
- $\boldsymbol{\alpha_H}$ temperature coefficient of the coercivity
- $\boldsymbol{P_j}$ joule losses
- $\boldsymbol{P_f}$ iron losses
- $\boldsymbol{P_{edd}}$ eddy current losses
- $\boldsymbol{P_{friction}}$ friction losses
- $\boldsymbol{P_{windage}}$ windage losses
- $\boldsymbol{\Omega}$ rotational speed
- $\boldsymbol{R_s}$ resistance
- $\boldsymbol{H_g}$ magnetic field strength
- $\boldsymbol{f}$ synchronous frequency
- $\boldsymbol{R_{thermal}}$ thermal resistance
- $\boldsymbol{e}$ thickness
- $\boldsymbol{S}$ surface
- $\boldsymbol{\lambda_{th}}$ thermal conductivity
- $\boldsymbol{j_{rms}}$ root mean square **(**RMS) of current density
- $\boldsymbol{A_{rms}}$ RMS of linear current density
- $\boldsymbol{A_m}$ amplitude of linear current density
- $\boldsymbol{BH_{max}}$ maximum energy product
- $\boldsymbol{\sigma}$ tangential stress
- $\boldsymbol{T_{em}}$ electromagnetic torque
- $\boldsymbol{S_b}$ inner stator surface
- $\boldsymbol{K}$ surface current density
- $\boldsymbol{B_{rs}}$ flux density resulting from the rotor source
- $\boldsymbol{B_{ss}}$ flux density resulting from the stator source
- $\boldsymbol{B_{tot}}$ amplitude of the total flux density in airgap
- $\boldsymbol{p}$ number of pole pairs
- $\boldsymbol{\theta}$ angular position
- $\boldsymbol{t}$ time
- $\boldsymbol{z}$ axial direction
- $\boldsymbol{\lambda}$ shape coefficient
- $\boldsymbol{B_m}$ max. value the airgap flux density
- $\boldsymbol{B_{rms}}$ RMS of the airgap flux density
- $\boldsymbol{K_m}$ max. value the surface current density
- $\boldsymbol{K_{rms}}$ RMS of the surface current density
- $\boldsymbol{q}$ number of phase
- $\boldsymbol{m}$ number of slots per pole and per phase
- $\boldsymbol{B_{ry}}$ rotor flux density
- $\boldsymbol{B_{sy}}$ stator yoke flux density
- $\boldsymbol{B_{st}}$ stator tooth flux density
- $\boldsymbol{R}$ stator bore radius
- $\boldsymbol{R_{out}}$ external stator radius
- $\boldsymbol{R_{fr}}$ external frame radius
- $\boldsymbol{L_m}$ active length
- $\boldsymbol{l_{ht}}$ half-turn length
- $\boldsymbol{L}$ axial motor length
- $\boldsymbol{e_g}$ airgap thickness
- $\boldsymbol{x_e}$ airgap ratio
- $\boldsymbol{h_s}$ slot heigh
- $\boldsymbol{l_s}$ slot width
- $\boldsymbol{l_t}$ tooth width
- $\boldsymbol{h_y}$ stator yoke thickness
- $\boldsymbol{R_r}$ external rotor radius
- $\boldsymbol{R_{sh}}$ shaft radius
- $\boldsymbol{e_{pm}}$ permanent magnet thickness
- $\boldsymbol{r_{tooth}}$ ratio between $\boldsymbol{l_t}$ to $\boldsymbol{R}$
- $\boldsymbol{\tau_r}$ ratio between $\boldsymbol{R_{fr}}$ and $\boldsymbol{R_{out}}$
- $\boldsymbol{\rho_{fr}}$ frame density
- $\boldsymbol{\rho_{insl}}$ insulation density
- $\boldsymbol{\rho_c}$ copper density
- $\boldsymbol{\rho_{rot}}$ rotor density
- $\boldsymbol{\rho_{air}}$ air density
- $\boldsymbol{W_{stat-wind}}$ stator winding weight
- $\boldsymbol{W_{stat-core}}$ stator core weight
- $\boldsymbol{W_{stat}}$ stator weight
- $\boldsymbol{W_{rot}}$ rotor weight
- $\boldsymbol{W_{mot}}$ motor weight
- $\boldsymbol{S_P}$ specific power
- $\boldsymbol{S_T}$ specific torque
- $\boldsymbol{k_{tb}}$ end-winding coefficient
- $\boldsymbol{\eta}$ efficiency
- $\boldsymbol{k_h}$ hysteresis loss coefficient
- $\boldsymbol{k_c}$ eddy loss coefficient
- $\boldsymbol{k_e}$ excess loss coefficient
- $\boldsymbol{\rho_{cu20°}}$ copper resistivity at 20°C
- $\boldsymbol{\alpha_{th}}$ temperature coefficient resistance
- $\boldsymbol{\rho_{cu}}$ copper resistivity
- $\boldsymbol{T_{win}}$ winding temperature
- $\boldsymbol{\alpha_{dis}}$ electric angular displacement
- $\boldsymbol{k_{fill}}$ fill factor
- $\boldsymbol{k_w}$ winding coefficient
- $\boldsymbol{h_{ry}}$ rotor yoke thickness
- $\boldsymbol{L_s}$ self-inductance per phase
- $\boldsymbol{M}$ mutual inductance per phase
- $\boldsymbol{L_{cs}}$ cyclic inductance per phase
- $\boldsymbol{\Phi_{vm}}$ max no-load magnetic flux
- $\boldsymbol{E_i}$ back-electromotive force per phase
- $\boldsymbol{A}$ magnetic vector potential
- $\boldsymbol{P_{em}}$ electromagnetic power
- $\boldsymbol{P_{mech}}$ mechanical power
- $\boldsymbol{P_{ele}}$ electric power

- S_{sy} stator yoke surface
- S_{slot} stator slot surface
- S_{tooth} tooth surface
- S_{cond} conductor cross section
- $S_{tot-cond}$ total cross section of conductors in one slot
- S_{rot} rotor surface
- ϕ_p magnetic flux per pole
- ϕ_{sy} stator yoke magnetic flux
- ϕ_{st} magnetic flux in stator teeth
- Aj_{eq} equivalent current density product
- l_c conductor length
- n_w number of wires
- l_w wire length
- **lay length** lay length
- W_c conductor width
- th_c conductor thickness
- S_w circular cross section of wire
- $S_{elliptical}$ elliptical cross section of wire
- $k_{fillcond}$ copper filling of conductor
- a_{ij} iron loss coefficient
- ω electrical pulse
- pr air pressure

- $P_{mech-loss}$ mechanical losses
- $P_{rot-loss}$ rotor windage losses
- P equivalent dynamic bearing load
- C_f friction coefficient in bearings
- C_{fa} friction coefficient in airgap
- C_{fr} friction coefficient in rotor ends
- R_{ea} Reynolds number of flow in airgap
- R_{erot} Reynolds number of flow in rotor ends
- N_{sin} sinewave distributed conductors
- N_{tsin} max number of turns
- E Young's modulus

- N_t number of stator teeth
- N_s number of slots
- N_c total number of conductors
- N_{cs} total number of conductors per slot
- n_l number of layers
- n_b number of segments

- I current
- I_m amplitude of current
- I_{rms} RMS value of the current

- Ψ_g airgap linkage flux
- N_{ts} number of turns per phase connected in series
- C conductor distribution function
- N winding distribution function
- N_e elementary coil function
- C_e elementary coil function
- MMF magnetomotive force function
- τ short pitch factor
- s skewing factor
- k_d distribution winding coefficient

- k_{pi} pitch coefficient
- k_s skewing coefficient
- k_{sc} coefficient taking into account elliptical cross-section
- k_{lc} coefficient taking into account twisting
- β_e angle between circular and elliptical cross sections
- β angular width
- α angular centre of permanent magnet
- γ orientation angle
- χ opening slot angle
- γ angular step between two neighbouring coils

- ξ angular step between two layers
- V_p peripheral speed
- σ_m mechanical stress
- ν Poisson's ratio

General introduction

Nowadays, protecting environment becomes an unavoidable requirement especially in the transport sector. Electrification of rail transport has led to weight decreasing, fuel consumption decreasing and hence to CO_2 emission decreasing. In aeronautics, transition to electric power was initiated by the electrification of non-propulsive systems (e.g. in Airbus A380 and Boeing B787 aircrafts) with the aim of extending it to possible hybrid or electric propulsion systems. In the context of doing that, several research projects and programs have been launched, among of them the "Clean Sky 2 program". The last one is a largest European research programme developing innovative, cutting-edge technology aimed for reducing of 20% CO_2 emissions and noise levels for the Horizon 2020.

Hybrid aircraft research on thermal and electrical components and systems "HASTECS" project is part of Clean Sky 2 research program. It aims to study the hybridization regional aircraft propulsion systems by means of developing tools and models for reducing weights and increasing efficiencies. "HASTECS" project includes six work packages. Each work package is dedicated to the following topics: electric motors, power converters, electric motors and power converters cooling systems, partial discharges and integration systems.

Works presented in this thesis are included in the first work package dedicated to the development of tools allowing satisfying the HASTECS specifications and targets concerning the electric motors. Two targets are set in the HASTECS consortium: increasing specific power of electric motors including their cooling systems to reach 5kW/kg for 2025 and to reach 10kW/kg for 2035 despite of particularly severe environmental constraints (thermal, partial discharges, etc.). So far, these targets are higher than the achieved specific powers of industrial electric motors including their cooling systems. Typically, for increasing specific power of electric motors, electric, magnetic and mechanical loads linked to the materials and design technologies should be increased and improved. However, these improvements often lead to higher losses that need to be extract and evacuate in the small areas which is hence challenging. Indeed, decreasing weight of electric motor may lead to an increasing weight of its cooling system. This thesis will respond to the following problematic: according to the actual and future technological levels can we reach the targets respectively in 2025and in 2035.

The thesis manuscript is organized around four chapters:

The first chapter presents an overall description of industrial context: specifications, problematics and goals for framing the thesis works. This chapter presents a state art of the actual industrial electric motors to situate the achieved specific power and to identify the involved technologies, namely: material technologies, construction technologies and cooling methods. They are overviewed in terms of topologies, weights and loads to identify the main limitations for increasing specific power. Issues and limitations are discussed in details. Future technological improvements for increasing specific power are also evoked although they are still under research.

A Target Setting Tool "TST" is carried out in Chapter II, for assessing the electric motor and cooling technologies presented in Chapter I. Based on the model of ideal sinewave non-salient electric motors and the loadability concepts, main sizes, weights and performances of electric motor are determined without specifying the structure. Thermal and mechanical constraint are the first limitations for increasing specific power. Thermal constraint is developed according to a particular electric load which depends on the cooling technology. Mechanical constraint is also developed according to rotor properties and to mechanical load. These constraints are introduced in Target Setting Tool in order to not exceed the limits in the electric motor assessment. The main purpose of TST is then to make from few data and huge assumptions quick trade-offs on the specific power and the efficiency for identifying the promising technologies. Nevertheless, TST outputs are not enough for the others Work Packages.

Chapter III deals with a sizing tool based on the analytical model of Surface Mounted Permanent Magnet Synchronous Motor "SM-PMSM" and based on the TST outputs. Motivations for choosing such topology are firstly outlined and discussed. 2D analytical model is dealt for sizing the rotor components as permanent magnets, rotor yoke and shaft. Additional stator sizes are derived from a chosen winding configuration. Through established conductor distribution functions, intrinsic electric parameters and performances are deduced. The intrinsic electric parameters are necessary for sizing power converters and their cooling systems. As the structure is specified, losses are updated for assessing the thermal constraint and for sizing the cooling systems of electric motors.

The fourth and last chapter focuses to the sizing of electric motors and their cooling systems for the medium and long term targets. Also, it aims to identify on the one hand the most actual promising and future technologies for achieving medium and long term targets using "TST" and "SM-PMSM" and on the other hand it aims to validate these tools using finite element analysis that are based on some assumptions especially the TST. According to the HASTECS flying profile, choice of sizing point is firstly discussed. To size both electric motors and their cooling system, a procedure is proposed. The last one includes the developed assessment tool "TST", sizing tool "SM-PMSM" and other sizing cooling system tools carried out by WP3. Sizing electric motor and its cooling system for 2025 HASTECS target begins with an analysis of issues, limitations and used strategy for achieving this target. Afterward, choice of technological levels is overviewed to carry out the assessment electric motor technologies with TST. After the assessment step, electric motor is sized using "SM-PMSM" and its cooling system is sized using tools developed by WP3. Validation of sizing of electric motor is carried out with Finite Element Analysis. Following the same approach, for long term target 2035 sizing electric motor including its cooling system is presented in this chapter. Finally, an emphasis is paid on the differences between the electric motor targeted for medium term target 2025 with the one targeted for long term target 2035 in order to identify achieved thermal limit for each target.

Eventually, several conclusions are presented and some perspectives are proposed.

Chapter I: State of the art

Contents

Introduction

This chapter provides an overall description of industrial context with a state of the art of electric motor technologies. Specifications, problematic, goals and solutions will be firstly detailed. Afterward a wide panorama of actual high specific power electric motors will be studied. It will include employed materials, cooling technologies and conventional industrial motors. Future technological improvements will be also highlighted. Finally, issues and limitations of increasing specific power electric motor will be discussed.

I.1 Specifications, problematic, goals and solutions

- *Project Framework: " Cleansky 2 Program: HASTECS Project "*

CleanSky2 is a big European research program in aeronautical innovation which aims to reduce noise and CO_2 emissions of regional aircraft. This research program includes several research projects, among them there is Hybrid Aircraft academic reSearch on Thermal and Electrical Components and Systems "HASTECS" project [Hor_20]. It consists in identifying the most promising technologies allowing increasing the specific power and efficiency of hybrid propulsion chain. Furthermore, HASTECS project aims also to identify the technological breakthroughs via the development of tools to meet these goals. HASTECS project involves "LAPLACE" laboratory, "Pprime" institute for power conversion systems associated with research center "CIRIMAT" for power supply, as shown in Figure I. 1. The HASTECS Work Packages (WPs) are organized into 6 WPs. The 1st WP is dedicated to the electric motor. The 2nd WP is dedicated to the power converter. These two WPs are leads by LAPLACE laboratory with its three research groups: Grem3, CS and GENESYS. While, the 3rd and 4th WP including the cooling systems of electric motor and power converter respectively are led by Pprime laboratory. The 5th and 6th WP carry on the partial discharge study in electric systems and the optimization study of propulsion chain, respectively. These latter are also leads by LAPLACE laboratory with its research groups: MDCE, Grem3 and GENESYS.

Figure I. 1. HASTECS Project research organization [Wor_18]

- *General aircraft configuration*

The electrical aircraft architecture is a serial architecture powered by some electrical generators mechanically linked (with or without gearbox) to the gas turbines shafts. Another electrical energy is supplied by batteries or fuel cells cf. Figure II. 2. This architecture is chosen as baseline architecture for assessment studies of HASTECS project. It has been taken also for "E-FanX" demonstrator [Air_19] and for hybrid electric aircraft "DA36 E-Star 2".

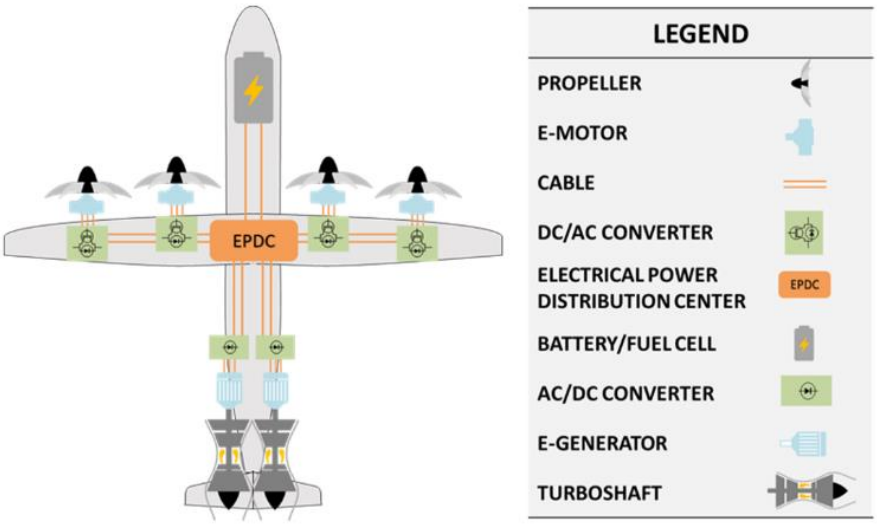

Figure I. 2. Baseline Architecture: Serial hybrid electric architecture [Wor_18] [All_17]

- *Specifications and targets*

According to Airbus specification [All_18], the electric motor should be ensuring a mechanical power 0.018 Per Unit[1] (PU) with a rotational speed per unit of 30% at shaft level during flying phases of taxi-in and taxi-out. In the take-off flying phase, the electric motor should be ensuring a mechanical power of 1PU with 100% of rotational speed. In the climb phase, the mechanical power decreases from 0.92PU to 0.746PU with the rotational speed comprised between 95% to 75%. During the cruise phase, mechanical power and rotational speed should be constant and equal respectively to 0.489PU and 70% as illustrated in Figure I. 3. In the descent phase, the mechanical power and the rotational speed of the electric motor is reduced to 0.02PU and 40%. In the approach and the landing phases, the mechanical power and the rotational speed are increased to 0.393PU and 82% due to go-around. Table I. 1 details each time flying phase.

HASTECS project fixes medium and long term targets to be achieved for electric motors including their cooling systems and for power converters with their cooling systems. Medium term target of 2025 is to achieve:

→ Specific power 5kW/kg for electric motor with its cooling system
→ Efficiency of electric motor at cruise point must be greater than 96%
→ Efficiency of electric motor at design point greater than 94.5%
→ Specific power 15kW/kg for power converter with its cooling system
→ Efficiency of power converter at optimization point must be greater than 98%
→ Efficiency of power converter at max power must be greater than 96.5%, without any allowed partial discharge in electric motor and power converter.

Long term target of 2035 is to achieve:

→ Specific power 10kW/kg for electric motor with its cooling system
→ Efficiency at cruise point greater than 98.5%
→ Efficiency at design point greater than 97%
→ Specific power 25kW/kg for power converter with its cooling system
→ Efficiency of power converter at optimization point must be greater than 98%
→ Efficiency of power converter at max power must be greater than 96.5%, with allowed partial discharge in electric motor and power converter [All_18].

Doubling specific power of electric machines and power converters from the 1st target to the 2nd target leads to weight reduction of 1.8 tons. It then allows a reduction of 3.5% fuel consummation and therefore a reduction of CO_2 emissions [Dis_18].

[1] For confidentiality reason, exact power value will not be provided, however, the maximum power is MW range

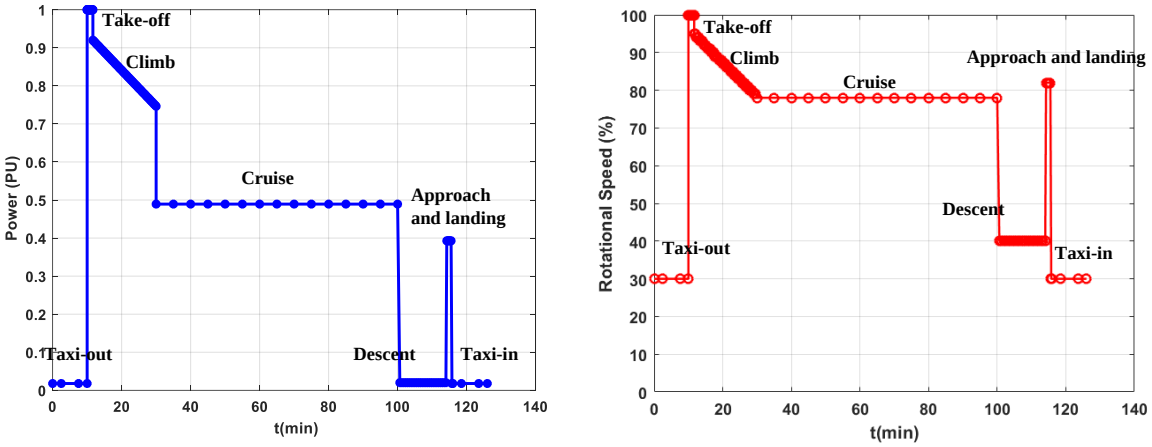

(a) (b)

Figure I. 3. (a) Power profile at shaft level vs flying time, (b) Rotational speed profile per unit vs flying time [All_18]

Table I. 1. Flight phases times [All_18]

Phases	Taxi out and in	Take-off	Climb	Cruise	Descent	Approach and Landing	Total flying time
Time(min)	10	1.66	18.33	70	14	2	**126 min**
Speed (%)	30	100	95 to 79	78	40	82	
Power (PU)	0.018	1	0.92 to 0.746	0.489	0.02	0.393	

This thesis interests only on tasks WP1 (electric motor). However, WP1 interacts directly with 2nd, 3rd, 5th and 6th WP (cf. Figure I. 4). With WP2 the interaction allows to fix the DC bus voltage from the given electric parameters of the electric motor. While, with WP3 the interaction allows to design cooling system of the electric motor from its losses and geometric sizes. Finally, WP5 interacts with WP1 in order to determine the insulation system required to avoid the partial discharge for the medium term target and to minimize partial discharge for the long term target. Once the sizing of electric motor is done, WP1 gives to WP6 the electrical models of the motor for overall optimizations of the hybrid propulsion system. Therefore, this thesis aims to fulfill the HASTECS expectations for the electric motor.

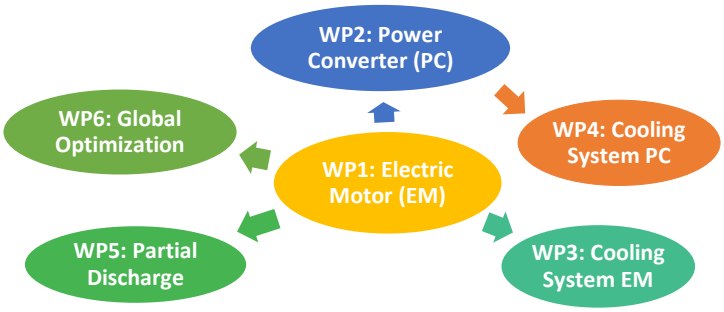

Figure I. 4. WP1 interaction with other WPs

- *Thesis problematic*

Specific power and efficiency of electric machines highly depend on available magnetic loading, electric loading and rotating speed, which are constrained by thermal and mechanical limitations of involved materials. Increasing both specific power and efficiency are a particular challenge. Indeed, increasing loads increases specific power on one side and decreases the efficiency on the other hand. Moreover, the electric machines for aircraft application should be high robustness and high reliability.

- *Goals and solutions*

This thesis aims to satisfy both the HASTECS specifications in terms of targets and the interaction requirements between all WPs. Develop assessment tools is the solution for these two expectations. Assessment tools allow making quick loads trade-off to achieve high specific power and efficiency in order to identify the existing and the future technologies the most promising. In addition, they allow identifying the physical and technological limits to overcome in the future. Assessment tools allow also to provide more information to other WPs and help to carry out global optimization for hybrid aircraft chain and local optimization for electric machine.

I.2 Actual specific power of electric machines

In order to develop assessment tools for electric machines, it is necessary to establish a detailed state of art of existing electric machines and their technologies. The focus will be on common topologies of electric motors, materials and cooling technologies. According to the power range required (some kW to some MW), only electric motors devoted to railway traction and hybrid electric vehicles will be overviewed to evaluate their actual specific power.

I.2.1 Electric motor topologies

Since AC power converter advances, alternative current rotating machines as synchronous and induction motors are the most used topologies in industrial applications.

- *Synchronous motors* are mostly built with permanent magnets in the rotor. Permanent Magnets (PMs) can be mounted on core rotor surface or positioned inside it, in order to develop a salience, as illustrated in Figure I. 5.a and b. A performance comparison between surface mounted and interior PMs is summarized in Table I. 2. It is possible to encounter wound synchronous motor without PMs; then the rotor can be salient or no salient depending on the shape of the pole shoe.
- *Induction motors* are built with short circuited rotor performed either squirrel cage or wound rotor or even solid rotor with or without slits as presented in Figure I. 5. c, d and e. In contrast to synchronous motors, induction motors are all no salient. Table I. 3 summarizes a brief performance comparison between synchronous and induction motors.

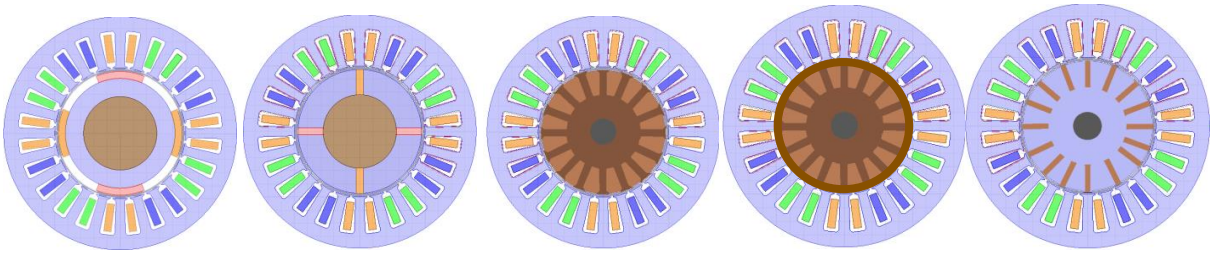

(a) (b) (c) (d) (e)

Figure I. 5. Synchronous motors: (a) Surface mounted permanent magnet, (b) Buried Magnet; Induction motors: (c) Wound Rotor (d) Squirrel cage, (e) Solid rotor

Table I. 2. Performance comparison between surfaces mounted PMs and interior PMs [Gie_10]

Surface Mounted PMs	Interior PMs
- Air-gap flux density lower than remanence flux density of PM - Lower armature reaction flux - Eddy current losses in PM - Low flux-weakening capability - No salient torque	- Air-gap flux density greater than remanence flux density of PM - Higher armature reaction flux which require high performance power converter - No eddy current losses in PM - Operating with wide flux-weakening is possible - Salient torque

Table I. 3. Performance comparison between synchronous motors and induction motors [Gie_10]

Synchronous motors	Induction motors
- Low rotor losses - High efficiency - Low inductance due to high magnetic air-gap thus requiring additional inductance for power converter	- High rotor losses due to induced currents thereby significant cooling effort can be required - Low efficiency - High inductance due to small magnetic air-gap, therefore reduced power converter weight

I.2.2 Magnetic Materials

The performances of electrical machines are strongly related to the magnetic materials used. The evolution of these materials contributes to the improvement of the performance of electrical machines. Two magnetic material categories are distinguished:

→ Soft magnetic materials which present magnetic properties in the presence of an external excitation,

→ Hard magnetic materials which have magnetic properties even in the absence of external excitation.

These two materials have a magnetic hysteresis curve depending both on their intrinsic characteristics and the magnetic excitation in which they are submitted. In fact, placed on a magnetic field *H* which varies alternately,

the induction B of the magnetic material presents a hysteresis curve. Figure I. 6 illustrates typical hysteresis cycles of soft and hard materials. B_r is the residual induction (remanence) corresponding to (H=0) and H_c is the coercive field defined as the field value when (B=0). From a certain value of H, the induction B is saturated and corresponds to B_s. In hard materials, the remanence B_r and the coercivity H_c are higher than soft ones as shown in Figure I. 6.
The general relationship between the magnetic induction B, and the magnetic field intensity H can be expressed as:

$$B = \mu_o \mu_r H + J \tag{I. 1}$$

where J is the magnetic polarization, μ_o is the magnetic vacuum permeability, μ_r is the relative magnetic permeability.
Permanent magnets are sensitive to the temperature. Their remanence B_r and coercive field H_c vary with temperature as following equation:

$$\begin{cases} B_r = B_{r20^\circ}\left(1 + \frac{\alpha_B}{100}(T - 20^\circ)\right) \\ H_c = H_{c20^\circ}\left(1 + \frac{\alpha_H}{100}(T - 20^\circ)\right) \end{cases} \tag{I. 2}$$

where T is the PM temperature of the permanent magnet, B_{r20° and H_{c20° are the remanence and the coercivity at 20°C and α_B<0 and α_H<0 are temperature coefficients in [%/°C].

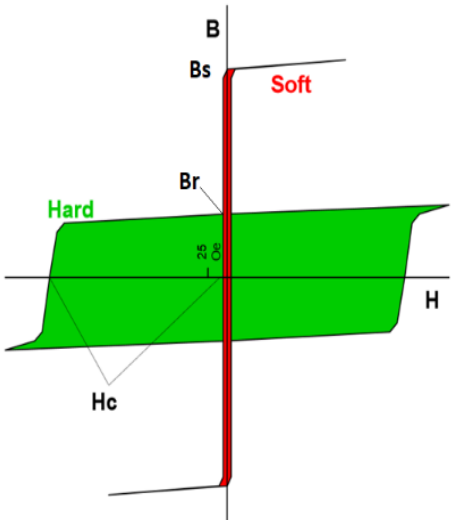

Figure I. 6. Hysteresis curves of soft and hard magnetic materials [Con_04]

- *Hard magnetic materials: Permanent Magnets (PMs)*

Alnico, Ferrites and Rare-earth materials are the three types of PMs commonly used in electric machines. Ferrites include Barium Ferrite and Strontium Ferrites. Rare-earth materials include Samarium-Cobalt (SmCo) and Neodymium-Iron-Boron (NdFeB). The operating point of the PM is located in the 2nd quadrant of the hysteresis loop. Figure I. 7 Presents the demagnetization curves and the magnetic energy of PM per volume unit. During the last few years, rare-earth materials have known huge magnetic energy improvement compared to Alnico and Ferrites (cf. Figure I. 8). In the following, we focused only on the rare earth PMs in terms of features given that Alnico materials have the lowest coercive field and are easy to demagnetize, and, Ferrite materials have the lowest remanence as shown in Figure I. 9.

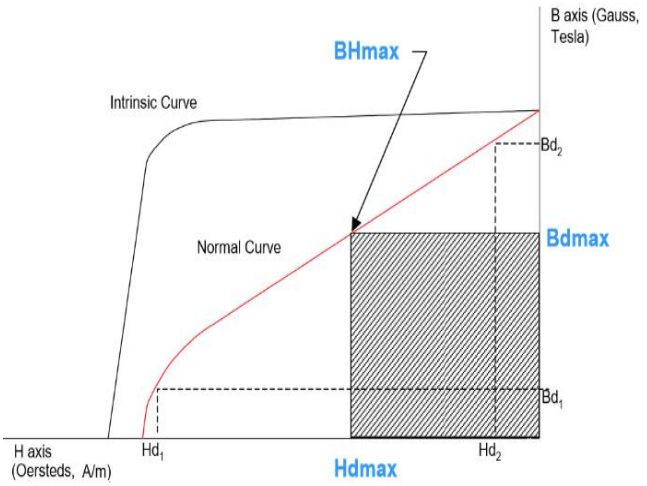

Figure I. 7. Maximum energy product (BH)max [Con_04]

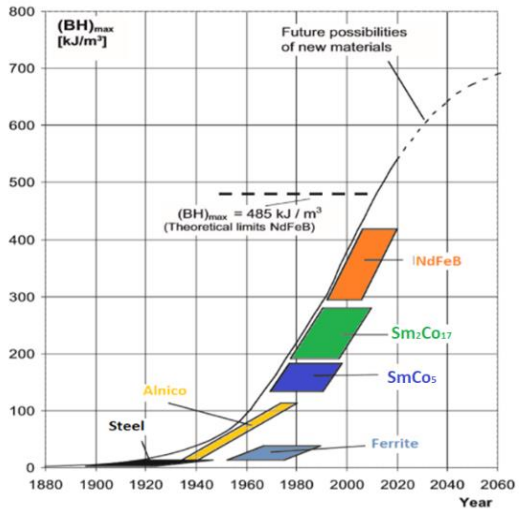

Figure I. 8. Development of energy densities [Vac_14]

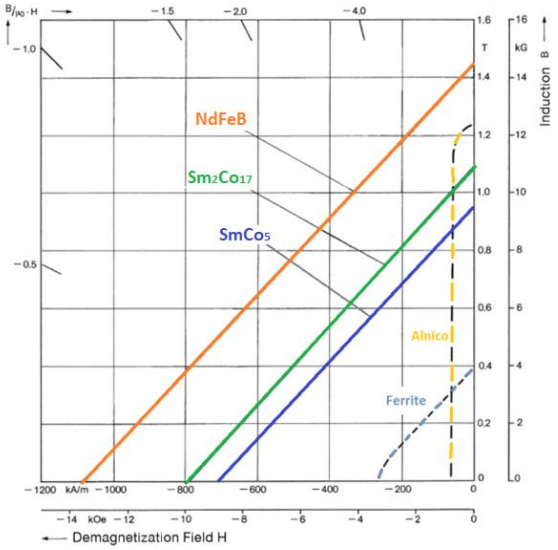

Figure I. 9. Typical demagnetization curves of Alnico and Ferrite in comparison to rare earth materials[Vac_14]

→ *Samarium-Cobalt (SmCo)*

Samarium-Cobalt magnets are the first generation of rare earth magnets. We distinguish two families: Sm_2Co_{17} and $SmCo_5$. Sm_2Co_{17} has the highest magnetic performance at high temperature unlike to $SmCo_5$. The latter has the best corrosion resistance of all rare earth magnets. SmCo are characterized by linear demagnetization curve, low temperature coefficients and by:

→ remanence between 0.87-1.19T,
→ coercivity between 1800-2400kA/m,
→ maximum energy product between 143-265 $kJ.m^{-3}$,
→ Maximum operating temperature 250-350°C as shown in Figure I.10.

→ *Neodymium-Iron-Boron (NdFeB)*

Neodymium-Iron-Boron magnets are the second generation of rare earth magnets. They are characterized by linear demagnetization curve, higher temperature coefficients compared to SmCo, and by:

→ remanence between 1.05-1.49T,
→ coercivity between 876-2706kA/m,
→ maximum energy product between 227-430 $kJ.m^{-3}$,
→ Maximum operating temperature 80-220°C.

Although NdFeB magnets are lightweight (cf Table I. 4), have better magnet properties and less eddy losses than those of SmCo. NdFeB are very sensitive to the high temperature. Polarization decreases dramatically with quick demagnetization of NdFeB compared to SmCo as illustrated in Figure I. 11. Moreover, from thermal

conductivity point of view, SmCo is better than NdFeB. It is also important to specify the mechanical properties of the PMs used in the rotor. Table I. 4 summarizes the mechanical properties of rare-earth PMs. Rare earth materials encounter degradation coming from corrosion, heat or mechanical impact. Therefore, their magnetic properties will degrade over time. In this way, NdFeB have relatively a low resistance to oxidation and corrosion without layer. They are usually covered by a surface protection, made of nickel for instance.

Table I. 4. Some properties of rare earth magnets [Arnold Cata]

	Density (kg/m^3)	electric resistance ($\mu\Omega.cm$)	Thermal conductivity ($W.m^{-1}.K^{-1}$)	Tensile strength (MPa)	Modulus of elasticity (GPa)	Hardness Vickers
$SmCo_5$	8400	55	11	120	140	600
Sm_2Co_{17}	8300	90	10	120	140	600
NdFeB	7600	180	7.6	285	-	620

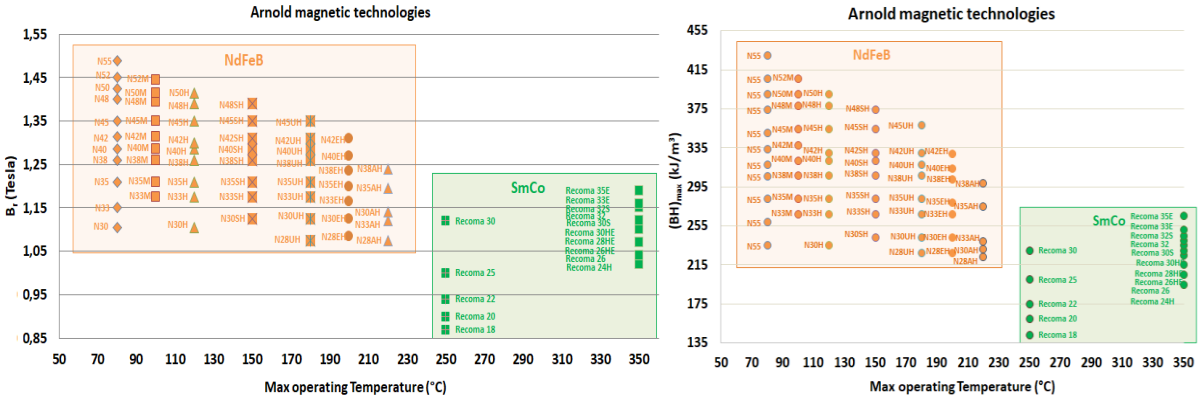

(a) (b)

Figure I. 10. NdFeB and SmCo permanent magnets of Arnold magnetic technologies: (a) remanence, (b) max magnetic energy [Arnold Cata]

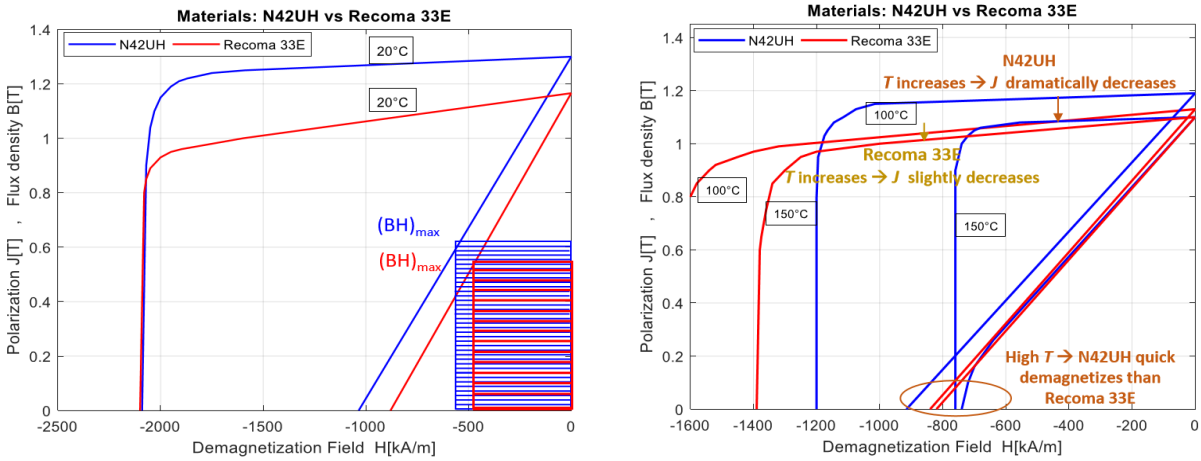

(a) (b)

Figure I. 11. Comparison between NdFeB (N42UH) and SmCO (Recoma33E): (a) Characteristics at 20°C, (b) Characteristics at 100°C and 150°C [Arnold Cata]

- *Electrical sheet*

Electrical machines are submitted in most cases to alternating fields. To limit losses in high frequency due to eddy currents, magnetic alloys are generally used as thin sheets. There are three kind of alloys: Nickel Iron alloy (NiFe), Iron Silicon alloy (SiFe) and Cobalt Iron alloy (CoFe).

→ *Nickel Iron alloy (NiFe)*

Nickel Iron alloy is based on nickel addition rates varying from 36% to 80%. The Nickel Iron alloy has very low magnetic coercivity, which leads to a superior relative permeability. The NiFe sheets have a thickness between 0.1-0.5mm. NiFe is characterized by high density 8200kg/m^3 with low flux density B_s=1.3-1.5T and H_c=3-5kA/m. Typically, Nickel Iron sheets are used for high speed very low power electric motors.

→ *Silicon Iron alloy (SiFe)*

In SiFe alloy, silicon makes iron mechanically harder; however, it decreases the saturation of flux density. We distinguish two types of SiFe sheets: Grain-Oriented and Non-Grain-Oriented sheets. The first one is

characterized by fixed magnetic flux orientation usually used in transformers, while Non-Grain-Oriented has multiple directions used in electrical machines. Non-Grain-Oriented SiFe alloys are often composed of iron with 1-3% of silicon, 1% of aluminum, 0.5% of manganese. Commonly, these sheets have flux density of 1.64T at 2.5kA/m as shown in Figure I. 12.a. Their typical thickness is between 0.35mm to 1mm. There are also non-grain-oriented sheets with thickness below 0.3mm manufactured for reducing losses (Figure I. 12.b). These sheets are called "Thin Non Oriented (NO)". They are composed of iron with 3% silicon content, 0.4% aluminum. The flux density of these laminations reaches 1.6T at 1.8kA/m. Table I. 5 presents all properties of some examples of these laminations.

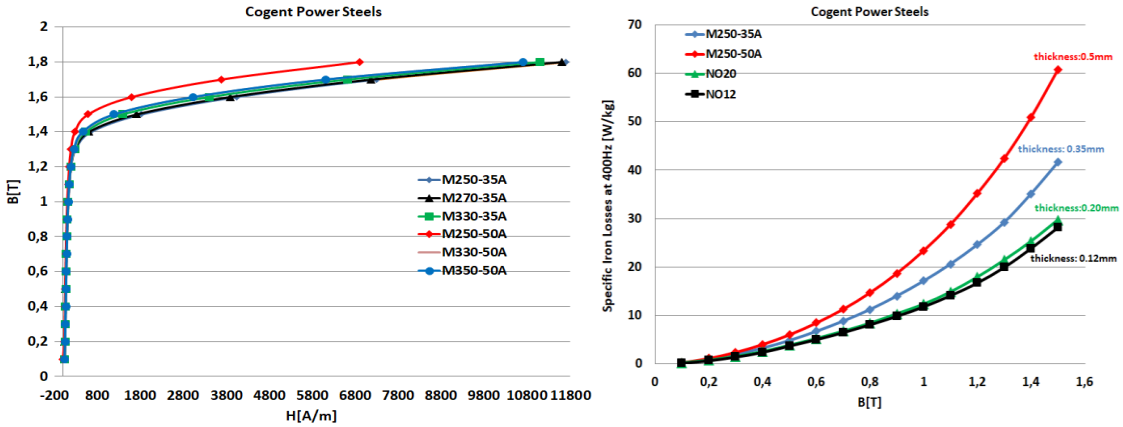

(a) (b)

Figure I. 12. B(H) curve of Non-Grain- Oriented sheets having 0.35mm and 0.5mm thicknesses, (b) Specific iron losses at 400Hz of Non-Grain-Oriented and Thin Non-Oriented [CogCat]

Table I. 5. Properties of Non-Grain- Oriented SiFe alloy [CogCat]

Name	Magnetic properties			Physical properties			Mechanical properties		
	Saturation induction [T]	Loss at (50Hz&1.5T) [W/kg]	Coercivity field [A/m]	Density [kg/m^3]	Electrical resistivity [µΩm]	Thermal conductivity [W.m^{-1}.K^{-1}]	Yield strength [MPa]	Tensile strength [MPa]	Modulus elasticity [GPa]
M235-35A	1.7	35	2.35	7600	0.59	36	460	580	185
M250-35A	1.76	40	2.50	7600	0.55	35	455	575	200
M250-50A	1.7	30	2.50	7600	0.59	36	475	590	175
M270-35A	1.77	40	2.70	7600	0.52	36	450	565	200
M310-50A	1.79	40	3.10	7650	0.55	36	385	500	185
M330-35A	1.77	40	3.30	7650	0.42	36	315	455	210
M350-50A	1.78	45	3.50	7650	0.42	36	320	460	200
M330-50A	1.77	40	3.30	7650	0.42	36	310	465	200
M400-50A	1.79	50	4.00	7700	0.42	36	325	465	200
M800-65A	1.85	100	8.00	7800	0.25	36	300	405	210

→ *Cobalt iron alloy* CoFe:

Cobalt iron alloys offer the most magnetic attractive features compared to FeSi alloys. In addition, their heat resistance makes them the suitable product for applications in severe environmental stress such as aerospace application. Typical CoFe laminations used in electrical machine have typical composition of 49% Cobalt, 49% Iron and 2% Vanadium. Typical thickness sheet is between 0.2 mm to 0.5mm. Prosperities of some CoFe alloys are summarized in Table I. 6. Cobalt Iron alloys has highest flux saturation level and lowest specific iron losses compared to Thin Non- Oriented. However, Cobalt Iron alloys remain heavyweight compared to SiFe alloys (cf. Figure. I. 13 and Figure I. 14). Therefore, to choose the suitable material, a trade-off between specific iron losses, induction and density should be carried out.

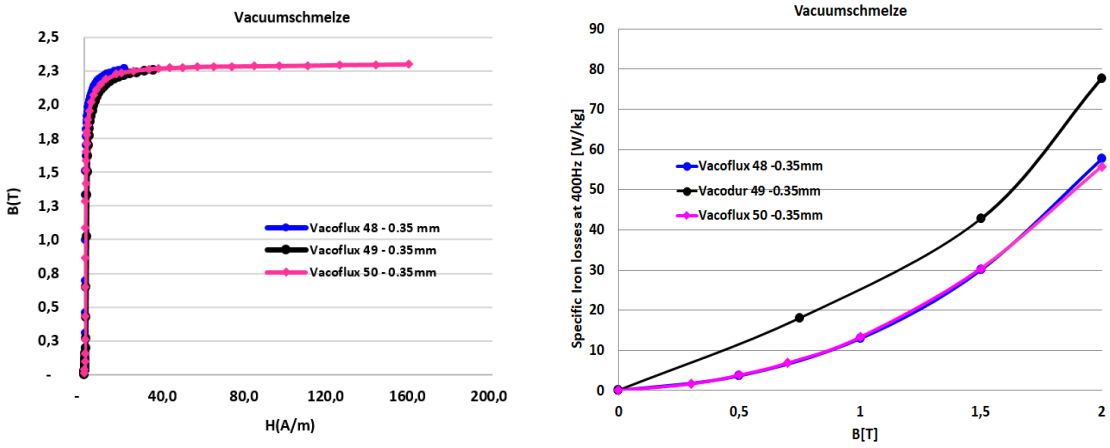

(a) (b)

Figure I. 13. Iron Cobalt alloy having 0.35mm: B(H) curve (b) Specific Iron losses at 400Hz [CogCat]

Table I. 6. Properties of Iron Cobalt alloy Vacuumschmelze materials [VacCat]

Name	Magnetic properties			Physical properties			Mechanical properties		
	Saturation induction [T]	Loss at (50Hz &1.5T) [W/kg]	Coercivity field [A/m]	Density [kg/m^3]	Electrical resistivity [µΩm]	Thermal conductivity [W.m^{-1}.K^{-1}]	Yield strength [MPa]	Tensile strength [MPa]	Modulus elasticity [GPa]
Vacoflux 48	2.35	1.5	35	8120	0.42	30	190	220	200
Vacodur 49	2.35	1.6	50	8120	0.42	32	210	400	200
Vacoflux 50	2.35	1.6	50	8120	0.42	30	250	550	210

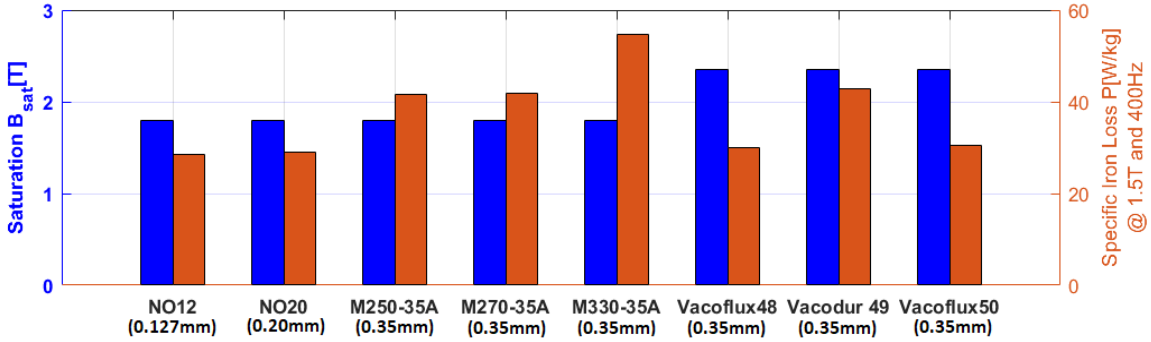

Figure I. 14. Comparison between Silicon-Iron and Cobalt-Iron alloys

I.2.3 Winding and insulations

- *Conductors*

Several conductor technologies are used in winding of electrical machines as summarized in Figure I. 15. The choice of the conductor type can be related to considerations regarding the filling factor, the losses at high frequency, the supply voltage...etc. In the following each conductor is detailed.

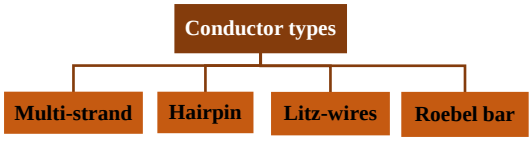

Figure I. 15. Conductor types used in winding of electrical machines

→ Multi-stranded conductors

Circular strand is a classical conductor type used in low and medium power electrical machines. Figure I. 16 illustrates an example of stranded random wound used in winding of HEV [Hen_14]. Usually, winding using this type of conductor has the lowest manufacture cost. However due to its circular shape, with a random wound the fill factor can be around 40-45% [Rey_16].

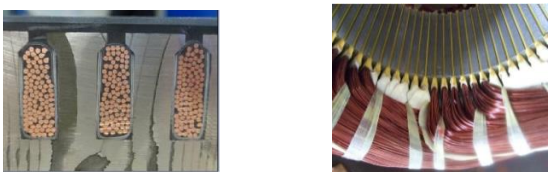

(a) (b)

Figure I. 16. Multi-stranded random wound: (a) inside slot, (b) end-winding [Hen_14]

→ Hairpin conductors

Hairpin or "Hair-pin" conductors are another type of conductors used in the winding of HEV electric motors as illustrated in Figure I. 17 [Bur_17] [Liu_19]. Hairpin conductors are often enamelled copper rectangular cross-sections, which can reach higher copper filling unlike to previous conductors [Bia_18] [Gla_20] [Bur_17] [Rog_18] [Mil_19]. They are assembled at the one end by welding which allows reducing end-winding length (cf. Figure I. 16. b). Furthermore, using these conductors allow ensuring high mechanical stiffness and overload capacity due to high thermal conductivity of winding. However, Hairpin conductors are not suitable for high speed operation due to the increase in electrical losses due to skin and proximity effects [Dub_18]. The latter can be moderately decreased by using transposition as presented in [Bia_18] [Ber_18] or by using flat shape of hairpin which results in a loss of profit in the filling factor.

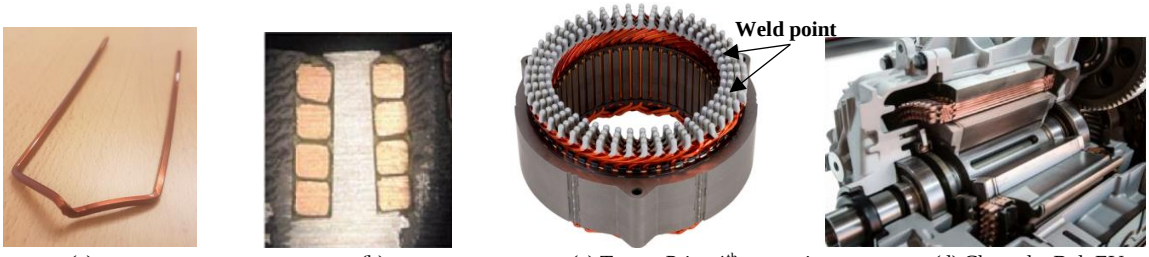

(a) (b) (c) Toyota Prius 4th generation (d) Chevrolet Bolt EV

Figure I. 17. Hairpin winding: (a) Hairpin single conductor [Deu_19], (b) inside slot, (c) Toyota Prius MY17 [Bur_17], (d) Chevrolet Bolt EV [Liu_19]

→ Litz wire conductors

Litz-wire conductors are an alternative solution to hairpin conductors for high speed electric motors as it is used in [Yoo_16] [Mar_17]. Litz-wire conductor consists of several enamelled copper wires assembled in parallel under round or rectangular shapes. Its wires are twisted as illustrated in Figure I. 18 in order to reduce or even to remove losses due to skin and proximity effects. Several Litz-wire constructions are proposed by manufacturers according to the sizes and recommended operating frequency ranges. These manufacturers ensure that Joule losses due to skin and proximity effects are hugely lower. Although Litz-wire conductor seems advantageous in high operating frequency, it is less attractive due to its low own fill factor. Table I. 7 gives the fill factor of rectangle Litz-wires used in high speed electric motor [Yoo_16].

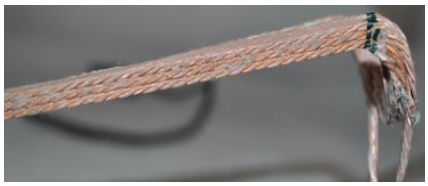

Figure I. 18. Rectangular Litz wire (Vendor data single-layer polyimide) [Yoo_16] [Mar_17]

Table I. 7. Fill factor of rectangular Litz-wire conductor "Vendor catalogue" [Mar_17]

AWG	30	32	34	36	38	40
Fill factor (%)	50.1	50.7	50.1	48.6	52.5	47.3

→ Roebel bar

Roebel bars are classical conductors used in very high power-high voltage electrical machines. They consisting of a large number of individual braided rectangular transposed strands as presented in Figure I. 19. Roebel bars ensure high fill factor in slots.

Figure I. 19. Roebel bar [Ast_cat]

Table I. 8 summarizes the fill factor for different conductors used in industrial electric machines.

Table I. 8. Fill factor of industrial electric machines with different conductor types

Conductor types	**Muti-stranded conductors**	**Hairpin conductors**	**Litz-wire conductors**
Electrical Machines EM Reference	BMWi3 [Bur_16][Mer_14]	Prius 4th generation [Bur_17]	Illinoi University [Yoo_16]
Fill factor (%)	**0.45**	**0.65**	**<0.5**

- *Winding configurations: "Concentrated and distributed windings"*

Two winding configurations are employed in slotted electrical machines: distributed winding and concentrated winding. Traditionally, distributed and concentrated windings can be referred by number of slots per pole and per phase N_{spp}. Distributed winding is characterized by $N_{spp}>1$, while when $N_{spp}\leq 1$, winding is concentrated overlapping for $N_{spp}=1$ and concentrated non-overlapping for $N_{spp}<1$. Figure. I. 20 illustrates these configurations. Distributed and concentrated windings present advantages and drawbacks summarized in Table. I. 9. To choose winding configuration, the trade-off study between weight and performances is required.

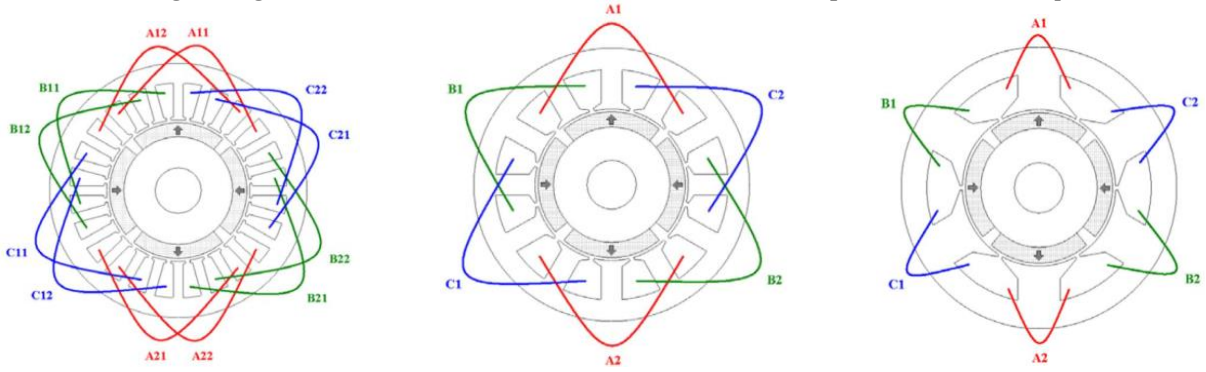

(a) (b) (c)

Figure I. 20. Winding configurations: (a) distributed winding, (b) concentrated overlapping winding, (c) concentrated non-overlapping winding [Ref_10]

Table I. 9. Comparison of advantages and drawback of concentrated and distributed winding [Sar_17] [Ref_10]

Winding configuration	**Concentrated winding**	**Distributed winding**
Advantages	→ less end-winding length → less weight winding → high slot fill factor → improved fault tolerance capability due to small mutual inductance → high self-inductance → easy implementation of inner cooling	→ high fundamental electromagnetic torque → lower iron losses due to poor harmonic content → lower eddy current losses in PM → lower mechanical vibration risk in winding
Drawbacks	→ high eddy current losses in PM → high iron losses due to high harmonic content → high mechanical vibration risk in winding → lower fundamental electromagnetic torque due wealthy harmonic content	→ high end-winding length → more weight winding → lower slot fill factor → lower self-inductance

- *Insulation materials*

Electrical machines use several insulation components as shown in Figure I. 21. Their material choices are very critical considering that electrical and thermal constraints are very harsh. The main insulation types are:

- Slot liner, slot separator
- Conductor or wire insulation

- Wedge
- Phase to phase insulation in slot and in end-winding
- Impregnating varnish and resin
- Insulation of the connection leads and the terminals.

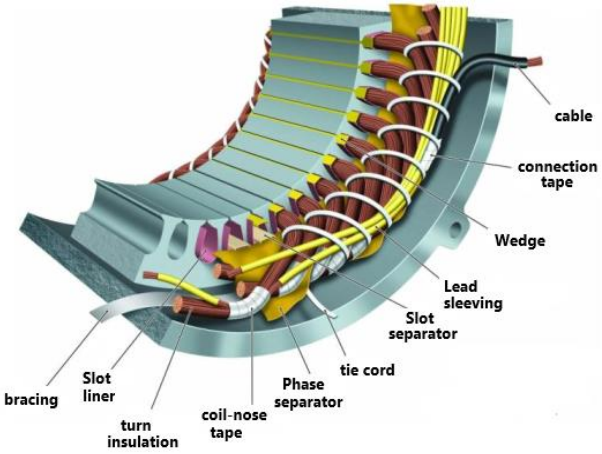

Figure I. 21. Insulation system in electrical motors [Cha_08]

Slot liner prevents conductors to be in contact with the electric sheets. Slot separator and phase insulation provide a high-voltage barrier between conductors, with good formability and mechanical strength. Most of insulation materials used for slot liner, slot separator, phase to phase insulations are made with organic paper, organic fibre, inorganic mica, organic laminated clothes and laminated papers. There are also laminated combinations of materials such as rag paper and organic polyester Film. Wedge is placed over the winding in each slot to close the slot and keep the wires compact and guard against vibration. Typically, wedges are made of paper, canvas and fibber Glass impregnated with a thermosetting resin such as silicone, and organic epoxy. Moreover, insulation comprises also impregnating with varnish and resin. They are used as protection and improve insulation life and reliability. Each insulation material has a characteristic temperature above which it should not operate. Several standard test procedures have been developed to rate the capability of the insulation to resist deterioration at high temperature. Among them there is IEEE standards. The characteristic temperature of IEEE standards is defined from nominal life of 20000 hours as presented in Figure. I. 22.a. Therefore, the following characteristic temperatures can be distinguished: 105°C, 130°C, 155°C and 180°C. Each characteristic temperature describes insulation and thermal class as:

- 105°C → Class "A"
- 130°C → Class "B"
- 155°C → Class "F"
- 180°C → Class "H"

Insulation and thermal classes are divided into maximum ambient temperature, allowable heating and thermal reserve, cf. Figure I. 22.b. Within technological thermal advances of insulation materials, other classes have been added: 200°C, 220°C and 240°C thermal classes. Usually, electric motors are sized to ensure that insulation does not operate above the maximum temperature capability. Furthermore, other characteristics linked to dielectric and mechanical strengths have to be taken into account. Dielectric strength of insulation materials defines the maximum voltage required to produce Partial Discharge (PD) leading progressive deterioration. Partial discharge usually takes place on the air bubbles located near to or inside the insulation material and under electric field higher than the dielectric strength. Moreover, under low pressure environment, PDs can be more prevalent. For high voltage strength, mixing organic insulation materials with inorganic material such as Mica is needed. Mica tolerates PDs during nominal operating of electric machines. Table I. 10 summarizes the intrinsic features of insulation materials.

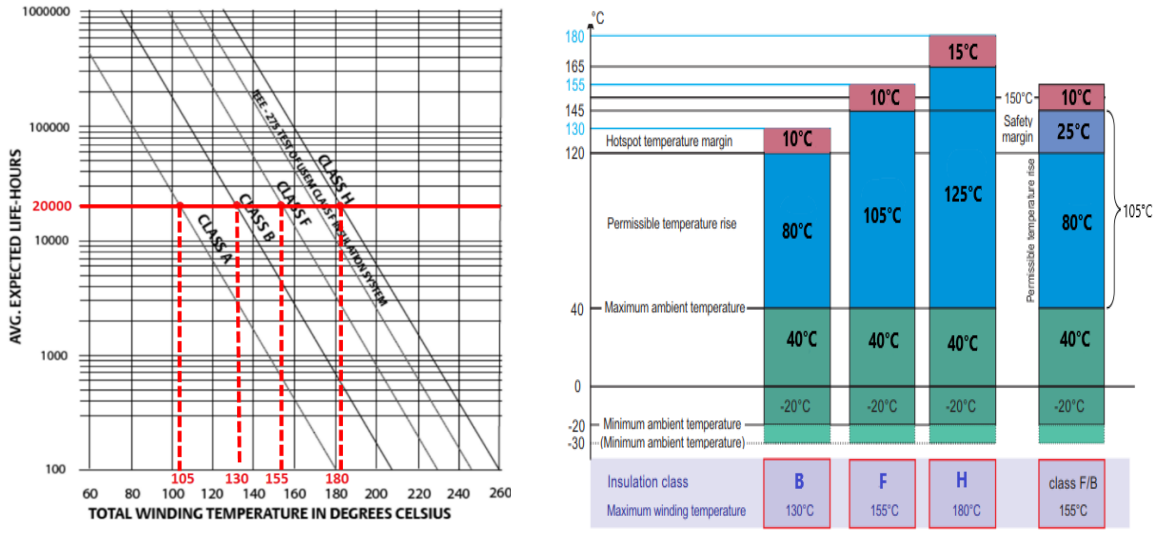

(a) (b)

Figure I. 22. (a) IEEE Standard tests of insulation classes, (b) Insulation and thermal classes

Table I. 10. Intrinsic features of insulators [Pyrh_08]

Insulator (with trade names)	Density [kg/m^3]	Dielectric strength [kV/mm]	Tensile strength [N/mm²]	Elasticity modulus [N/mm²]	Operating temperature [°C]	Thermal conductivity [W.m^{-1}.K^{-1}]
Polyester PTEP film (Mylar, Melinex, Hostaphan)	1380	150	140-160	3900	130	0.29
Polyimide film(Kapton)	1420	280	180	3000	220	0.12
Polysulphone PS film (Flacron, PES)	1370	175	90	2500	180	-
Polyamide(Teflon)	2150	260	13-27	500	180	0.20
Mica folium (silicone binder)	2883	20 to 200	30-50	-	180	0.5-0.6
Epoxy resin	1299	30	-	-	155	0.64
Glass Fiber	2560	18	1000-2000	70000	180	0.99
Cotton Fiber	1520		250-500	5000	105	0.07-0.14

I.2.4 Further improvements in terms of materials and technological solutions

Several technological solutions and material improvements are proposed in order to reduce their weaknesses and losses.

- *Technological solution for reducing losses*

Some technological solutions are under study to reduce main losses in electrical machines. Among these solutions, we can cite electrical steel sheets up to 50µm to reduce iron losses at high frequency (cf. Figure I. 23.b) and axial, radial and circumferential segmentations of permanent magnets up to 0.5mm in order to reduce eddy current losses.

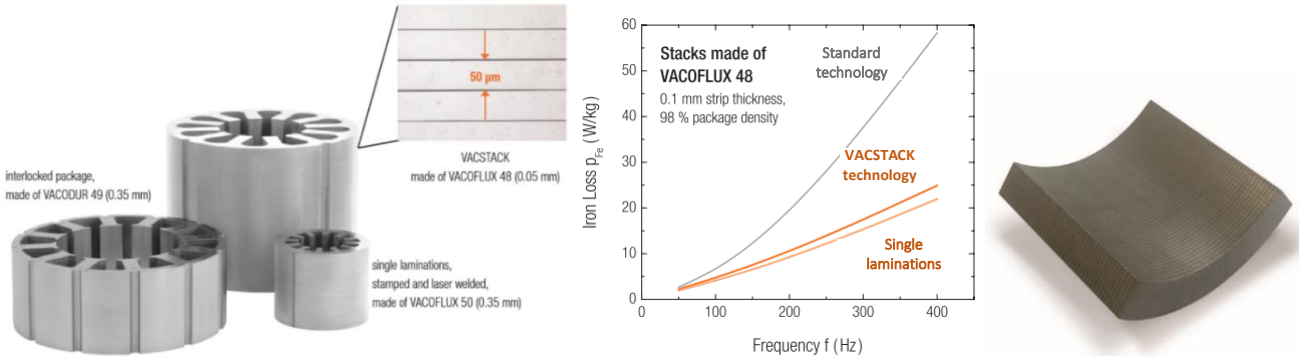

(a) (b) (c)

Figure I. 23. Technological solution for reducing losses: (a) Vacuumschmelze lamination (Vacstack):50µm, (b) Specific iron losses, (c) segmentation in permanent magnets up to 0.5mm (Arnold Magnets)

- *High temperature NdFeB magnets*

In 2018, Arnold magnetic technologies manufacturer proposed new NdFeB magnets called "Grain Boundary Diffused Neodymium Iron Boron *GBD Neo*" suitable for high operating temperature with high magnetic energy [ArnoldsCata]. GBD Neo is made with reducing Dysprosium (Dy) and Terbium (Tb) contents. Figure I. 24 compares the traditional NdFeB magnets with the new generation of NdFeB.

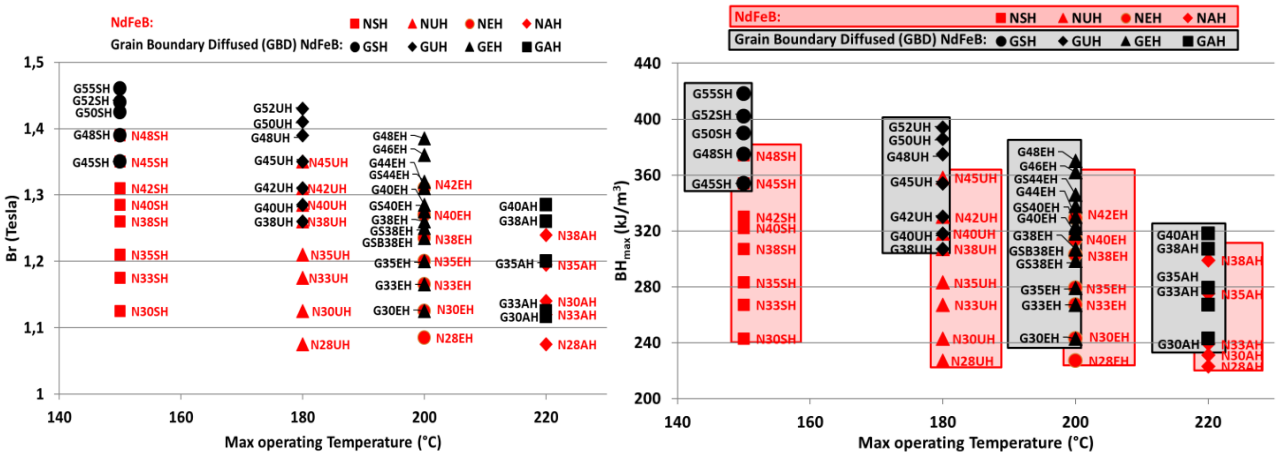

(a) (b)

Figure I. 24. Comparison of High temperature NdFeB with New high temperature GBD NdFeB: (a) Remanent flux density vs max. operating temperature, (b) Magnetic energy vs max. operating temperature (Arnold Magnets) [ArnoldsCata]

- *Wires for very high temperature*

New wires with very thin ceramic insulation are proposed to improve the thermal resistance and the dielectric strength [CerCat]. These wires are made of 73% copper and 27% nickel. Their insulation thickness is between 5 to 20µm as shown in Figure I. 25. Using ceramic as insulation offers advantage of operating at high temperature up to +500°C, however ceramic insulator has very low dielectric strength. Its breakdown voltage is 150V AC. Therefore, ceramic insulator is attractive for electric motors with allowed partial discharges (case of long term target). Otherwise, ceramic insulator is less attractive (case of medium term target). It is also important to note that ceramic is mechanically sensitive to vibrations.

Figure I. 25. Ultra-thin and high temperature ceramic wire [CerCat]

I.2.5 Bearings

Bearings in electrical machines are used to eliminate friction, to carry loads, to locate and align the shaft axially [Mal_06] [TimPr]. There are two types of bearings: magnetic bearings and mechanical bearings. Magnetic bearings support loads using magnetic levitation as illustrated in Figure I. 26. They do not require lubrication and maintenance since there is no contact. Due to requirement of control device, electric supply and sensors for magnetic levitation operating, magnetic bearings are heavy and not compact unlike mechanical bearings. Mechanical bearings can be classified into: thrust bearings and radial bearings. Thrust bearings accommodate loads that are predominantly in the direction of shaft. In this thesis thrust bearings are not considered. Radial bearings accommodate loads that are perpendicular to the shaft. The commonly radial bearings used in electrical machines are:

- *Deep groove ball bearings*: rings of deep groove ball bearings are made with steel as illustrated in Figure I. 27.a. They are suitable for high speeds and small radial and axial loads as illustrated in Table I. 8.
- *Angular contact ball bearings*: have inner and outer ring raceways that are displaced relative to each other in the direction of the bearing axis (cf. Figure I. 27. b). Usually they are suitable for high combined loading. In addition, as deep groove ball bearings, angular contact ball bearings are used for high speed.

- *Cylindrical roller bearings*: rollers are cylindrical as shown in Figure I. 27. c. The shape of rollers allows bearings to handle high radial loads. Cylindrical roller bearings are also suitable to high speed.
- *Spherical roller bearings*: have two rows of spherical rollers. A common sphere outer ring raceway and two inner ring raceways inclined (see Figure I. 27d). This type of bearings can handle very heavy radial and lower axial loads at low speed.
- *Toroidal roller bearings*: have one row of long, slightly barrel-shaped symmetrical rollers and torus-shaped raceway profiles as presented in Figure I. 27e. They are designed to accommodate high radial loads and for high speed as noted in Table I. 11. Figure I. 28 shows limit speeds function of inner diameter and handle static loads of bearings manufactured by SKF.

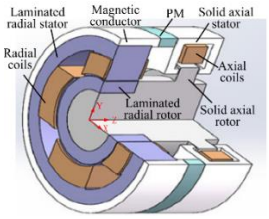

Figure I. 26. Magnetic bearings [Le_16]

(a) (b) (c) (d) (e)

Figure I. 27. SKF Radial bearings types (a) Deep groove ball bearing, (b) Angular contact ball bearing, (c) Cylindrical roller bearing, (d) Spherical roller bearing (e) Toroidal roller bearings [SKFCat]

Table I. 11. Bearing performance characteristics [Mal_06] [TimPr]

Bearing type	Speed capability	Radial loading	Axial loading	Combined loading
Deep groove ball bearing	5	3	3	3
Angular contact ball bearing	5	3	4	4
Cylindrical roller bearing	5	5	2	2
Spherical roller bearing	3	5	2	3
Toroidal roller bearing	4	5	1	2

Notation is scaled from 1(being poor) to 5 (being excellent)

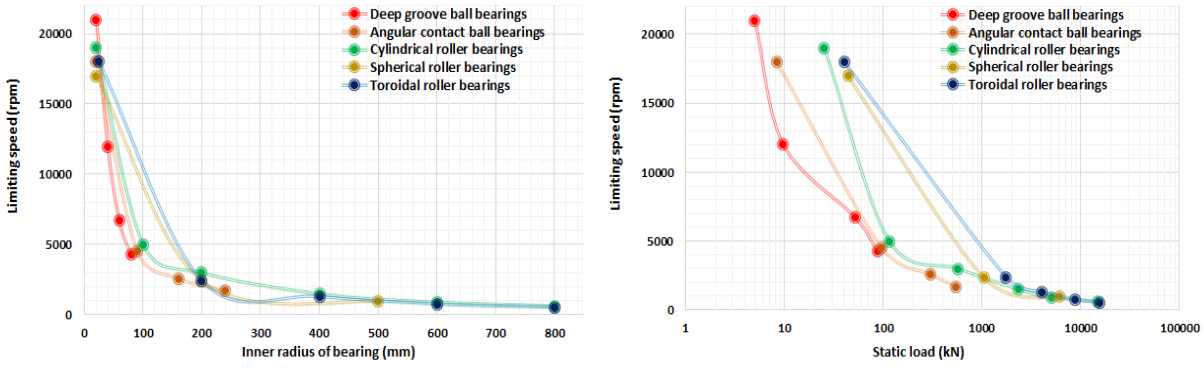

(a) (b)

Figure I. 28. SKF bearings: (a) Limiting speed vs inner radius of bearing, (b) Limiting speed vs static load [SKFCat]

- Further radial bearing type: "Hybrid bearings"

Hybrid bearings have rolling element made with ceramic as shown in Figure I. 29. They are characterized by lower density of rolling element about 60% than other types of bearings with the same sizes. The reduced lower density and inertia offer a higher speed capability.

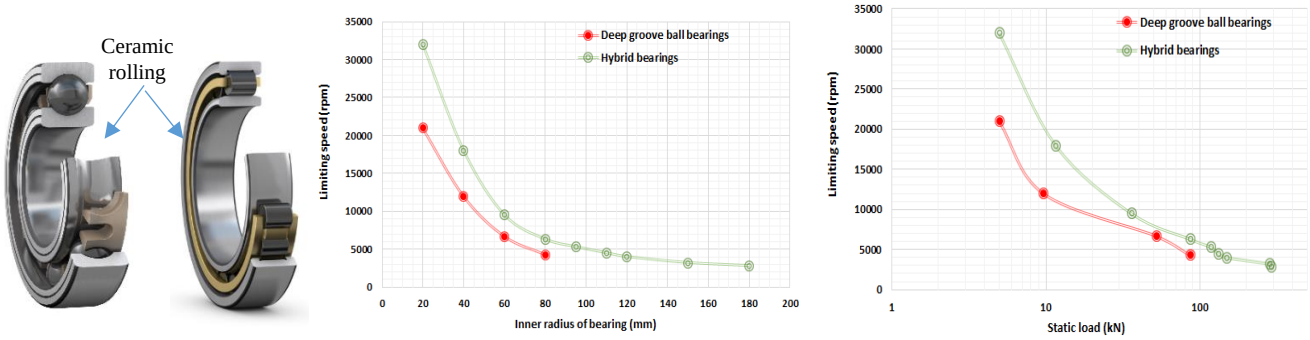

(a) (b) (c)

Figure I. 29. (a) Hybrid Bearings, comparison between classic deep groove ball bearings: (b) limiting speed vs inner radius, (c) limiting speed vs static load [SKFCat]

I.2.6 Sleeves

In high speed electric machines, permanent magnets are usually retained by sleeves for magnets mounted on the surface or by electrical sheets for buried magnets. Two groups of sleeves can be distinguished:

- Non-magnetic metallic sleeves: made with Titanium or Inconel,
- Non-metallic wound sleeves: made with Carbon Fiber or Glass Fiber as shown in Figure I. 30.

Due to their high permissible stress, non-metallic wound sleeves ensure high permitted peripheral speed up to 320m/s compared to non-magnetic metallic sleeves (cf. Table I. 12). Moreover, non-metallic wound sleeves are lighter weight than the non-magnetic metallic sleeves and have lower eddy current losses for Carbon Fiber and none losses for Glass Fiber. However, for high temperature environment higher than 180°C only non-magnetic metallic sleeves are suitable. Trade-off between mechanical, thermal and electrical properties should be done to choose sleeves for surface mounted permanent magnets electrical machines.

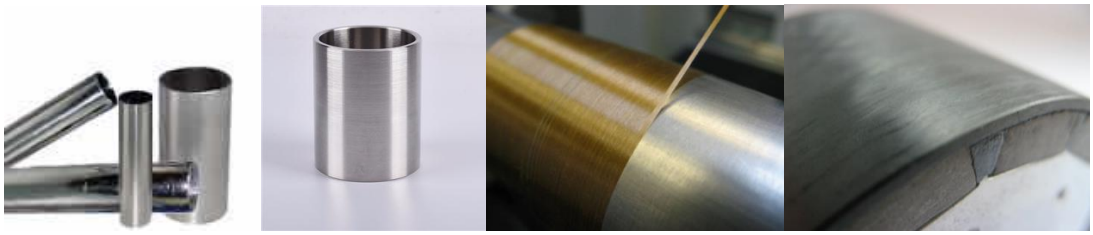

(a) (b) (c) (d)

Figure I. 30. Sleeves: (a) Titanium, (b) Inconel, (c) Carbon Fiber, (d) Glass Fiber [ArnoldCata]

Table I. 12. Properties of retaining sleeve materials used in surface mounted permanent magnet synchronous machines [Zha_15] [Gie_10] [Fan_15]

Sleeve materials		Non-magnetic metallic sleeve		Non-metallic wound sleeve		
		Titanium	Inconel	Carbon Fiber		Glass Fiber
Properties	Unite			Radial	Tangential	
Density	[kg.m^{-3}]	7850	4400	1620		1900
Elastic modulus	[GPa]	206	205	140	8.8	45
Poisson ratio	-	0.31	0.28	0.28	0.015	0.2
Maximum permissible stress	[MPa]	-	1100	1400	-100	1200
Thermal conductivity	[W.m^{-1}.K^{-1}]	16	7.5	0.71		<1
Electric conductivity	[S.m^{-1}]	6.1×10^5	8×10^5	3×10^4		0
Eddy current losses	-	high	high	low		none
Maximum peripheral speed	[m/s]	240		320		
Maximum temperature	[°C]	290		180		

I.2.7 Cooling technologies

Cooling for electric machines is mandatory for remove heat and for decrease temperature within electric machine. In addition, cooling electric machines allow preserving the life of bearings and insulation system, to prevent the demagnetization of permanent magnets and to prevent excessive heating of the surroundings.

Typically, in industrial and commercial electric machines, heat transfer is: natural, forced or combination between natural and forced heat transfer modes.

In low power electric machines, heat is removed:

- by natural convection on the external surface of fins for closed configuration,

- by natural convection on all surfaces of opened configuration,
- by conduction on all solid area,
- by radiation to ambient environment.

In medium and high power electric machines, heat is removed:

- by conduction on all solid area,
- by forced convection of liquid coolant,
- by forced convection of air due to rotor rotation.

Natural and forced heat transfer modes can be distinguished by heat transfer coefficient "h_{cv}". Table I. 13 shows some typical values of heat transfer coefficient of some common coolants and depending on cooling modes. Forced heat transfer mode is characterized by high heat transfer coefficient up to 7000W.m^{-2} K^{-1} while natural mode is characterized by low heat transfer coefficient.

There are several classical forced cooling methods used electric machines. They can be classified according to their location and to their cooling approach as given in Table I. 14.

Table I. 13. Typical values of heat transfer coefficient of some coolants [Wei_14]

Coolant	Heat transfer coefficient h_{cv} [W.m^{-2}.K^{-1}]	
	Natural convection	Force convection
Air	5 to 20	20 to 200
Water	30 to 300	300 to 7000
Engine Oil	100 to 300	400 to 2000

Table I. 14. Summary of forced cooling methods

Location	**Cooling approach**	**Cooling technology**	**Used coolant**
Housing	Indirect cooling method	Housing jacket	Oil, Water, Ethylene Glycol Water 50/50
Stator core	Direct cooling method	Cooling channels	Water, oil, air
Slot	Direct cooling method	• Cooling channels • Inner coolant ducts	• Air, oil • Water, Polyalphaolefin Oil (PAO)
	Indirect cooling method	• Direct heat exchanger • Cooling channels	• Water • Ethylene Glycol Water 50/50
End-winding	Indirect cooling method	• Liquid jet impingement • Spray cooling • Potting materials	• Oil • potting materials
Rotor core	Direct cooling method	Axial ducts	Air
Shaft	Direct cooling method	Cooling channels	Water, oil

- ***Housing cooling***

Housing jacket is an indirect cooling method. It is used for improving the heat transfer from the active part of the stator to the housing through conduction by contact between the housing and the stator and by convection in the coolant ducts, cf. Figure I. 31. There are many housing jacket topologies: spiral housing jacket, U-shaped with one duct, U-shaped with bifurcations, axial housing jacket as shown in Figure I. 31. Due to its practical manufacturing, U-shaped with one duct topology is the most used in industrial motors, especially, electric motor of hybrid electric vehicles as given in Table I. 15.

Effectiveness and limitations: housing jacket is an efficient cooling method for stator active parts; however, it is not efficient to dissipate heat from end winding and rotor. Moreover, its heat transfer capacity strongly depends on the cooling surface [Satru_17].

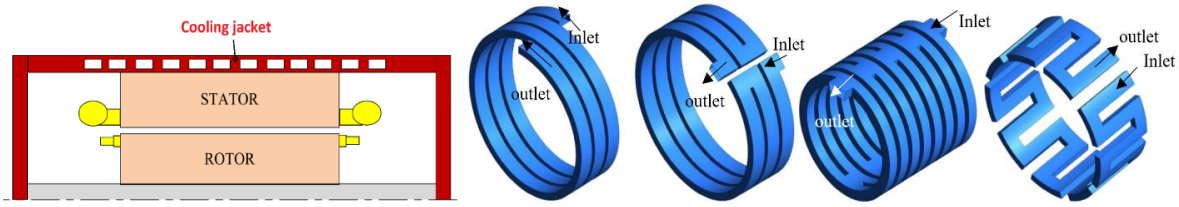

(a) (b) (c) (d) (e)

Figure I. 31. (a) Cooling jacket in housing, configurations: (b) spiral, (c) U-shaped (one duct), (d) U-shaped (bifurcated), (e) axial [Satru_2017]

Table I. 15. Industrial electric motors of HEV use housing jacket

HEV electric motor	Peak power [kW]	Specific power [kW/kg]	Coolant of housing jacket
Toyota Prius 2010	60	1.6	Oil
Sonata 2011	30	1.1	Oil
Nissan Leaf 2012	80	1.4	Ethylene Glycol Water 50/50
SRM 2015 Newcastle University	80	1.5	water

- ***Stator core cooling***

Core stator can be directly cooled by channels as shown in Figure I. 32. Integrate cooling channels inside stator core allows to decrease the temperature winding more efficiently than housing jacket. However, high saturation magnetic flux can be achieved around cooling channels which leads to an increasing of iron losses and a decreasing in electromagnetic torque. For this purpose, cooling channels should be having small sizes. As previous cooling method, stator core cooling method is not enough efficient to dissipate heat of end-windings.

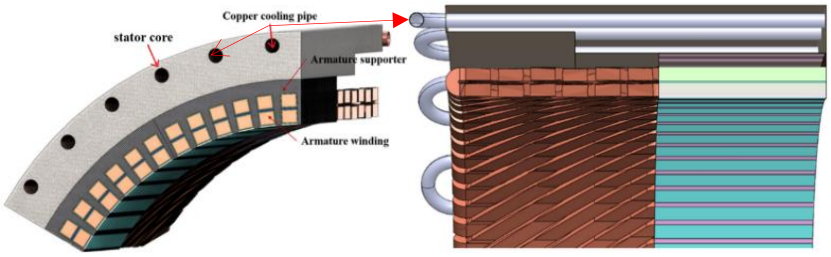

(a) (b)

Figure I. 32. cooling channels inside stator core: (a) stator structure (b) cooling channels [Kim_17]

- ***Slot cooling***

Several cooling methods used in slot are proposed given that losses in winding are the most difficult losses to remove due to the low thermal conductivity of insulation materials. We distinguish two cooling methods:

- indirect cooling methods: include all cooling techniques which are based on cooling applied between conductors,
- direct cooling methods: include all cooling techniques which are based on cooling inside conductors.

Indirect cooling method: "Direct Heat Exchanger":

Direct heat exchanger is an indirect cooling method. It is made up of several axial flow channels placed between slot winding as illustrated in Figure I. 33. These flow channels are connected through nonconductive bulkhead where the inlet and the outlet of fluid are located. Each flow channel is made of two copper plates using microfeature mesochannel technology to enhance the heat transfer coefficient. These copper plates are covered by insulation layer to separate them from conductors of winding. The fluid coolant is pumped by external pump [Sem_14].

Effectiveness and limitations: according to experimental tests carried out, direct heat exchanger cooling method is an efficient method by considering that the achieved current density was 24.7A/mm² for F (155°C) winding class [Sem_14]. Direct heat exchanger is straightforward to apply to the concentrated winding. However, the direct heat exchanger could be challenging to apply to a distributed winding due to significant end-winding length.

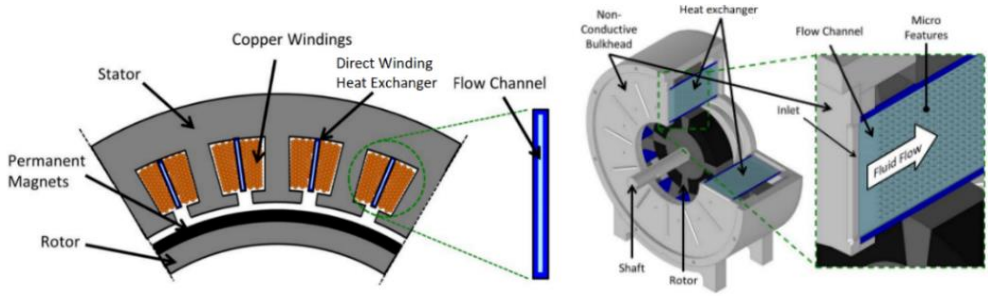

(a) (b)

Figure I. 33. (a) Direct winding heat exchanger placed between winding, (b) machine prototype [Sem_14]

Indirect cooling method: "Cooling channels"

Cooling channels inside slot is another indirect cooling method applied on concentrated winding as illustrated in Figure I 34. The gaps resulting by chosen flat wires are used to insert parallel connected cooling channels in the bottom and in the middle as proposed in [Sch_15]. These channels are made of copper surrounded by a polyamide film which circulates inside the Ethylene Glycol Water 50/50.

Effectiveness and limitations: as previous cooling method, this technology is efficient when considering the high achieved current density (i.e. 20A/mm² according to [Sch_15]). However, it remains challenging to implement in distributed winding.

(a) (b) (c)

Figure I. 34. Indirect slot cooling: (a) cooling concept of slot with flat wires, (b) cooling in single tooth (c) assembly electric machine with indirect slot cooling [Sch_15]

Direct cooling methods:

Otherwise, for indirect cooling methods, the flow of coolant is directly integrated inside each conductor. Several direct cooling methods are proposed depending on the conductor types and structures:

- Litz wire winding with inner coolant ducts,
- Laminated winding with air and oil channels.

Inner coolant ducts for Litz-wire winding: are chosen by *Lindh et al* [Lin_16] to achieve high current density of axial electric motor winding. Figure I. 35 shows the conductor with its coolant conduit. 14A/mm² is achieved in steady state using this cooling technology.

Air and oil cooling channels for laminated winding: are proposed by [Rei_14] [Tig_16]. Coolant passes between laminations as illustrated in Figures I. 36 and 37. With an air flow rate of 600L/min, the achieved current density is 22.5A.mm^{-2} with H (180°) thermal class [Rei_14], whereas for an oil flow rate of 2L/min, the achieved current density is 50A.mm^{-2} [Tig_16].

Effectiveness and limitations: integration of coolant directly inside conductor has the advantage to reduce significantly the thermal resistance between conductor and coolant which improves cooling efficiency. However, this cooling method is more sensitive to damage risks compared to indirect cooling methods.

The heat transfer coefficients of indirect and direct cooling methods are summarized in Table I. 16.

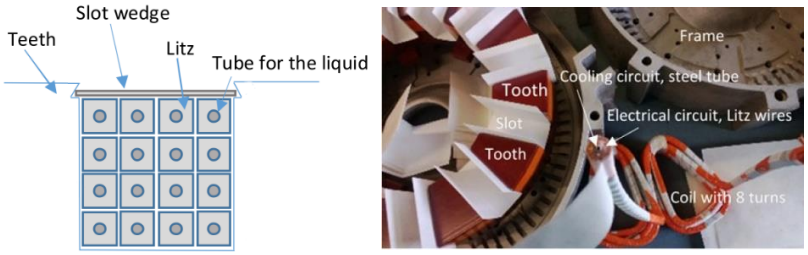

(a) (b)

Figure I. 35. (a) Stranded and transposed winding conductors with coolant ducts, (b) Prototype of the stator with its coils [Lin_16]

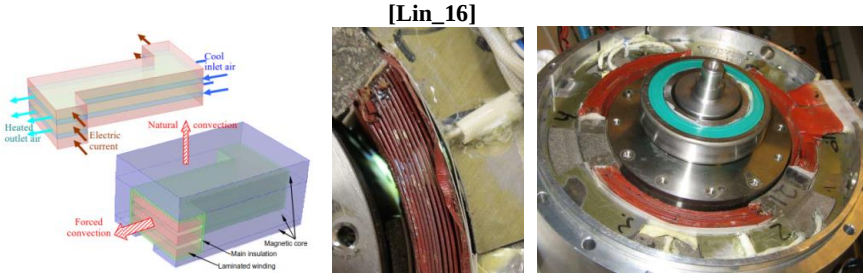

(a) (b) (c)

Figure I. 36. Laminated winding with electric conductive strips and air channel cooling, (b) zoom in prototype laminated winding, (c) machine prototype [Rei_14]

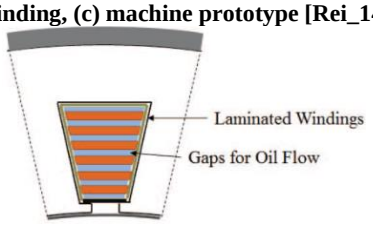

Figure I. 37. laminated winding with oil channel cooling [Tig_16]

Table I. 16. Heat transfer coefficients and achieved current densities according to slot cooling methods

Cooling methods			**Current density (steady state)**	**Thermal class**	**Heat transfer coefficient ($W.m^{-2}.K^{-1}$)**	**Reference**
slot	Indirect cooling	Heat exchanger	**24.7A.mm^{-2}**	F (155°C)	5000 to 10000	[Sem_14]
		Cooling channel	**20A.mm^{-2}**	-	6000	[Sch_15]
	Direct cooling	Litz wire winding with inner coolant conduits	**14A.mm^{-2}**	-	-	[Lin_16]
		Laminated winding	**22.5A.mm^{-2}**	H(180°C)	325 to 400	[Rei_14]

- ***End-winding cooling***

Usually due to rotor rotation, end windings are naturally cooled by forced convection. Its efficiency requires important end-winding surface. To improve cooling of end-winding other methods are applied. We distinguish two cooling methods for end-windings using oil: Impingement of liquid jets or sprays and another cooling method using potting materials.

Oil jet impingements: as flat jet nozzle injections and dripping jets have been studied by [Dav_15]. Figure I. 38 illustrates oil jet impingements applied in end-winding. Oil jet impingement cooling method requires high flow rate for improving the heat dissipation in end-windings.

Oil sprays: in contrast to oil jet impingement, oil spray cooling method requires only low flow rate with high pressure [Lud_17]. Figure I. 39 shows examples of oil spray applied on distributed and hairpin end-windings.

Effectiveness and limitations: according to [Dav_15] the dissipation heat in end-winding using oil jet impingements cooling method can be mutiplied by a factor of 2.5 to 5. In addition, through experimentally tests of oil sprays on stator and rotor end-winding performed by [Lud_17], high current densities are achieved: 18A/mm^2 for stator and 17A/mm^2 for rotor. As the coolant is in direct contact with the winding, damage risks limit the use of oil jet impingements and oil sprays cooling methods.

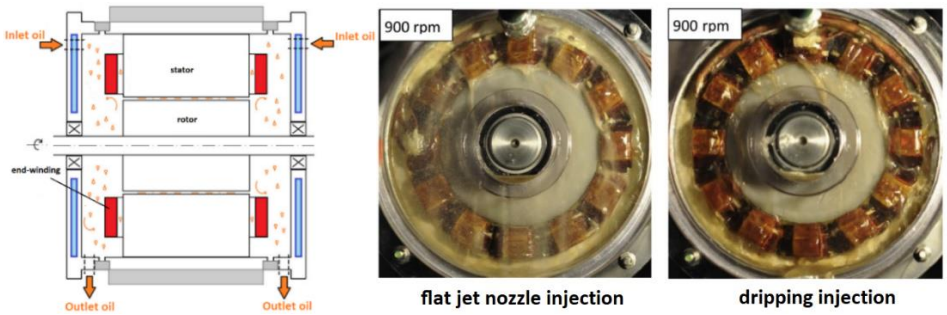

(a) (b)

Figure I. 38. (a) oil jet cooling system for end-winding, (b) experimental two jet impingement methods [Dav_15]

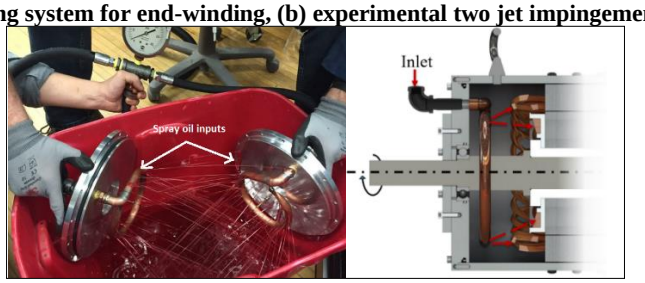

Figure I. 39. Oil spray cooling on the stator and rotor distributed end-winding [Lud_17]

Potting materials: consist of creating a conductive thermal path between end-windings and the housing, by using materials with a thermal conductivity higher than the thermal conductivity of the air, as it is illustrated in Figure I. 40. Table I. 17 summarizes some examples of potting materials applied in end-windings. Often, potting material cooling method requires a combination with water jacket in order to improve heat dissipation.

Effectiveness and limitations: a decreasing of 7°C and 6°C can be reached in end-winding according to [Pol_14]. However, potting material cooling method is less efficient than the previous two end-winding cooling methods.

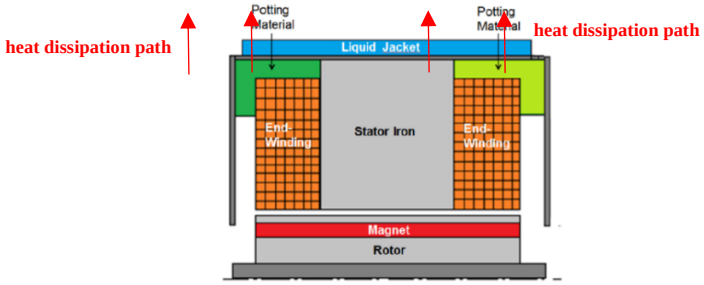

Figure I. 40. Potting materials for end-windings cooling [Pol_14]

Table I. 17. Electrical and thermal properties of potting materials [Pol_14]

Potting Materials	*Thermal conductivity [$W.m^{-1}.K^{-1}$]*	*Heat capacity [$J.kg^{-1}.K^{-1}$]*	*Density [$kg.m^{-3}$]*	*Limit temperature [C°]*	*Dielectric strength [kV/m]*	*Electric resistivity [Ω.m]*
Ceramacast 675N	*100*	*740*	*3260*	*1200*	*1.2×10^{4}*	*10×10^{11}*
Epoxy 2315	*58*	*1000*	*1800*	*185*	*1.9×10^{4}*	*10×10^{14}*
Alumina Filled Epoxy	*20-25*	-	-	-	-	*10×10^{15}*
AIN Filled Epoxy	*3.8*	-	*2470*	*143*	-	*10×10^{16}*
Silicone	*2.0*	-	*1960*	*250*	-	*10×10^{16}*

- ***Rotor core cooling***

Often rotor cores are cooled by axial ducts as shown in Figure I. 41. An axial air flow passes through rotor ducts. Its flow rate increases within rotational speed increasing as it is experimentally demonstrated in [Ch_15]. Therefore, axial rotor ducts cooling method is efficient only for high rotational speed. Dipping rotor core to implement axial ducts allows to decrease the rotor weight and then to increase specific power of electric machine. However, the dipping should be carefully studied in sizing rotor phase in order to not decrease electromagnetic performances due to the increase in saturation of the flux density in the rotor core.

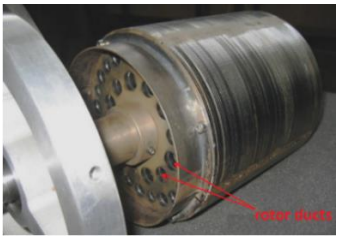

Figure I. 41. Axial rotor ducts: forced air convection cooling method [Ch_15]

- ***Shaft cooling***

Liquid cooling method is the most involved in shaft. Figure I. 42 illustrates the proposed liquid coolant channel implemented in hollow shaft. A stationary cooling channel is implemented inside the shaft with a cross-section small enough to leave a gap between the shaft and the cooling channel. The liquid coolant enters through a stationary channel and exits through the gap between the shaft and the stationary cooling channel. Due to the shaft rotation, the cooling channel should be well maintained to avoid any vibration between the cooling channel and the shaft. Moreover, the shaft hollowing should be well studied due to mechanical stresses applied on the shaft, therefore, manufacture this cooling method remains complicated.

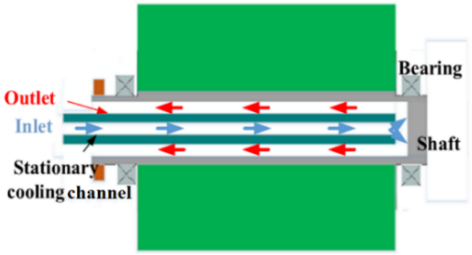

Figure I. 42. Cooling channel in shaft [Gia_17]

Further cooling methods "change phase cooling method: Heat pipes"

Another cooling methods of electrical machines based on change phase principle are currently being developed. The phase change principle consists on a self-transportation of coolant from vapour phase located near the hot source to liquid phase near the cold source. In fact, the coolant is driven by an inner wick which does not require any external pumping as illustrated in Figure I. 43. This cooling method is widely used in electronic devices and it is known as "heat pipes". In the presence of temperature gradient, heat pipes can operate passively. In otherwise, heat pipes operate actively thanks an external condenser. In literature several structures using heat pipes actively operated are proposed:

- on the external surface of housing [Put_17],
- inside slots and stator core [Has_12],
- inside the shaft (Tesla motor patent [Tes_13]) as presented in Figure I. 44.

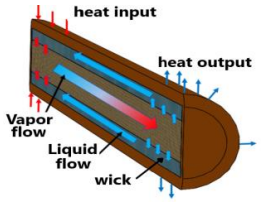

Figure I. 43. Heat transfer principle in heat pipe

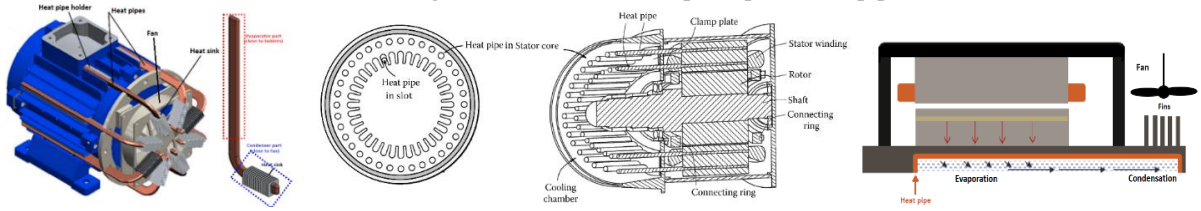

(a) (b) (c)

Figure I. 44. Heat pipe cooling methods proposed in electric machines: (a) housing [Put_17], (b) slots and stator core [Has_12], (c) shaft [Tes_13]

I.2.8 Conventional industrial motors

- ***Electric motors for railway traction application***

In industrial applications with power range between 300kW-3MW such as railway tractions, three conventional electric motor topologies are involved:

- Wound Rotor Synchronous Machines (WRSM)
- Permanent Magnet Synchronous Machines (PMSM)
- Induction Machines (IM)

These topologies are most used due to:

- The high starting torque and high power factor of WRSM,
- The high efficiency and compactness of PMSM,
- The high robustness and low cost manufacturing and maintenance of IM.

In railway traction, the achieved specific power of WRSM and IM is less than 1kW/kg and equal to 1kW/kg for PMSM as shown in Figure I. 45.

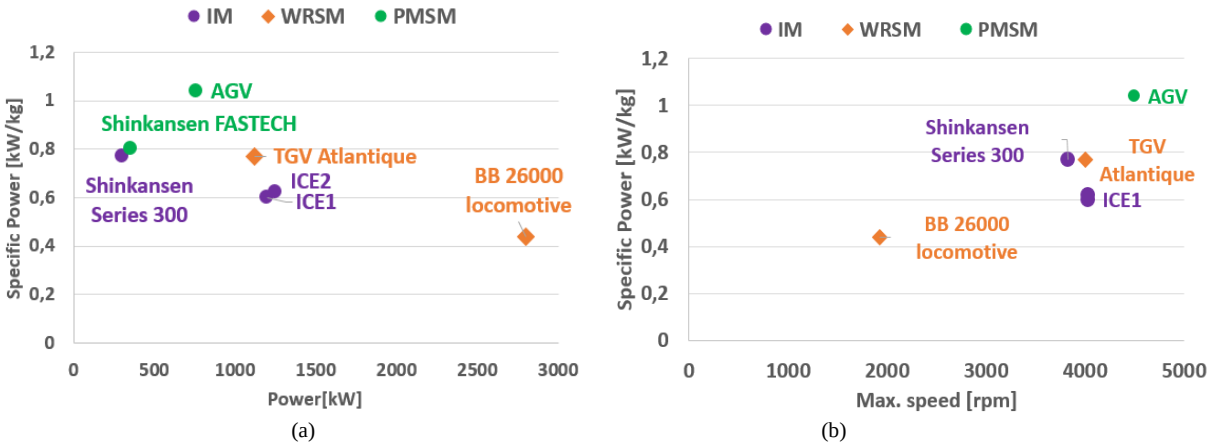

(a) (b)

Figure I. 45. Conventional electric motors used in railway traction: (a) specific power vs power, (b) specific power vs max. speed [Aab_14]

- ***Electric motors of Hybrid Electric Vehicle application***

In Hybrid Electric Vehicles (HEV), the electrical machines have been designed to reach high-specific power and high performances. Several topologies of electrical machines have been proposed as interior permanent magnet synchronous machine IPM, surface mounted permanent magnet synchronous machine PMSM, solid induction machine IM and hybrid permanent magnet synchronous machine HSM. IPM having a V shape is the most used topology in HEV (power range ≤ 200kW) due to their advantages [Sar_17]. HEV using IPMs are: 2004 Prius, 2006 Accord, 2007 Camry, 2008LS600h and 2012 Leaf. IPM ensures high airgap flux density (greater than PM remanent flux density B_r) with no losses in PM. In addition, due to the reluctance torque generated by PM saliency, IPM can be designed with reduced electric loads compared to PMSM. Figure I. 46 illustrates the different rotor structures. Moreover, IPMs are suitable for high rotating speed up to 14000rpm (rotor magnetic sheet ensures mechanically holding, therefore no sleeve is used). However, the armature reaction flux of IPM is high, consequently high performances are required for power converter unlike to PMSM. The highest specific power density achieve with IPMs is 2.5kW/kg for a maximum rotating speed of 10230rpm and for a mechanical power of 110kW as shown in Figure I. 47. HSM is a special IPM designed for generating an high torque. BMWi3 used this topology to improve the efficiency of classic IPMs over the operating range. The achieved specific power of HSM is 1.9kW/kg for a maximum rotating speed of 11400rpm and for a mechanical power of 125kW. The surface Mounted PMSM is used in Sonata 2011 HEV. The achieved specific power is 1.1kW/kg for 6000rpm and 30kW. Tesla S60 has selected solid rotor induction topology for its electric motor (cf. Figure I. 47). Solid rotor ensures a highest mechanical strength for high speed electric machine, which allows to improve specific power [Bin_14]. IM of Tesla S60 has a power of 225kW with a rotation speed of 14800rpm. Its achieved specific power is 4.3kW/kg. The latter value is the highest specific power for electric motor of HEV [Hend_14].

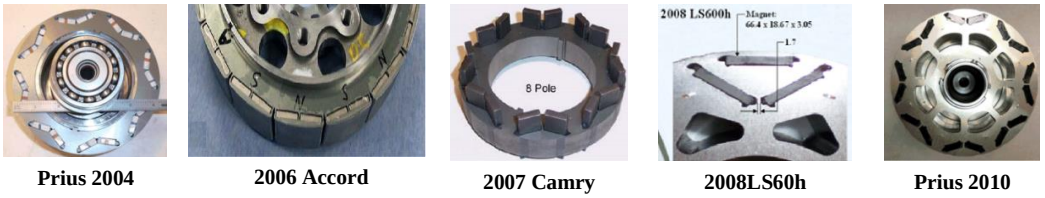

Figure I. 46. Rotor topologies of electric motors used in HEV [Hend_14] [Sar_17] [Sta_17]

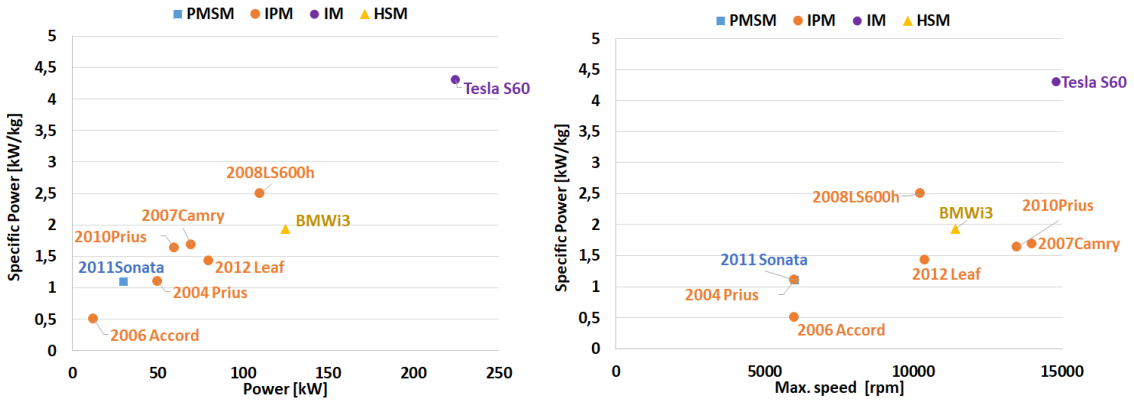

(a) (b)

Figure I. 47. High Specific Power Electric Motor in Hybrid Electric Vehicle: (a)specific power vs Power, (b) specific power vs max. speed [Hend_14] [Sar_17] [Sta_17]

I.3 Limitations of specific power

Several aspects limit the increase of the specific power of electric motors; we can cite three main limits:

- Mechanical limits,
- Electromagnetic limits,
- Thermal limits.

I.3.1Mechanical limits

Rotational speed of electric machines is limited by static and dynamic limits:

- Static limit is linked to the centrifugal forces,
- Dynamic limit is linked to the vibrations of rotor-bearings.

Under high speed rotation, centrifugal forces applied on rotor components become very significant and two vibration types can be arising. Centrifugal forces have ability to radially push out the rotor components as permanent magnet and winding as presented in Figure I. 48.a. While vibrations generate instability operating due to self-excited vibrations and elastic distortion due to resonant vibrations as presented in Figure I. 48.b. Self-exited vibrations arise after a certain threshold speed that is correlate with intrinsic properties of system. Above these vibrations, the rotor cannot operate. Resonant vibrations occur when the speed of the rotor coincides with one of the resonant frequencies as explained in [Sin_12] [Bor_10].

Furthermore, for high speed rotation, mechanical losses as windage losses are significant due to their nonlinearly increasing with rotational speed. Therefore, these losses induced additional heating on all rotor components causing then an irreversible demagnetised risk in permanent magnets. In chapter 2, the mechanical limits will be detailed.

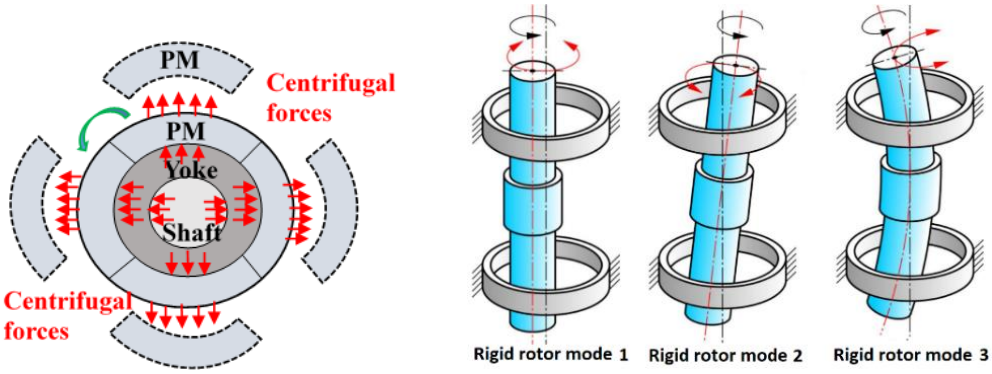

(a) (b)

Figure I. 48. (a) Static limit (centrifugal forces), (b) Dynamic limit (vibrations and elastic distortion) [Can_14]

I.3.2Electromagnetic limits

- *Power Converter-Electric Motor limit:*

Limits coming from connection "Power Converter-Electric Motor" are not insignificant. Usually, power converters with Pulse Width Modulation "PWM" control are used to limit the electric motor harmonics and their corresponding losses. However, high electric motor frequency may become problematic for power converter with PWM control due to its maximum allowed switch frequency (20kHz to 50kHz). Full Wave Control "FWC" may be an alternative to this problem of the power converter. However, using FWC for power converter can causes significant thermal issues for electric motor due to the FWC high harmonic contents [Dri_05].

- *Dielectric insulation limit:*

Another electric limit comes from high induced voltage due to high operating speed or from voltage rise generated by power converter. Therefore, insulation winding undergoes huge electric stress. The latter leads to recurrent partial discharge risks that create in turn degradation on insulation surface, an increasing of temperature and accelerate ageing. According to [Bra_92], time life of insulation winding decreases by half for every increasing of 10°C over their thermal class as shown in Figure I. 49.

To avoid partial discharge risks, insulation winding is often enhanced by using additional insulation systems. Nevertheless, as insulation materials are bad thermal conductors, extraction of heat from winding becomes a huge challenge for cooling. On other side, enhancing insulation of electric machines prevents the increase of the specific power.

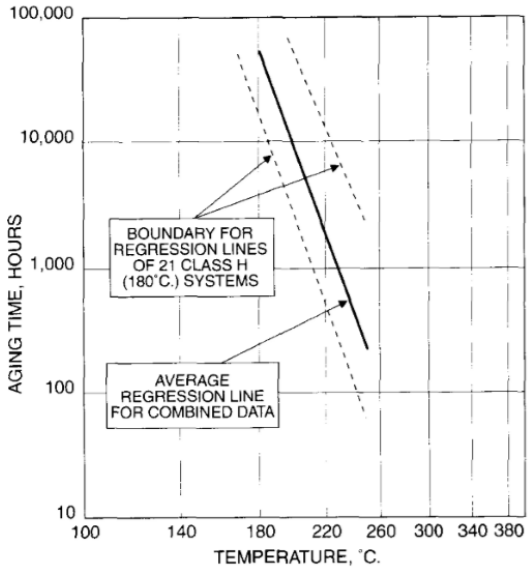

Figure I. 49. Temperature-life characteristics for Class H (180°C) insulation systems [Bra_92]

- *Magnetic limit:*

As highlighted previously, main magnetic limit is linked to hard materials due to irreversible demagnetization risk. The last one is due to the temperature sensitive of hard materials. Indeed, magnetic limits are strongly linked to thermal limits as discussed in the following section.

I.3.3Thermal limits

Maximum temperatures sustained by insulation and hard magnetic materials define the main thermal limits in electric machines. Commonly, rising of temperature is caused by the heat sources due to electromagnetic and mechanical losses, including:

- joule losses in conductors $P_j \propto R_s(\rho(T), \Omega) j^2$,
- iron losses in electrical sheets $P_f \propto k\, \Omega^{\alpha} B^{\beta}$,
- eddy current losses in hard magnetic materials $P_{edd} \propto \rho(T)\, \Omega^2\, B^2$,
- friction losses in bearings $P_{friction} \propto \Omega$,
- windage losses in all rotating surfaces $P_{windage} \propto \Omega^{\gamma}$.

Where: Ω is the rotational speed, *k*, α and β are the coefficients of iron losses, R_s is the resistance function of resistivity ρ and temperature *T*.

In fact, increasing technological levels for instance the rotation speed, the flux density level in hard and soft materials improve the specific power. But in the same time, losses increase. In this case, extraction and evacuation of the latter may be a serious issue due to the low thermal conductivity of the construction parts of the electric machine, with the exception of the conductors (cf Table I.18). Moreover, evacuation through small areas makes it more complicated from thermal standpoint as expressed thermal resistance:

$$R_{thermal} = \frac{e}{\lambda_{th} S} \qquad \text{(I. 3)}$$

where λ_{th} is the thermal conductivity, *S* is the surface and *e* is the thickness.

On the other hand, rising temperature may be dangerous when significant changes in material properties for instance in hard magnetic materials. Therefore, performance of electric machine can be easily affected.

Table I. 18. Typical values of thermal conductivity of constructional parts of electric machine

Construction parts of electrical machine	Thermal conductivity range [$W.m^{-1}.K^{-1}$]
Insulation materials	0.15 to 1
Hard magnetic materials	7 to 11
Electrical sheet materials	10 to 46
Conductors: "copper"	380

Conclusion

Hybrid **A**ircraft academic re**S**earch on **T**hermal and **E**lectrical **C**omponents and **S**ystem "HASTECS" project is one of the **Clean Sky 2** program projects which aims to reduce noise and CO_2 emissions. Thereupon, increasing specific power of each hybrid propulsion components is the main HASTECS goal: electric motors, power converters, cooling systems...etc. This thesis focuses on the increasing specific power and efficiency of electric motors including their cooling systems for reaching:

- Specific power of 5kW/kg, efficiency greater than 94.5% at sizing point and greater than 96% at cruise point for 2025 HASTECS target.
- Specific power of 10kW/kg, efficiency greater than 97% at sizing point and greater than 98.5% at cruise point for 2035 HASTECS target.

Specific power and efficiency usually depend on several technological levels which are often limited. Within this context, it is being essential to identify all technologies currently employed in electrical motors and as well as the future technologies. These technologies are conventionally involved to materials used in electrical machines.

The chapter gives a state of the art of the electric machines to situate the actual specific power and identify the involved technologies. We have broadly compared the different synchronous and asynchronous motors topologies. It is difficult to select one topology and to discard the others considering that the selected topology is usually suitable for only one or two given performances as it has been attested by the established benchmarked of the industrial electric motors employed in transportation applications.
Besides, we have studied and compared in terms of weights, loads and limits:

- The different technologies linked to the materials such as magnetic, the insulating and the sleeve materials,
- The different technologies linked to the construction such as conductors, the winding configurations and the bearings,
- The technologies linked to the cooling methods.

As well as for electric motor topologies, it is difficult to identify and select the promising technologies allowing achieving high specific power. For instance, NdFeB permanent magnets seem magnetically and lightweight relevant compared to the other magnets, but due to their temperature sensitivity they may be not interesting for reaching high specific power. Also, Hairpin conductors are relevant for high copper filling and reduced end-winding, however, they are a disadvantage for high speed operating.

We have also surveyed the improvement of some technologies currently either proposed or carried out for overcome some thermal, mechanical and electromagnetic limits. However, most of them are still under research. Eventually, considering the current limits, establishing trade-offs between technologies is suggested for reaching targets.

The next chapter presents a tool which allows assessing these technologies for hybrid aircraft propulsion. This tool also allows to make trade-offs on specific power and efficiency.

References

Project Framework

[All_17] Jean-François Allias, AIRBUS HASTECS deliverable 2017, July 2017

[All_18] Jean-François Allias, AIRBUS HASTECS deliverable 2018, July 2018

[Hor_20] Horizon 2020: 'Hybrid Aircraft; academic research on Thermal and Electrical Components and Systems'[Available Online]: https://cordis.europa.eu/project/rcn/205619/factsheet/fr

[Wor_18] Workshop dissemination 29th Oct 2019, http://www.laplace.univtlse.fr/IMG/pdf/hastecs workshop dissemination_program-2.pdf

[Dis_18] https://www.cleansky.eu/power-trip-hastecs-energizes-the-path-to-hybrid-powered-flight-0

[Air_19] https://www.airbus.com/innovation/future-technology/electric-flight/e-fan-x.html

Machines performances

[Gie_10] J. F. Gieras, 'Permanent Magnet Motor Technology: Design and Applications', 3rd edition, Taylor and Francis Group, Chapter 3, pp. 104-106, 2010.

Magnets materials

[Con_04] S. Constantinides, D. Guilck, 'NdFeB for High Temperature Motor Applications', SMMA Fall Technical Conference, Arnolds Magnetic, 3rd-5th November 2004

[Vac_14]'Rare earth permanent magnets Vacodym and Vacomax', Vacuumschmelze Catalogue, https://vacuumschmelze.com/Assets-Web/VACODYM-VACOMAX-PD002_2015_in pdf

Conductors

[Rog_18] S. Roggia, M. Iacchetti, 'Muti-physics analysis of electric vehicles (EV) power train' *Tutorial in IEEE International Conference Electrical Machines 2018, 3-6 Sept 2018, Alexandroupoli*, Greece. http://www.globalevents.gr/2018/icem/tutorial/ICEM-Tutorials-MultiphysicsEV.pdf

[Sto_04] G. C. Stone, E. A. Boulter, I. Culbert, H. Dhirani, 'Electrical Insulation for Rotating Machines, Design, Evaluation, Aging, Testing, and Repair', IEEE Press and John Wiley and Sons, INC, 2008

[Bur_17] T. Burress, 'Electrical Performance, Reliability Analysis, and Characterization', Oak Ridge National Laboratory National Transportation Research Center June 6, 2017

[Liu_19] Y. Liu, 'Rectangular conductor winding for electric motor with high performance and high production volume', Report of Swedish Electromobility Center, Chalmers University of Technology 25 June, 2019

[Deu_19] D. Deurell, V. Josefsson, ' FEA study of proximity effect in hairpin windings of a PMSM for automotive applications' Master thesis, CHALMERS UNIVERSITY OF TECHNOLOGY, Sweden 2019

[Rhy_15] Se-Hyun Rhyu and *al.*, 'Design of the end-coil structure with square conductor for automobile ISG', *International Electric Vehicle Symposium and Exhibition*, KINTEX, Korea, May 3-6, 2015

[Mil_19] D. Miljavec, ' Integrated Modular Distributed Drivetrain for Electric & Hybrid Vehicles DRIVEMODE Project', Report on considered electrical motor technologies, evaluation matrix, concept decision, https://ec.europa.eu/research/participants/documents/downloadPublic?documentIds=080166e5c18d75cf&appId=PPGMS

[Yoo_16] A. Yoon, X. Yi, J. Martin, Y. Chen, K. Haran, 'A high-speed, high-frequency, air-core PM Machine for Aircraft Application', *IEEE Power and Energy Conference (PECI)*, 19-20 Feb. 2016, USA

[Mar_17] J. Martin, A. Yoon, A. Jin, K. S. Haran, 'High-Frequency litz "Air-Gap" windings for high-power density electrical machines', *Electric Power Components and Systems Journal*, Issue. 7, Vol. 45, May 2017

[Kha_14] H.V. Khang, J. Saari, A. Arkkio, 'Form-wound Stator Winding for High-Speed Induction Motors', *IEEE International Conference on Electrical Machines*, 2-5 Sept 2014, Germany

[Mer_14] J. Merwerth, 'The Hybrid-Synchronous Machine of the New BMWi3 and i8: Challenges with electric traction drives for vehicles workshop university lund', BMW Presentation, April 2014, http://hybridfordonscentrum.se/wp-content/uploads/2014/05/20140404_BMW.pdf

[Bia_18] N. Bianchi, G. Berardi, 'Analytical Approach to design Hairpin Windings in High Performance Electric Vehicle Motors', *IEEE Energy Conversion Congress and Exposition (ECCE)*, 23-27 Sept. 2018, USA

[Gla_20] T. Glaessel, J. Seefried, A. Kuel, J. Franke, 'Skinning of insulated copper wires within the production chain of hairpin windings for electric tractions drives', *Int. J. Mech. and Rob. Research* vol.9, no.2, March 2020

[Dub_18] C. Du-Bar, A. Mann, O. Wallmark, M. Werke, 'Comparison of performance and manufacturing aspects of an insert winding and a hairpin winding for an automotive machine application', *IEEE 8th International Electric Drives Production Conference (EDPC)*, 4-5 Dec. 2018.

[Ber_18] G. Berardi, N. Bianchi, 'Design Guideline of an AC Hairpin winding', *IEEE International Conference on Electrical Machine (ICEM)*, 3-6 Sept 2018, Greece.

[Rey_16] Dominique Rey, 'Tooth coils with litz wire: Advantages for E-Drives', Von Roll Schweiz AG presentation in CWIEME 2016, Berlin 2016

[Hen_14] J. R. Hendershot, 'Electric traction machine choices for hybrid and electric vehicles', Presentation in Florida International University, 20th Nov.2014, https://site.ieee.org/miami/files/2014/11/Hendershot-FIU-Lecture.pdf
[Ast_cat] Available website: http://www.asta-austria.com/en/roebel-bars.html.
[CerCat] Cerafil, 'Miniature ceramic insulation conductor wire for very high temperatures: -90°C to +500°C, peak +1000°C', available website: http://www.cables-cgp.com/en/produits/high-temperature-miniature-ceramic-wires/.

Insulations

[Cha_08] M. Chapman, N. Frost, R. Bruetsch, 'Insulation systems for rotating low-voltage machines', Conference Record of the 2008 IEEE International Symposium on Electrical Insulation, 9-12 June 2008, Canada
[Dupcat] 'Setting the standard for electrical insulation' DuPont Catalogue, 2008
[Nema] 'NEMA Magnet Wire Thermal Class Ratings'
[Pyrh_08] J. Pyrhönen, T. Jokinen, V. Hrbovcovà, 'Design of rotating electrical machines', 2nd edition, John Wiley and Sons, 2008, pp.429-455
[Sto_04] G. C. Stone, E. A. Boulter, I. Culbert, H. Dhirani, 'Electrical Insulation for Rotating Machines, Design, Evaluation, Aging, Testing, and Repair', IEEE Press and John Wiley and Sons, INC, 2008
[Len_18] J. D. Lenz, N. J. Renner, X. Yi, K. S. Haran, 'Insulation considerations in from-wound armature windings for high-frequency electric machines', *IEEE Power and Energy Society General Meeting (PESGM)* 5-10 August 2018, USA
[AxaCat] Axalta Electrical Insulation Materials, https://www.axalta.com/electricalinsulation_global/en_US/wire-enamels/what-are-wire-enamels.html
[ElaCat] Elantas wire enamel, https://www.elantas.com/tongling/products-services/wire-enamels/polyimide-enamels.html
[Hem_19] R. Hemmati, F. Wu, A. El-Refaie, 'Survey of Insulation Systems in Electrical Machines', IEEE International Electric Machines & Drives Conference (IEMDC), 12-15 May 2019, USA
[Data]https://plastics.ulprospector.com/generics/45/c/t/polyurethane-pur-properties-processing
[Data2] Database of thermal materials: https://www.engineeringtoolbox.com/thermal-conductivity-d_429.html
[VitCat] Victrex High Performance Polymers Catalogue: Vitrex PEEK 450G, https://www.victrex.com/~/media/datasheets/victrex_tds_450g.pdf
[Oht_85] S. Ohta, 'Temperature Classes of Electrical Insulators', Three Bond Technical News, Issued 1st Dec. 1985

Winding

[Ref_10] A. M. El-Refaie 'Fractional slot concentrated-windings synchronous permanent magnet machines: opportunities and challenges', *IEEE Trans. On. Indus. Electr*., vol.57, no.1, pp.107-121, January 2010

Bearing

[Mal_06] J. Malinowski, D. R. Snyder, 'Choosing an antifriction bearing', *IEEE Industry Applications Magazine*, vol.12, iss.6, pp.49-56, 2006
[TimPr] Timken presentation 'Bearing basics', Available website: http://dunbelt.com/palestra-29-04-2016/1.%20Apres%20ANFITEATRO%20Pav%20Mec%20II.pdf [SKFCat] https://www.skf.com/fr/index.html
[Le_16] Y. Le, K. Wang, 'Design and optimization method of magnetic bearing for high-speed motor considering eddy current effects', *IEEE Transactions on Mechatronics*, vol.21, no.4, pp.2061-2072, August 2016

Sleeves

[Zha_15] F. Zhang, G. Du, T. Wang, G. Liu, W. Cao, 'Rotor retaining sleeve design for a 1.12-MW High-Speed PM Machine', *IEEE Trans. On. Indus. Appl*., vol. 51, no. 5, pp. 3675-3685, Sept/Oct 2015
[Gie_10] J. F. Gieras, 'Permanent magnet motor technology: design and applications', 3rd edition CRC Press 2010
[Fan_15] H. Fang, R. Qu, J. Liu, P. Zheng, X. Fan, 'Rotor design for a high-speed high-power permanent-magnet synchronous machine', *IEEE Energy Conversion Congress and Exposition (ECCE)*, 2015

Cooling

[Yan_17] Y. Yang, B. Bilgin, M. Kasprzak, S. Nalakath, H. Sadek, M. Preindl, J. Cotton, N. Schofield, A. Emadi, 'Thermal management of electric machines', *IEEE IET Electr. Syst. in Transp*.pp.1-13. May 2016
[Satru_17] M. Satrustegui, M. Martinez-Iturralde, J. C. Ramos, P. Gonzalez, G. Astarbe, I. Elosegui, 'Design criteria for water cooled systems of induction machines', *Applied Thermal Engineering Journal*, vol.114, pp.1018-1028, 2017
[Dav_15] T. Davin, J. Pelle, S. Harmand, R. Yu, 'Experimental study of oil cooling systems for electric motors', Applied Thermal Engineering Journal, vol.75, pp.1-13, 2015
[Lud_17] D. C. Ludois, 'Brushless and Permanent Magnet Free Wound Field Synchronous Motors for EV Traction', Technical report, University of Wisconsin-Madison, Illinois Institute of Technology, 2017, doi:10.2172/1349258

[Sem_14] S. A. Semidey, J. R. Mayor, 'Experimentation of an Electric Machine Technology Demonstrator Incorporation Direct Winding Heat Exchangers', *IEEE Trans. On. Ind. Electr*. vol.61, no.10, October 2014

[Sch_15] M. Scheifer, M. Doppelbauer, 'Indirect Slot Cooling for High-Power-Density Machines with Concentrated Winding', *IEEE International Electric Machines & Drives Conference (IEMDC)*, USA, 10-13 May 2015

[Rhe_15] C. Rhebergen, B. Bilgin, A. Emadi, E. Rowan, J. Lo, 'Enhancement of Electric Motor Thermal Management through Axial Cooling Methods: A materials approach', IEEE Energy Conversion Congress and Exposition (ECCE 2015), Canada, 20-24 Sept 2015

[Lin_16] P. M. Lindh, I. Petrov, R. S. Semken, M. Niemelä, J. J. Pyrhönen, L. Aarniovuori, T. Vaimann, A. Kallaste, 'Direct Liquid Cooling in low-power electrical machines: proof of concept', *IEEE Trans. On. Ener. Conv*. Vol.31, no.4., Dec.2016, pp. 1257-1266

[Tig_16] C. Tighe, C. Gerada, S. Pickering, 'Assessment of cooling methods for increasing power density in electrical machines', *IEEE XXII International Conference on Electrical Machines* (ICEM), 4-7 Sept.2016

[Rei_14] A. Reinap, F.J. Marquez-Fernandez, R. Andersson,C. Hogmark, M. Alakula, A. Goransson, 'Heat Transfer Analysis of a traction machine with directly cooled laminated windings', IEEE 4th International Electric Drives Production Conference (EDPC), 30 Sept-1 Oct 2014, Germany

[Pol_14] M. Polikarpova, P. M. Lindh, J. A. Tapia, J. J. Pyrhönen, 'Application of potting material for 100kW radial flux PMSM', *IEEE International Conference on Electrical Machines* (ICEM), 2-5 Sept. 2014, Germany

[Min_17] M. Liu, Y. Li, H. Ding, B. Sarlioglu, 'Thermal management and cooling of windings in electrical machines for electric vehicle and traction application', *IEEE Transportation Electrification Conference and Exposition* (ITEC), 22-24 June 2017, USA

[Tuy_17] A. Tuysuz, F. Meyer, M. Steichen, C. Zwyssig, J. W. Kolar, 'Advanced cooling methods for high-speed electrical machines', *IEEE Trans. On. Ind. Appl*., vol.53, no.3., May/June 2017, pp.2077-2087

[Ch_15] Yew Chuan Chong, 'Thermal Analysis and air flow modelling of electrical machines' PhD thesis manuscript, The University of Edinburgh, 2015

[Kim_17] J. H. Kim *et al.* "Design and analysis of cooling structure on advanced air-core stator for megawatt-class HTS Synchronous Motor" *IEEE Trans. On. Applied Supercond*., vol.4, June 2017.

[Wei_14] Wei Tong 'Mechanical design of electric motors', chapter 6: Motor Cooling, CRC Press Taylor and Francis group, edition 2014

[Gia_17] Y. Gia, M. Kimiabeigi, J. D. Widmer, Y. C. Chong, J. Goss, U. San Andres, D. A. Staton, 'Shaft cooling and the influence on the electromagnetic performance of traction motors', *IEEE International Electric Machines and Drives Conference (IEMDC)*, 21-24 May 2017, USA

[Has_12] T. Hassett, M. Hodowanee, 'Electric motor with heat pipes', Patent n° US8134260B2, 2012, https://patents.google.com/patent/US8134260B2/en

[Tes_13] L. Fedoseyev, E. Marcum Pearce Tesla motor patent 'Rotor Assembly with Heat Pipe Cooling System', , Patent n°US20140368064A1, 2013, https://patents.google.com/patent/US20140368064A1/in pdf

Actual specific power

[Zha_18] X. Zhang, C. L. Bowman, T. C. O'Connell, K. S. Haran, 'Large electric machines for aircraft electric propulsion', *IET Electr. Power Appl.*, vol. 12, Iss. 6, pp. 767-779, 2018

[Jan_17] R. H. Jansen, C. Bowman, A. Jankovsky, R. Dyson, J. Felder, 'Overview of NASA Electrified Aircraft Propulsion Research for Large Subsonic Transports', *Aircraft Electrical Propulsion*, AIAA 2017-4701 https://arc.aiaa.org/doi/abs/10.2514/6.2017-4701 , July 2017

[Sar_17]B. Sarlioglu, C. T. Morris, D. Han, S. Li, 'Driving Toward Accessibility: A Review of Technological Improvements for Electric Machines, Power Electronics, and Batteries for Electric and Hybrid Vehicles', *IEEE Ind. Appl. Magazine*, vol.23, issue.1, 2017

[Hend_14] J. R. Hendershot 'Electric traction machine choices for hybrid and electric vehicles', Nov 2014, https://site.ieee.org/miami/files/2014/11/Hendershot-FIU-Lecture pdf

[Bin_14] A. Binder, W-R. Canders, 'Tutorial "High Speed Drives" ', *IEEE International Conference on Electrical Machines*, 2nd-5th September 2014, Germany

[Bur_12] T. Burress, 'Benchmarking of competitive technologies', Oak Ridge National Laboratory, 15th May 2012, https://www.energy.gov/sites/prod/files/2014/03/f10/ape006_burress_2012_p.pdf

[Sta_17] D. Staton, J. Goss, 'Open source electric motor models for commercial EV and Hybrid Traction Motors', CWIEME Berlin 2017, https://www.coilwindingexpo.com/berlin/__media/pages/Tutorial-1-D--Staton-&-J--Goss-MDL.PDF

[Pet_15] K. Petermaier, Transformative Vertical Flight Workshop, 'Electric propulsion components with high power densities for aviation' Siemens presentation, 8th march 2015, https://nari.arc.nasa.gov/sites/default/files/attachments/Korbinian-TVFW-Aug2015.pdf

[Che_17] Y. Chen, R. Sanchez, A. Yoon, K. Sivasubramanianm, 'Mechanical design considerations of an "Ironless" high-specific-power electric machine', *IEEE Transaction On Transportation Electrification*, vol.3, no.4, Dec.2017

[Aab_14] S. Al Aabid, Y. Lefevre, J. F. Llibre, 'Assessment of electric motor technologies for long-term aircraft propulsion', Internal report, Electromagnetism Research Group Laplace Laboratory, July 2014

Limits for increasing specific power

[Sin_12] S. Singal, 'Vibration and rotor dynamics of large high-speed motors driving compressors in the oil and gas industry', Petroleum and Chemical Industry Technical Conference, 2012 Record of Conference Papers Industry Applications Society IEEE

[Bor_10] A. Borisavljevic, H. Polinder, J.A. Ferreira, On the speed limits of Permanent Magnet Machines, *IEEE Transaction On Industrial Electronics*. vol. 57, no.1, January 2010

[Can_14] W. R. Canders, J. Hoffmann, 'Tutorial on High Speed Drives, Part two-mechanical aspects', *IEEE International Conference on Electric Machines*, Germany, 1st-5th Sept 2014

[Bra_92] E. L. Brancato, "Estimation of Lifetime Expectancies of Motors", *IEEE Electrical Insulation Magazine*, vol. 8, Issue 3, May-June 1992, pp.5-13

[Dri_05] J. Driesen, R. Belmans, 'Specific problems of high-speed electrical drives', Micro Gas Turbines, p. 12–1, 2005.

Chapter II: Target Setting Tool

Contents

Introduction

In the previous chapter, different technologies employed in electrical machines were overviewed. Besides, their advantages and drawbacks were presented to identify the main limitations for increasing specific power of electric motor with its cooling system. In this chapter, a Target Setting Tool will be developed to make quick trade-offs on the specific power including the technological levels. For the purpose, loadability concept will be firstly reminded. Afterward, sizing model of nonsalient radial flux of ideal sinewave electric motors based on magnetic flux, electrical current densities and thermal balances will be developed to assess main sizes, active part volumes and weights from material choices. Losses of electric motor will be assessed by analytical models. As well specific power, specific torque and efficiency will be assessed. Sizing model will be implemented in Target Setting Tool. Finally, inputs, outputs and validity conditions of Target Setting Tool will be evoked.

II. 1 Load concepts in electrical machines

From well-designed AC electric motors, manufactures have drafted some ranges of both magnetic and electric loads for given thermal class and cooling method [Pyr_08]:

- **Magnetic loads** indicate flux densities in airgap, stator and rotor cores allowed by the soft and hard magnetic materials. Table II. 1 gives varying ranges of flux densities for various standard induction and synchronous electric machines.
- **Electric loads** indicate current densities in stator and rotor windings allowed by the cooling methods. These densities ranges are summarized in Table II. 2.
- **Electromagnetic loads** indicate the tangential stress in airgap allowed by the soft, hard magnetic materials, the insulation materials and the cooling methods as presented in Table II. 3.

Magnetic and electric loads characterize the technologies involved in electric motors as well as their performances as mentioned in [Gee_15] [Mar_15]. Therefore, to reach high specific powers of electric motors, load concepts may constitute baselines to identify the most promising technologies.

Table II. 1: Allowed flux densities for various standard induction and synchronous electrical machines [Pyr_08]

Flux density	Salient-pole		Nonsalient-pole synchronous machines
	Induction machines	Synchronous machines	
Airgap	0.7-0.9	0.85-1.05	0.8-1.05
Stator yoke	1.4-1.7	1.0-1.5	1.1-1.5
Stator tooth	1.4-2.1	1.6-2.0	1.5-2.0
Rotor yoke	1-1.6	1.0-1.5	1.3-1.6
Pole core	-	1.3-1.8	1.1-1.7

Table II. 2: Allowed RMS values of current and linear current "j_{rms} and A_{rms}" densities for various standard induction and synchronous electrical machines and according to cooling method [Pyr_08]

Cooling method	Induction machines	Salient-pole synchronous machines	Nonsalient-pole synchronous machines		
			Indirect		Direct
			Air	Hydrogen	Water
Current density j_{rms} [A.mm^{-2}]					
- **Stator winding**	3-8	4-6.5	3-5	4-6	7-10
- **Rotor winding**	3-8	2-3.5	-	-	13-18
Linear current density A_{rms}[A.mm^{-1}]	30-65	35-65	30-80	90-110	150-200
Max current density product A_{rms}×j_{rms} [A².m^{-3}]	9×10^{10}-52×10^{10}	14×10^{10}-42.5×10^{10}	9×10^{10}-40×10^{10}	36×10^{10}-66×10^{10}	1.05×10^{12}-2×10^{12}

Table II. 3: Allowed tangential stress values for various standard induction and synchronous electrical machines and according to cooling method [Pyr_08]

Cooling method	Induction machines	Salient-pole synchronous machines	Nonsalient-pole synchronous machines		
			Indirect		Direct
			Air	Hydrogen	Water
Linear current density A_{rms}[A.mm^{-2}]	30-65	35-65	30-80	90-110	150-200
Airgap flux density B_m[T]	0.7-0.9	0.85-1.05	0.8-1.05	0.8-1.05	0.8-1.05
Tangential stress σ [Pa]					
- **Minimum value**	12000	21000	17000	51000	85000
- **Maximum value**	33000	48000	59500	81500	148500

II. 2 Sizing model of the electric motors

Until recently, modelling for the purpose of sizing electric motors remains complex and often inaccurate in the case of nonconventional structures or in the case of salient electric motors. In contrast, nonsalient radial flux electric motors supplied with sinewave currents are usually fairly modelled and sized. Their windings are assumed sinewave distributed. Moreover, flux density in the airgap is assumed sinewave to simplify expressing model and design [Sle_94] [Hen_94]. To develop a Target Setting Tool, the emphasis will be paid, in this thesis, only on sizing model of nonsalient radial flux sinewave electric motors. However, it could be extended for instance to the radial flux square-wave electric motors.

II.2.1. Electromagnetic torque, fundamental waves and tangential stress

Electromagnetic torque of an electric machine results from interaction between two fundamental space-time waves on the stator bore [Han_94] [Sle_94] [Hen_94] [Gie_10]. The first fundamental wave is radial airgap flux density due to the rotor magnetic sources $B_{rs}(\theta,t)$. The second fundamental wave is the axial surface current density due to the stator currents $K(\theta,t)$. The electromagnetic torque can be calculated using *Maxwell stress tensor* or using *Lorentz force*. Thereby, the general expression of transient electromagnetic torque of a radial flux electric machine is given by:

$$T_{em}(t) = \iint_{S_b} R^2 B_{rs}(\theta,t) K(\theta,t) d\theta dz \quad \text{(II- 1)}$$

Where: R is the radius of stator bore, S_b is the inner stator surface as shown in Figure II. 1, θ is the angular position, t is the time and z is the axial direction.

Ideal sinewave electric machine is characterized by sinewave distributed winding and sinewave airgap flux density as illustrated in Figure II. 2. They are expressed by:

$$\begin{cases} K(\theta,t) = K_m \cos(p\Omega t - p\theta + \alpha_{dis}) \\ B_{rs}(\theta,t) = B_m \cos(p\Omega t - p\theta) \end{cases} \quad \text{(II- 2)}$$

Where: K_m is the maximum amplitude of the surface current density, B_m is the maximum amplitude of the airgap flux density, p is the number of pole pairs, Ω is the rotor speed and α_{dis} is the electric angular displacement.

Therefore, from equations (II-1) and (II-2), the electromagnetic torque leads to the well-known constant torque of non-salient pole electric motor.

$$T_{em} = \pi R^2 L_m K_m B_m \cos(\alpha_{dis}) \quad \text{(II- 3)}$$

Where: L_m is the axial active length.

Mechanically, it is possible to define approximatively the maximum electromagnetic torque from the forces applied over the rotor and then from the tangential stress σ (cf. Figure II. 3) as written in the following equation:

$$T_{em_{max}} = R_r S_{rot} \sigma \quad \text{(II- 4)}$$

With:

$$S_{rot} = 2\pi R_r L_m$$

Where: S_{rot} is the rotor surface and R_r is the external rotor radius.

Thereby, from the equations (II-3), (II-4) and using the following approximation:

$$R \approx R_r \quad \text{(II- 5)}$$

The tangential stress can be then deduced:

$$\sigma = \frac{B_m K_m}{2} = B_{rms} K_{rms} \quad \text{(II- 6)}$$

Where: B_{rms} and K_{rms} are the root mean square values of the airgap flux density and the surface current density respectively.

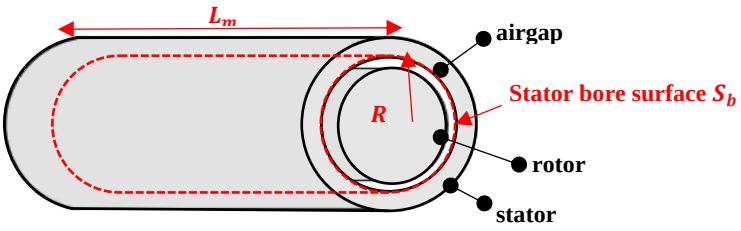

Figure II. 1. Stator bore of a radial flux electric machine

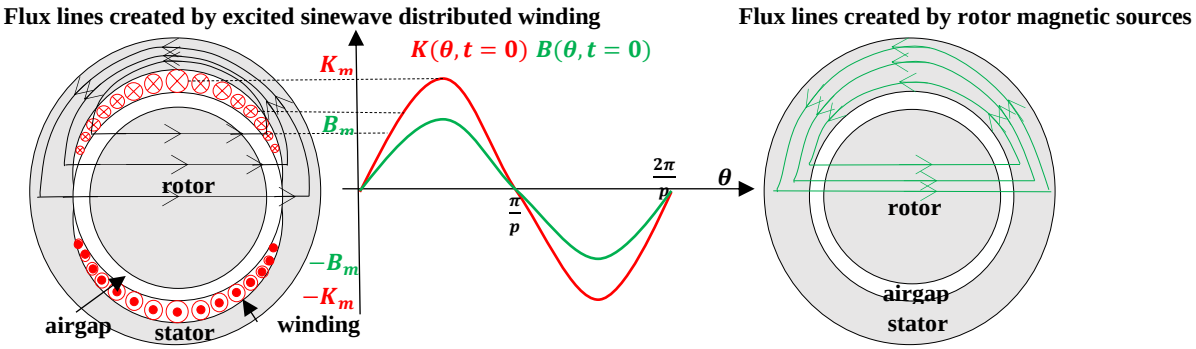

(a) (b)

Figure II. 2. (a) Two-pole sinewave distributed winding, (b) two-pole sinewave airgap flux density [Hen_94]

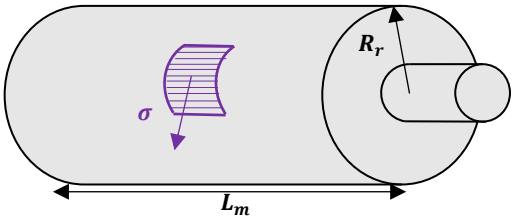

Figure II. 3. Tangential stress applied to the rotor surface

II.2.2.Magnetic flux balances

Due to magnetic nature of stator and rotor laminations, the magnetic flux crosses the rotor to the stator through teeth and closes through the stator yoke as illustrated in Figure II. 4. Therefore, the magnetic flux conservation and the balances in stator yoke and teeth can be applied. For the purpose, some assumptions are made:

- ✓ the magnetic leakage fluxes mainly crossing in the airgap and the end-winding are neglected,
- ✓ the slot effect is not taking into account,
- ✓ the saturation of magnetic sheets is not taking into account.

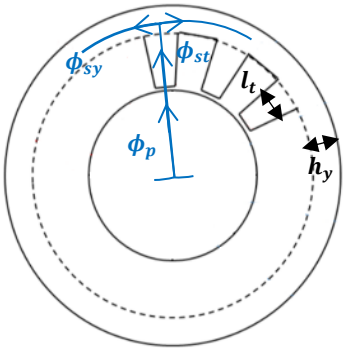

Figure II. 4. Magnetic Flux path in radial electric motor

a. Magnetic flux per pole

By applying Gauss law, the magnetic flux per pole is given by integration of the magnetic airgap flux density resulting from stator and rotor sources on the airgap surface as demonstrated in the following equation:

$$\phi_p = \iint_{S_b} \left(\overrightarrow{B_{ss}} + \overrightarrow{B_{rs}}\right).\overrightarrow{dS} = \iint_{S_b} B_{tot}\, dS \tag{II- 7}$$

Where: B_{ss} is the flux density resulting from the stator currents, B_{tot} is the amplitude of the total flux density in airgap, S_b is the inner stator surface and $dS = L_m R d\theta$.
The flux density per pole resulting from the stator source can be deduced from the *Maxwell's equations* (equations II-8 and II-9) applied on the study domain shown in Figure II. 5.

$$\overrightarrow{rot}\left(\vec{H}\right) = \vec{0} \tag{II- 8}$$

$$div\left(\vec{B}\right) = 0 \tag{II- 9}$$

and knowing that:

$$\vec{B} = \mu\vec{H} \tag{II- 10}$$

Where: $\vec{B}$ is the magnetic field, $\vec{H}$ is the magnetic field strength and μ is the permeability.

Equation II-9 leads to the definition of the magnetic vector potential $\vec{A}$:

$$\vec{B} = \overrightarrow{rot}(\vec{A}) \tag{II- 11}$$

Therefore, previous equations (II-8, 9, 10, 11) can be reduced to:

$$\overrightarrow{rot}\left(\overrightarrow{rot}(\vec{A})\right) = \vec{0} \tag{II- 12}$$

In cylindrical coordinates, equation (II-12) can be expressed by:

For $R_r < r < R$ $$\frac{\partial^2 A_z}{\partial r^2} + \frac{1}{r}\frac{\partial A_z}{\partial r} + \frac{1}{r^2}\frac{\partial^2 A_z}{\partial \theta^2} = 0 \tag{II- 13}$$

Where: A_z is the z component of magnetic potential vector.
Boundary conditions in study domain are given by:

$$\begin{cases} H_\theta(R,\theta,t) = -\frac{1}{\mu_o}\frac{\partial A_z}{\partial r}\Big|_{r=R} = K_m \cos\left(p\Omega t - p\theta + \alpha_{dis}\right) \\ H_\theta(R_r,\theta,t) = -\frac{1}{\mu_o}\frac{\partial A_z}{\partial r}\Big|_{r=R_r} = 0 \end{cases} \tag{II- 14}$$

Therefore, the general solution of a partial differential equation (II-13) is governed by:

$$A_z(r,\theta,t) = \left(C_1 r^p + \frac{C_2}{r^p}\right)\cos\left(p\Omega t - p\theta + \alpha_{dis}\right) \tag{II- 15}$$

Where: C_1 and C_2 are constants given by boundary conditions (II-14) as expressed by:

$$\begin{cases} C_1 R^{p-1} - C_2 R^{-p-1} = -\frac{\mu_o K_m}{p} \\ C_1 R_r^p - C_2 R_r^{-p} = 0 \end{cases} \tag{II- 16}$$

Then, constants C_1 and C_2 are:

$$\begin{cases} C_2 = -\frac{\mu_o K_m}{p}\frac{R^{p+1}}{\left(R^{2p} - R_r^{2p}\right)} R_r^{2p} \\ C_1 = -\frac{\mu_o K_m}{p}\frac{R^{p+1}}{\left(R^{2p} - R_r^{2p}\right)} \end{cases} \tag{II- 17}$$

Therefore, magnetic vector potential is given by:

$$A_z(r,\theta,t) = \frac{\mu_o K_m R^{p+1}}{p}\left(\frac{R_r^{2p} r^{-p} + r^p}{R_r^{2p} - R^{2p}}\right)\cos\left(p\Omega t - p\theta + \alpha_{dis}\right) \tag{II- 18}$$

The flux density resulting from the stator currents is given by:

$$B_{ss}(R,\theta,t) = \frac{1}{r}\frac{\partial A_z}{\partial \theta}\Big|_{r=R} = \mu_o K_m \left(\frac{R_r^{2p} + R^{2p}}{R_r^{2p} - R^{2p}}\right)\sin\left(p\Omega t - p\theta + \alpha_{dis}\right) \tag{II- 19}$$

Thus, the magnetic flux per pole at $t = 0$ and $\alpha_{dis} = 0$:

$$\phi_p = \iint_{S_p} B_{tot}\, dS = \iint_{S_p} \left(B_m \cos(p\theta) + \mu_o K_m \left(\frac{R^{2p}+R_r^{2p}}{R^{2p}-R_r^{2p}} \right) \sin(p\theta) \right) dS \quad \text{(II- 20)}$$

After calculation:

$$\phi_p = \iint_{S_p} B_{mtot} \cos(p\theta - \psi)\, dS \quad \text{(II- 21)}$$

Where: $\psi = artang\left(\frac{\mu_o K_m}{B_m} \left(\frac{R^{2p}+R_r^{2p}}{R^{2p}-R_r^{2p}} \right) \right)$ and $B_{mtot} = \sqrt{B_m^2 + \mu_o^2 K_m^2 \left(\frac{R^{2p}+R_r^{2p}}{R^{2p}-R_r^{2p}} \right)^2}$

Then:

$$\phi_p = RL_m \int_{-\frac{\pi}{2p}+\frac{\psi}{p}}^{\frac{\pi}{2p}+\frac{\psi}{p}} B_{mtot} \cos(p\theta - \psi) d\theta \quad \text{(II- 22)}$$

Therefore, the magnetic flux per pole is deduced by:

$$\phi_p = \frac{2RL_m B_{mtot}}{p} \quad \text{(II- 23)}$$

By setting the x ratio defined as:

$$x = \frac{R_r}{R} \quad \text{(II- 24)}$$

Finally, the magnetic flux per pole is given by:

$$\phi_p = \frac{2RL_m}{p} \sqrt{B_m^2 + \mu_o^2 K_m^2 \left(\frac{1+x^{2p}}{1-x^{2p}} \right)^2} \quad \text{(II- 25)}$$

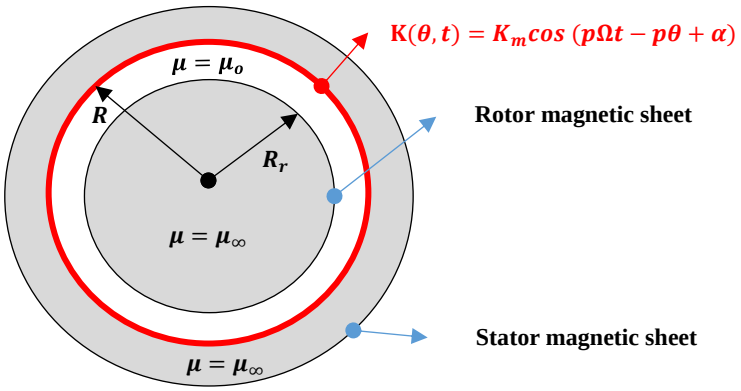

Figure II. 5. Study domain of magnetic flux per pole

b. Magnetic flux in stator yoke

Through the conservation of magnetic flux (cf. Figure II. 4), the magnetic flux in stator yoke can be expressed by:

$$\phi_{sy} = \frac{\phi_p}{2} = \frac{L_m R}{p} \sqrt{B_m^2 + \mu_o^2 K_m^2 \left(\frac{1+x^{2p}}{1-x^{2p}} \right)^2} \quad \text{(II- 26)}$$

On other hand, using Gauss law, the magnetic flux in stator yoke can be written by:

$$\phi_{sy} = B_{sy} S_{sy} \quad \text{(II- 27)}$$

Where: B_{sy} is the mean flux density in stator yoke, S_{sy} is the surface of stator yoke (with $S_{sy} = h_y L_m$) and h_y is the stator yoke thickness.

Hence, the magnetic flux balance in stator yoke is:

$$B_{sy} h_y = \frac{R}{p} \sqrt{B_m^2 + \mu_o^2 K_m^2 \left(\frac{1+x^{2p}}{1-x^{2p}} \right)^2} \quad \text{(II- 28)}$$

c. Magnetic flux in stator teeth

Likewise, the total magnetic flux in stator teeth is deduced from the conservation of magnetic flux in electrical machines:

$$N_t \phi_{st} = 2p\phi_p \quad \text{(II- 29)}$$

With:

$$\phi_{st} = B_{st} S_{st} = B_{st} l_t L_m \quad \text{(II- 30)}$$

The magnetic flux balance in stator teeth is deduced by:

$$B_{st} N_t l_t = 4R \sqrt{B_m^2 + \mu_o^2 K_m^2 \left(\frac{1+x^{2p}}{1-x^{2p}}\right)^2} \quad \text{(II- 31)}$$

Where: B_{st} is the mean flux density in stator yoke, S_{st} is the tooth surface crossed by the flux, N_t is the number of teeth, l_t is the tooth width.

In fact, magnetic flux balances established in stator yoke and tooth (equations II-28 and II-31) allow to determine the stator sizes from the flux density level of the soft materials and from flux density level in the airgap.

II.2.3. Electric current balances

a. Current density

By applying the Ampere law, the rms current density is expressed by:

$$j_{rms} = \frac{I_{rms}}{S_{cond}} = \frac{N_{cs} I_{rms}}{k_{fill} k_{sc} S_{slot}} \quad \text{(II- 32)}$$

With:

$$N_{cs} = \frac{N_c}{N_s} \quad , \quad S_{slot} = h_s \, l_s \quad \text{and} \quad S_{cond} = \frac{S_{tot-cond}}{N_{cs}} = \frac{k_{sc} k_{fill} S_{slot}}{N_{cs}} \quad \text{(II- 33)}$$

Where: I_{rms} is the rms value of current, S_{cond} is the cross section of a conductor and S_{slot} is the slot cross section. N_c is the total number of conductors, N_s is the number of slots (with $N_s = N_t$). So N_{cs} is the total number of conductors per slot connected in series. $S_{tot-cond}$ is the total cross section of conductors in one slot. k_{fill} is the fill factor which represents the ratio of the conductor area over the total slot area. k_{sc} is a coefficient that takes into account the elliptical cross-section of the conductors generated by twisting and splitting [Tan_03] as it is shown in Figures II. 6 and II. 7.

At high frequency, current density is nonuniform distributed in the conductor cross-section due to the skin and proximity effects. Skin effect is caused by the magnetic field induced by the own current flowing inside the conductor. Proximity effect is caused by magnetic fields induced by currents circulating in adjacent conductors [Pyr_08] [Gia_10] [Hen_94] [Han_94]. Usually, splitting and twisting conductors into several wires connected in parallel allow to reduce Ohmic losses due to these effects. Nevertheless, twisting and splitting conductors requires more conductor length and more outer conductor surface. A coefficient k_{lc} is introduced to take into account this conductor length in regards to a lay length (cf. Figure II. 7).

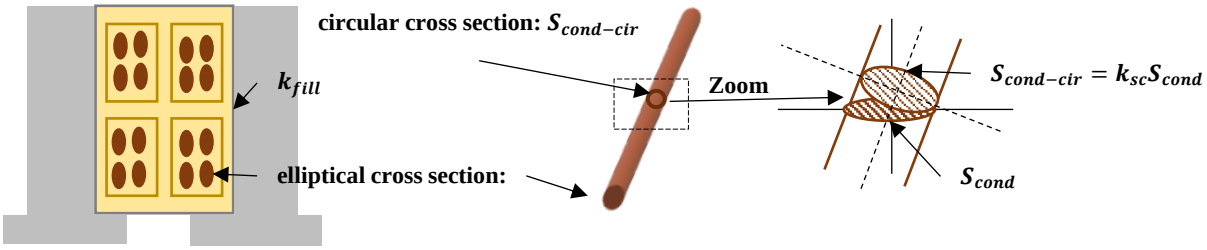

Figure II. 6. Slot and conductor cross section showing the slot filling and elliptical and circular cross sections of conductor

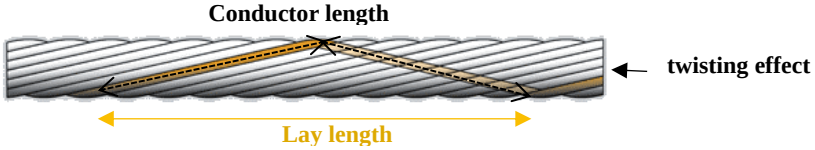

Figure II. 7. Twisting of conductors

b. Linear and surface current density

Linear current density expressed in [A/m], may be defined from the total number of conductors and from sinewave current by the following equation:

$$A_{rms} = \frac{N_c I_{rms}}{2\pi R} \quad \text{(II- 34)}$$

According to [Sle_94], linear current density can be linked to the surface current density by:

$$A_{rms} = \frac{K_m}{\sqrt{2}\, k_w} = \frac{\sqrt{2}\sigma}{k_w B_m} \quad \text{(II- 35)}$$

Where: k_w is the winding coefficient.

c. Current density product

From equations (II-32) and (II-34), the current density product is obtained by:

$$A_{rms} j_{rms} = \frac{k_{sc} k_{fill} h_s N_s l_s j_{rms}^2}{2\pi R} \quad \text{(II- 36)}$$

Knowing that:

$$N_s l_s + N_t l_t = 2\pi R \quad \text{(II- 37)}$$

and using equation (II-31), equation (II-36) can be written by:

$$A_{rms} j_{rms} = k_{sc} k_{fill} h_s j_{rms}^2 \left(1 - \frac{2}{\pi}\sqrt{\left(\frac{B_m}{B_{st}}\right)^2 + \mu_o^2 \left(\frac{K_m}{B_{st}}\right)^2 \left(\frac{1+x^{2p}}{1-x^{2p}}\right)^2}\right) \quad \text{(II- 38)}$$

Therefore, winding and slot sizes can be deduced from the levels of linear surface current density A_{rms}, current density j_{rms}, airgap flux density B_m and flux density in stator teeth B_{st}.

II.2.4.Power balance

a. Electromagnetic, mechanical and electric powers

Electromagnetic power developed by electric motor is given by:

$$P_{em} = T_{em}\Omega \quad \text{(II- 39)}$$

According to the power balance applied to an electric motor, mechanical power at the shaft level and input electric power are given by:

$$P_{mech} = P_{em} - (P_{mech-loss} + P_{rot-loss}) \quad \text{(II- 40)}$$

and

$$P_{ele} = P_{em} + P_{js} + P_{fs} \quad \text{(II- 41)}$$

Where: $P_{mech-loss}$ are the total mechanical losses, $P_{rot-loss}$ are the total electromagnetic rotor losses, P_{js} is the stator joule losses and P_{fs} is the stator iron losses.

b. Efficiency

Efficiency of an electric motor is evaluated by:

$$\eta = \frac{P_{mech}}{P_{ele}} \quad \text{(II- 42)}$$

In the thesis context, mechanical power at the shaft level is set as our baseline specification.

II.2.5.Main sizes of electric motor

Main sizes of an ideal sinewave electric motor having unspecified winding and rotor structures include:

- the stator bore radius "R",
- the active length of active part "L_m",
- the slot height "h_s",
- the stator yoke thickness "h_y", as shown in Figure II. 8.

As demonstrated through electric and magnetic balances previously established, for given electromagnetic power "P_{em}" and given rotational speed "Ω", the main sizes are linked to the magnetic, electric, thermal and mechanical loads:

- Max airgap flux density "B_m"

- Flux density in teeth "B_{st}"
- Flux density in yoke "B_{sy}"
- Tangential stress "σ"
- Current density "j_{rms}".

Moreover, for given parameters as:

- number of pole pairs "p",
- fill factor "k_{fill}",
- shape coefficient "$\lambda = 2R/L_m$", these sizes can be deduced by the following equations:

$$R = \sqrt[3]{\left(\frac{\lambda}{4\pi\sigma}\frac{P_{em}}{\Omega}\right)} \quad \text{(II- 43)}$$

$$L_m = \left(\frac{2}{\lambda}\right)\sqrt[3]{\left(\frac{\lambda}{4\pi\sigma}\frac{P_{em}}{\Omega}\right)} \quad \text{(II- 44)}$$

$$h_y = \frac{R}{p}\sqrt{\left(\frac{B_m}{B_{sy}}\right)^2 + \mu_o^2\left(\frac{K_m}{B_{sy}}\right)^2\left(\frac{1+x^{2p}}{1-x^{2p}}\right)^2} \quad \text{(II- 45)}$$

$$h_s = \frac{\sqrt{2}\sigma_t}{k_w B_m j_{rms}} \frac{1}{k_{sc}k_{fill}\left(1-\frac{2}{\pi}\sqrt{\left(\frac{B_m}{B_{st}}\right)^2+\mu_o^2\left(\frac{K_m}{B_{st}}\right)^2\left(\frac{1+x^{2p}}{1-x^{2p}}\right)^2}\right)} \quad \text{(II- 46)}$$

From theses main sizes, external stator radius is given by:

$$R_{out} = R + h_y + h_s \quad \text{(II- 47)}$$

and ratio between tooth length to bore radius can be given:

$$r_{tooth} = \frac{N_t l_t}{2\pi R} = \frac{2}{\pi}\sqrt{\left(\frac{B_m}{B_{st}}\right)^2 + \mu_o^2\left(\frac{K_m}{B_{st}}\right)^2\left(\frac{1+x^{2p}}{1-x^{2p}}\right)^2} \quad \text{(II- 48)}$$

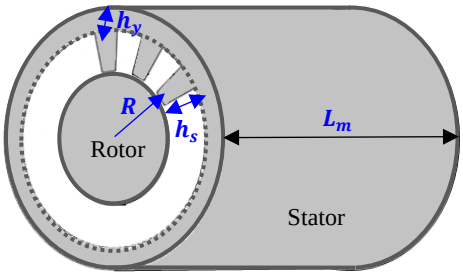

Figure II. 8. Main sizes of an electric motor

To obtain more intrinsic sizes as the end-winding length, the axial length of electric motor, the airgap of thickness and the radius of shaft, some approximations are made:

- *Approximation on end-winding length*

Stator winding is composed from two parts: the first one is located inside slot in the active part, the second one is located on the end-side of the electric motor as illustrated in Figure II. 9. End-winding length depends on winding configurations as mentioned in Chapter I. It can be measured in terms of active length L_m and a half-turn length l_{ht} as expresses the end-winding coefficient k_{tb}:

$$k_{tb} = l_{ht}/L_m \cong L/L_m \quad \text{(II- 49)}$$

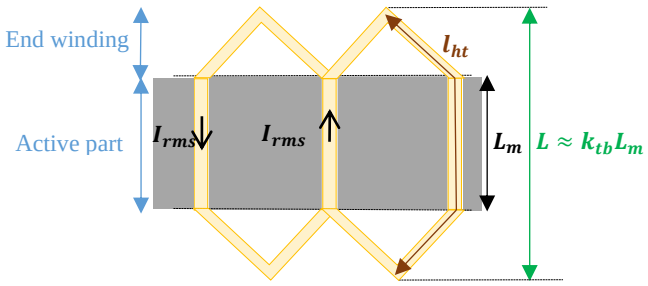

Figure II. 9. End-winding sizes

- *Approximation on the airgap length and the rotor radius*

Airgap length e_g can be approximated using the airgap ratio x_e:

$$e_g = x_e R \tag{II- 50}$$

Therefore, external rotor radius R_r is obtained by:

$$R_r = R - e_g \tag{II- 51}$$

- *Approximation on shaft radius*

To assess mechanical losses, sizes of shaft should be determined although rotor structure is not defined. For the purpose, shaft radius is approximated by:

$$R_{sh} \approx \frac{1}{3} R_r \tag{II- 52}$$

- *Approximation on frame sizes*

To estimate the frame sizes, a benchmarking has been established on Etel TMB and TMK electric motors with air and water cooling method [EteCat]. These motors have been chosen given that more data of electric motors are available. The benchmarking on frame allows to obtain ratio τ_r between external frame radius R_{fr} and external stator radius R_{out} as established in [Lef_19]. Frame sizes expressed using ratio τ_r are shown in Figure II. 10.a. The ratio between external frame radius R_{fr} and external stator radius R_{out} is given by equation (II-53). Figure II. 10.b shows its variation according to R_{out}.

$$\tau_r(R_{out}) = \begin{cases} 0.7371\, R_{out}^2 - 0.580\, R_{out} + 1.1599 & \text{for } R_{out} \leq 400mm \\ 1.04 & \text{for } R_{out} > 400mm \end{cases} \tag{II- 53}$$

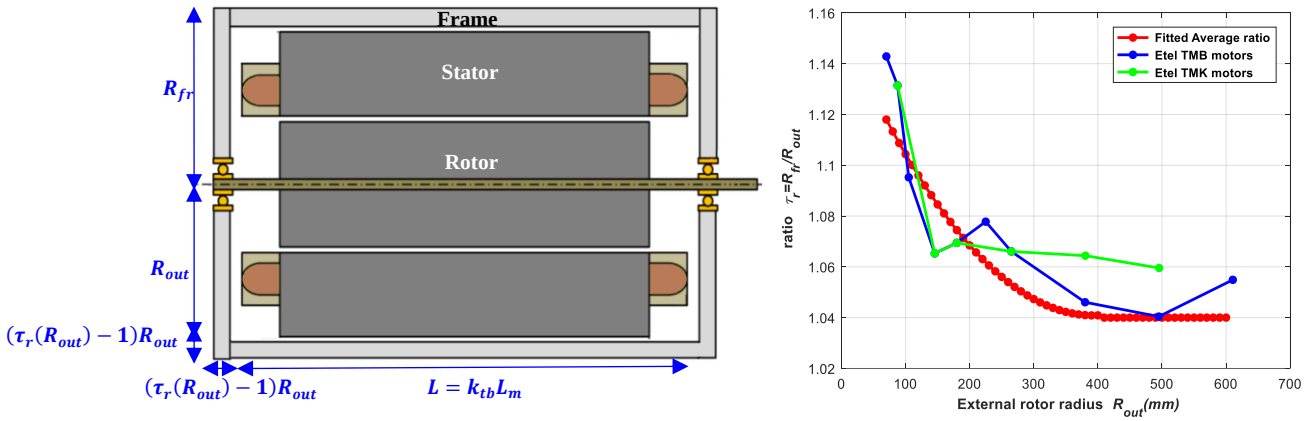

(a) (b)

Figure II. 10. (a) Frame sizes, (b) ratio function of housing diameter to external stator radius [Lef_19]

II.2.6. Electric motor weight

a. Stator weight

Once stator sizes are determined, stator weight can be evaluated from chosen conductor, insulation and magnetic soft materials previously introduced (cf. Chapter I). The following equations summarized the weight of stator core and stator winding:

- **stator core**

$$W_{stat-core} = [\pi L_m (R_{out}^2 - R^2) - (h_s L_m N_s l_s)]\rho_{sf} \quad \text{(II- 54)}$$

Where: ρ_{sf} is the density of soft magnetic material.

- **stator winding**

$$W_{stat-wind} = [k_{tb} k_{lc} h_s L_m N_s l_s]\left[k_{fill}\rho_c + \left(1 - k_{fill}\right)\rho_{insl}\right] \quad \text{(II- 55)}$$

Where: ρ_c is the density of conductor material and ρ_{insl} is the density of insulation material.

Therefore, the weight of stator is deduced by:

$$W_{stat} = W_{stat-core} + W_{stat-wind} \quad \text{(II- 56)}$$

b. Rotor weight

Usually, rotor is mainly composed of shaft, rotor core and winding or magnets depending to electric motor topology. Rotor components are made with different materials. Assess of rotor weight is difficult if the rotor structure is not specified. In our case, only external rotor volume is known. To overcome this difficulty, benchmarking established on Etel TMB and TMK electric motors can be used since more than one hundred detailed electric motors with large range of number of pole pairs are available. Moreover, benchmarking on large number of pole pairs allows to fit all rotor possible shapes. On other side, the available details are enough for establishing equivalent rotor density as illustrated in Figure II. 11. Equivalent of rotor density ρ_{rot} is given by [Lef_19]:

$$\rho_{rot}(p) = \begin{cases} -431.67p + 7932 & \text{for } p \leq 10 \\ 1.09p^2 - 117.45p + 4681 & \text{for } 10 < p \leq 50 \\ 1600 & \text{for } p > 50 \end{cases} \quad \text{(II- 57)}$$

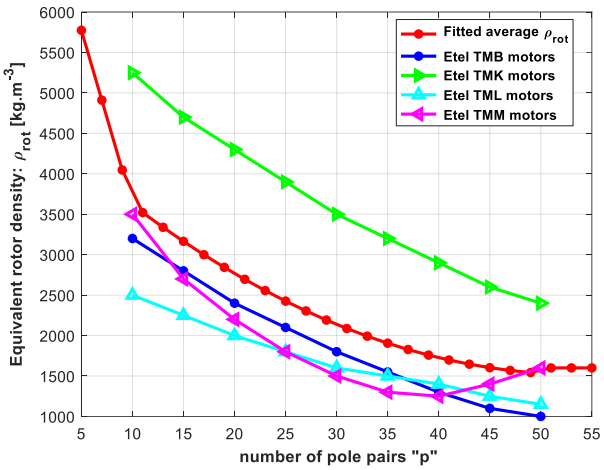

Figure II. 11. Equivalent rotor density vs number of pole pairs [Lef_19]

Therefore, rotor weight is given by:

$$W_{rot} = \pi R_r^2 L_m \rho_{rot}(p) \quad \text{(II- 58)}$$

c. Frame weight

Through estimation on frame sizes, the weight frame is:

$$W_{frame} = \rho_{fr}\left(\pi L_m k_{tb}\left(R_{fr}^2 - R_{out}^2\right) + 2\pi(\tau_r(R_{out}) - 1)R_{out}R_{fr}^2\right) \quad \text{(II- 59)}$$

Where: ρ_{fr} is the density of the frame.

Eventually, electric motor weight is:

$$W_{mot} = W_{rot} + W_{stat} + W_{frame} \quad \text{(II- 60)}$$

II.2.7. Specific power and specific torque

Specific power and specific torque of an electric motor expressed in [W/kg] and [Nm/kg] respectively, are deduced by:

$$S_P = \frac{P_{mec}}{W_{mot}} \quad \text{(II- 61)}$$

and

$$S_T = \frac{T_{emmax}}{W_{mot}} \quad \text{(II- 62)}$$

In this sizing model of the electric motor, specific power and torque take into account the all parts of the electric motor without the cooling system.

II. 3 Loss assessment models

Losses in electrical machines are mainly composed of Joule losses in winding, iron losses in magnetic core and mechanical losses. These losses are consistently critical to reach high performances especially specific power as well as efficiency. Therefore, their assessment is mandatory for sizing electric machines. The following sections presents the analytical models used for assessing losses.

II.3.1. Analytical model of Joule losses

Joule losses are often the first largest losses in electric motors [Pyr_08] [Hen_94] [Han_94]. They arise mainly due to Ohmic heating in conductors supplied by current. At low operating speed, current density is uniformly distributed in the cross-section of conductors. Joule losses are governed by:

$$P_j = qR_sI_{rms}^2 \quad \text{(II- 63)}$$

With:

$$R_s = \frac{N_c}{q}\rho_{cu}(T_{win})\frac{l_c}{S_{cond}} \quad \text{and} \quad \rho_{cu}(T_{win}) = \rho_{cu20°}\left(1 + \alpha_{th}(T_{win} - 20°)\right) \quad \text{(II- 64)}$$

Where: q is the number of phase, I_{rms} is the rms current and R_s is the resistance. $\rho_{cu20°}$ is the copper electric resistivity at 20°C, T_{win} is the winding temperature, α_{th} is the temperature coefficient resistance (for copper $\alpha_{th} = 3{,}81.10^{-3}$ K^{-1}). l_c is the length of one conductor of a half-turn ($l_c = k_{tb}k_{lc}L_m$) and S_{cond} is the conductor cross section.

Using equations (II-32) and (II-34), Joule losses can be also written by:

$$P_j = \rho_{cu}(T_{win})k_{tb}k_{lc}L_m 2\pi R A_{rms} j_{rms} \quad \text{(II- 65)}$$

II.3.2. Analytical model of Iron losses

In electric motors, iron losses arise from the variation of magnetic flux density in magnetic core. They are the second largest losses after Joule losses [Pyr_08] [Gie_10]. Variations of magnetic flux density usually induce two losses namely hysteresis losses and eddy current losses. Variation of flux density in magnetic core is cyclically due to hysteretic characteristic of magnetic core (cf. Chapter I). Each cyclic variation induces "hysteresis" losses proportional to enclosed hysteresis area [Lip_04] [Pyr_08]. Eddy current losses induce current occurring in magnetic core at the same frequency as the variation in magnetic flux density [Mil_02] [Pyr_08]. Iron losses are difficult to accurately estimate. However, there are several proposed models to estimate them: [Ber_85] [Mil_02] [Zha_12] [Egg_12] [Roy_16] [Ion_16]. From among, Bertotti model [Ber_85] is the well-known and the most used in the finite element analysis software. His corresponding equation is given by:

$$P_f = k_h f B_m^2 + k_c f^2 B_m^2 + k_e f^{3/2} B_m^{3/2} \quad \text{(II- 66)}$$

Where: B_m is the maximum magnetic flux density, f is the frequency, k_h is the hysteresis loss coefficient, k_c is the eddy loss coefficient and k_e is the excess loss coefficient.

Figure II. 12 shows a comparison of specific iron losses given by manufacturers and specific iron losses modeled using Bertotti formulation. Indeed, Bertotti model gives specific losses close to those given experimentally by manufacturers as shown for "Vacodur 49" in Figure II. 12.a. However, specific losses of "Vacoflux 48" given by Bertotti model are less close to those given by manufacturers (cf. Figure II. 12.b). Moreover, usually specific iron loss data given by manufacturers are not enough for modelling using Bertotti model. For the purpose, new formulation of iron losses based on Least Square Method is proposed:

$$P_f = \sum_{i=1}^{i=4}\sum_{j=1}^{j=4} a_{ij}\left(\sqrt{B_m}\right)^j\left(\sqrt{f}\right)^i \quad \text{(II- 67)}$$

Where: a_{ij} is the iron loss coefficient determined by the Least Square Method.

The results using equation (II-67) are shown in Figure II. 13. More results are given in Appendix A.

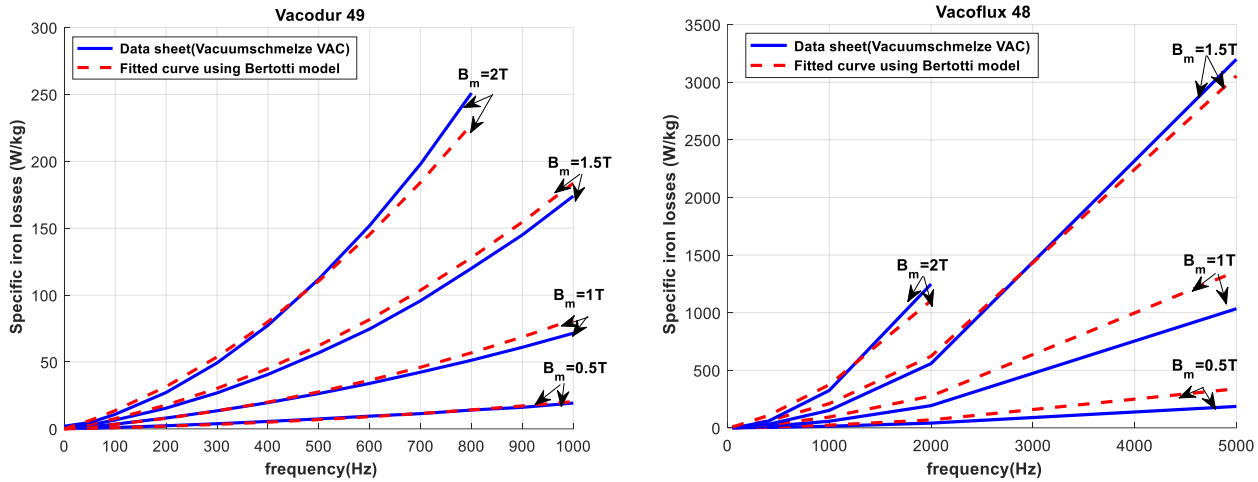

(a) (b)

Figure II. 12. Specific iron losses using Bertotti model

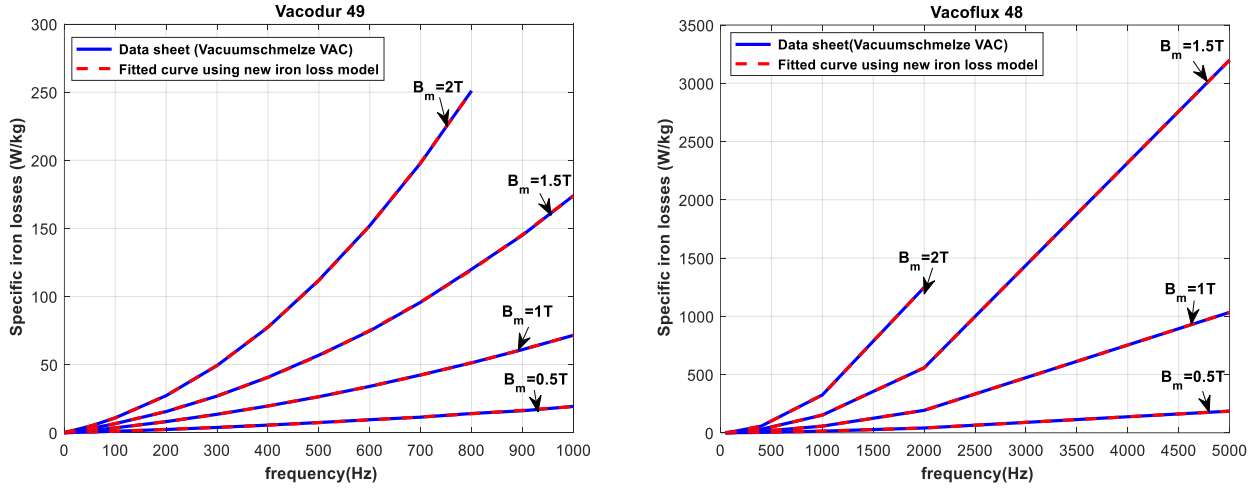

(a) (b)

Figure II. 13. Specific iron losses using proposed model

II.3.3. Semi-empirical models of mechanical losses

Mechanical losses are consequence of frictions between gas and rotating solid or between rotating solid and stationary solid. We distinguish then two losses in electric motors: windage losses and friction bearing losses. Therefore, total mechanical losses are given by (II-68). At high rotational speed these losses may be very significant. The following sections provide more detail to estimate them.

$$P_{mech-loss} = P_{windage} + 2P_{friction} \quad \text{(II- 68)}$$

Where: $P_{windage}$ is the total windage losses, $P_{friction}$ is the friction losses in one bearing.

a. Windage losses

Windage losses are due to friction between the air and rotor surfaces. These frictions occur in airgap and in rotor ends as shown in Figure II. 14. The rotating movement of rotor gives to air a tangential velocity component. This component affects the friction windage torque and then generated losses. [Saa_98] has proposed formulas

of windage losses for high speed electrical motors which are used by several authors [Lip_04] [Ner_08] [Pyr_08] [Luo_09] [Rei_10] [Kol_11] [Hua_16].

Total windage losses are given by:

$$P_{windage} = P_{windage-airgap} + 2P_{windage-rotor} \quad \text{(II- 69)}$$

where $P_{windage-airgap}$ is the windage losses in airgap and $P_{windage-rotor}$ is the windage losses in one rotor ends.

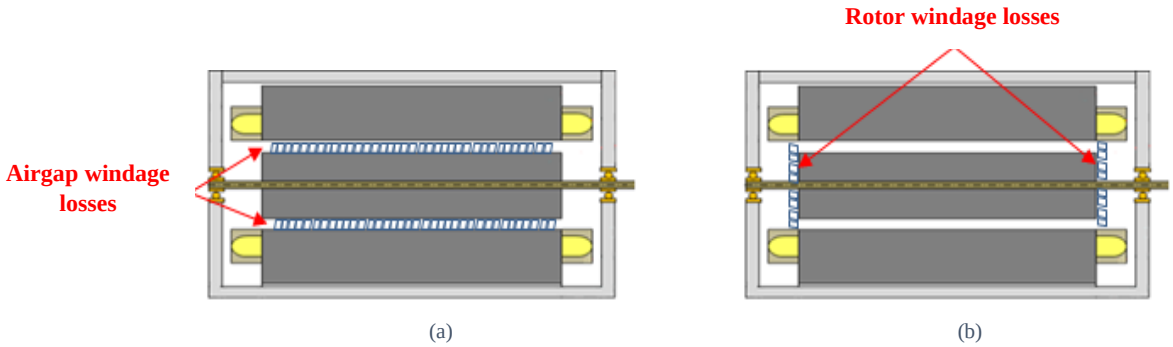

Figure II. 14. Windage losses in electrical motors (a) airgap, (b) rotor ends

- *Windage losses in airgap*

The windage losses in airgap can be estimated by the following equation:

$$P_{windage-airgap} = k_1 C_{fa} \pi \rho_{air} \Omega^3 R_r^4 L \quad \text{(II- 70)}$$

Where: k_1 is the roughness coefficient. k_1=1 for smooth rotor and stator surfaces, k_1=2 to 4 for other type of surfaces.

ρ_{air} is the air density given by:

$$\rho_{air}(T, pr) = 1.293 \times \frac{273.15}{T} \times pr \quad \text{(II- 71)}$$

With: T is the air temperature [K] and pr is the air pressure [atm].

C_{fa} is the friction coefficient depending on the flow regimes.

The nature of flow is determined by the Reynolds number R_{ea} by:

$$Re_a = \frac{\rho_{air} R_r e_g}{\mu_{air}} \Omega \quad \text{(II- 72)}$$

With:

For laminar flow $500 < R_{ea} < 10^4$:

$$C_{fa} = 0.515 \frac{(e_g/R_r)^{0.3}}{Rea^{0.5}} \quad \text{(II- 73)}$$

For turbulent flow $R_{ea} > 10^4$:

$$C_{fa} = 0.0325 \frac{(e_g/R_r)^{0.3}}{Rea^{0.2}}$$

Where: μ_{air} is the air dynamic viscosity given at 1 atm by:

$$\mu_{air}(T, p = 1atm) = 8.88.10^{-15}T^3 - 3.23\,10^{-11}T^2 + 6.26.10^{-8}T + 2.35.10^{-6} \quad \text{(II- 74)}$$

- *Windage losses rotor end*

The windage losses in rotor ends can be estimated by:

$$P_{windage-rotor} = \frac{1}{2} C_{fr} \pi \rho_{air} \Omega^3 \left(R_r^5 - R_{sh}^5\right) \quad \text{(II- 75)}$$

As for the airgap, the friction coefficient C_{fr} depends on the flow regime:

For laminar flow $R_{e\,rot} < 3.10^5$:

For turbulent flow $R_{e\,rot} > 3.10^5$:

$$C_{fr} = \frac{3.87}{R_{e_{rot}}^{0.5}} \qquad C_{fr} = \frac{0.146}{R_{e_{rot}}^{0.2}} \tag{II- 76}$$

with $R_{e\,rot}$ is the Reynolds number of the flow in rotor ends. It can be calculated by:

$$R_{e_{rot}} = \frac{\rho_{air} R_r^2}{\mu} \Omega \tag{II- 77}$$

b. Friction bearing losses

The friction in bearings comes from surface contacts between rolling elements and raceways, between the rolling elements and cage, and between the rolling elements. The bearing losses depend on the loads and several other factors such as bearing type, lubrication type, bearing sizes and rotational speed. Therefore, it is hard to accurately define the friction losses in bearings. However, bearing manufacturers propose often models for estimating friction losses such as SKF proposes in the condition of good lubrication and normal operating conditions [Skf_13-Skf_16]:

$$P_{friction} = \frac{1}{2} C_f P d \Omega \tag{II- 78}$$

Where: C_f is the friction coefficient which depends on the type bearing (cf. Table II. 4), d is the bearing bore diameter, Ω is the speed and P is the equivalent dynamic bearing load (cf. Figure II. 15) expressed by:

$$\vec{P} = \overrightarrow{F_a} + \overrightarrow{F_r} \tag{II- 79}$$

Where: $\overrightarrow{F_a}$ is the axial load and $\overrightarrow{F_r}$ is the radial load.

Usually bearings for radial flux electric machines are subjected to both radial and axial loads. To approximate the calculation of equivalent dynamic bearing load, only radial load is considered. Therefore, radial load can be approximated by the rotor weight (ie. $\vec{P} = W_{rot}\,\vec{g}$ with $\vec{g}$ is the gravitational force).

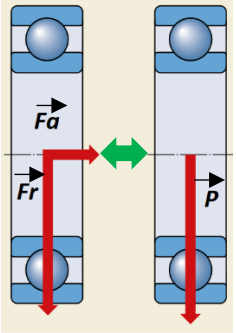

Figure II. 15. Axial and radial loads applied on rotor [Skf_16]

Table II. 4: Friction coefficient according to the bearing types used mainly to withstand the radial loads [Skf_13-Skf_16]

Bearing types	Friction coefficient C_f
Deep groove ball bearings	0.0015
Cylindrical roller bearings	
- with cage	0.0011
- full complement	0.0020
Spherical toroidal roller bearings	0.0018
CARB toroidal roller bearings	0.0016
Angular contact ball bearings	
- single row	0.0020
- double row	0.0024
- four-point contact	0.0024
Hybrid bearings	-

In other conditions and for more advanced calculation of friction bearing losses, SKF proposes a model of the calculation of different friction torques generated in surface contacts. This model is detailed in [Skf_16].

II. 4 Thermal constraint

To not exceed the thermal limits in sizing of electric motors, thermal constraint based on the current density product definition is introduced in the sizing model of electric motor. In [Pyr_08], it has been demonstrated that current density j_{rms} and linear current density A_{rms} depend only on the effectiveness of cooling system and not on the sizes of electric motor. [Pyr_08] has demonstrated it from the Joule losses relationship (equation II-65). To take into account all losses, we propose as thermal constraint the equivalent current density product evaluated by bringing them to the bore stator surface as it shown in Figure II. 16. This equivalent current density product allows also to quantify the cooling effort required to reach targeted specific power.

$$< Aj_{eq} >= \frac{P_{js}+P_{fs}+P_{mech-loss}+P_{rot-loss}}{2\pi R k_{tb} L_m \rho_{cu}(T_{win})} \quad \text{(II- 80)}$$

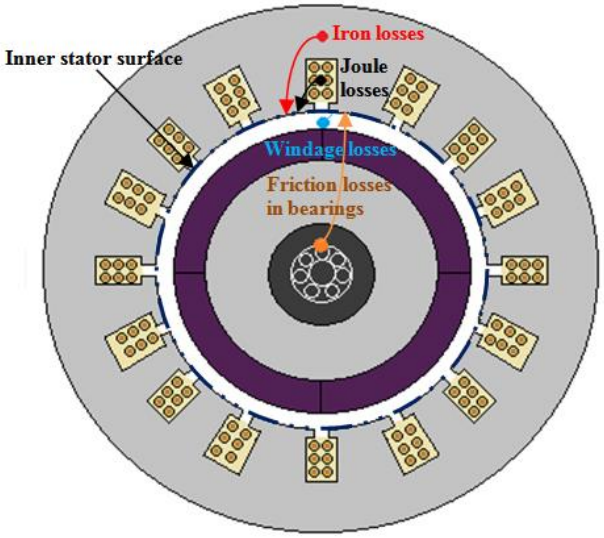

Figure II. 16. Losses taken back to the bore stator surface

II. 5 Mechanical constraint

Regarding to not exceed static and dynamic mechanical limits in sizing high speed electric motors requires a mechanical constraint (cf. Chapter I). It will be obtained through a combination between these both limits.

- **Static mechanical limit**

The maximum mechanical stress generating by the centrifugal forces applying on the external rotor surface (cf. Figure I. 48.a) is given by:

$$\sigma_m = C\rho_{rot}R_r^2\Omega^2 \quad \text{(II- 81)}$$

It can be also written using maximum peripheral speed $V_{p_{max}}$:

$$\sigma_m = C\rho_{rot}V_{p_{max}}^2 \quad \text{(II- 82)}$$

With:

$$V_{p_{max}} = R_r\Omega \quad \text{(II- 83)}$$

Where: C is a coefficient depending of rotor shape, $C = \frac{3+\nu}{8}$ for a smooth homogeneous cylinder, $C = \frac{3+\nu}{4}$ for a cylinder with small bore, ν is the Poisson's ratio, R_r is the maximum rotor radius and ρ_{rot} is the rotor density.

Therefore, maximum rotor radius can be expressed by maximum mechanical stress:

$$R_r = \sqrt{\frac{\sigma_m}{C\ \rho_{rot}}}\frac{1}{\Omega} \quad \text{(II- 84)}$$

- **Dynamic mechanical limit**

Axial length of rotor is limited by the critical rotational speeds (cf. Figure I. 48.b). According to [Bor_11] [Lah_02] [Bin_07] [Aho_07] [Mul_99] [Can_14] [Sin_12] [Bor_10] [Pyr_08], these critical speeds are defined by:

$$\Omega_{cr}^* = n^2\Omega_{cr} = n^2\sqrt{\frac{96}{5}\frac{E}{\rho_{rot}}}\frac{k_a}{k_p^2}\frac{R_r}{L_m^2} \quad \text{(II- 85)}$$

Where: n is the order of the critical rotor speed, E is the young's modulus of the rotor material, k_a is the ratio between shaft radius and rotor radius ($k_a = \frac{R_{sh}}{R_r}$) and k_p is the ratio between axial length L and the active length L_m ($k_p = \frac{L}{L_m}$)

By matching the 1st order critical rotational (i.e. Equation (II-85)) with rotational speed expressed with the maximum mechanical stress (i.e. Equation (II-81)):

$$\Omega \leq \Omega_{cr} \tag{II- 86}$$

The ration between rotor radius is obtained by:

$$k_p \sqrt{\frac{1}{k_a}\sqrt{\frac{\sigma_m}{C}\frac{5}{6E}}} \leq \frac{2R_r}{L_m} \tag{II- 87}$$

And knowing that:

$$\lambda \cong \frac{2R_r}{L_m} \tag{II- 88}$$

Mechanical constraint can be written as follows:

$$k_p \sqrt{\frac{1}{k_a}\sqrt{\frac{\sigma_m}{C}\frac{5}{6E}}} \leq \lambda \tag{II- 89}$$

By taking: $k_p = 1.4$, $k_a = \frac{1}{3}$ and the mechanical properties of rotor materials as " Silicon Iron Alloy":

- $E = 160\text{GPa}$
- $\sigma_m = 250\text{MPa}$
- ν=0.33
- $C = \frac{3+\nu}{4} = 0.83$

Finally, mechanical constraint for high and low rotational speeds is given by:

$$0.4 \leq \lambda \tag{II- 90}$$

Equation (II-90) is obtained from the superposition of the static and dynamic mechanical limits at high rotational speed ($V_p \geq 100$m/s) and at low rotational speed ($V_p \leq 100$m/s) as illustrated in Appendix B.

II. 6 Inputs and outputs of Target Setting Tools

Equations (II-1) to (II-90) developed previously, can be organised on a Tool having inputs and outputs to assess the technology levels. For the purpose, inputs should be specifications, loads, geometrical and material choices. For outputs should be sizes, weights, specific power and torque, and further intrinsic parameters as listed in Table II. 5. Graphic user interface can be also programed in Matlab software as illustrated in Figure II. 17.

Table II. 5: Target Setting Tool inputs/outputs list

TST inputs	**TST outputs**
Mechanical specifications - Electromagnetic power "P_{em}" - Rotational speed "Ω" Thermal specifications - Winding temperature "T_{win}" Magnetic and electric loads - Tangential stress "σ" - Current density "j_{rms}" - Max airgap flux density "B_m " - Flux density in yoke "B_{sy}" - Flux density in teeth "B_{st} " Geometrical choice - Shape coefficient "$\lambda = 2R/L_m$" - Fill factor "k_{fill}" - End-winding coefficient "k_{tb}" - Number of pole pairs "p"	Main sizes - External stator radius "R_{out}" - Stator bore radius "R" - Active length "L_m" - Stator yoke height "h_y" - Tooth (or slot) height "h_s" Weight - Stator magnetic core weight "$W_{stat-core}$" - Winding stator weight "$W_{stat-wind}$" - Rotor weight "W_{rot}" - Frame weight "W_{frame}" - Total motor weight "W_{mot}" Specific power and torque - Specific power "S_P" - Specific torque "S_T" Further intrinsic parameters

Materials library - Magnetic soft material (Iron Cobalt alloys (CoFe) and Silicon Iron alloys (SiFe))	- Peripheral speed "V_p" - Joule losses "P_{js}" - Iron losses "P_{fs}" - Mechanical losses "$P_{mech-loss}$" - Efficiency "η"

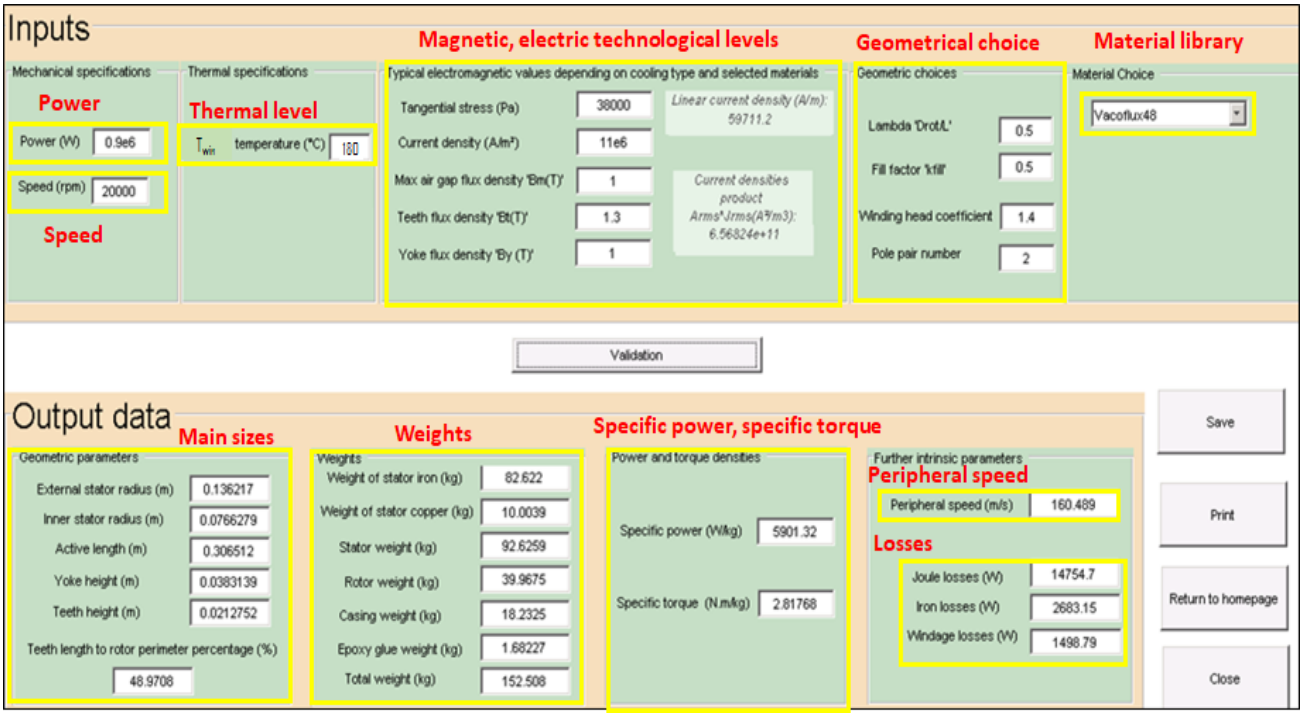

Figure II. 17. Graphic user interface of Target Setting Tool "TST"

Conclusion

This chapter deals with a model elaborated for the assessment electric motor technologies. It uses the loadability concepts tying set of magnetic, electric, mechanical loads and cooling methods to the different technologies involved in electric motors. Also, it involves an analytical model of non-salient sinewave electric machines. This model helps to identify the most promising technological levels allowing to achieve high targets.

The performances targeted result mainly from the used magnetic and electric balance equations which determine the main sizes and weights without needing to describe the stator and rotor structure. So that leads us to avoid selecting one given electric motor topology while disqualifying the others. Hence, the model deals the strong feature of the developed model since that the topology is usually beforehand selected by the electric motor designers. Moreover, in this context, loadability concepts are very useful.

In order to not exceed the limits, we have introduced two constraints in this performed model: a thermal constraint and a mechanical constraint.

We have programmed in Matlab software the model's equations as a tool called **T**arget **S**etting **T**ool "TST". Within TST, it gives as inputs the specifications, loads and materials library and gives as outputs set of data such as main sizes, weights, losses, efficiency, specific power and torque. Target Setting Tool inputs are very few compared to the many given outputs. Therefore, TST allows to provide results in a short time which is very useful.

Through sizing electric motors for Hastecs targets, Target Setting Tool could be validated. This led us to develop another more precise sizing tool in the next chapter.

Appendices

- **Appendix A: Iron losses in magnetic cores fitted by the new proposed equation**

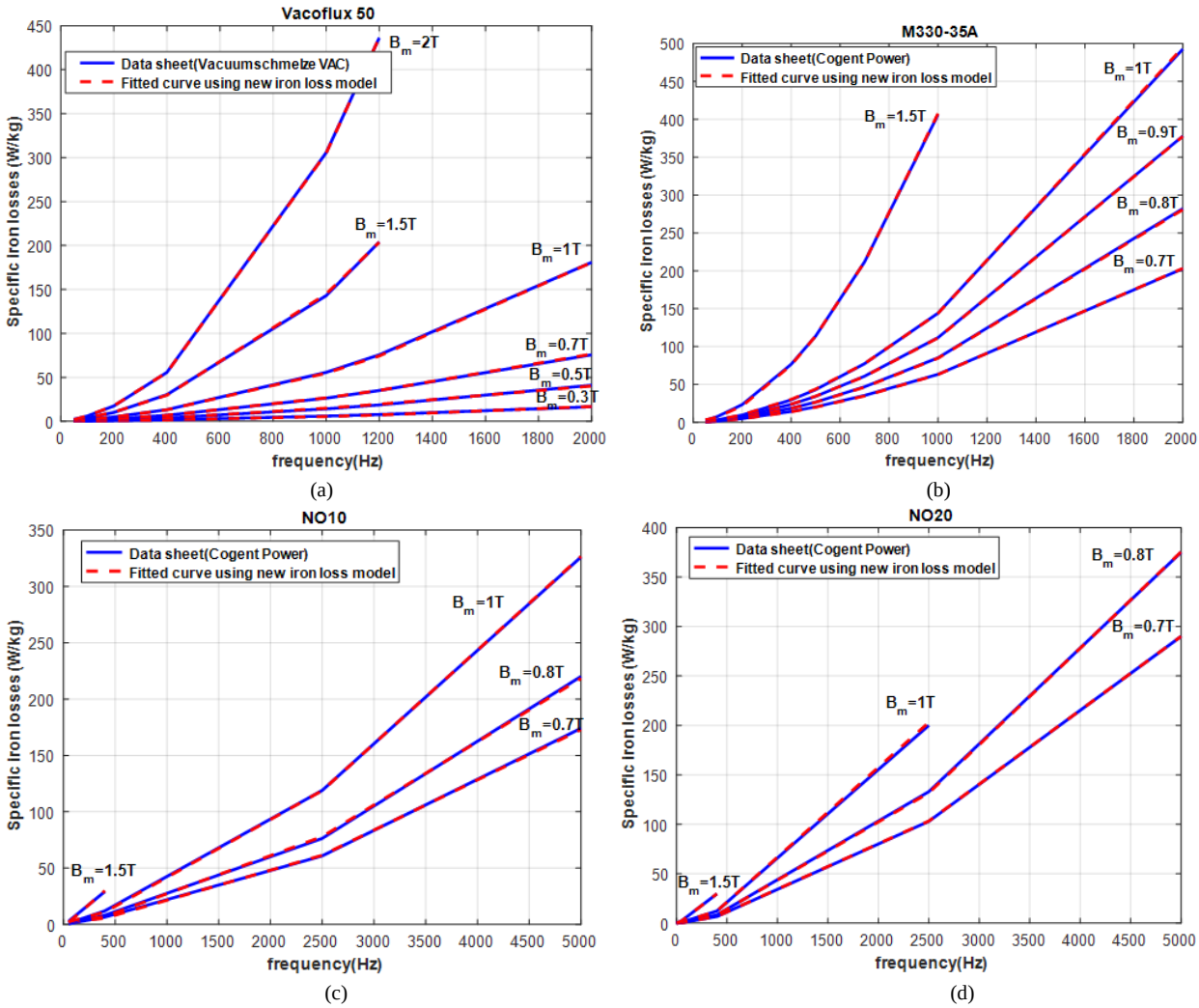

Figure II. 18: specific iron losses using new model: (a) Iron Cobalt alloy (Vacoflux 50)-0.35mm (b) Silicon Iron alloy (M330-35A)-0.35mm, (c) Silicon Iron alloy (NO20)-0.20mm , (d) Silicon Iron alloy (NO10)-0.10mm

- **Appendix B: Mechanical constraint at low rotational speed ($V_{pmax} < 100$ m/s) and high rotational speed ($V_{pmax} \geq 100$ m/s)**

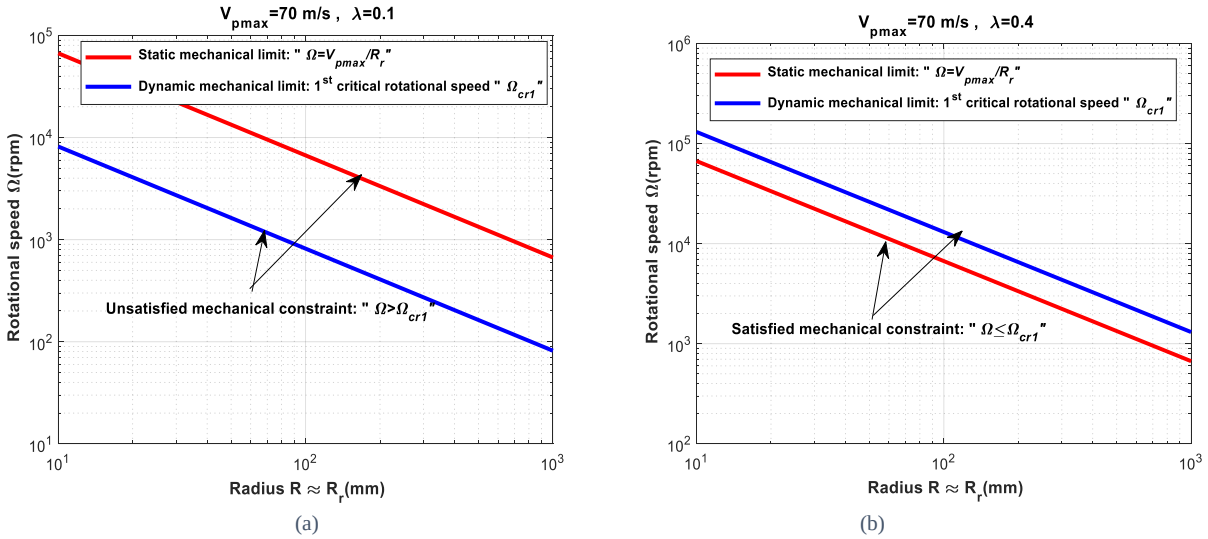

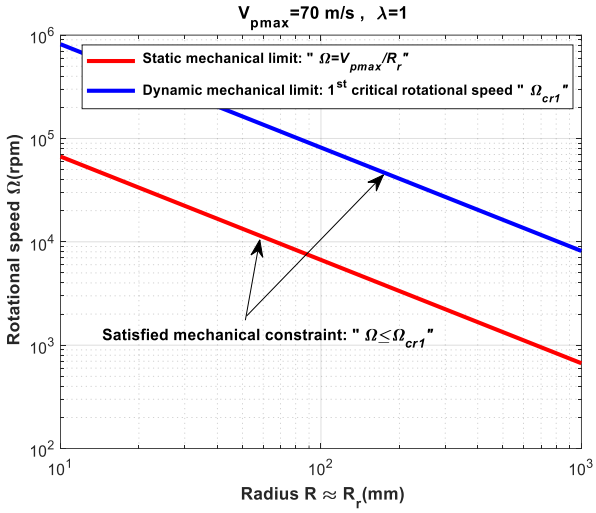

(c)

Figure II. 19: Mechanical constraint at low rotational speed $V_{pmax} < 100m/s$: (a) $\lambda = 0.1$, (b) $\lambda = 0.4$, (c) $\lambda = 1$

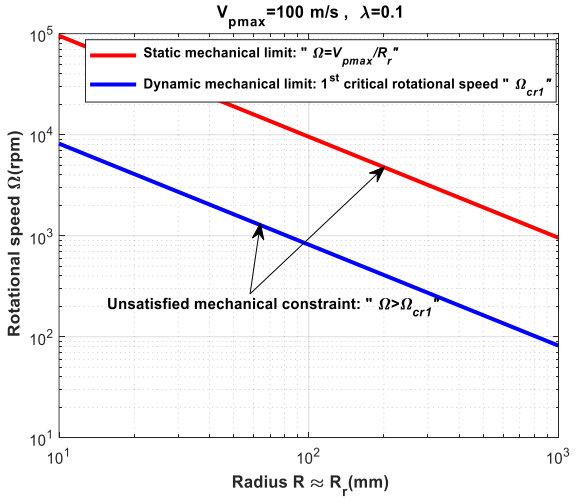

(a)

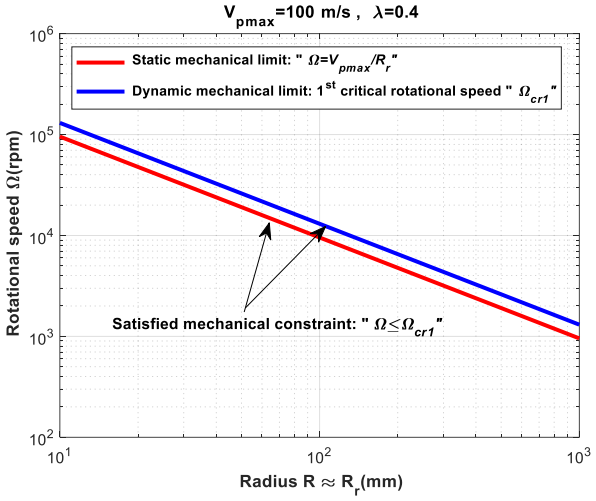

(b)

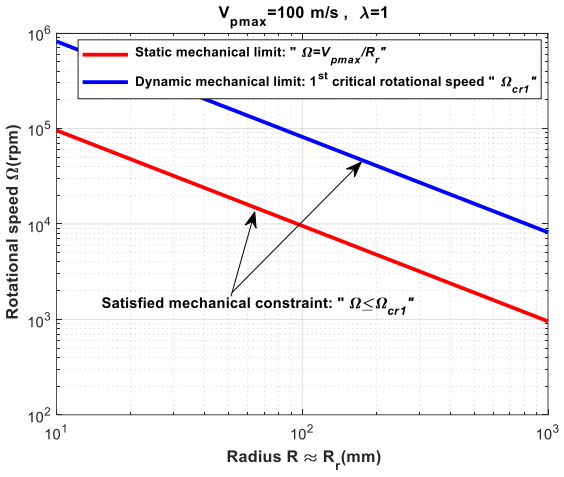

(c)

Figure II. 20: Mechanical constraint at high rotational speed $V_{pmax} \geq 100m/s$: (a) λ=0.1, (b) λ=0.4, (c) λ=1

References

Load concept of electrical machines

[Pyr_08] J. Pyrhönen, T. Jokinen, V. Hrbovcovà, 'Design of rotating electrical machines', Edition John Wiley 2008.

[Gee_15] M. Van der Geest, H. Polinder, J.A. Ferreira, M. Christmann, 'Power density limits and design trends of high-speed permanent magnet', *IEEE Transaction On Transportation Electrification*, vol.1, Issue. 3, pp.266-276, Oct. 2015

[Mar_15] M. Van der Geest, 'Design and modelling of high performance Permanent Magnet Synchronous Machines', PhD thesis manuscript, Delft University of Technology, 2015

Analytical model of no salient sinewave electric machines

[Hen_94] J. R. Hendershot Jr, THE Miller, 'Design of Brushless Permanent-Magnet Motors', Magna Physics and oxford science publications, edition 1994

[Sle_94] G. R. Slemon, 'On the design of High-Performance Surface-Mounted PM Motors', *IEEE Transactions On Industry Applications*, vol.30, no.1, pp. 134-140, January/February 1994

[Gie_10] J. F. Gieras, 'Permanent Magnet Motor Technology: Design and Applications', 3rd edition, Taylor and Francis Group, Chapter 3, pp. 104-106, 2010

[Han_94] D. C. Hanselman, 'Brushless Permanent-Magnet Motor Design' McGraw-Hill, Inc., Chapter 2, pp 20-24, 1994.

[Lip_04] T. A. Lipo, 'Introduction to AC Machine design', University of Wisconsin-Madison, 2nd edition 2004.

[EteCat] ETEL Motors Catalogue, www.etel.ch/torque-motors/overview/

[Lef_19] Y. Lefevre, S. El Aabid, J. F. Llibre, C. Henaux, S. Touhami, 'Performance assessment tool based on loadability concepts', *International Journal of Applied Electromagnetics and Mechanics*, vol.59, no.2, pp.687-694, 2019. https://oatao.univ-toulouse.fr/21430/

Twisting

[Tan_03] X. Tang, C. R. Sullivan, 'Stranded wire with uninsulated strands as a low-cost alternative to litz wire', *IEEE 34th Annual Conference on Power Electronics Specialist*, 15-19 June 2003.

Analytical model of iron losses

[Ber_85] G. Bertotti, 'Physical interpretation of eddy current losses in ferromagnetic materials, I. Theoretical considerations, *Journal of Applied Physics*, vol. 57, no.6, pp.2110-2117, March 1985.

[Zha_12] H. Zhao, Y. Luo, H. Wang Ren, B. Peter, 'A complete model for iron losses prediction in electric machines including material measurement, data fitting, FE Computation and Experimental Validation', Przeglad Elektrotechniczny, 2012.

[Roy_16] R. Roy, A. Dalal, P. Kumar, 'Prediction of high frequency core loss for electrical steel using data provided by manufacturer', *Journal of Magnetism and Magnetic Materials*, vol. 410, pp.248-256, 2016.

[Mil_02] TJE Miller, 'Speed's electric motors', University of Glasgow 2002.

[Egg_12] D. Eggers, S. Steentjes K. Hameyer, Advanced Iron-Loss estimation for nonlinear material behaviour, *IEEE Transactions on magnetics*, vol.48, no.11, pp.3021- 3024, November 2012.

[Ion_06] D.M. Ionel, M. Popescu, S. J. Dellinger, T. J. E. Miller, R. J. Heideman and M. I. McGilp, 'On the Variation with flux and frequency of the core loss coefficients in electrical machines, *IEEE Transactions On Industry Applications*, vol. 42, no.3, May/June 2006.

Analytical model of windage losses

[Saa_98] J. Saari, 'Thermal analysis of high-speed induction machines', PhD Dissertation, Helsinki University Technology, Espoo, Finland, 1998.

[Ner_08] J. Nerg, M. Rilla, J. Pyrhönen, 'Thermal analysis of radial-flux electrical machine with a high power density', *IEEE Transactions On Industrial Electronics*, vol.55, no.10, October 2008.

[Luo_09] J. Luomi, C. Zwyssig, A. Looser, J. W. Kolar, 'Efficiency optimization of a 100W-500000r/min permanent magnet machine including air-friction losses', *IEEE Transactions On Industry Applications*, vol.45, no.4, July/August 2009.

[Rei_10] B. Reimer, M. Lebmann, K. Hameyer, 'Rotor design of a high-speed permanent magnet synchronous machine rating 100000rpm at 10kW', *IEEE Energy Conversion Congress and exposition*, 2010.

[Gie_10] J. F. Gieras, 'Permanent magnet motor technology', 3rd edition CRC Press Taylor & Francis Group 2010, pp.565-574.

[Kol_11] Z. Kolondzovski, A. Arkkio, J. Larjola, P. Sallinen, 'Power limits of high-speed permanent-magnet electrical machines for compressor applications', *IEEE Transactions On Energy Conversion*, vol.26, no.1, pp.73-82 March 2011.

[Hua_16] Z. Huang, J. Fang, X. Liu, B. Han, 'Loss calculation and thermal analysis of rotors supported by active magnetic bearing for high-speed permanent magnet electrical machines', *IEEE Transactions On Industrial Electronics*, vol.63, no.4, April 2016.

Analytical model of friction bearing losses

[Skf_13] Rolling bearings and seals in electric motors and generators, SKF datasheet publication 5320E, August 2013.

[Skf_05] Bearings handbook for electric motors, SKF datasheet publication 140-430, 2005.

[Skf_04] Rolling bearings in electric motors and generators, SKF datasheet publication 5230E, 2004.

[Skf_01] Hybrid bearings for electrical machinery electrically insulating higher speeds longer grease life, SKF datasheet publication 5128E, 2001.

[Skf_16] Rolling bearings, SKF datasheet publication Pub/P110000/3E, August 2016.

Mechanical limits

[Lah_02] J. Lähtennmäki, 'Design and voltage supply of high-speed induction machines', PhD thesis manuscript, Helsinki University of Technology, Finland, 2002.

[Mul_99] B. Multon, J. Bonal, 'Les entrainements électromécaniques directs: diversité, contraintes et solutions', La conversion électromécanique direct, "https://hal.archives-ouvertes.fr/hal-00674081".

[Bin_07] A. Binder, T. Schneider, 'High-speed inverter-fed AC drives', I*EEE International Aegean Conference on Electrical Machines and Power Electronics*,10-12 Sept. 2007.

[Aho_07] T. Aho, 'Electromagnetic design of a solid steel rotor motor for demanding operation environments', Lappeenranta University of Technology, Finland 2007.

[Bor_11] A. Borisavljevic, 'Limits, modeling and design of high-speed permanent magnet machines', PhD thesis manuscript, Delft University of Technology, Netherlands, 20111.

[Can_14] W. R. Canders, J. Hoffmann, 'Tutorial on high speed drives, part-two mechanical aspects', *IEEE International Conference on Electric Machines*, Germany, 1st -5thl Sept 2014.

[Sin_12] S. Singal, 'Vibration and rotor dynamics of large high-speed motors driving compressors in the oil and gas industry', *IEEE Petroleum and Chemical Industry Technical Conference, Record of Conference Papers Industry Application Society*, 2012.

[Bor_10] A. Borisavljevic, H. Polinder, J. A. Ferreira, 'On the speed limits of Permanent Magnet Machines', *IEEE Transactions On Industrial Electronics*, vol.57, no.1, pp.220-227, January 2010.

Chapter III: Surface Mounted Permanent Magnet Synchronous Motor Tool

Contents

Introduction

Usually, designers of electric motors early chose and fixed the electric motor topology in sizing procedure. Nevertheless, using Target Setting Tool "TST" the topology becomes an option of second level required only to give more details and specifications of the electric motors such as intrinsic electric parameters. In this chapter, these last ones will be given from an analytical model established on a chosen topology of electric motor. Motivations to choose the topology will be firstly outlined. Then, the analytical model with its study domain and its assumptions of chosen topology will be illustrated. Also, the performances and the intrinsic electric parameters will be deduced. Eventually, the analytical model will be implemented in a new sizing tool by specifying its inputs and outputs.

III.1 Motivation for choosing Surface Mounted Permanent Magnet Synchronous Motor Topology

As demonstrated in previous chapter, the main sizes of a radial flux electric motor satisfying the TST assumptions can be deduced from the electric, the magnetic and the thermal loads. The other sizes can be obtained only if the topology of electric motor is specified. In this context, several electric motor topologies satisfying TST assumptions can be selected mainly as the synchronous and asynchronous electric motor topologies (cf. Chapter I). Nowadays, several research works try to develop more accurate analytical models towards to size these electric motors. Only the analytical model of permanent magnet synchronous motors that is most accurate and less complex. Indeed, wound rotor synchronous motors are often sized by means of numerical models [Lel_18]. Moreover, this topology is excluded given that could not be beneficial for reaching a high specific power. Besides, due to the significant electromagnetic transient state of asynchronous motors, their analytical modelling remains more complex and less accurate.

There are several permanent magnet synchronous motor topologies, we can quote, namely:

- Surface mounted permanent magnet synchronous motors,
- Buried permanent magnet synchronous motors,
- Interior permanent magnet synchronous motors.

Surface Mounted-Permanent Magnet Synchronous Motor "SM-PMSM" topology includes the classical mounted permanent magnet and the bread loaf permanent magnet illustrated respectively in Figure III.1. a and b. This topology can ensure flux density in airgap very close to the sine wave with very low saliency due to the shape and polarization of permanent magnets.

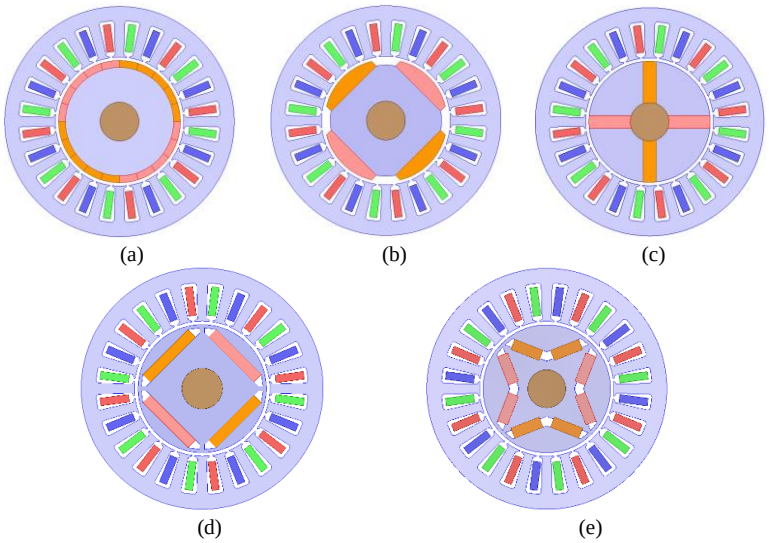

Figure III. 1. Permanent Magnet Synchronous Motors:(a) Surface Mounted Halbach Permanent Magnet, (b) Bread Loaf Permanent Magnet, (c) Buried Permanent Magnet, (d) Interior Permanent Magnet, (e) Interior Folded Permanent Magnet

Buried and interior permanent magnet synchronous motor topologies presented respectively in Figure III.1.c, d and e can also ensure flux density in airgap close to the sine wave with highest value of the airgap flux density. Moreover, these topologies are characterized by an important salience. Indeed, all these permanent magnet synchronous machine topologies can be candidate for sizing using TST,

whereas, due to the salience that is not taking into account in the TST, only surface mounted permanent magnet with Halbach structure topology is selected (cf. Figure III.1.a)

III.2 Assumptions and study domain

To establish the 2D analytical model of SM-PMSM on three regions (cf. Figure III. 2) some assumptions are made for simplifying the conception of the analytical model, such as:

- The slot effect is not taking into account,
- The permeability of stator and rotor magnetic sheets is infinite.

The region I is the permanent magnet, the region II is the airgap and the region III is the rotor magnetic sheet.

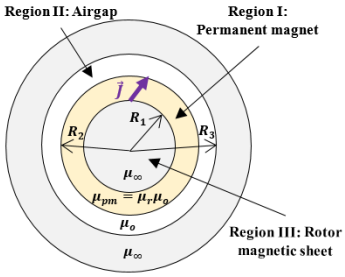

Figure III. 2. Study domain for general 2D analytical field model

III.3 Analytical model of Surface Mounted Permanent Magnet Synchronous Motor

Establishing analytical model allows to determine further sizes and to assess further performances by choosing rotor and stator configurations. The following sections will describe the analytical model applied on the rotor and airgap regions to analyse the magnetic field created by Permanent Magnets and the stator winding design.

III.3.1 Rotor configuration

III.3.1.1 Analytical 2D magnetic field model

a. General 2D Analytical Field Model

To analyse the magnetic field created by the PM in SM-PMSM, only airgap and permanent magnet regions are considered. For these both regions, the magnetic flux density B and the magnetic field strength H vectors are respectively expressed as:

$$\begin{cases} \overrightarrow{B^I} = \mu_{pm}\overrightarrow{H^I} + \vec{J} \\ \overrightarrow{B^{II}} = \mu_o\overrightarrow{H^{II}} \end{cases} \quad \text{(III- 1)}$$

Where μ_o is the airgap permeability, μ_{pm} is the PM permeability ($\mu_{pm} = \mu_o\mu_r$), μ_r is the relative permeability and J is the polarization vector of PM.

The polarization vector of permanent magnet can be written in cylindrical coordinates and by using Fourier's series:

$$\vec{J} = \begin{cases} J_r = \sum_{n=1}^{n=\infty} J_{rcn}\cos(np\theta) + J_{rsn}\sin(np\theta) \\ J_\theta = \sum_{n=1}^{n=\infty} J_{\theta cn}\cos(np\theta) + J_{\theta sn}\sin(np\theta) \\ J_z = 0 \end{cases} \quad \text{(III- 2)}$$

Where: J_{rcn}, J_{rsn}, $J_{\theta cn}$ and $J_{\theta sn}$ are the Fourier's series components of the radial and tangential polarization J_r, J_θ respectively, p is the pole pair number and n is the harmonic rank.

In region I and II, Maxwell's equations are given by:

$$\begin{cases} \overrightarrow{rot}\left(\overrightarrow{H^I}\right) = \vec{0} \\ \overrightarrow{rot}\left(\overrightarrow{H^{II}}\right) = \vec{0} \end{cases} \quad \text{(III- 3)}$$

Using equation (III-1), equation (III-3) can be rewritten as follow:

$$\begin{cases} \overrightarrow{rot}\left(\overrightarrow{B^I}\right) = \overrightarrow{rot}\left(\vec{J}\right) \\ \overrightarrow{rot}\left(\overrightarrow{B^{II}}\right) = \vec{0} \end{cases} \quad \text{(III- 4)}$$

With vector potential definition in cylindrical coordinates $\vec{A}$ (cf. Chapter II equation (II-11)), equation (III- 4) can be expressed as:

$$\begin{cases} \frac{\partial^2 A_z^I}{\partial r^2} + \frac{1}{r}\frac{\partial A_z^I}{\partial r} + \frac{1}{r^2}\frac{\partial^2 A_z^I}{\partial \theta^2} = \frac{1}{r}\frac{\partial J_r}{\partial \theta} - \frac{J_\theta}{r} - \frac{\partial J_\theta}{\partial r} \\ \frac{\partial^2 A_z^{II}}{\partial r^2} + \frac{1}{r}\frac{\partial A_z^{II}}{\partial r} + \frac{1}{r^2}\frac{\partial^2 A_z^{II}}{\partial \theta^2} = 0 \end{cases} \quad \text{(III- 5)}$$

Where: A_z^I and A_z^{II} are the vector potential in the permanent magnet and airgap respectively. The general solution of A_z^I and A_z^{II} are obtained by solving equations (III-5):

$$\begin{cases} A_z^I(r,\theta) = \sum_{n=1}^{n=\infty} \left(\left[C_{1n} r^{np} + \frac{C_{2n}}{r^{np}} + k_{cn}(r) \right] \cos(np\theta) + \left[S_{1n} r^{np} + \frac{S_{2n}}{r^{np}} + k_{sn}(r) \right] \sin(np\theta) \right) \\ A_z^{II}(r,\theta) = \sum_{n=1}^{n=\infty} \left(\left[E_{1n} r^{np} + \frac{E_{2n}}{r^{np}} \right] \cos(np\theta) + \left[E_{3n} r^{np} + \frac{E_{4n}}{r^{np}} \right] \sin(np\theta) \right) \end{cases} \quad \text{(III- 6)}$$

With:

$$\begin{cases} k_{cn}(r) = \begin{cases} \frac{npJ_{rsn} - J_{\theta cn}}{1-n^2p^2} r & np \neq 1 \\ \frac{J_{rs1} - J_{\theta c1}}{2} r \ln(r) & np = 1 \end{cases} \\ k_{sn}(r) = \begin{cases} -\frac{npJ_{rcn} + J_{\theta sn}}{1-n^2p^2} r & np \neq 1 \\ -\frac{J_{rc1} + J_{\theta s1}}{2} r \ln(r) & np = 1 \end{cases} \end{cases} \quad \text{(III- 7)}$$

And: C_{1n}, C_{2n}, S_{1n}, S_{2n} and $E_{1n\ldots4n}$ are constants determined by boundary conditions and continuity conditions on interfaces as expressed by:

$$\begin{cases} H_\theta^I(r = R_1, \theta) = 0 \\ H_\theta^{II}(r = R_3, \theta) = 0 \\ H_\theta^I(r = R_2, \theta) = H_\theta^{II}(r = R_2, \theta) \\ B_r^I(r = R_2, \theta) = B_r^{II}(r = R_2, \theta) \end{cases} \quad \text{(III- 8)}$$

The value of these constants C_{1n}, C_{2n}, S_{1n}, ,S_{2n} and $E_{1n\ldots4n}$ are given in Appendix A.
After determining A_z^I and A_z^{II}, we can write:

$$\begin{cases} B_r^I(r,\theta) = \frac{1}{r}\frac{\partial A^I}{\partial \theta} \\ H_\theta^I(r,\theta) = -\frac{1}{\mu_{pm}}\frac{\partial A^I}{\partial r} - \frac{J_\theta}{\mu_{pm}} \\ B_r^{II}(r,\theta) = \frac{1}{r}\frac{\partial A^{II}}{\partial \theta} \\ H_\theta^{II}(r,\theta) = -\frac{1}{\mu_o}\frac{\partial A^{II}}{\partial r} \end{cases} \quad \text{(III- 9)}$$

B_r^I, H_θ^I, B_r^{II} and H_θ^{II} are the radial flux density and the tangential magnetic field of the permanent magnet and the airgap regions respectively:

$$\begin{cases} B_r^I(r,\theta) = \sum_{n=1}^{n=\infty} B_{mc}^I(r)\cos(np\theta) + B_{ms}^I(r)\sin(np\theta) \\ B_r^{II}(r,\theta) = \sum_{n=1}^{n=\infty} B_{mc}^{II}(r)\cos(np\theta) + B_{ms}^{II}(r)\sin(np\theta) \\ H_\theta^I(r,\theta) = \sum_{n=1}^{n=\infty} H_{mc}^I(r)\cos(np\theta) + H_{ms}^I(r)\sin(np\theta) \\ H_\theta^{II}(r,\theta) = \sum_{n=1}^{n=\infty} H_{mc}^{II}(r)\cos(np\theta) + H_{ms}^{II}(r)\sin(np\theta) \end{cases} \quad \text{(III- 10)}$$

Where:

$$\begin{cases} B_{mc}^{I}(r) = \frac{np}{r}\left(S_{1n}r^{np} + \frac{S_{2n}}{r^{np}} + k_{sn}(r)\right) \\ B_{ms}^{I}(r) = -\frac{np}{r}\left(C_{1n}r^{np} + \frac{C_{2n}}{r^{np}} + k_{cn}(r)\right) \\ B_{mc}^{II}(r) = \frac{np}{r}\left(E_{3n}r^{np} + \frac{E_{4n}}{r^{np}}\right) \\ B_{ms}^{II}(r) = -\frac{np}{r}\left(E_{1n}r^{np} + \frac{E_{2n}}{r^{np}}\right) \\ H_{mc}^{II}(r) = -\frac{1}{\mu_o}\frac{np}{r}\left(E_{1n}r^{np} - \frac{E_{2n}}{r^{np}}\right) \\ H_{ms}^{II}(r) = -\frac{1}{\mu_o}\frac{np}{r}\left(E_{3n}r^{np} - \frac{E_{4n}}{r^{np}}\right) \end{cases} \quad \text{(III- 11)}$$

With:

$$\begin{cases} H_{mc}^{I}(r) = -\frac{np}{\mu_{pm}r}\left(C_{1n}r^{np} - \frac{C_{2n}}{r^{np}} + \frac{k_{cn}(r)+rJ_{\theta cn}}{np}\right) & \text{for } np \neq 1 \\ H_{ms}^{I}(r) = -\frac{np}{\mu_{pm}r}\left(S_{1n}r^{np} - \frac{S_{2n}}{r^{np}} + \frac{k_{sn}(r)+rJ_{\theta sn}}{np}\right) & \text{for } np \neq 1 \\ H_{mc}^{I}(r) = -\frac{1}{\mu_{pm}r}\left(C_{1n}r - \frac{C_{2n}}{r} + k_{c1}(r) + \frac{J_{rs1}+J_{\theta c1}}{2}r\right) & \text{for } np = 1 \\ H_{ms}^{I}(r) = -\frac{1}{\mu_{pm}r}\left(S_{1n}r - \frac{S_{2n}}{r} + k_{s1}(r) + \frac{J_{\theta s1}-J_{rc1}}{2}r\right) & \text{for } np = 1 \end{cases}$$

b. Radial, tangential and parallel polarizations

There are three types of permanent magnet polarization: radial polarization, tangential polarization and parallel polarization as shown in Figure III. 3.

→ *Radial polarization* characterized by polarization only along radial axis (cf. Figure III.3. a) as given by the equation:

$$\vec{J} = \begin{cases} J_r = \frac{J\beta p}{\pi}\sum_{n=1}^{n=\infty}(1-(-1)^n)\frac{\sin(0.5np\beta)}{0.5np\beta}\cos\big(np(\theta-\alpha)\big) \\ J_\theta = 0 \\ J_z = 0 \end{cases} \quad \text{(III- 12)}$$

Where: J is the polarization amplitude, β is the angular width, α is the angular center of permanent magnet.

→ *Tangential polarization* characterized by polarization only along angular axis (cf. Figure III. 3. b) as given by the equation:

$$\vec{J} = \begin{cases} J_r = 0 \\ J_\theta = \frac{J\beta p}{\pi}\sum_{n=1}^{n=\infty}(1-(-1)^n)\frac{\sin(0.5np\beta)}{0.5np\beta}\cos\big(np(\theta-\alpha)\big) \\ J_z = 0 \end{cases} \quad \text{(III- 13)}$$

→ *Parallel polarization* characterized by polarization parallel-oriented from the center of permanent magnet α with γ angle as shown in Figure III.3. c. Parallel polarization is governed by:

$$\vec{J} = \begin{cases} J_r = \frac{J\beta p}{\pi}\sum_{n=1}^{n=\infty}\frac{\sin(0.5m_1\beta)}{0.5m_1\beta}\cos(np(\theta-\alpha)+\gamma) + \frac{\sin(0.5m_2\beta)}{0.5m_2\beta}\cos(np(\theta-\alpha)-\gamma) \\ J_\theta = \frac{J\beta p}{\pi}\sum_{n=1}^{n=\infty}\frac{\sin(0.5m_1\beta)}{0.5m_1\beta}\sin(np(\theta-\alpha)+\gamma) - \frac{\sin(0.5m_2\beta)}{0.5m_2\beta}\sin(np(\theta-\alpha)-\gamma) \\ J_z = 0 \end{cases} \quad \text{(III- 14)}$$

With: $m_1 = 1 + np$ and $m_2 = 1 - np$.

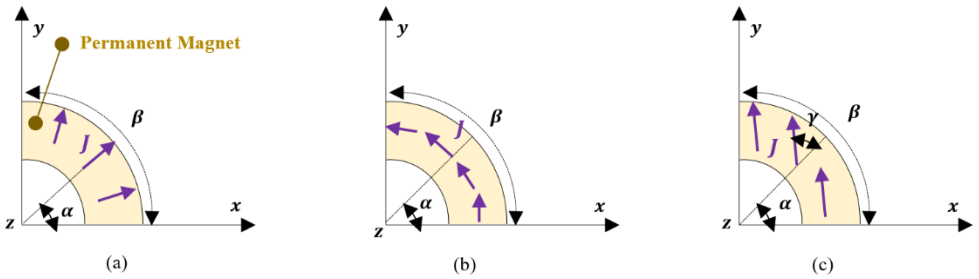

Figure III. 3. Permanent Magnet Polarizations: (a) Radial polarization, (b) Tangential polarization, (c) Parallel polarization

c. Ideal Halbach Permanent Magnet

According to [Zhu_10] sine wave airgap flux density is ensured by an ideal Halbach Permanent Magnet.

The last one is characterized in cylindrical coordinates by sine wave polarization as expressed in equation (III-15). Ideal Halbach PM polarization can be either internal or external as shown in Figure III. 4. Practically, it is hard to manufacturer ideal Halbach PM, for the purpose, Halbach PMs are often segmented into some number of segments having different parallel polarizations.

$$\overrightarrow{J(\theta)} = \overrightarrow{J_r(\theta)} + \overrightarrow{J_\theta(\theta)} = \begin{cases} J_r(\theta) = J\cos(p\theta) \\ J_\theta(\theta) = \pm J\sin(p\theta) \end{cases} \quad \text{(III- 15)}$$

"+" being for internal field Halbach and "-" for external field Halbach.

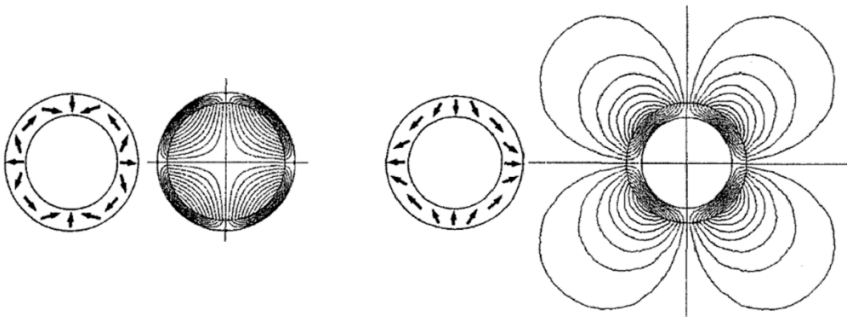

(a) (b)

Figure III. 4. Ideal Halbach Permanent Magnet in 2 pole pairs: (a) internal field Halbach, (b) external field Halbach [Zhu_01]

III.3.1.2 Permanent magnet thickness calculation

From definition of an ideal Halbach PM, sizes and structure of Halbach PM with external field can be deduced. Indeed, for a desired maximum airgap sine wave flux density B_m and from a given value of airgap thickness $e_g = R_3 - R_2$, the thickness of a Halbach Permanent Magnet $e_{pm} = R_2 - R_1$ can be analytically determined by using the 2D general analytical field model and by considering only the fundamental harmonic ($n = 1$).

Thereby from equation (III-11), the radial flux density and the tangential magnetic field in airgap and PM can be reduced to:

$$\begin{cases} B_r^I(r,\theta) = B_{mc}^I(r)\cos(p\theta) + B_{ms}^I(r)\sin(p\theta) \\ H_\theta^I(r,\theta) = H_{mc}^I(r)\cos(p\theta) + H_{ms}^I(r)\sin(p\theta) \\ B_r^{II}(r,\theta) = B_{mc}^{II}(r)\cos(p\theta) \\ H_\theta^{II}(r,\theta) = H_{ms}^{II}(r)\sin(p\theta) \end{cases} \quad \text{(III- 16)}$$

As the airgap flux density is desired equal to $B_m\ cos(p\theta)$, the $B_{ms}^{II}(r)$ should be null. For the purpose, E_{11} and E_{21} should be null. Therefore, $H_{mc}^{II}(r)$ becomes null.

With:

$$\begin{cases} B_{mc}^{I}(r) = p\left(S_{11}r^{p-1} + \frac{S_{21}}{r^{p+1}} + \frac{k_{s1}(r)}{r}\right) \\ B_{ms}^{I}(r) = -p\left(C_{11}r^{p-1} + \frac{C_{21}}{r^{p+1}}\right) \\ B_{mc}^{II}(r) = p\left(E_{31}r^{p-1} + \frac{E_{41}}{r^{p+1}}\right) \\ H_{ms}^{II}(r) = \frac{-p}{\mu_o}\left(E_{31}r^{p-1} - \frac{E_{41}}{r^{p+1}}\right) \end{cases} \quad \text{(III- 17)}$$

With:

$$\begin{cases} H_{mc}^{I}(r) = \frac{-p}{\mu_{pm}r}\left(C_{11}r^{p} - \frac{C_{21}}{r^{p}} + \frac{k_{c1}(r)}{p}\right) & \text{for } p \neq 1 \\ H_{ms}^{I}(r) = \frac{-p}{\mu_{pm}r}\left(S_{11}r^{p} - \frac{S_{21}}{r^{p}} + \frac{k_{s1}(r)}{p} - \frac{J}{p}r\right) & \text{for } p \neq 1 \\ H_{mc}^{I}(r) = \frac{-1}{\mu_{pm}r}\left(C_{11}r - \frac{C_{21}}{r} + k_{c1}(r)\right) & \text{for } p = 1 \\ H_{ms}^{I}(r) = \frac{-1}{\mu_{pm}r}\left(S_{11}r - \frac{S_{21}}{r} + k_{s1}(r) - Jr\right) & \text{for } p = 1 \end{cases}$$

And:

$$\begin{cases} k_{c1}(r) = 0 \\ k_{s1}(r) = \begin{cases} \frac{J}{1+p}r & p \neq 1 \\ 0 & p = 1 \end{cases} \end{cases} \quad \text{(III- 18)}$$

By applying boundary conditions and continuity conditions on interfaces (i.e. Equations III-8 and III-9) we obtain:

$$\begin{cases} H_{\theta}^{I}(r = R_1, \theta) = 0 \\ H_{\theta}^{II}(r = R_3, \theta) = 0 \\ H_{\theta}^{I}(r = R_2, \theta) = H_{\theta}^{II}(r = R_2, \theta) \\ B_{r}^{I}(r = R_2, \theta) = B_{r}^{II}(r = R_2, \theta) \end{cases} \quad \text{(III- 19)}$$

Then $\forall\, p$:

$$\begin{cases} S_{11}R_1^{p-1} - \frac{S_{21}}{R_1^{p+1}} + \frac{k_{s1}(R_1)}{R_1 p} - \frac{J}{p} = 0 \\ C_{11}R_1^{p-1} - \frac{C_{21}}{R_1^{p+1}} = 0 \\ E_{31}R_3^{p-1} - \frac{E_{41}}{R_3^{p+1}} = 0 \\ S_{11}R_2^{p-1} - \frac{S_{21}}{R_2^{p+1}} + \frac{k_{s1}(R_2) - R_2 J}{R_2 p} = \mu_r E_{31}R_2^{p-1} - \mu_r \frac{E_{41}}{R_2^{p+1}} \\ C_{11}R_2^{p-1} - \frac{C_{21}}{R_2^{p+1}} + \frac{k_{c1}(R_2)}{R_2 p} = 0 \\ S_{11}R_2^{p-1} + \frac{S_{21}}{R_2^{p+1}} + \frac{k_{s1}(R_2)}{R_2} = E_{31}R_2^{p-1} + \frac{E_{41}}{R_2^{p+1}} \\ C_{11}R_2^{p-1} + \frac{C_{21}}{R_2^{p+1}} + \frac{k_{c1}(R_2)}{R_2} = 0 \end{cases} \quad \text{(III- 20)}$$

Furthermore, knowing that:

$$B_{mc}^{II}(R_3) = B_m \quad \text{(III- 21)}$$

To obtain permanent magnet thickness, radius R_1 should be determined. For the purpose, only S_{11}, S_{21}, E_{31}, E_{41} coefficients should be calculated function of R_3 and R_2, therefore only 3rd, 4th and 7th equations of (III-20) and equation (III-21) are considered as:

$$\begin{cases} E_{31}R_3^{p-1} - \frac{E_{41}}{R_3^{p+1}} = 0 \\ E_{31}R_3^{p-1} + \frac{E_{41}}{R_3^{p+1}} = \frac{B_m}{p} \\ S_{11}R_2^p + \frac{S_{21}}{R_2^p} + k_{s1}(R_2) = E_{31}R_2^p + \frac{E_{41}}{R_2^p} \\ S_{11}R_2^p - \frac{S_{21}}{R_2^p} + \frac{k_{s1}(R_2) - R_2 J}{p} = \mu_r E_{31}R_2^p - \mu_r \frac{E_{41}}{R_2^p} \end{cases} \quad \text{(III- 22)}$$

Therefore,

- For $p \neq 1$:

$$\begin{cases} E_{31} = \frac{B_m}{2p} R_3^{1-p} \\ E_{41} = \frac{B_m}{2p} R_3^{1+p} \\ S_{11} = \frac{(1+\mu_r)}{4p} R_3^{1-p} B_m + \frac{(1-\mu_r)}{4p} \frac{R_3^{1+p}}{R_2^{2p}} B_m \\ S_{21} = \frac{(1-\mu_r)}{4p} R_3^{1-p} R_2^{2p} B_m + \frac{(1+\mu_r)}{4p} R_3^{1+p} B_m - \frac{R_2^{p+1}}{p+1} J \end{cases} \quad \text{(III- 23)}$$

- For $p = 1$:

$$\begin{cases} E_{31} = \frac{B_m}{2} \\ E_{41} = \frac{B_m}{2} R_3^2 \\ S_{11} = \frac{(1+\mu_r)}{4} B_m + \frac{(1-\mu_r)}{4} \frac{R_3^2}{R_2^2} B_m + \frac{J}{2} \\ S_{21} = \frac{(1-\mu_r)}{4} R_2^2 B_m + \frac{(1+\mu_r)}{4} R_3^2 B_m - \frac{R_2^2}{2} J \end{cases}$$

Consequently, thickness of permanent magnet can be deduced from the following equation:

$$\begin{cases} S_{11}R_1^{p-1} - \frac{S_{21}}{R_1^{p+1}} + \frac{k_{s1}(R_1)}{R_1 p} - \frac{J}{p} = 0 & \text{for } p \neq 1 \\ S_{11} - \frac{S_{21}}{R_1^2} - J = 0 & \text{for } p = 1 \end{cases} \quad \text{(III- 24)}$$

Then:

$$\begin{cases} S_{11}R_1^{2p} - S_{21} - R_1^{p+1} \frac{J}{1+p} = 0 & \text{for } p \neq 1 \\ R_1 = \sqrt{\frac{S_{21}}{S_{11} - J}} & \text{for } p = 1 \end{cases} \quad \text{(III- 25)}$$

Knowing that:

$$e_{pm} = R_2 - R_1 \quad \text{(III- 26)}$$

Where: e_{pm} is the thickness of permanent magnet.

Equation (III-25) becomes:

$$\begin{cases} S_{11}R_2^{2p}\left(1 - \frac{e_{pm}}{R_2}\right)^{2p} - S_{21} - R_2^{p+1}\left(1 - \frac{e_{pm}}{R_2}\right)^{p+1} \frac{J}{1+p} = 0 & \text{for } p \neq 1 \\ e_{pm} = R_2 - \sqrt{\frac{S_{21}}{S_{11} - J}} & \text{for } p = 1 \end{cases} \quad \text{(III- 27)}$$

By using the Newton-Raphson's method in the case of $p > 1$ of the equation (III-27), the PM thickness can be directly deduced as given below:

- For 1st order approximation

$$\begin{cases} \left(1 - \frac{e_{pm}}{R_2}\right)^{2p} \approx 1 - 2p\frac{e_{pm}}{R_2} \\ \left(1 - \frac{e_{pm}}{R_2}\right)^{p+1} \approx 1 - (p+1)\frac{e_{pm}}{R_2} \end{cases} \quad \text{(III- 28)}$$

Then, the thickness of permanent magnet at the 1st order approximation:

$$e_{pm} = \frac{R_2^{p+1} J - S_{11}(1+p)R_2^{2p} + S_{21}(1+p)}{R_2^p J(1+p) - 2pS_{11}(1+p)R_2^{2p-1}} \quad \text{(III- 29)}$$

- For 2nd order approximation:

$$\begin{cases}\left(1-\frac{e_{pm}}{R_2}\right)^{2p} \approx 1-2p\frac{e_{pm}}{R_2}+\frac{2p(2p-1)}{2}\left(\frac{e_{pm}}{R_2}\right)^2 \\ \left(1-\frac{e_{pm}}{R_2}\right)^{p+1} \approx 1-(p+1)\frac{e_{pm}}{R_2}+\frac{(p+1)p}{2}\left(\frac{e_{pm}}{R_2}\right)^2\end{cases} \quad \text{(III- 30)}$$

Then:

$$\frac{1}{2}D_2\, e_{pm}^2 - D_1 e_{pm} + D_0 = 0 \quad \text{(III- 31)}$$

With: $D_2 = 2p(2p-1)S_{11}R_2^{2p-2} - JpR_2^{p-1}$, $D_1 = 2pS_{11}R_2^{2p-1} - JR_2^p$, and $D_0 = S_{11}R_2^{2p} - S_{21} - \frac{JR_2^{p+1}}{p+1}$

Then, the thickness of permanent magnet at the 2nd order approximation is:

$$e_{pm} = \frac{D_1 + \sqrt{D_1^2 - 2D_oD_2}}{D_2} \quad \text{(III- 32)}$$

III.3.1.3 Halbach permanent magnet design

a. Direct design of segmented Halbach permanent magnet

The realization of the polarization of PM Halbach, illustrated in Figure III. 4, is very difficult. For the purpose, the discretization method is often the used solution. Discretization of PM Halbach can be approached by several equal length PM blocs with different parallel polarizations (cf. Figure III. 5) or can be approached by several optimized PM blocs. The parallel polarization approached by several equal lengths PM blocs is governed by the following equation:

$$\overrightarrow{J(\theta_k)} = \begin{cases} J_r(\theta_k) = J\cos(p\theta_k) \\ J_\theta(\theta_k) = \pm J\sin(p\theta_k)\end{cases} \quad \text{with} \quad \theta_k = \theta_{k-1} + \frac{\delta\theta}{2} \quad \text{(III- 33)}$$

Where: θ_k is the angle at the center of PM bloc k, θ_{k-1} is the angle at the center of PM bloc $k-1$, $\delta\theta$ is the PM bloc angular width ($\delta\theta = \pi/pn_b$), n_b is the number of segments, $J(\theta_k)$ is the polarization of PM bloc k, $J_r(\theta_k)$ and $J_\theta(\theta_k)$ are the radial and tangential components of the polarization of PM block.

Indeed, to get closer to an ideal Halbach PM, the number of blocs should be increased as shown in the resulting airgap flux density Figure III. 6.

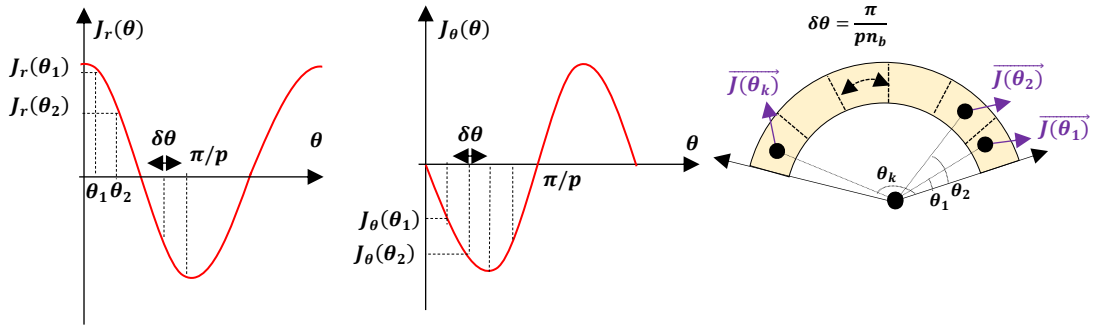

(a) (b) (c)

Figure III. 5. Discretized ideal Halbach PM:
(a) radial component of polarization, (b) tangential component of polarization, (c) segmented Halbach PM

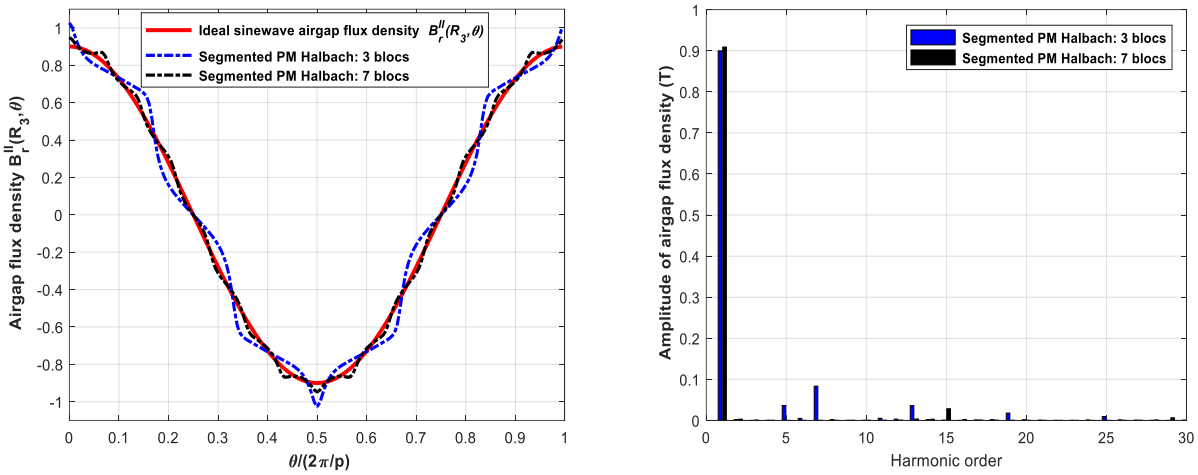

(a) (b)

Figure III. 6. (a) Resulting airgap flux density of discretized Halbach PM, (b) harmonic analysis of resulting airgap flux density

b. Design of segmented Halbach permanent magnet using optimization

For different polarization types of Halbach PM, design is often carried out using optimization procedures [Chen_17] [Mel_07] [Hua_18] [Mar_09]. Indeed, airgap flux density can be written as linear superposition of elementary airgap flux densities generated by each polarization of PM bloc. For instance, airgap flux density can be written as linear superposition of elementary airgap flux density generated by unit radial $J_{rk}(\theta)$ and unit tangential $J_{\theta k}(\theta)$ polarizations in each PM segment as given by:

$$B_r^{II}(R_3,\theta) = \Sigma_k (J_r^k b_{rk}^{II}(R_3,\theta) + J_\theta^k b_{\theta k}^{II}(R_3,\theta)) \quad \text{(III- 34)}$$

Where: J_r^k is the amplitude of radial polarization of k PM segment, J_θ^k is the amplitude of tangential polarization of k PM segment, b_{rk}^{II} and $b_{\theta k}^{II}$ are the elementary airgap flux densities generated by unit radial and unit tangential polarization in each segment k as illustrated in Figure III.7.

Therefore, Halbach PM can be optimized by taking as variables the polarizations and the sizes of all PM segments. Sequential Quadratic Programming Method (SQPM) optimization can be used given that it is the most used optimization method. In fact, thanks to the linear superposition applied to the airgap flux density, Least Squares (LS) method can be used inside (SQPM) to reduce the number of optimization variables. (LS) method allows finding the required radial and tangential polarizations of segmented PM Halbach of each optimization solution of SQPM. SQPM allows finding the required sizes of segmented PM Halbach as illustrated in Figure III.8. This procedure is characterized by reduced time computation although sizes and polarizations are variables. This optimization procedure can be suitable for all PM polarization types. Figure III. 9 compares the direct designed segmented PM Halbach with the one optimized segmented PM Halbach. Direct design gives result close to the one obtained using optimization.

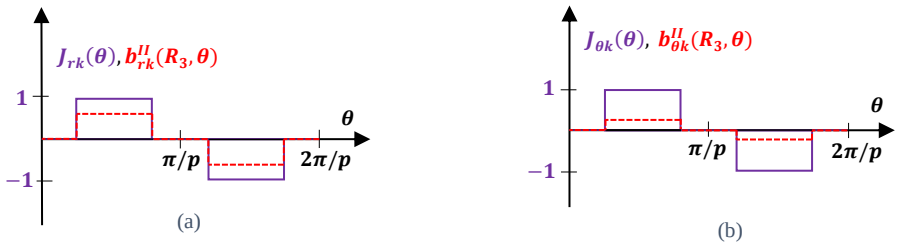

(a) (b)

Figure III. 7. (a) Unit radial polarization with its resulting elementary airgap flux density, (b) Unit tangential polarization with its resulting elementary airgap flux density

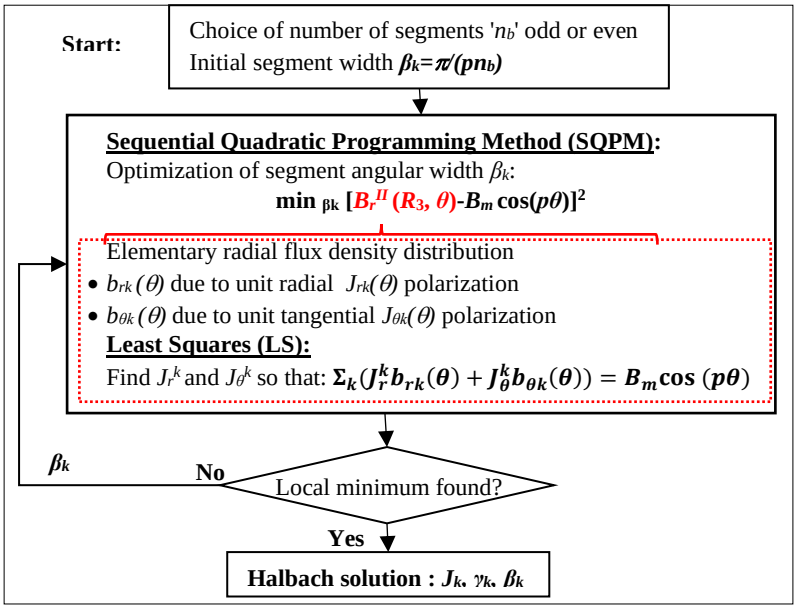

Figure III. 8. Optimization procedure: LS method inside the SQPM

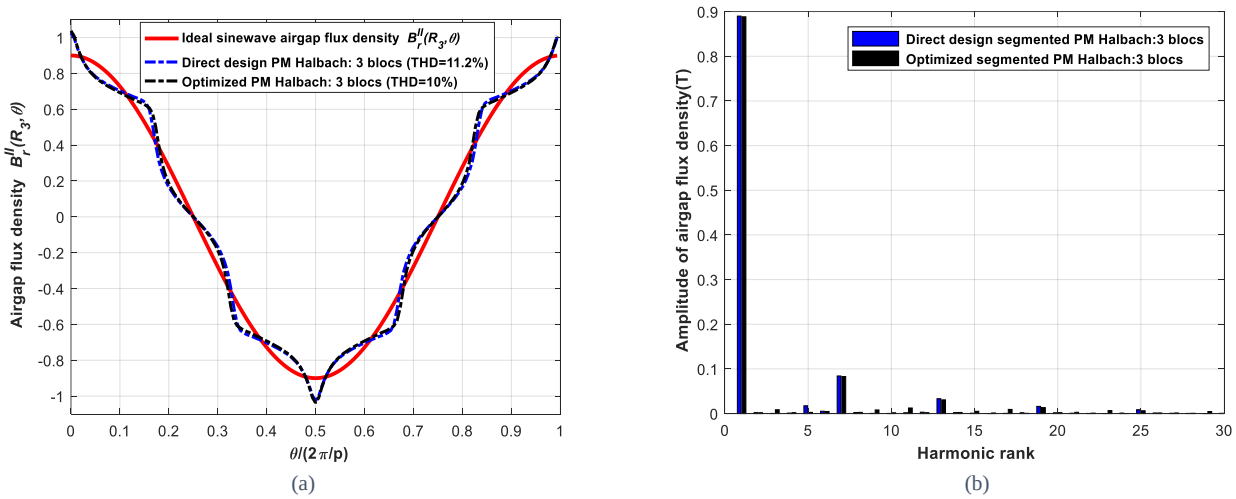

(a) (b)

Figure III. 9. Comparison of optimized and direct design Parallel Polarization of segmented Halbach PM: (a) airgap flux density, (b) harmonic analysis of airgap flux density

III.3.2 Stator configuration

As it is hard to realize ideal Halbach PM, sine wave stator winding is also difficult to realize. However, it can be designed as closer as possible to a sine wave stator winding by means of conductor distribution functions. The following section will describe these functions. These last ones are useful to determine the surface current density function.

III.3.2.1 Conductor distribution functions

Basically, conductor distribution functions are not often employed for sizing winding. It's rather the Magnetomotive Force (MMF) functions which are mostly used. Although conductor distribution functions are the real winding functions. They are given by:

$$C(\theta)=\frac{1}{R\chi}N(\theta) \qquad \text{(III- 35)}$$

Where: $N(\theta)$ is the winding distribution function expressed by the number of conductors, R is the stator bore radius and χ is the opening slot angle.

MMF are the integrated function of conductor distribution functions as demonstrated in Appendix B. Conductor distribution functions can be described for all winding configurations as distributed and concentrated windings. In our analysis we will focus only on the distributed winding.

a. Elementary coil with full pith

An elementary coil with full pitch is characterized by go-conductors placed in one slot and return-conductors placed in a slot located at angle π/p from the go-conductors as shown in Figure III.10. a. Hence, the winding function of elementary coil with full pitch can be expressed using Fourier's series:

$$N_e(\theta) = \sum_{k=1}^{k=\infty} \frac{4N_{cs}}{\pi} \frac{sin(0.5(2k-1)p\chi)}{(2k-1)} \cos\big((2k-1)p\theta\big) \quad \text{(III- 36)}$$

Where: N_{cs} is the number of conductor per slot and k is the harmonic rank.

The conductor distribution function of elementary coil with full pitch (cf. Figure III.10. b) is expressed by:

$$C_e(\theta) = \sum_{k=1}^{k=\infty} \frac{4N_{cs}}{\pi R} \frac{sin(0.5(2k-1)p\chi)}{(2k-1)\chi} \cos\big((2k-1)p\theta\big) \quad \text{(III- 37)}$$

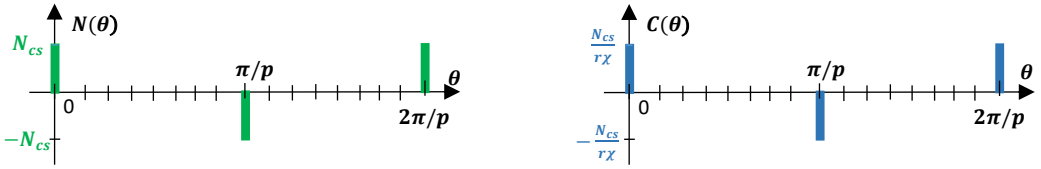

(a) (b)

Figure III. 10. Elementary coil with full pitch: (a) winding function, (b) distributed winding function

b. Full pitch distributed winding: several coils per poles and per phases

For full pitch distributed winding with several coils per pole and per phase as shown in Figure III.11, the winding function can be deduced from the winding function of elementary coil by:

$$N(\theta) = \sum_{j=1}^{j=m} \sum_{k=1}^{k=\infty} \frac{4N_{cs}}{\pi} \frac{sin(0.5(2k-1)p\chi)}{(2k-1)} \cos\big((2k-1)p(\theta-(j-1)\gamma)\big) \quad \text{(III- 38)}$$

Where: m is the number of slots per pole and per phase (i.e.: $m = N_s/(2pq)$), N_s is the number of slots, q is the number of phases and γ is the angular step between two neighboring coils of the same phase.

Using equation (III-35), the conductor distribution function is given by:

$$C(\theta) = \sum_{k=1}^{k=\infty} \frac{4N_{cs}}{\pi R} \frac{sin(0.5(2k-1)p\chi)}{(2k-1)\chi} \frac{\sin(0.5(2k-1)pm\gamma)}{\sin(0.5(2k-1)p\gamma)} \cos\big((2k-1)p\theta\big) \quad \text{(III- 39)}$$

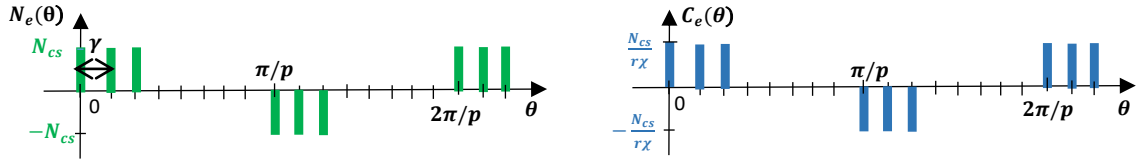

(a) (b)

Figure III. 11. Full pitch distributed winding "several coils per poles and per phases": (a) winding function, (b) distributed winding function

c. Full pitch distributed winding: several coils per poles and per phases with several layers

For winding with several layers (cf. Figure III. 12), the winding function can be deduced from equation (III-38) by:

$$N(\theta) = \sum_{l=1}^{l=nl} \sum_{k=1}^{k=\infty} \frac{4N_{cs}}{\pi n_l} \frac{sin(0.5(2k-1)p\chi)}{(2k-1)} \frac{\sin(0.5(2k-1)mp\gamma)}{\sin(0.5(2k-1)p\gamma)} \cos\big((2k-1)p(\theta-(l-1)\xi)\big) \quad \text{(III- 40)}$$

Where: ξ is the angular step between two layers of the same phase and n_l is the number of layers.

The corresponding conductor distribution function is given by:

$$C(\theta) = \sum_{k=1}^{k=\infty} \frac{4N_{cs}}{\pi R n_l} \frac{sin(0.5(2k-1)p\chi)}{(2k-1)\chi} \frac{\sin(0.5(2k-1)pm\gamma)}{\sin(0.5(2k-1)p\gamma)} \frac{\sin(0.5(2k-1)n_l p\xi)}{\sin(0.5(2k-1)p\xi)} \cos\big((2k-1)p\theta\big) \quad \text{(III- 41)}$$

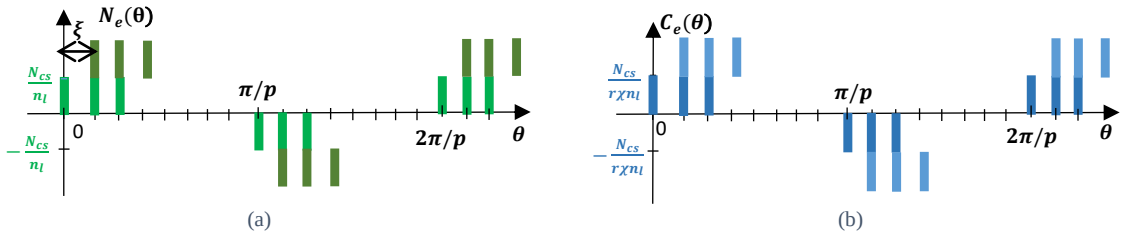

(a) (b)

Figure III. 12. Full pitch distributed winding "several coils per poles and per phases with several layers": (a) winding function, (b) distributed winding function

d. Several phases

The conductor distribution functions of a winding with q phases, N_{cs} number of conductors per slot, m number of slots per pole and per phase and n_l number of layers are governed by:

$$C_i(\theta) = \sum_{k=1}^{k=\infty} A_{2k-1} D_{2k-1} L_{2k-1} \cos\left((2k-1)\left(p\theta - \frac{(i-1)2\pi}{q}\right)\right) \quad \text{(III- 42)}$$

With:

$$\begin{aligned} A_{2k-1} &= \frac{2pN_{cs}}{\pi R} \frac{sin(0.5(2k-1)p\chi)}{0.5(2k-1)p\chi} \\ D_{2k-1} &= \frac{\sin(0.5(2k-1)pm\gamma)}{\sin(0.5(2k-1)p\gamma)} \\ L_{2k-1} &= \frac{\sin(0.5\,(2k-1)pn_l\xi)}{n_l \sin(0.5\,(2k-1)p\xi)} \end{aligned} \quad \text{(III- 43)}$$

Where: A_{2k-1} expresses the full pitch winding, D_{2k-1} expresses the distributed winding and L_{2k-1} expresses winding having several layers.

III.3.2.2 Surface current density function

As mentioned in previous chapter (cf. § II.2.2), the surface current density is useful to take into account the armature reaction field in the 2D magnetic vector potential model of electric motors. Surface current density wave can be defined by the separation of space functions of the conductor distribution functions along stator bore and time functions of currents:

$$K(\theta, t) = \sum_{i=1}^{q} C_i(\theta) \times I_i(t) \quad \text{(III- 44)}$$

Where: $I_i(t)$ is the time function of the q of the *i* phase current.

For three phase sine wave currents, the surface current density function is then given by:

$$K(\theta, t) = \sum_{i=1}^{i=3} \sum_{k=1}^{k=\infty} A_{2k-1} D_{2k-1} L_{2k-1} \cos\left[(2k-1)\left(p\theta - \frac{(i-1)2\pi}{3}\right)\right] I_m \cos\left[\omega t - \frac{(i-1)2\pi}{3}\right] \quad \text{(III- 45)}$$

With: I_m is the amplitude of current, ω is the electrical pulse and t is the time.

For fundamental component ($k = 1$), equation (III-45) is reduced to:

$$K_1(\theta, t) = \sum_{i=1}^{i=3} A_1 D_1 L_1 I_m \cos\left(p\theta - \frac{(i-1)2\pi}{3}\right) \cos\left(\omega t - \frac{(i-1)2\pi}{3}\right) \quad \text{(III- 46)}$$

Where:

$$\begin{cases} A_1 = \frac{2pN_{cs}}{\pi R} \frac{sin(0.5p\chi)}{0.5p\chi} \\ D_1 = \frac{sin(0.5pm\gamma)}{sin(0.5p\gamma)} \\ L_1 = \frac{sin(0.5pn_l\xi)}{n_l sin(0.5p\xi)} \end{cases} \quad \text{(III- 47)}$$

Therefore, the fundamental component of surface current density wave is governed by:

$$K_1(\theta, t) = K_{m1} \cos(p\theta - \omega t) \quad \text{(III- 48)}$$

With:

$$K_{m1} = \frac{3A_1 D_1 L_1 I_m}{2} \quad \text{(III- 49)}$$

Where: K_{m1} is the fundamental amplitude of the surface current density.

III.3.2.3 Winding coefficient

Winding coefficient characterizes the harmonic content of a winding configuration. It is therefore involved in performances of electric motors namely electric parameters. Classically, winding coefficient is defined using fundamental component of MMF [Pyr_14] by:

$$k_w = k_d k_{pi} k_s \quad \text{(III- 50)}$$

With:

$$\begin{cases} k_d = \frac{\sin(0.5pm\gamma)}{m\sin(0.5p\gamma)} \\ k_{pi} = \sin\left(\frac{\tau\pi}{2}\right) \\ k_s = \frac{\sin\left(\frac{s\pi}{2}\right)}{\frac{s\pi}{2}} \end{cases} \quad \text{(III- 51)}$$

Where: τ is the short pitch factor, s is the skewing factor, k_d is the distribution winding coefficient, k_{pi} is the pitch coefficient and k_s is the skewing coefficient.

Using conductor distribution functions, winding coefficient is defined [Sle_94] by:

$$k_w = \frac{K_{m1}}{A_m} \quad \text{(III- 52)}$$

Where A_m is the amplitude of linear current density defined by:

$$A_m = \frac{N_s N_{cs} I_m}{2\pi R} \quad \text{(III- 53)}$$

Therefore, according to equations (III-47) and (III-49), the winding coefficient is given by:

$$k_w = \frac{\sin(0.5p\chi)}{0.5p\chi}\frac{sin(0.5pm\gamma)}{msin(0.5p\gamma)}\frac{sin(0.5pn_l\xi)}{n_l sin(0.5p\xi)} \quad \text{(III- 54)}$$

Equation (II-54) can be written also as: $k_w = \frac{D_1 B_1}{mL_1}$ with $B_1 = \frac{2pN_{cs}A_1}{\pi R}$. For small opining slot and one-layer winding, winding coefficient calculated using conductor distribution function is equal to the winding coefficient calculated using MMF (cf. also to the Appendix B).

III.4 Stator and rotor additional sizes

Main sizes of the surface mounted permanent magnet synchronous motor have been previously determined in Chapter II. By considering a chosen winding configuration, a chosen magnetic flux density level in rotor yoke and polarization in permanent magnets, the additional stator and rotor sizes will be determined in the next sections. This allows to accurate, consequently, the assessment of specific power of electric motor.

III.4.1 Additional stator sizes

Additional stator sizes can be obtained by choosing a winding configuration set by:

- a number of phases "q",
- a number of slots per poles and per phases "m",
- a number of conductors per slot "N_{cs}",
- a full pitch winding "$\tau = 1$" or a short pitch winding "$\tau < 1$".

With taking into account rectangular geometry for slots, the slot and tooth widths with their corresponding surfaces are assessed by:

$$l_s = (1 - r_{tooth})\frac{2\pi R}{N_s} \quad \text{(III- 55)}$$

$$l_t = r_{tooth}\frac{2\pi R}{N_s} \quad \text{(III- 56)}$$

$$S_{tooth} = \pi h_s(h_s + 2R)/N_t - S_{slot} \quad \text{(III- 57)}$$

With S_{slot} is the slot surface (cf to equation (II-33)), N_t is the number of teeth and it's equal to the number of slots N_s given by:

$$N_s = 2pqm \quad \text{(III- 58)}$$

Where: r_{tooth} is the ratio between tooth length to bore radius determined by equation (II-48) and h_s is the slot height determined by equation (II-46).

Indeed, once the winding configuration is chosen, end winding sizes can be accurately assessed by means of "k_{tb}". It is given by:

$$k_{tb} = \frac{l_{ht}}{L_m} = 1 + \frac{\tau\pi}{p}\frac{R}{L_m} + \frac{\pi r_{tb}}{L_m} \quad \text{(III- 59)}$$

With:

$$r_{tb} = \frac{2\pi R}{N_s} \quad \text{(III- 60)}$$

Where: l_{ht} is the length of one half turn (cf. Figure III. 13).

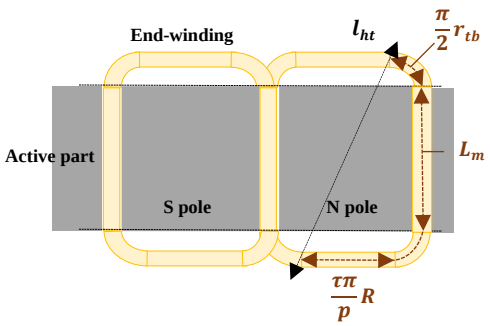

Figure III. 13. Approximated end winding geometry

III.4.2 Additional rotor sizes

Likewise, additional rotor sizes can be obtained by choosing some parameters and materials such as:

- Magnetic flux density in rotor yoke "B_{ry}" to specify the rotor yoke thickness,
- Rotor magnetic sheets: " Silicon Iron alloys" or "Iron Cobalt alloys",
- Magnetic polarization and relative permeability of permanent magnets "J"and "μ_r" to assess the Halbach PM thickness (cf. § III.3.1.2),
- Permanent magnets: "Samarium-Cobalt" or "Neodymium Iron Boron".

By neglecting the leakage flux, rotor yoke thickness can be deduced using the flux conservation principle:

$$h_{ry} = \frac{B_{sy}}{B_{ry}} h_y \quad \text{(III- 61)}$$

Where: h_y is the stator yoke thickness calculated using equation (II-45) and B_{sy} is the flux density in stator yoke.

Hence, shaft radius is governed by:

$$R_{sh} = R_r - e_{pm} - h_{ry} \quad \text{(III- 62)}$$

Where: R_r is the external rotor yoke.

III.5 Electric parameters of surface mounted permanent magnet synchronous motor

III.5.1 Noload magnetic flux

Considering the fundamental component of conductor distribution function $C_1(\theta)$ and the fundamental component of magnetic potential vector at the stator bore $A_z^{II}(R_3, \theta)$ due to Halbach PM source with adequate rotor position (i.e. $\frac{\pi}{2}$ for maximum torque) , the magnitude of no-load flux is written as:

$$\Phi_{vm} = R_3 L_m \int_0^{2\pi} A_{z_1}^{II}(R_3, \theta) \times C_1(\theta) d\theta \quad \text{(III- 63)}$$

With:

$$\begin{cases} C_1(\theta) = A_1 D_1 L_1 \cos(p\theta) \\ A_{Z_1}^{II}(R_3, \theta) = \left(E_{31} R_3^p + \frac{E_{41}}{R_3^p} \right) \sin\left(p\theta + \frac{\pi}{2} \right) \end{cases} \quad \text{(III- 64)}$$

And

$$\begin{cases} E_{31} = \frac{B_m}{2p} R_3^{1-p} \\ E_{41} = \frac{B_m}{2p} R_3^{1+p} \end{cases} \quad \text{(III- 65)}$$

Then:

$$\Phi_{vm} = R_3 L_m \int_0^{2\pi} \frac{B_m}{p} R_3 \cos(p\theta) \times A_1 D_1 L_1 \cos(p\theta)\, d\theta \quad \text{(III- 66)}$$

Therefore, the magnitude of the no-load flux is:

$$\Phi_{vm} = \frac{\pi L_m B_m R_3^2 A_1 D_1 L_1}{p} \quad \text{(III- 67)}$$

With: $R_3 = R$, R is the stator bore radius. By using equations (III-47) and (III-54), the magnitude of the no-load flux can be written:

$$\Phi_{vm} = 2 L_m B_m R_3 m N_{cs} k_w \quad \text{(III- 68)}$$

Or:

$$\Phi_{vm} = \frac{2L_m B_m R_3 N_{ts} k_w}{p} \quad \text{(III- 69)}$$

With: N_{ts} is the number of turns per phase connected in series and defined as $N_{ts} = pmN_{cs}$. The fundamental component of no-load flux wave given per phase is:

$$\Phi_{vi}(\theta) = \Phi_{vm} \cos\left(p\theta - \frac{(i-1)2\pi}{q}\right) \quad \text{(III- 70)}$$

III.5.2 Back-electromotive force

The back-electromotive force per phase can be then derived from the no-load flux using the Faraday's law:

$$E_i = -\frac{d\Phi_{vi}(\theta)}{d\theta}\dot{\theta} = \omega\Phi_{vm}\, sin\left(p\theta - \frac{(i-1)2\pi}{q}\right) \quad \text{(III- 71)}$$

Where: ω is the electric pulse ($\omega = p\dot{\theta}$).

III.5.3 Resistance, self and mutual inductances

Resistance per phase is directly derived from the Joule losses (cf. equation (II-64)) by:

$$R_s = 2N_{ts}\rho_{cu}(T_{win})\frac{k_{lc}k_{tb}L_m}{S_{cond}} \quad \text{(III- 72)}$$

Where: ρ_{cu} is the resistivity of copper at temperature T_{win}, k_{lc} is a coefficient which takes into account the twisting of conductors or wires (its calculation is presented in Chapter IV), S_{cond} is the cross section of conductor (calculated in equation (II-33)).

Self and mutual inductances can be calculated from the flux linkage or from the stored energy although they are more complex to evaluate due to the magnet flux [Lip_04]. Self and mutual inductances have mainly three components which are linked to the airgap linkage flux, the slot leakage flux and the end-winding leakage flux [Hen_94]. Usually, the component linked to the airgap linkage flux is the main component of self and mutual inductances. Therefore, we will focus only on the calculation of this component to approximate the evaluation of self and mutual inductances.

The self-inductance calculated using the total airgap linkage flux per phase is given by:

$$L_s = \frac{\Psi_g}{I_m} \quad \text{(III- 73)}$$

Where: I_m is the amplitude of current and Ψ_g is the total airgap linkage flux.

The total airgap linkage flux per phase calculated in the stator bore is given by:

$$\Psi_g = p\int_0^{\frac{\pi}{p}} \phi_p(\theta) N_s(\theta)\, d\theta \quad \text{(III- 74)}$$

Where: $\phi_p(\theta)$ is the flux per pole given by:

$$\phi_p(\theta) = \frac{2RL_m}{p} B_{ss}\cos(p\theta) \quad \text{(III- 75)}$$

And: B_{ss} is the flux density produced by the supplied conductors as given by the following equation:

$$B_{ss} = \mu_o H_g \quad \text{(III- 76)}$$

With: H_g is the magnetic field strength calculated by the Ampere's law applied on the magnetic flux lines established by the sinewave distributed conductors $N_{sin}(\theta)$ as illustrated in Figure III.14:

$$2(e_{pm} + e_g)H_g = \frac{N_{tsin}}{p} I_m \quad \text{with} \quad \mu_r \approx 1 \quad \text{(III- 77)}$$

And:

$$N_{sin}(\theta) = \frac{N_{tsin}}{2}\cos(p\theta) \quad \text{(III- 78)}$$

With: N_{tsin} is the max number of turns of sine wave distributed conductor.

Therefore, using the equations (III-76) to (III-79) the total airgap linkage flux per phase for sine wave distributed conductors can be deduced by:

$$\Psi_g = \frac{\pi}{4}\mu_o\left(\frac{N_{tsin}}{p}\right)^2 \frac{RL_m}{(e_{pm}+e_g)}\, I_m \quad \text{(III- 79)}$$

The self-inductance per phase for sine wave distributed conductors is:

$$L_s = \frac{\pi}{4}\mu_o\left(\frac{N_{tsin}}{p}\right)^2 \frac{R}{e_{pm}+e_g} L_m \quad \text{(III- 80)}$$

Practically, the actual number of turns is linked to the sine wave distributed conductors by the following equation according to [Hen_94]:

$$N_{tsin} = \frac{4}{\pi} k_w N_{ts} \quad \text{(III- 81)}$$

Eventually, the self-inductance per phase for the real winding is approximated by:

$$L_s = \frac{4}{\pi} \mu_o \left(\frac{k_w N_{ts}}{p}\right)^2 \frac{R}{e_{pm}+e_g} L_m \quad \text{(III- 82)}$$

Moreover, according to [Hen_94] for waves close to sine wave the mutual inductance for three phase winding can be approximated by:

$$M \approx -\frac{L_s}{2} \quad \text{(III- 83)}$$

Therefore, the cyclic inductance can be deduced by:

$$L_{cs} = L_s - M \quad \text{(III- 84)}$$

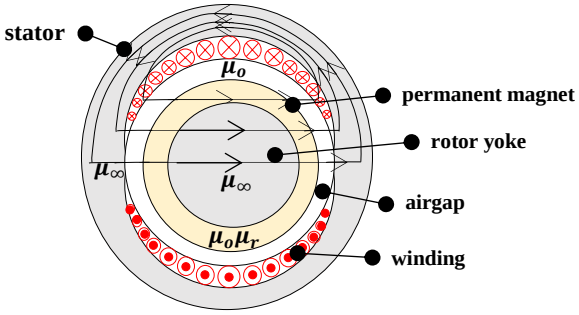

Figure III. 14. Magnetic flux lines established by the sinewave distributed winding

III.5.4 Electromagnetic torque

According to equation (II-3) and using established equation (III-49), the maximum average electromagnetic torque can be expressed also by:

$$T_{em_{max}} = \frac{3}{2} \pi R^2 L_m A_1 D_1 L_1 I_m B_m \quad \text{(III- 85)}$$

III.6 Inputs and outputs of SM-PMSM Tool

Figure III.15 summarizes the inputs and outputs of SM-PMSM. As SM-PMSM is based on TST assumptions it takes as inputs:

- The main sizes of electric motor,
- Some parameters defining the stator and the rotor configurations that are close to TST assumptions.

Therefore, SM-PMSM gives as outputs the additional rotor and stator sizes. Those will consequently modify the approximate weights assessed by TST to more accurate weights of SM-PMSM. For chosen rotor materials, the weights are recalculated in SM-PMSM Tool using equations (II-54) to (II-60). Moreover, the specific power and torque are revisited using equations (II-61) and (II-62). In contrast to TST, winding parameters such as winding and end-winding coefficients are accurately calculated in SM-PMSM Tool. Electric parameters are calculated for different number of conductors per slots. And lastly, performances and equivalent current density product are also recalculated by using equations (II-65) to (II-78) and (II-80) respectively.

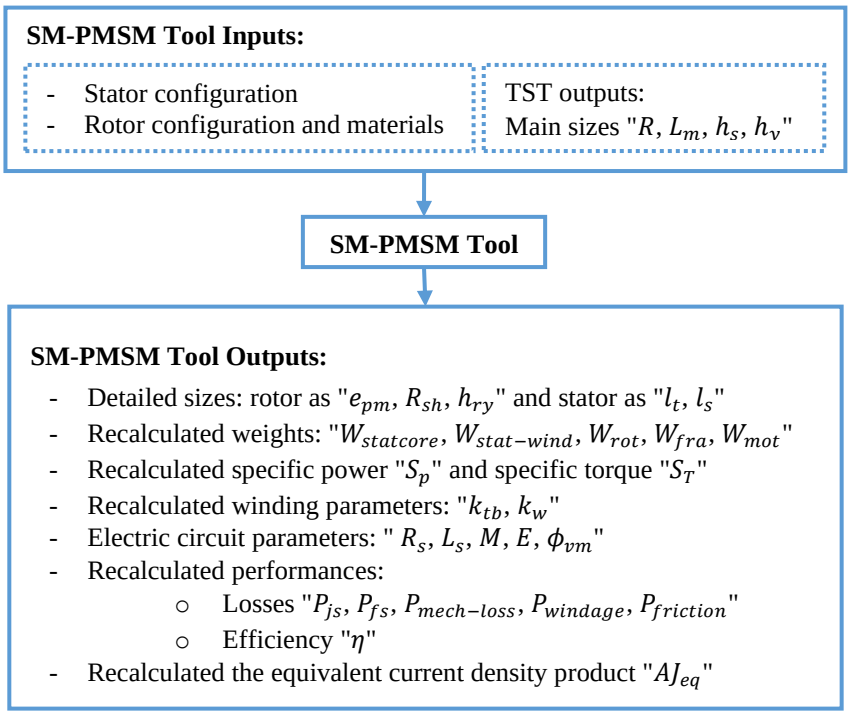

Figure III. 15. Inputs and outputs of SM-PMSM Tool

Conclusion

Surface **M**ounted **P**ermanent **M**agnet **S**ynchronous **M**otor "SM-PMSM" structure is chosen due to its simple analytical model at hand and also to satisfy the Target Setting Tool assumptions. Analytical model is developed to give more details of electric motor which allows more accurate sizing.

Firstly, we have determined the additional stator sizes from the chosen winding configuration. From chosen rotor configurations and materials we have determined the rotor sizes. To ensure sinewave airgap flux density (i.e. TST assumption), we have chosen the Halbach structure for permanent magnets.

Thickness of permanent magnets is calculated from the ideal Halbach definition and from the analytical model. We have determined Halbach polarization using the two proposed methods: a direct design method and optimization method.

Therefore, we have updated in SM-PMSM model some Target Setting Tool outputs namely the weights, the specific power and the specific torque, the winding parameters, the performances and the thermal constraint.

The conductor distribution functions were permitting us to determine the electric circuit parameters, namely: the inductances, the noload flux and the back electromotive force. We have also updated the Joule losses considering that end-winding size is more defined.

We have programmed in Matlab software the SM-PMSM model's equations as a tool called SM-PMSM tool. It considers set of inputs: the main sizes of electric motor, the stator and rotor configurations and gives set of outputs, namely: the additional sizes, the weights, the electric parameters and the performances. These outputs are required to the other work packages (WP2, 3, 5 and 6).

As well as for Target Setting Tool, SM-PMSM Tool will be validated in the next chapter through sizing electric motors for medium and long term targets.

Appendices

- **Appendix A: "Constants of potential vector in airgap and permanent magnet regions"**

$$\begin{bmatrix} R_1^{np} & -R_1^{-np} & 0 & 0 & 0 & 0 & 0 & 0 \\ 0 & 0 & R_1^{np} & -R_1^{-np} & 0 & 0 & 0 & 0 \\ R_2^{np} & R_2^{-np} & 0 & 0 & -R_2^{np} & -R_2^{-np} & 0 & 0 \\ 0 & 0 & R_2^{np} & R_2^{-np} & 0 & 0 & -R_2^{np} & -R_2^{-np} \\ \mu_r R_2^{np} & -\mu_r R_2^{-np} & 0 & 0 & -R_2^{np} & R_2^{-np} & 0 & 0 \\ 0 & 0 & \mu_r R_2^{np} & -\mu_r R_2^{-np} & 0 & 0 & -R_2^{np} & R_2^{-np} \\ 0 & 0 & 0 & 0 & R_3^{np} & -R_3^{-np} & 0 & 0 \\ 0 & 0 & 0 & 0 & 0 & 0 & R_3^{np} & -R_3^{-np} \end{bmatrix} \begin{bmatrix} C_{1n} \\ C_{2n} \\ S_{1n} \\ S_{2n} \\ E_{1n} \\ E_{2n} \\ E_{3n} \\ E_{4n} \end{bmatrix} = - \begin{bmatrix} \frac{k_{cn}(R_1)+R_1 J_{\theta cn}}{np} \\ \frac{k_{sn}(R_1)+R_1 J_{\theta sn}}{np} \\ k_{cn}(R_1) \\ k_{sn}(R_1) \\ \frac{k_{cn}(R_1)+R_2 J_{\theta cn}}{np} \\ \frac{k_{sn}(R_1)+R_2 J_{\theta sn}}{np} \\ 0 \\ 0 \end{bmatrix}$$

- **For *np*≠1**

$$\begin{cases} E_{1n} = \frac{\mu_r(J_{tcn}-npJ_{rsn})\left(R_2R_1^{2np}-R_2^{2np+1}\right)-(J_{rsn}-npJ_{tcn})\left(R_2R_1^{2np}+R_2^{2np+1}\right)+2\mu_rR_1^{np+1}R_2^{np}(J_{rsn}-npJ_{tcn})}{(n^2p^2-1)\left((1+\mu_r)R_2^{2np}\left(R_1^{2np}-R_3^{2np}\right)+(1-\mu_r)\left(R_2^{3np}-R_2^{-np}R_1^{2np}R_3^{2np}\right)\right)} \\ E_{2n} = E_{1n}R_3^{2np} \\ E_{3n} = \frac{\mu_r(J_{tsn}+npJ_{rcn})\left(R_2R_1^{2np}-R_2^{2np+1}\right)+(J_{rcn}+npJ_{tsn})\left(R_2R_1^{2np}+R_2^{2np+1}\right)-2\mu_rR_1^{np+1}R_2^{np}(J_{rcn}+npJ_{tsn})}{(n^2p^2-1)\left((1+\mu_r)R_2^{2np}\left(R_1^{2np}-R_3^{2np}\right)+(1-\mu_r)\left(R_2^{3np}-R_2^{-np}R_1^{2np}R_3^{2np}\right)\right)} \\ E_{4n} = E_{3n}R_3^{2np} \end{cases}$$

$$\begin{cases} C_{1n} = \frac{(J_{rsn}-npJ_{tcn})(\mu_rR_1^{np+1}(R_2^{2np}+R_3^{2np})+R_1^{np+1}R_2^{2np}-R_1^{np+1}R_3^{2np}-R_2^{3np+1}-R_2^{np+1}R_3^{2np})-(J_{tcn}-npJ_{rsn})R_2^{np+1}(R_2^{2np}-R_3^{2np})}{(n^2p^2-1)\left((R_1^{2np}R_2^{2np}-R_2^{2np}R_3^{2np})(1+\mu_r)+(R_2^{4np}-R_1^{2np}R_3^{2np})(1-\mu_r)\right)} \\ C_{2n} = \frac{(J_{rsn}-npJ_{tcn})(\mu_rR_1^{np+1}R_2^{2np}(R_2^{2np}+R_3^{2np})-R_2^{4np}R_1^{np+1}+R_1^{np+1}R_2^{2np}R_3^{2np}-R_1^{2np}R_2^{3np+1}-R_1^{2np}R_2^{np+1}R_3^{2np})-(J_{tcn}-npJ_{rsn})R_1^{2np}R_2^{np+1}(R_2^{2np}-R_3^{2np})}{(n^2p^2-1)\left((R_1^{2np}R_2^{2np}-R_2^{2np}R_3^{2np})(1+\mu_r)+(R_2^{4np}-R_1^{2np}R_3^{2np})(1-\mu_r)\right)} \\ S_{1n} = \frac{-(J_{rcn}+npJ_{tsn})(\mu_rR_1^{np+1}(R_2^{2np}+R_3^{2np})+R_1^{np+1}R_2^{2np}-R_1^{np+1}R_3^{2np}-R_2^{3np+1}-R_2^{np+1}R_3^{2np})-(J_{tsn}+npJ_{rcn})R_2^{np+1}(R_2^{2np}-R_3^{2np})}{(n^2p^2-1)\left((R_1^{2np}R_2^{2np}-R_2^{2np}R_3^{2np})(1+\mu_r)+(R_2^{4np}-R_1^{2np}R_3^{2np})(1-\mu_r)\right)} \\ S_{2n} = \frac{-(J_{rcn}+npJ_{tsn})(\mu_rR_1^{np+1}R_2^{2np}(R_2^{2np}+R_3^{2np})-R_2^{4np}R_1^{np+1}+R_1^{np+1}R_2^{2np}R_3^{2np}-R_1^{2np}R_2^{3np+1}-R_1^{2np}R_2^{np+1}R_3^{2np})-(J_{tsn}+npJ_{rcn})R_1^{2np}R_2^{np+1}(R_2^{2np}-R_3^{2np})}{(n^2p^2-1)\left((R_1^{2np}R_2^{2np}-R_2^{2np}R_3^{2np})(1+\mu_r)+(R_2^{4np}-R_1^{2np}R_3^{2np})(1-\mu_r)\right)} \end{cases}$$

- **For *np*=1**

$$\begin{cases} E_{11} = \frac{R_2\left(R_2^2+R_1\right)(J_{rs1}+J_{tc1}+ln(R_2)(J_{rs1}-J_{tc1}))-R_1\mu_r\left(R_2^2+R_2\right)(J_{rs1}+J_{tc1}+ln(R_1)(J_{rs1}-J_{tc1}))+R_2^2ln(R_2)\mu_r(R_1-R_2)(J_{rsn}-J_{tcn})}{2\left(R_2(R_1-R_3\mu_r)+R_2^2(R_1\mu_r-R_3)+R_2^3(1-\mu_r)-R_1R_3(1-\mu_r)\right)} \\ E_{21} = R_3E_{11} \\ E_{31} = \frac{-R_2\left(R_2^2+R_1\right)(J_{rc1}-J_{ts1}+ln(R_2)(J_{rc1}+J_{ts1}))+R_1\mu_r\left(R_2^2+R_2\right)(J_{rc1}-J_{ts1}+ln(R_1)(J_{rc1}+J_{ts1}))-R_2^2log(R_2)\mu_r(R_1-R_2)(J_{rcn}+J_{tsn})}{2\left(R_2(R_1-R_3\mu_r)+R_2^2(R_1\mu_r-R_3)+R_2^3(1-\mu_r)-R_1R_3(1-\mu_r)\right)} \\ E_{41} = R_3E_{31} \end{cases}$$

$$\begin{cases} C_{11} = \frac{R_2\left(R_2^2+R_3\right)(J_{rs1}+J_{tc1}+ln(R_2)(J_{rs1}-J_{tc1}))-R_1(J_{rs1}+J_{tc1}+ln(R_1)(J_{rs1}-J_{tc1}))\left(\mu_rR_2^2+R_2+R_3(\mu_r-1)\right)-R_2^2ln(R_2)(R_2-R_3)(J_{rs1}-J_{tc1})}{2\left(R_2(R_1-R_3\mu_r)+R_2^2(R_1\mu_r-R_3)+R_2^3(1-\mu_r)-R_1R_3(1-\mu_r)\right)} \\ C_{2n} = R_1\frac{R_2\left(R_2^2+R_3\right)(J_{rs1}+J_{tc1}+ln(R_2)(J_{rs1}-J_{tc1}))-R_2(J_{rs1}+J_{tc1}+ln(R_1)(J_{rs1}-J_{tc1}))(R_2R_3+R_2^2(\mu_r-1)+R_3\mu_r)-R_2^2ln(R_2)(R_2-R_3)(J_{rs1}-J_{tc1})}{2\left(R_2(R_1-R_3\mu_r)+R_2^2(R_1\mu_r-R_3)+R_2^3(1-\mu_r)-R_1R_3(1-\mu_r)\right)} \\ S_{1n} = \frac{R_1(J_{rc1}-J_{ts1}+ln(R_1)(J_{rc1}+J_{ts1}))(\mu_rR_2^2+R_2-R_3+R_3\mu_r)-R_2\left(R_2^2+R_3\right)(J_{rc1}-J_{ts1}+ln(R_2)(J_{rc1}+J_{ts1}))+R_2^2ln(R_2)(R_2-R_3)(J_{rc1}+J_{ts1})}{2\left(R_2(R_1-R_3\mu_r)+R_2^2(R_1\mu_r-R_3)+R_2^3(1-\mu_r)-R_1R_3(1-\mu_r)\right)} \\ S_{2n} = R_1\frac{-R_2\left(R_2^2+R_3\right)(J_{rc1}-J_{ts1}+ln(R_2)(J_{rc1}+J_{ts1}))+(J_{rc1}-J_{ts1}+ln(R_1)(J_{rc1}+J_{ts1}))R_2(R_2R_3+R_2^2(\mu_r-1)+R_3\mu_r)+R_2^2ln(R_2)(R_2-R_3)(J_{rc1}+J_{ts1})}{2\left(R_2(R_1-R_3\mu_r)+R_2^2(R_1\mu_r-R_3)+R_2^3(1-\mu_r)-R_1R_3(1-\mu_r)\right)} \end{cases}$$

- **Appendix B: " Magnetomotive force functions (MMF)"**

The magnetomotive force (MMF) is linked to the distribution conductor $C(\theta)$ by the following equation:

$$MMF(\theta) = IR \int C(\theta) d\theta \quad \text{(III- 86)}$$

Where: θ is the angular position, I is the current, R is the airgap bore radius

- *Elementary full pitch winding*

The magnetomotive force (MMF) waveform of an elementary full pitch winding is illustrated in Figure III.16.

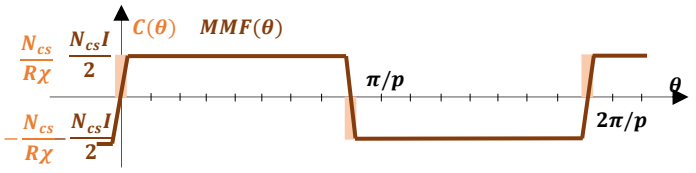

Figure III. 16: Elementary full pitch winding: distribution conductor and magnetomotive force functions

Due to the periodicity of MMF, it can be expressed by the Fourier's series decomposition by:

$$MMF(\theta) = \sum_{n=1}^{n=\infty} b_n \sin(np\theta) \quad \text{(III- 87)}$$

Where: n is the harmonic rank, p is the pole pair number, b_n is the Fourier's series component defined by:

$$b_n = \frac{2p}{\pi} \int_0^{\frac{\pi}{p}} mmf(\theta) \sin(np\theta)\, d\theta \quad \text{(III- 88)}$$

Where: $mmf\ (\theta)$ is magnetic force defined between 0 and $\frac{\pi}{p}$, it given by:

$$mmf(\theta) = \begin{cases} mmf_1(\theta) = \frac{N_{cs}I}{\chi}\theta & \text{for } 0 \le \theta \le \frac{\chi}{2} \\ mmf_2(\theta) = \frac{N_{cs}I}{2} & \text{for } \frac{\chi}{2} \le \theta \le \frac{\pi}{p} - \frac{\chi}{2} \\ mmf_3(\theta) = -\frac{N_{cs}I}{\chi}\theta + \frac{N_{cs}}{\chi}\frac{\pi}{p} & \text{for } \frac{\pi}{p} - \frac{\chi}{2} \le \theta \le \frac{\pi}{p} \end{cases} \quad \text{(III- 89)}$$

with: N_{cs} is the number of conductors per slot, χ is the angular opening slot, p is the pole pair number.

Using equation (III-89) in equation (III-88), we obtain:

$$b_n = \frac{2p}{\pi}\left[\int_0^{\frac{\chi}{2}} mmf_1(\theta)\sin(np\theta)\, d\theta + \int_{\frac{\chi}{2}}^{\frac{\pi}{p}-\frac{\chi}{2}} mmf_2(\theta)\sin(np\theta)\, d\theta + \int_{\frac{\pi}{p}-\frac{\chi}{2}}^{\frac{\pi}{p}} mmf_3(\theta)\sin(np\theta)\, d\theta\right] \quad \text{(III- 90)}$$

By calculation the 1st integration of equation (III-90), we have:

- *1st integration is:*

$$\int_0^{\frac{\chi}{2}} mmf_1(\theta)\sin(np\theta)\, d\theta = \frac{N_{cs}I}{\chi}\int_0^{\frac{\chi}{2}} \theta \sin(np\theta)\, d\theta = \frac{N_{cs}I}{\chi np}\left[-\theta\cos(np\theta) + \frac{1}{\text{np}}\sin(np\theta)\right]_0^{\frac{\chi}{2}}$$

then:

$$\int_0^{\frac{\chi}{2}} mmf_1(\theta)\sin(np\theta)\, d\theta = \frac{N_{cs}I}{\chi np}\left[-\frac{\chi}{2}\cos\left(\frac{np\chi}{2}\right) + \frac{1}{\text{np}}\sin\left(\frac{np\chi}{2}\right)\right]$$

- *2nd integration is:*

$$\int_{\frac{\chi}{2}}^{\frac{\pi}{p}-\frac{\chi}{2}} mmf_2(\theta)\sin(np\theta)\, d\theta = \int_{\frac{\chi}{2}}^{\frac{\pi}{p}-\frac{\chi}{2}} \frac{N_{cs}I}{2}\sin(np\theta)\, d\theta = \frac{N_{cs}I}{2}\left[-\frac{\cos(np\theta)}{np}\right]_{\frac{\chi}{2}}^{\frac{\pi}{p}-\frac{\chi}{2}}$$

then:

$$\int_{\frac{\chi}{2}}^{\frac{\pi}{p}-\frac{\chi}{2}} mmf_2(\theta)\sin(np\theta)\, d\theta = \frac{N_{cs}I}{2np}\left[1-(-1)^n\right]\cos\left(\frac{np\chi}{2}\right)$$

- *3rd integration is:*

$$\int_{\frac{\pi}{p}-\frac{\chi}{2}}^{\frac{\pi}{p}} mmf_3(\theta)\sin(np\theta)\,d\theta = \int_{\frac{\pi}{p}-\frac{\chi}{2}}^{\frac{\pi}{p}}\left[-\frac{N_{cs}I}{\chi}\theta + \frac{N_{cs}I}{\chi}\frac{\pi}{p}\right]\sin(np\theta)\,d\theta = \frac{N_{cs}I}{\chi np}\left[\left[\theta\cos(np\theta)\right]_{\frac{\pi}{p}-\frac{\chi}{2}}^{\frac{\pi}{p}} - \left[\frac{\sin(np\theta)}{np}\right]_{\frac{\pi}{p}-\frac{\chi}{2}}^{\frac{\pi}{p}}\right] + \frac{N_{cs}I\pi}{np\chi}\left[\cos(np\theta)\right]_{\frac{\pi}{p}}^{\frac{\pi}{p}-\frac{\chi}{2}}$$

$$\int_{\frac{\pi}{p}-\frac{\chi}{2}}^{\frac{\pi}{p}} mmf_3(\theta)\sin(np\theta)\,d\theta = \frac{N_{cs}I}{2np}\left[\cos\left(\frac{np\chi}{2}\right) - \frac{2(-1)^n}{np\chi}\sin\left(\frac{np\chi}{2}\right)\right]$$

Equation (III-88) becomes:

$$b_n = \frac{N_{cs}I}{n\pi}\left[1-(-1)^n\right]\frac{\sin\left(\frac{np\chi}{2}\right)}{\frac{\chi np}{2}} \qquad \text{(III- 91)}$$

Therefore:

$$b_n = \begin{cases} 0 & \text{when} \quad n = 2k \\ \frac{4N_{cs}I}{(2k-1)\pi}\frac{\sin(0.5(2k-1)p\chi)}{(2k-1)p\chi} & \text{when} \quad n = 2k-1 \end{cases} \qquad \text{(III- 92)}$$

Eventually, MMF of elementary full pitch winding:

$$MMF(\theta) = \sum_{k=1}^{k=\infty}\frac{4N_{cs}I}{(2k-1)\pi}\frac{\sin\left(\frac{(2k-1)p\chi}{2}\right)}{(2k-1)p\chi}\sin\left((2k-1)p\theta\right) \qquad \text{(III- 93)}$$

Equation (III-93) can be also written by:

$$MMF(\theta) = \sum_{k=1}^{k=\infty}\frac{RI}{(2k-1)p}A_{2k-1}\sin\left((2k-1)p\theta\right) \qquad \text{(III- 94)}$$

With: $A_{2k-1} = \frac{4N_{cs}}{\pi R}\frac{sin(0.5(2k-1)p\chi)}{(2k-1)\chi}$

- *Distributed winding with full pitch*

The MMF of a full pitch distributed winding is shown in Figure III.17. From the MMF of an elementary full pitch winding, the MMF of distributed winding can be deduced by:

$$MMF(\theta) = \sum_{j=1}^{m}\sum_{k=1}^{k=\infty}\frac{RI}{(2k-1)p}A_{2k-1}\sin\left((2k-1)p(\theta-(j-1)\gamma)\right) \qquad \text{(III- 95)}$$

where γ is the angular step between two neighboring coils of the same phase.

with $D_{2k-1} = \frac{\sin(0.5(2k-1)pm\gamma)}{\sin(0.5(2k-1)p\gamma)}$, equation (III-95) can be written by:

$$MMF(\theta) = \sum_{k=1}^{\infty}\frac{RI}{(2k-1)p}A_{2k-1}D_{2k-1}\sin\left((2k-1)p\theta\right) \qquad \text{(III- 96)}$$

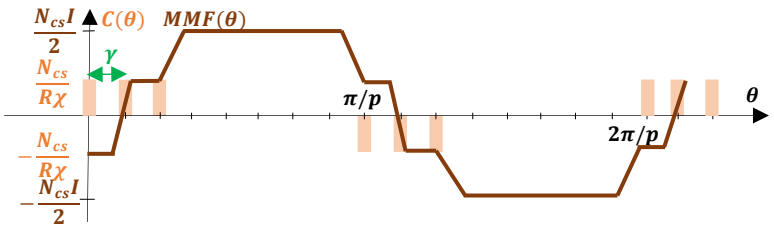

Figure III. 17: Distributed winding: distribution conductor and magnetomotive force functions

- *Distributed winding with several layers*

Distributed winding with layers has MMF function illustrated in Figure III.18. By considering the layers of winding shifted an angular step between two layers ξ, $MMF(\theta)$ function is expressed by:

$$MMF(\theta) = \sum_{l=1}^{l=nl}\sum_{k=1}^{\infty}\frac{RI}{(2k-1)p}A_{2k-1}D_{2k-1}\sin\left((2k-1)p(\theta-(l-1)\xi)\right) \qquad \text{(III- 97)}$$

with $L_{2k-1} = \frac{\sin(0.5(2k-1)pn_l\xi)}{n_l\sin(0.5(2k-1)p\xi)}$, the MMF function can be written

$$MMF(\theta) = \sum_{k=1}^{k=\infty}\frac{RI}{(2k-1)p}A_{2k-1}D_{2k-1}L_{2k-1}\sin\left((2k-1)p\theta\right) \qquad \text{(III- 98)}$$

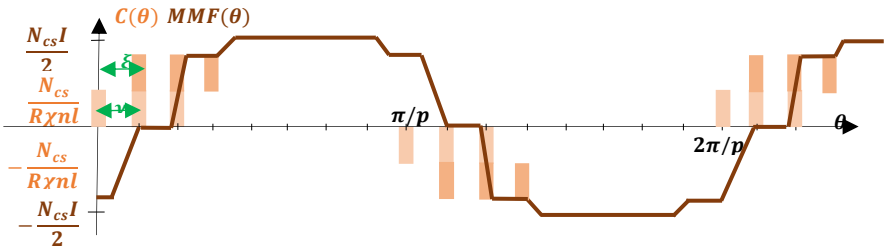

Figure III. 18: Distributed winding with several layers: distribution conductor and magnetomotive force functions

References

[Lel_18] Houng Thao Le Luong, 'Conception optimale d'un moteur synchrone à rotor bobiné modulaire à hautes performances pour une application embarqué', PhD manuscript, University of Toulouse, 2018

[Zhu_01]Z. Q. Zhu, D. Howe, 'Halbach permanent magnet machines and applications: a review', *IEE Proc. Electr. Power Appl.*, vol. 148, no.4, pp.299-308, July 2001.

[Che_17]Y. Chen, R.Sanchez, A.Yoon, K. Sivasubramniam, 'Mechanical design considerations of an Ironless high specific power electric machine,' *IEEE Trans. on Transp. Elect.*, vol.3, no.4, Dec 2017.

[Mel_07] P. H. Mellor, R. Wrobel, 'Optimization of a multipolar permanent-magnet rotor comprimising two arc segments per pole,' *IEEE Trans. Ind. Appl.*, vol.43, no.4, pp.951-942, Jul/Aug 2007.

[Hua_18]H. Huang, R. Qu, D.Li, 'Analysis and application of discrete Halbach magnet array with unequal arc lengths and unequally changed magnetization directions,' *IEEE Trans. Appl. Supercond*, vol. 28, no.3, Apr 2018.

[Mar_09]M. Markovic, Y. Perriard, 'Optimization deisgn of a segmented halbach permanent-magnet motor using an analytical model,' *IEEE Trans.On. Magn.*, vol.45, no.7, July 2009.

[Pyr_14] J. Pyrhönen, T. Jokinen, V. Hrbovcovà, "Design of rotating electrical machines," 2nd Edition, John Wiley & Sons, 2014

[Sle_94] G. R. Slemon, "On the design of high-performance surface-mounted PM motors," *IEEE Trans. Ind. App.*, vol.30, no.1, Jan/Feb 1994, pp.134-141

[Hen_94] J. R. Hendershot Jr, TJE Miller, 'Design of brushless permanent-magnet motors', GNA Physics Publications, Oxford Science Publications, 1994

[Lip_04] T. A. Lipo 'Introduction to AC Machine Design', Wisconsin Power Electronics Research Center University of Wisconsin, 2nd edition, 2004.

Chapter IV: Sizing of Electrical Motors for Medium and Long Term Targets

Contents

Introduction

After introducing the assessment and sizing tools of electric motors, sizing surface mounted permanent magnet synchronous motors satisfying the medium and long term targets will be performed in this chapter. Specifications of targeted electric motors with their cooling systems will be firstly reminded. Besides, considering the flying profiles, the choice of sizing point will be discussed. Secondly, a sizing procedure will be proposed for reaching targets. It includes tools using for the assessment electric motor technologies, for sizing electric motors and for sizing cooling systems. Thereupon, sizing electric motor for medium term target 2025 will be given. It will be validated using finite element analysis. Moreover, thanks to close interaction with WP3 the sizing cooling system as well as whole thermal behaviour of electric motor with its cooling will be illustrated. To exceed the medium term target 2025 for reaching the long term target 2035, several technological promising solutions will be discussed and identified to overcome issues and limitations of increasing specific power. Besides, a highlight will be payed to the differences between the electric motor targeted for medium term target 2025 with the one targeted for long term target 2035. Thereafter, sizing electric motor for long term target 2035 will be given with validation using finite element analysis. Still with WP3 interaction, sizing cooling system with thermal behaviour for long term target will be illustrated.

IV.1 Specifications and choice of sizing point

In terms of specific power and efficiency, sizing electric motors with their cooling systems should be performed to reach:

→ Specific power 5kW/kg with efficiency at cruise point must be greater than 96% and efficiency at design point greater than 94.5% for medium term target 2025,

→ Specific power 10kW/kg with efficiency at cruise point must be greater than 98.5% and efficiency at design point greater than 97% for long term target 2035.

On the other hand, electric motors should be sized for providing during a flying mission a mechanical power ranging from 0.018PU to 1PU with rotational speed ratio ranging from 30% to 100% as represented in Figure IV.1. It is therefore important to define the sizing point for electric motors with their cooling system. In other terms, to set the levels of mechanical power and rotational speed ratio on which sizing will be carried out. Indeed, according to the power flying mission three flying phases which sizing can be considered, namely take-off phase, climb phase and cruise phase as indicated in Figure IV.1. Take-off flying phase is the most thermally critical phase in contrast to the climb and cruise flying phases for electric motors. Due to the lake of time, we study the sizing for medium and long term targets only at take-off flying phase considering that sizing at climb and cruise flying phases will require several loopbacks to check the most thermal critical phase (i.e. the take-off flying phase). Besides, sizing electric motors at another sizing point does not change the used method in this manuscript.

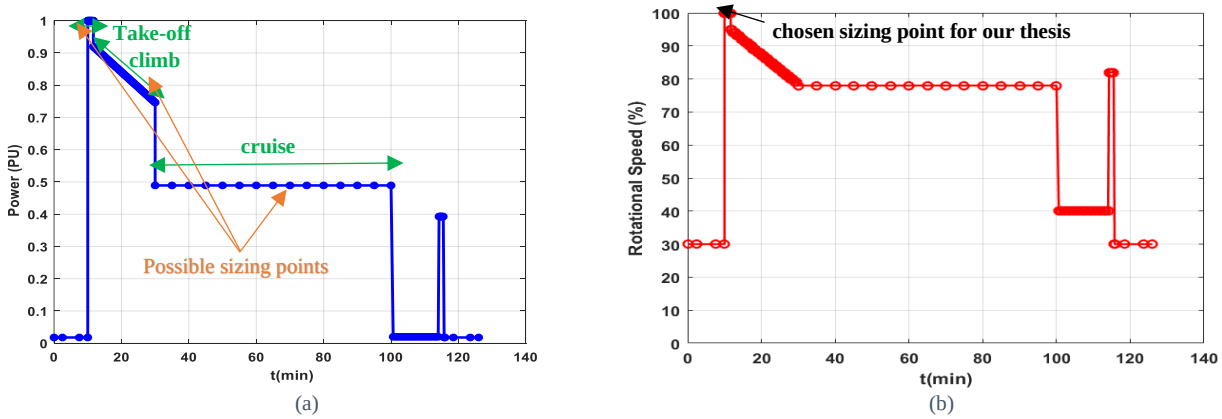

(a) (b)

Figure IV. 1 (a) Power profile vs flying time , (b) Rotational speed profile per unit vs flying time with sizing point

IV.2 Sizing procedure

As mentioned in Chapter I, sizing electric motors is strongly linked to cooling methods. Furthermore, design of cooling system depends on the sized electric motors. For the purpose, we propose a sizing procedure including in a loop the sizing of electric motor and the design of cooling system. We recall

that design of cooling system is carried out by WP3[2]. Therefore, this procedure expresses the strong interaction between the 1st and 3rd WP. To reach high specific power, sizing procedure consists of six steps:

- *Step 1*: consists of assessing the electric motor technologies required to reach high specific power and high efficiency using the Target Setting Tool.
- *Step 2:* consists to size Surface Mounted Permanent Magnet synchronous motor using the SM-PMSM tool for specific power of electric motor well above to the target.
- *Step 3:* checks thermal constraint according to cooling method chosen in the 1st step and check the efficiency at cruise point.
- *Step 4:* assesses the temperature inside electric motor by using Lumped Parameter Thermal Model.
- *Step 5:* designs cooling system taking into account the temperature assessing.
- *Step 6:* assesses the total weight of electric motor with its cooling system as illustrated in Figure IV.2.

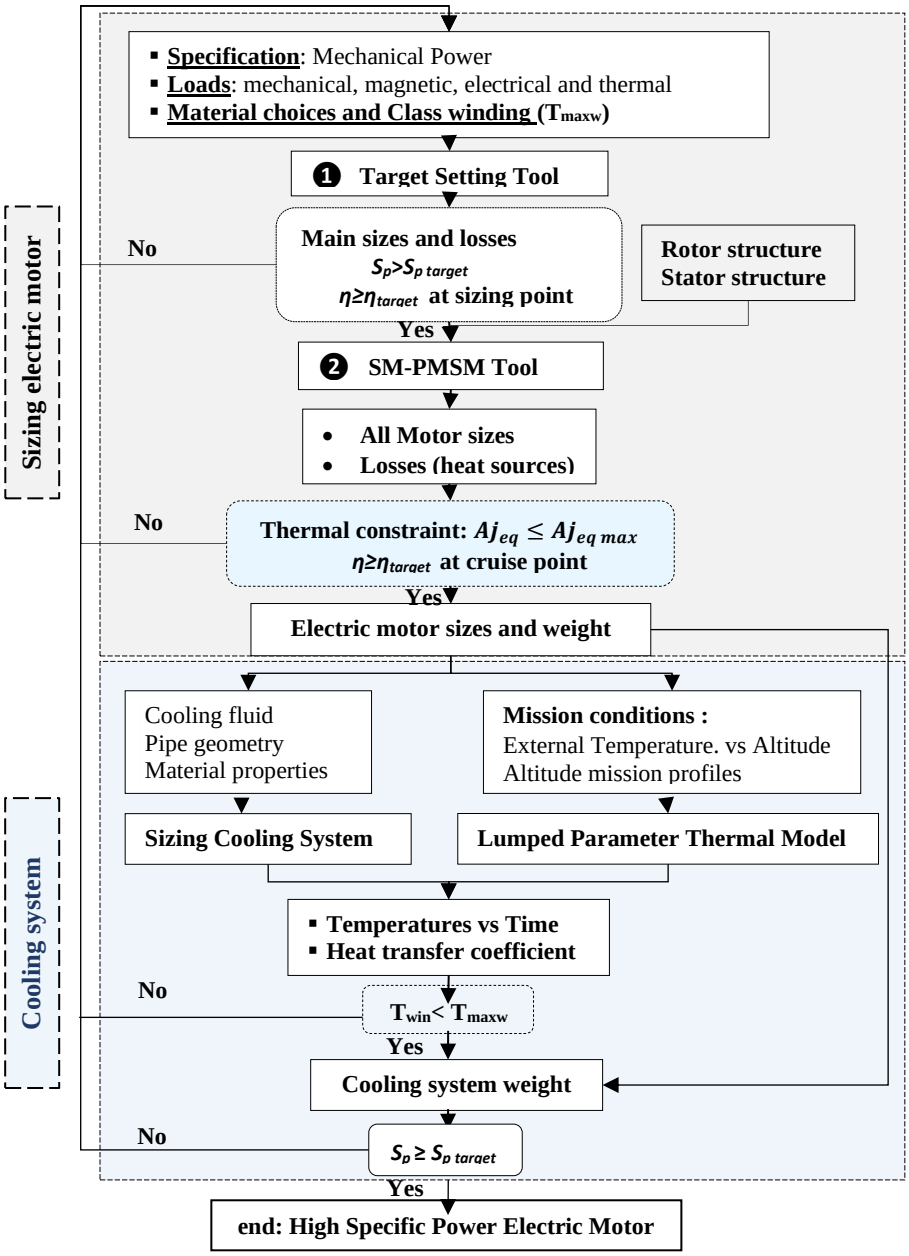

Figure IV. 2. Sizing procedure of high specific electric motor with its cooling system

Sized electric motor using this procedure allows, on the other hand, to provide the needed data for the other work packages especially 2nd and 5thWPs as illustrated in Figure IV.3. Synchronous frequency and

[2]"*Thermal modelling and cooling of an electric motor. Application to a Hybrid Aircraft Propulsion*", PhD thesis prepared by Amal Zeaiter and Supervised by Matthieu Fénot and Etienne Videcoq, Ecole Nationale Supérieure de Mécanique et d'Aéronautique ENSMA, France, https://www.theses.fr/s174528 .

electric parameters of electric motor are required for sizing power converters of the hybrid electric aircraft power chain. Data relating to winding, for instance, the conductor voltages and the slot sizes are required for partial discharge study of the electric motor. Regarding to the 6th WP, it is rather the assessment and sizing tools of electric motors which are provided.

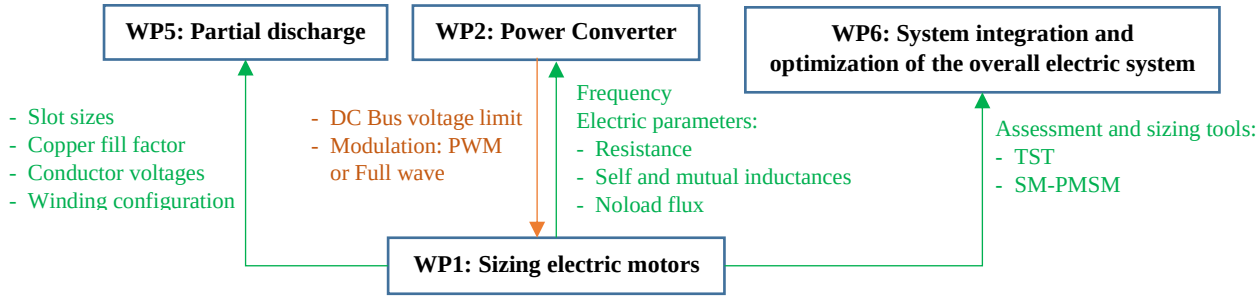

Figure IV. 3. Interaction sizing electric motor work package with others WPs

IV.3 Sizing of electric motor for medium term target 2025

IV.3.1 Issues, limitations and strategy to achieve target 2025

In electric motors, tangential stress level in airgap quantifies the electromagnetic torque as expressed in (II-4):

$$T_{em_{max}} = R_r S_{rot} \sigma$$

Increasing magnetic, electric, thermal and mechanical loads, for instance, the rotational speed allows decreasing rotor volume and thus its weight. Simultaneously, it leads to increase iron, Joule and mechanical losses (cf. Equations (II-65) to (II-69)) and thus temperatures and decrease efficiency.

Usually, insulation and permanent magnet materials are the most critical parts in electric motors as mentioned in Chapter I. As insulation materials are thermally bad conductors, the evacuation of the heat generated due to losses through winding is the main limitation for increasing specific power of electric motors.

Despite of issues and limitations for increasing specific power and efficiency, it is wise to increase loads and decrease losses. Moreover, reducing losses not only increases efficiency but also reduces the cooling system weight of the cooling system. In other words, our work will consist of identifying the most promising available technologies that allow us to achieve our 2025 goals.

For the purpose, our first strategy is to select, according to the actual cooling technologies, a conventional cooling method for medium term target 2025: external liquid cooling method performed through the frame for stator cooling and internal liquid cooling method through the shaft for rotor cooling. Joule losses are usually the hardest losses to extract and to evacuate, their limitation is crucial for 2025 target. Joule losses can be limited, for this target, by using stranded and twisted conductors.

The second strategy consists of identifying the other magnetic material technological levels according to the chosen conventional cooling method. This identification will be performed using Target Setting Tool. Afterward sizing of surface mounted permanent magnet synchronous motor will be carried out using SM-PMSM. Finite Element Analysis will be used to validate the sizing of electric motor. The thermal behaviour of the latter will be given with its cooling system design.

IV.3.2 Choice of technological levels

Electric, magnetic and thermal loads are linked to the materials used in electric machine as it illustrated in the previous Chapters. For reaching and satisfying both Hastecs targets and specifications, the choice of loads should be wise considering the all limitations. Therefore, the choice of loads involves material selecting that allow achieving the chosen loads. Electric motor designers [Pyr_14] have been draft typical values of loads according to the cooling method as presented in Table IV.1. The loads given in this table are drafted for non-salient synchronous machines. Since, we are going to size for 1st and 2nd Hastecs targets, surface mounted permanent magnet synchronous motors, loads given in this table will constitute a good basic for identifying the required technologies in TST and SM-PMSM.

Table IV. 1:Magnetic, electric and thermal loads of Non-salient pole synchronous machines

Loads	Indirect air cooling	Indirect hydrogen cooling	Direct water cooling
Airgap flux density B_m[T]	0.8-1.05		
Stator yoke flux density B_{sy}[T]	1.1-1.5		
Stator tooth flux density B_{st}[T]	1.5-2.0		
Current density j_{rms} [A.mm^{-2}]	3-5	4-6	7-10
Linear current density A_{rms}[A.mm^{-1}]	30-80	90-110	150-200
Max tangential stress σ [Pa]	17000-59500	50000-81500	85000-148500
Current density product $A_{rms} \times j_{rms}$ [A².m^{-3}]	9×10^{10}-40×10^{10}	36×10^{10}-66×10^{10}	1.05×10^{12}-2×10^{12}

IV.3.3 Assessment of electric motor technologies: Target Setting Tool

For sizing electric motor, we define a range values of electric, magnetic and thermal loads on which we will make several trade-offs on losses, efficiency and specific power. Table IV.2 summarizes the used range value of electric, magnetic and thermal loads. These range values are defined from the typical values given in Table IV.1. Range values of magnetic loads such as flux density levels in airgap, yoke and tooth are chosen the same as typical values.

Range values of tangential stress, current density and linear current density are chosen from the typical values corresponding to the direct water and indirect hydrogen cooling methods although the chosen cooling method for the 1st target is conventional with liquid coolant. This choice is carried out in order to not underestimate the thermal limit expressed by equivalent current density product in Target Setting Tool.

Table IV. 2:Range values of electric, magnetic and thermal loads for medium term target 2025

Loads	Range values
Airgap flux density B_mT]	0.8-1.05
Stator yoke flux density B_{sy}[T]	1.1-1.5
Stator tooth flux density B_{st}[T]	1.5-2.0
Current density j_{rms} [A.mm^{-2}]	4-10
Linear current density A_{rms}[A.mm^{-1}]	80-200
Max tangential stress σ [Pa]	50000-148500
Current density product $A_{rms} \times j_{rms}$ [A².m^{-3}]	0.32×10^{12}-2×10^{12}

In the 1st step of sizing procedure, we apply at the beginning

- limited values of loads,
- high rotational speed,
- high number of pole pairs,
- high thermal class such as 200°C,
- high copper fill factor,
- shape coefficient greater than the limit value (i.e. $\lambda \geq 0.4$) in order to assess the maximum reached specific power regardless of resulting losses.

If the achieved specific power is not enough greater than the target, we increase again the speed and number of pole pairs until to exceed 5kW/kg. Once it is done, we adjust these loads, speed, the number of pole pairs and copper fill factor in order to decrease the losses while controlling the specific power and efficiency by using some technological solutions:

→ Using twisted strands in order to reduce Joule losses resulting in less skin and proximity effects (i.e. R_{AC}/R_{DC}=1 at high frequency) as shown in Figure IV. 4. These strands are splitted and twisted such as: $k_{lc} = 1.25$ and $k_{sc}k_{fill} = 0.5$.

Figure IV. 4. Twisted strands

→ Using Vacoflux 48 with thickness of 0.35mm for stator and rotor yokes considering that has the lower specific iron losses (cf. to Figure I. 14);

→ Halbach permanent magnet with radial and axial segmentation to ensure sinewave airgap flux density to reduce eddy current losses.

On the other hand, these loads, the speed and the number of pole pairs are adjusted in order to ensure a loss distribution suitable to the chosen cooling method and not to exceed the thermal limit (i.e. $Aj_{eq} \leq 2 \times 10^2$ A².m^{-3}). For this target, as stator is cooled through its frame, Joule losses should be well distributed in the stator surface. Furthermore, to not exceed mechanical limit, using of Fiber Carbon Sleeve for retaining permanent magnets at high rotational speed is required. In this manuscript, sleeve will not be modelled, however the airgap will be sized largely enough to take into account the sleeve thickness.

Table IV.3 illustrates the adjusted loads, rotational speed, number of poles pairs, copper fill factor and others adjusted parameters which allow achieving target without exceeding thermal and mechanical limits. The main sizes, weights of electric motor and further intrinsic parameters are also summarized in this table.

Table IV. 3: Target Setting Tool inputs/outputs for medium term target 2025

Target Setting Tool inputs	Target Setting Tool outputs
Mechanical specifications - Electromagnetic power "P_{em}= 1PU" - Rotational speed "Ω=15970rpm" **Thermal specifications** - winding temperature "T_{win}=180°C" **Magnetic and electric loads** - Tangential stress "σ=50000Pa" - Current density "j_{rms}=8.1A/mm²" - Max surface current density "K_m=111.1kA/m" - RMS linear current density: "A_{rms}=81.4kA/m" - Current density product "$A_{rms}j_{rms}$=6.59×10^{11} A²/m^3" - Max airgap flux density "B_m=0.9T" - Flux density in teeth "B_{st}=1.3T" - Flux density in yoke "B_{sy}=1.2T" **Geometrical choice** - Shape coefficient "λ=0.6" - Slot copper fill factor "50%" - End-winding coefficient "k_{tb}=1.4" - Number of pole pairs "p=2" **Material of stator electrical sheet:** "Vacoflux 48- 0.35mm"	**Main sizes** - Frame external stator radius "R_{fr}=172.9mm" - External stator radius "R_{out}=162.9mm" - Stator bore radius "R=92.5mm" - Active length "L_m=317.4mm" - Stator yoke height "h_y=34.3mm" - Tooth (or slot) height "h_s=36.1mm" - Airgap thickness "e_g=2.77mm" **Weights** - Stator magnetic core weight"$W_{stat-core}$=115.4kg" - Winding stator weight "$W_{stat-wind}$=33.8kg" - Rotor weight "W_{rot} =56.7kg" - Frame weight "W_{fra}=19.7kg" **Specific power and torque of electric motor** - Specific power "S_p=6.3kW/kg" - Specific torque "S_T=3.8Nm/kg" **Further intrinsic parameters** - Peripheral speed "V_p=150m/s" - Joule losses "P_{js}=5960W" - Iron losses "P_{fs}=3620W" - Mechanical losses "$P_{mech-loss}$=1740W" - Efficiency "η=98%" **Equivalent current density product "Aj_{eq}= 1.565×10^{12} A²/m^3"** Electromagnetic torque "T_{em}=1PU" Synchronous frequency "f_s=532Hz"

In fact, there are several other load combinations allowing to achieve our target such as: low rotational speed with high number of pole pairs, high current density with low flux density levels, etc. For instance, low rotational speed with high number of pole pairs leads to design electric motor at low speed without gearbox which can be an interesting solution for removing the gearbox from the hybrid power chain. In contrast, in power converter point of view this solution could be not interesting given that it leads to electric motor with low cyclic inductance (i.e. electric motor with small sizes of stator magnetic sheet parts).

IV.3.4 Size electric motor: Surface Mounted Permanent Magnet Synchronous Motor

After determining the main sizes of electric motor in the 1st step of sizing procedure, the structure of electric motor is defined by choosing the winding and rotor configurations. Although it is difficult to carry out sinewave winding, we choose conventional winding having full pitch winding, single layer, three phases and two slot per pole and per phases as summarized in Table IV.4. This corresponds to stator with 24 slots. For rotor, we select Samarium Cobalt "SmCo" for permanent magnets due to its less temperature sensitivity (cf. Appendix B) and Iron Cobalt magnetic sheet "Vacoflux 48" for rotor yoke. Flux density in rotor yoke and polarization of permanent magnets are given in Table IV.4.

Outputs as further sizes, recalculated weight and recalculated losses of surface mounted permanent magnet synchronous motor are given in Table IV.5. Deviations between TST and SM-PMSM on weights, losses, specific power and torque are less than 15% although TST takes many assumptions. In Table IV.5, performances as electric parameters are given for example for one conductor per slot.

Table IV. 4: SM-PMSM Tool Inputs for medium term target 2025

Stator configuration	**Rotor configuration**
- Full pitch winding "τ=1" - Number of layers "n_l=1" - Number of phases "q=3" - Number of slots per pole and per phase "m=2"	- Flux density in rotor yoke "B_{ry}=1.4T" - Polarization of permanent magnets "J=1.16T"

Table IV. 5: SM-PMSM Tool Outputs for medium term target 2025

Further sizes	**Electric parameters for "N_{cs}=1"**
- Permanent magnet thickness "e_{pm}=9mm" - Rotor yoke thickness "h_{ry}=29.72mm" - Rotor shaft radius "R_{sh}=50.98mm" - Stator slot width "l_s=13.48mm" - Stator tooth width "l_t=10.73mm"	- Resistance "R_s=0.62mΩ" - Self-inductance "L_s=14.89µH" - Mutual inductance "M=-7.44µH" - Rms back electromotive force "E_i=241.32V" - No-load magnetic flux "φ_{vm}=0.1021Wb"
Recalculated winding parameters	**Recalculated the equivalent current density product**
- Winding coefficient "k_w=0.9659" - End winding coefficient "k_{tb}=1.6974"	- Equivalent current density product "Aj_{eq}=1.522×10^{12}A²/m^3"
Recalculated weights	**Recalculated specific power and specific torque (without cooling system)**
- Stator magnetic core weight "$W_{stat-core}$=115.4kg" - Winding stator weight "$W_{stat-wind}$=41kg" - Rotor weight "W_{rot} =80.14kg" - Frame weight "W_{fra}=22.4kg"	- Specific power "S_p=5.5kW/kg" - Specific torque "S_T=3.30Nm/kg"
Recalculated performances:	
- Joule losses "=7213W" - Iron losses "=3621W" - Mechanical losses "=2507W" - Efficiency "η=98%"	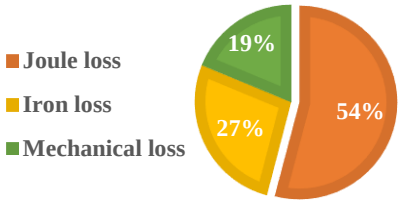

Efficiency at sizing point is greater than the targeted efficiency at sizing point. Performances such as electric parameters and losses will be validated by Finite Element Analysis in the next paragraph.

IV.3.5 Validation with Finite Element Analysis

Classically to validate the analytical models, numerical methods as finite element analysis are the most used. Ansys Maxwell software is one of these numerical tools. It is increasingly used due to its fast time solving and its compatibility with other software. Therefore, we will use it for analysing and validation. According to assumptions used in TST and SM-PMSM Tool, two models will be performed in Finite Element Analysis namely: slotless and slotted models. The first one will be performed in order to check the TST and SM-PMSM formula, given that these latter are based on slotless model assumptions. The second one will be performed to evaluate the deviations on loads and performances due to the slot effect. In all finite element analysis, simulations will be carried out for one conductor per slot.

IV.3.5.1. Slotless model

As the analytical model established in Target Setting Tool is based on the slotless model (cf. Chapter II), no-load and load 2D simulations will be performed to validate the electric machine performances. The structure of slotless model is represented by one-layer current at the airgap bore, segmented Halbach permanent magnet and magnetic rotor yoke. Due to the pole periodicity and the axisymmetric of the structure, 2D numerical model can be performed as shown in Figure IV.5.a. Therefore, the employed boundary conditions are illustrated in Figure IV.5.b. Within, master and slave boundary conditions employed on the model extremities are used for ensuring the periodicity and zero flux boundary

condition (or the Dirichlet boundary condition i.e. $A = 0$) applied on shaft bore radius for ensuring the closure of the flux lines in slotless model.

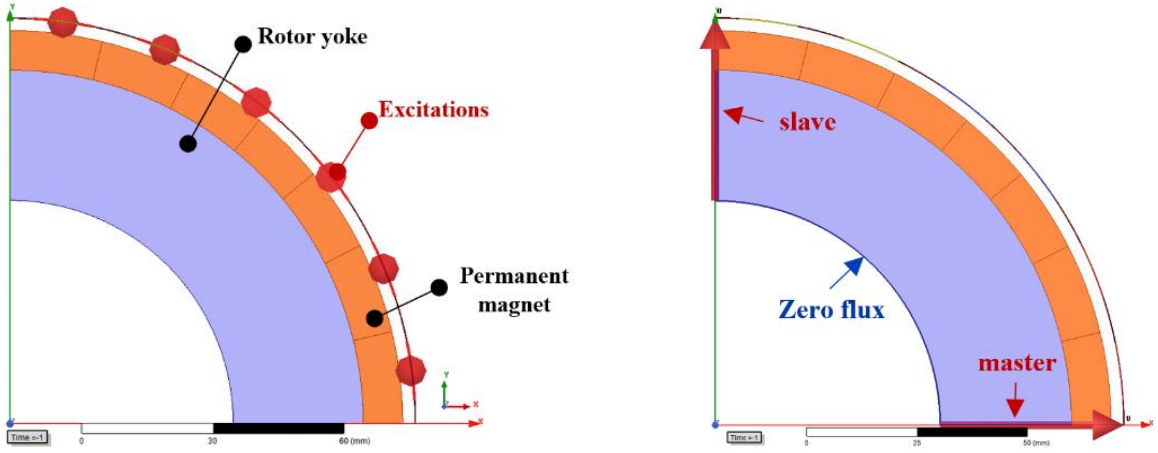

(a) (b)

Figure IV. 5. Slotless model electric motor of medium term target 2025: (a) Slotless model structure on one pole, (b) boundary conditions applied on one pole structure

a. No-load simulation

No-load simulation consists to ensure and to validate the airgap flux density set as an input of TST and the performances calculated by SM-PMSM such as the no-load magnetic flux and the back electromotive force.

In order to obtain a sinusoidal waveform of the airgap magnetic flux density, we determine the width using the direct design (cf. Table IV.5) and the orientation of segmented Halbach PMs by optimization established in Chapter III. For 7 segments of Halbach PMs and max airgap flux density equal to 0.9T, the structure of segmented Halbach PMs is given in Table IV. 6 and shown in Figure IV.6.a. The airgap flux density waveform is validated in Figure IV.6.b.

The resulting no-load magnetic flux and back electromotive force are shown in Figure IV.7. We notice that they are quasi-sinusoidal and their amplitudes are close to those calculated by SM-PMSM (cf. equations (III-70) and (III-71)).

Table IV. 6: Electric motor of medium term target 2025: Structure of 7 segment Halbach PMs

Segment	**1**	**2**	**3**	**4**	**5**	**6**	**7**
Orientation γ(°)	74	50	24	0	-24	-50	-74
Angular width:$\frac{\beta}{\pi/p}$ (%)	15.09	14.85	13.89	12.34	13.89	14.85	15.09

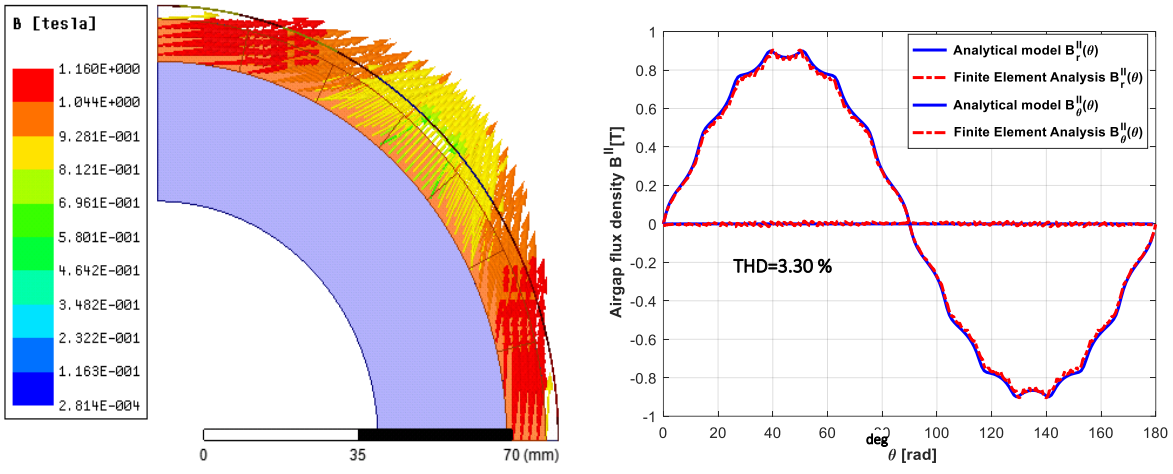

(a) (b)

Figure IV. 6. (a) Halbach array 7 segment PMs, (b) Airgap flux density

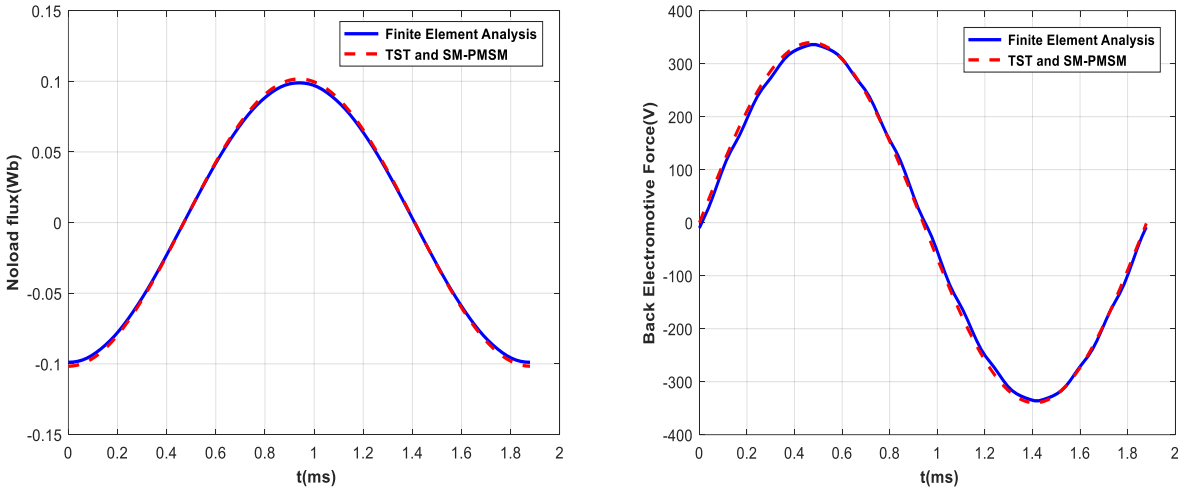

(a) (b)

Figure IV. 7. Slotless model: (a) No-load magnetic flux, (b) Back electromotive force

b. Load simulation

Load simulation consists to validate the airgap flux density due to the armature reaction and the performances as:

- the self, mutual and cyclic inductances,
- the electromagnetic torque.

The airgap flux density due to the Halbach PMs and the armature reaction is shown in Figure IV.8. By considering the fundamental component of the airgap flux density given by finite element analysis we notice that the analytical model performed in TST and SM-PMSM is validated (cf. equation (II-21)).

Figure IV.9 shows the comparisons of the self, mutual and cyclic inductances given by finite element analysis and those calculated by analytical model of SM-PMSM (cf. equations (III-82), (III-83) and (III-84)). The values of inductances given by finite element analysis are respectively 15.7µH, -6.208µH and 21.91µH. The deviations on self, mutual and cyclic inductances are respectively 5%, 20% and 2%. Deviation on mutual inductance remains allowable considering that deviation on cyclic inductance is insignificant.

The electromagnetic torque calculated in SM-PMSM results from the interaction of the surface current density and the airgap flux density as presented in Figure IV.10.a. The electromagnetic torque given by finite element analysis is compared to the analytical electromagnetic torque in Figure IV.10.b. The average electromagnetic torque given by simulation is 0.98PU. The deviation on electromagnetic torque is 2%. In slotless model, deviation on efficiency will not be assessed considering that iron losses in stator are not analysed. It can be evaluated only in slotted model.

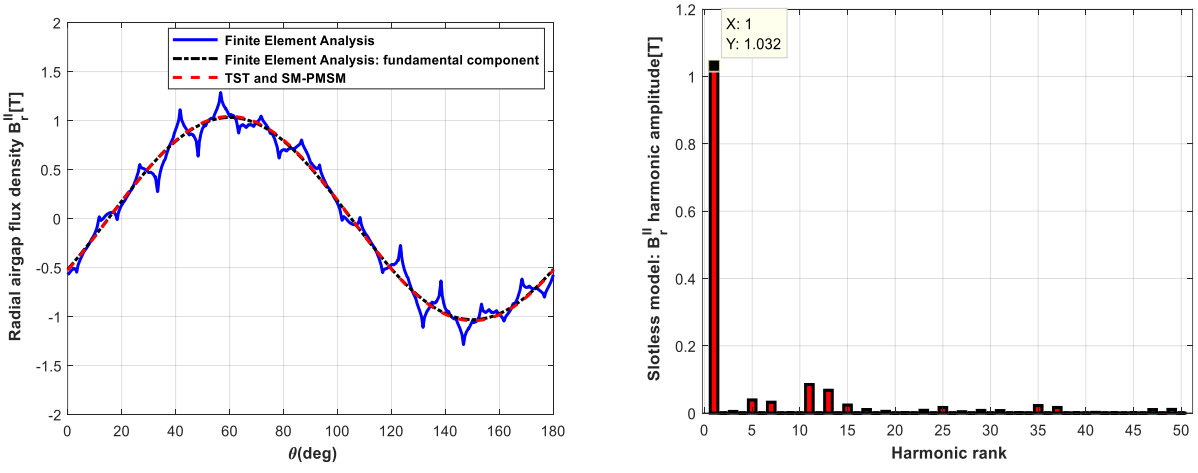

(a) (b)

Figure IV. 8. Slotless model: (a) Airgap flux density, (b) harmonic analysis

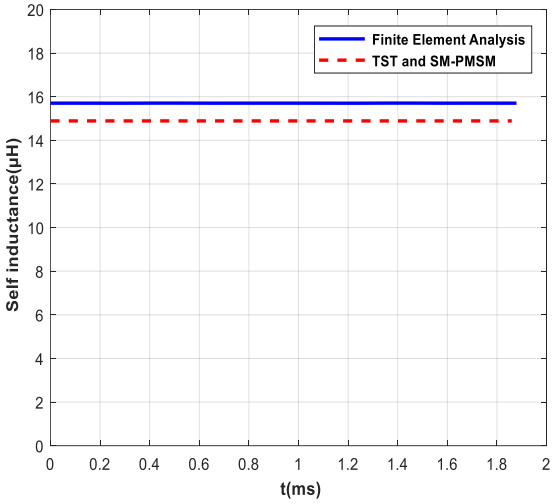

(a)

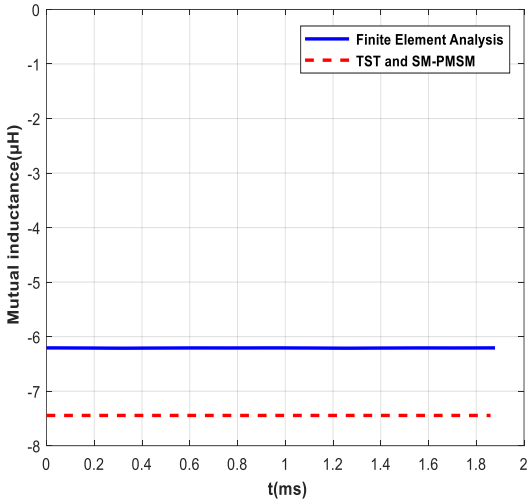

(b)

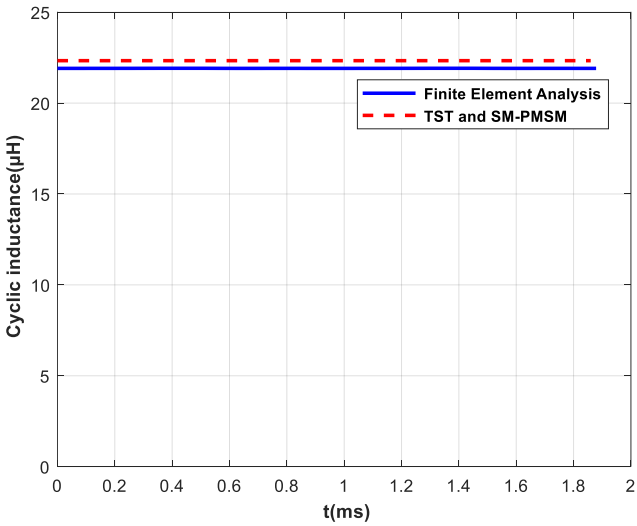

(c)

Figure IV. 9. Slotless model: (a) Self-inductance, (b) Mutual inductance, (c) cyclic inductance

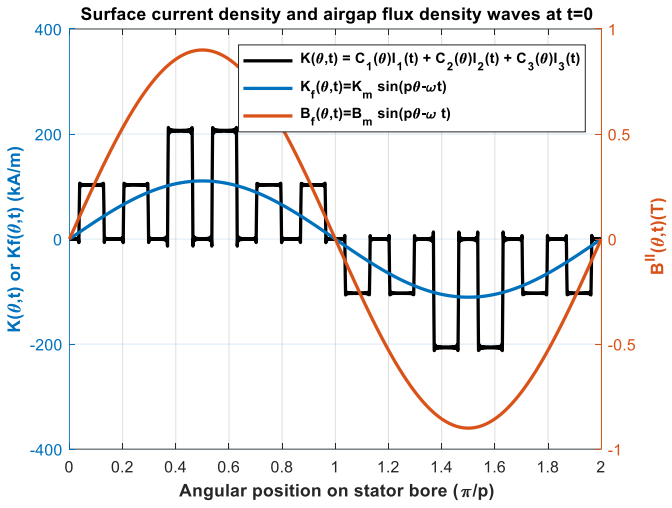

(a)

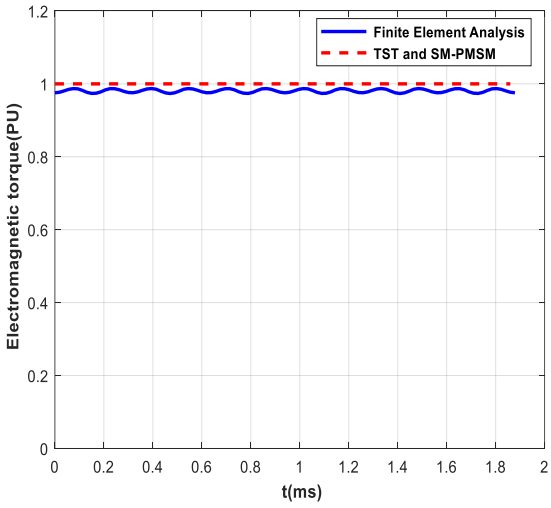

(b)

Figure IV. 10. Slotless model: (a) Surface current density and airgap flux density waves, (b) The electromagnetic torque

IV.3.5.2. Slotted model

After dealing the slotless model, this part is devoted to the slotted model of the electric motor. Slotted model is the most representing structure of electric motor in contrast to slotless model. Slotted model allows to assess deviations due to slot effect on performances between the slotless model which SM-PMSM is based on it and the real electric motor structure. Figure IV.11.a shows the 2D structure of electric motor on one pole. The corresponding boundary conditions are illustrated in Figure IV.11.b.

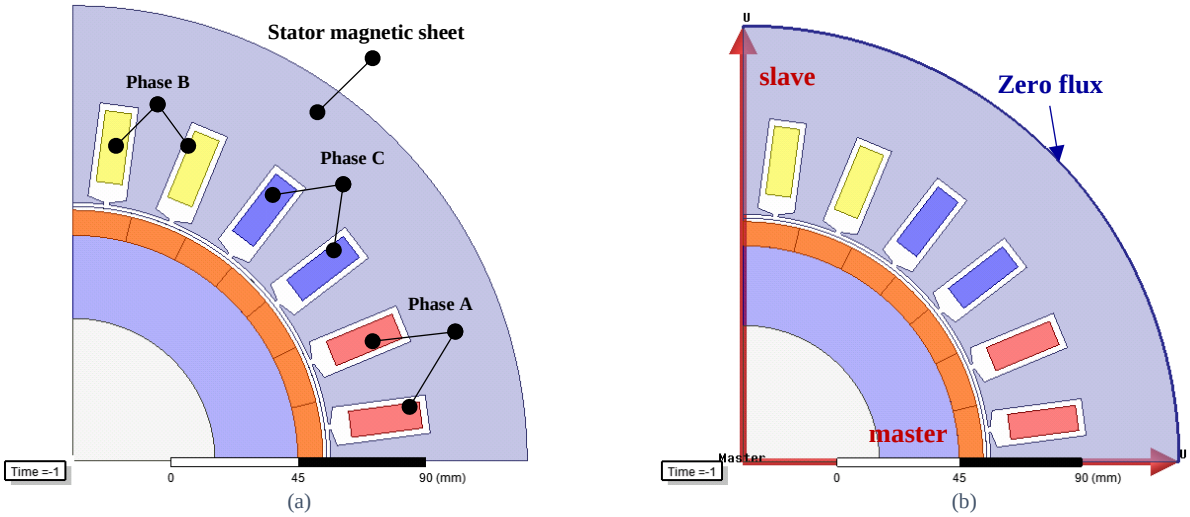

Figure IV. 11. Slotted model electric motor of medium term target 2025: (a) Slotted model structure on one pole, (b) boundary conditions applied on one pole structure

a. <u>No-load simulation</u>

The airgap flux density at no-load simulation is presented in Figure IV.12. We notice that airgap flux remains close to the sinewave despite of slot effect structure as indicated by the harmonic analysis. The amplitude of fundamental component is equal to 0.88, therefore it is close to TST target. Stator yoke and tooth flux densities can be checked by integrating potential vector on the magnetic paths as shown on Figure IV.13.a. The resulting flux densities are presented in Figure IV.13.b and c. These peak flux densities (i.e. 1.18T for yoke flux density and 1.33T for tooth flux density) are very close to those set in TST.

The no-load magnetic flux and back electromotive force are presented in Figure IV.14. Compared to SM-PMSM results, we notice that slot effect on no-load magnetic flux and back electromotive is insignificant.

At no-load simulations, it is interesting to assess the cogging torque although it does not contribute to the rated electromagnetic torque. Cogging torque arises from the magnetic interaction between rotor permanent magnets and slotted stator at no-load. Figure IV.15 shows the cogging torque. Its maximum ripple is $\Delta T_{cogging}$=1.9Nm. This value is low compared to the average electromagnetic torque. Figure IV.16 shows the magnetic flux and the flux line distributions. The mean magnetic flux density in teeth is about 1.25T. In yoke, the mean magnetic flux density is 1.09T.

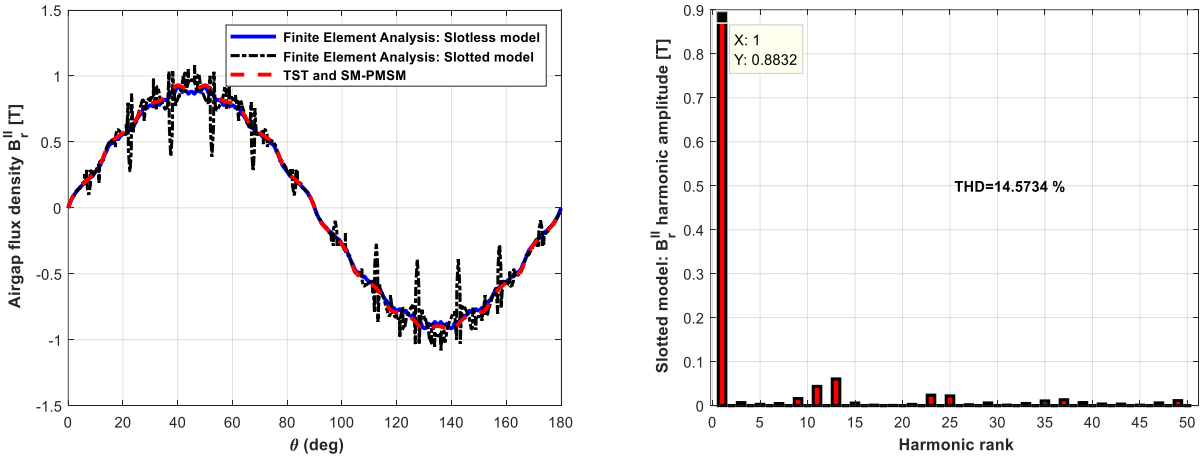

(a) (b)

Figure IV. 12. Airgap flux density at no-load: (a) slotless and slotted models, (b) harmonic analysis

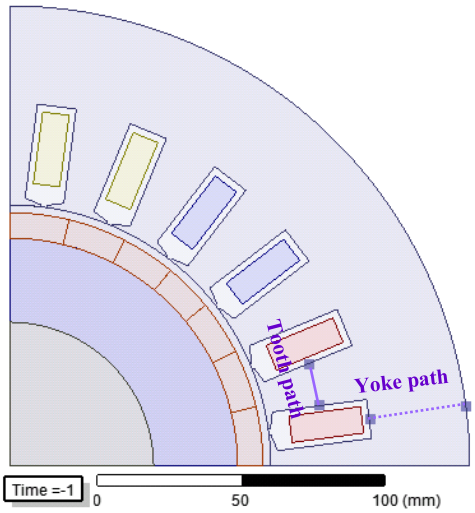

(a)

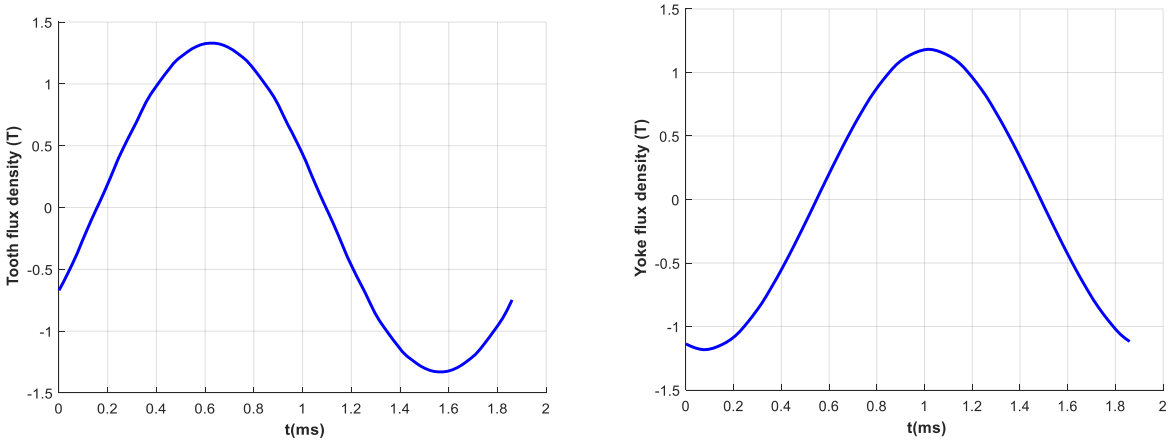

(b) (c)

Figure IV. 13. Slotted model at no-load: (a) Magnetic paths, (b) tooth flux density, (c) stator yoke flux density

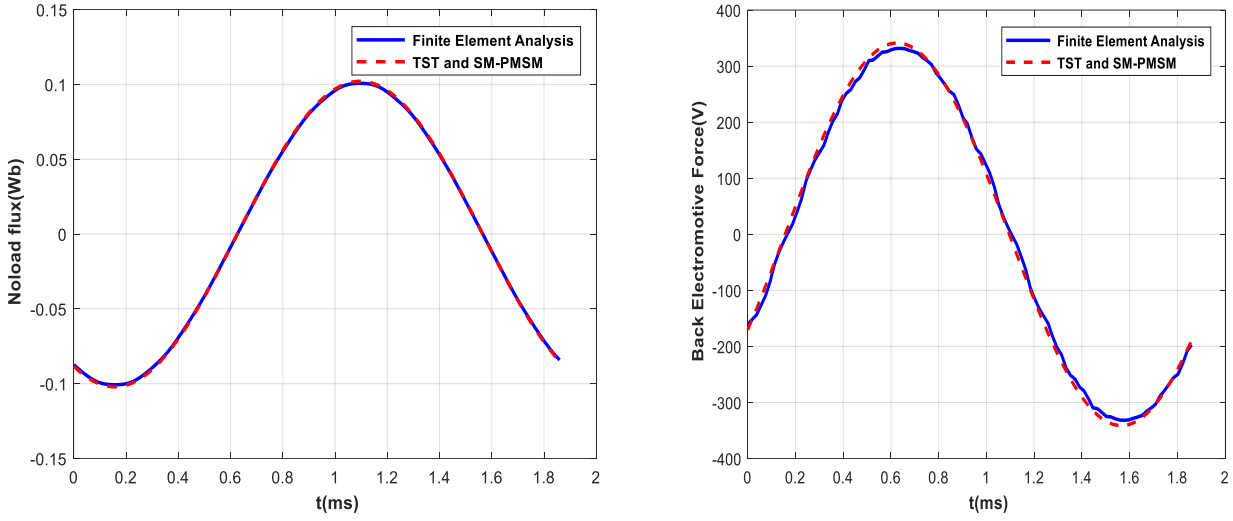

(a) (b)

Figure IV. 14. Slotted model: (a) No-load magnetic flux, (b) Back electromotive force

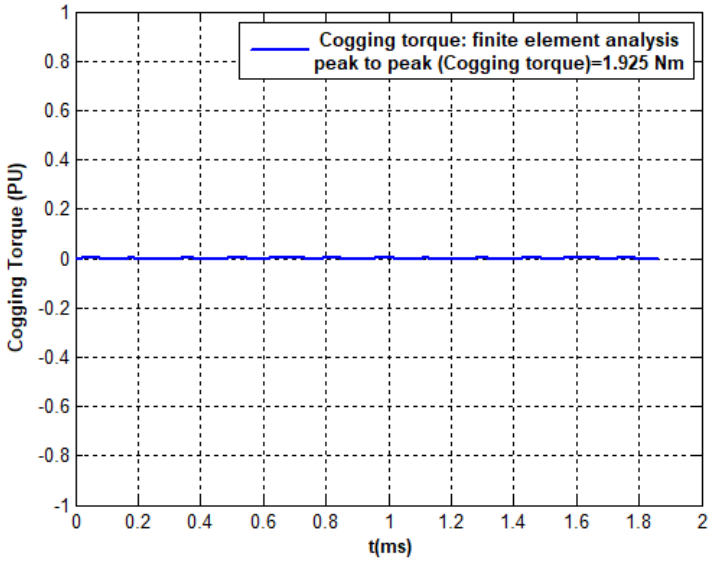

Figure IV. 15. Noload simulation: cogging torque

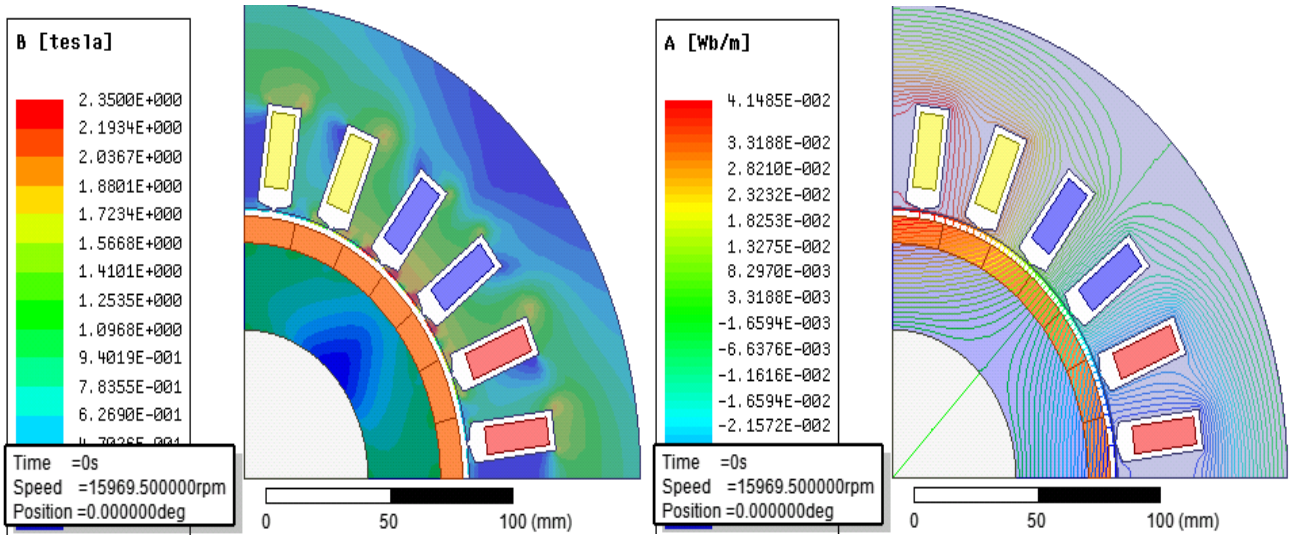

(a) (b)

Figure IV. 16. Slotted model at no-load simulation: (a) Magnetic flux density distribution, (b) Flux line distribution

b. Load simulation

Airgap flux density taking into account the armature reaction is presented in Figure IV.17. By comparison to the no-load simulation we notice that the influence of the armature reaction on the airgap flux density is negligible (increasing of 0.1T due to the armature reaction). Moreover, we notice that the airgap flux density taking into account the armature reaction analytically calculated in TST and SM-PSM is close to that given by simulation of slotted model.

Taking the same paths of stator tooth and yoke, the assessing of flux densities is illustrated in Figure IV.18. By comparison to the no-load simulation, we find that flux densities in stator tooth and stator yoke increase respectively by 0.16T and 0.36T from the values obtained by the no-load simulation. The reached peak values are 1,49T and 1,54T respectively in stator tooth and stator yoke.

The self, mutual and cyclic inductances given by slotted model are shown in Figure IV.19. They have saliency around their average values. Saliency can be explained by mildly noteworthy saturation in the bottom teeth as shown in Figure IV.20. The average values are respectively 22µH, -6.2µH and 28.2µH. By comparison to the inductances calculated in SM-PMSM, we observe deviations which may be the consequence of not taking into account the inductances due to leakage fluxes in TST and SM-PMSM.

The electromagnetic torque is given in Figure IV.21. Its average value is equal to 0.97PU which is close to the value calculated in analytical model of TST and SM-PMSM.

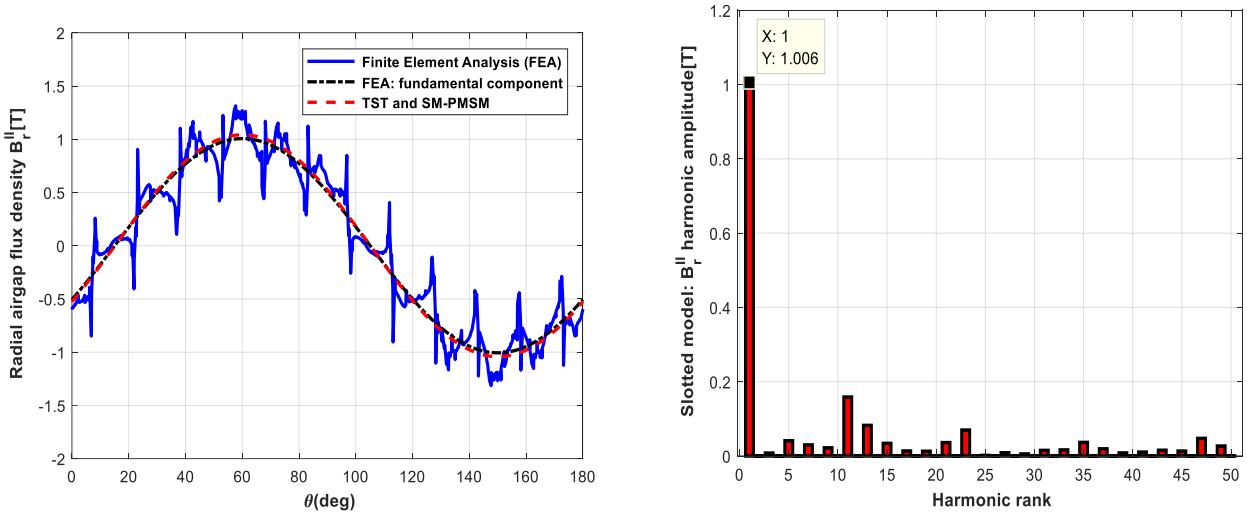

(a) (b)

Figure IV. 17. Slotted model at load: (a) airgap flux density, (b) harmonic analysis

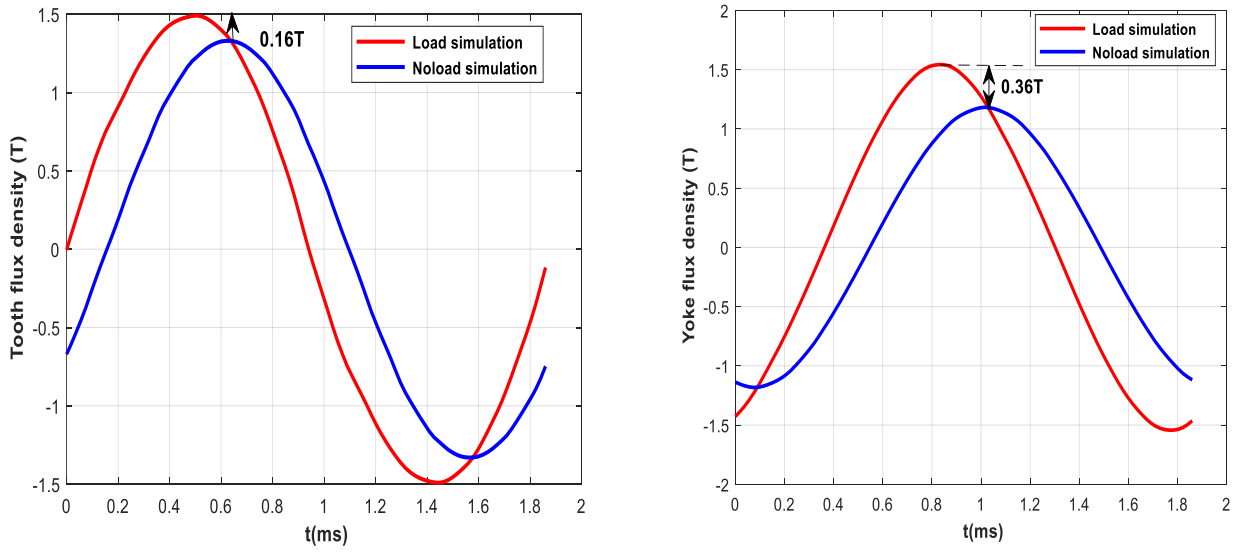

(a) (b)

Figure IV. 18. Slotted model at load: (a) tooth flux density, (b) stator yoke flux density

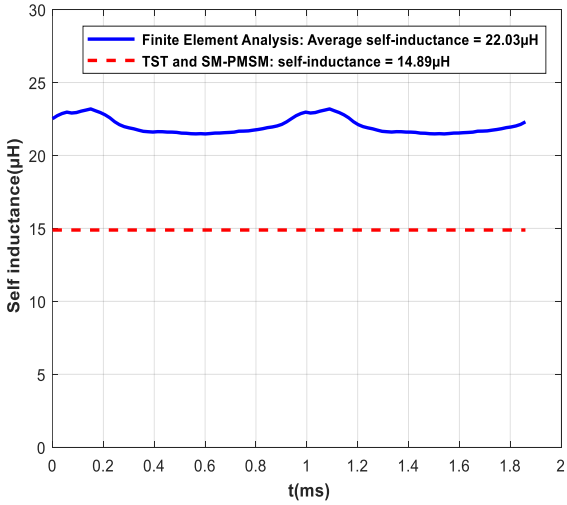

(a)

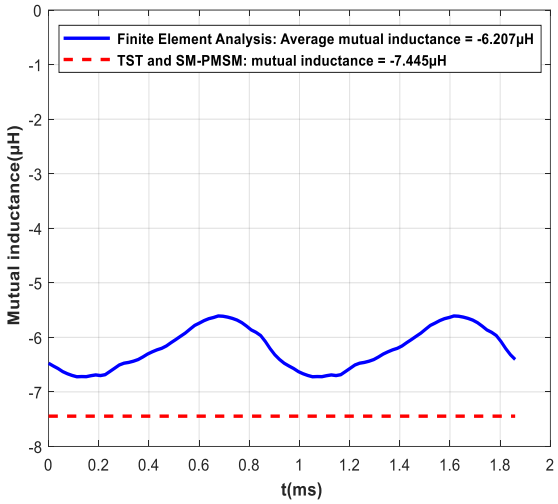

(b)

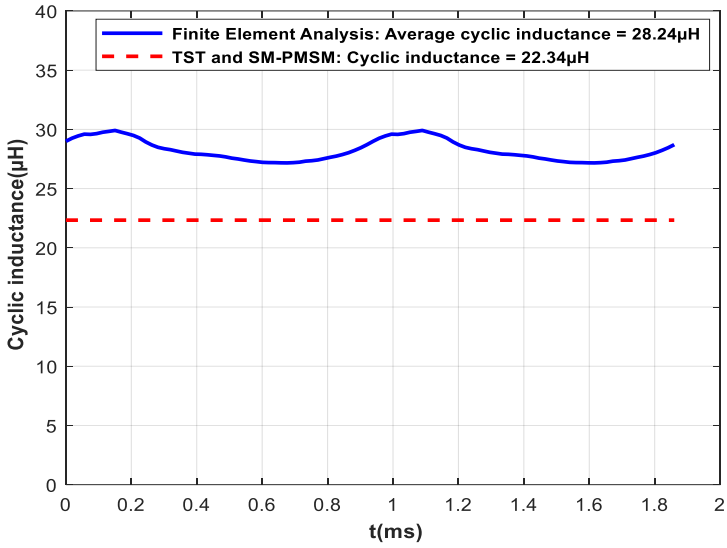

(c)

Figure IV. 19. Slotted model: (a) Self-inductance, (b)Mutual inductance, (c) cyclic inductance

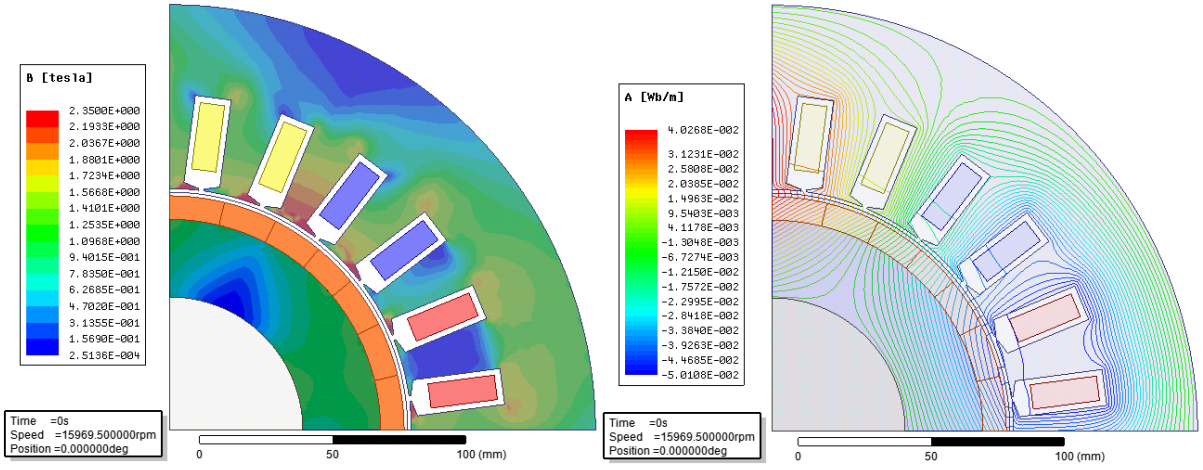

(a) (b)

Figure IV. 20. Slotted model at load simulation: (a) Magnetic flux density distribution, (b) Flux line distribution

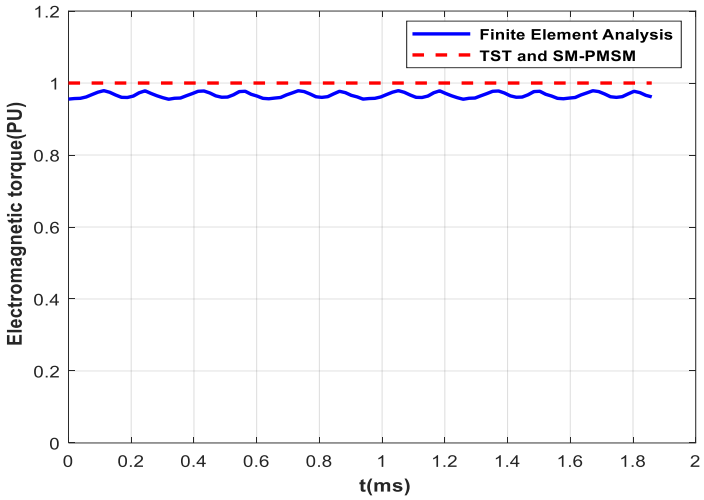

Figure IV. 21. Slotted model: The electromagnetic torque

In TST and SM-PMSM, iron losses are assessed by assuming that flux density distribution is homogeneous in the magnetic sheets. However, through finite element analysis flux density distribution is not homogeneous considering that often magnetic sheet saturates in some areas as shown in Figure IV.20. Therefore, it is interesting to compare the iron losses assessed by finite element analysis which takes into account the saturation with those assessed in TST and SM-PMSM. Figure IV.22 shows a comparison of iron losses calculated using analytical model of TST and SM-PMSM with those calculated by finite element analysis. At synchronous frequency, iron losses in rotor yoke are zero which is quite obvious. The mean value of iron losses in stator magnetic sheet is 7.5kW. This value is significantly higher than the one calculated by TST and SM-PMSM. This deviation can be explained firstly by the difference of basic iron loss model used in TST and SM-PMSM (cf. equation II-67 and Appendix A) with the one used in Finite Element Analysis (cf. equation II-66 and Appendix A). Secondly, the deviation can be explained by the deviation of flux density levels in stator magnetic sheet set in TST with those checking by finite element analysis. Thirdly, deviations can come from the nonlinear behaviour of magnetic material. In addition, from the electromagnetic torque and the iron losses analysed using FEA, efficiency is recalculated. Its value is closer to 98%, it remains higher than targeted efficiency at sizing point. Deviation on efficiency is quasi-zero.

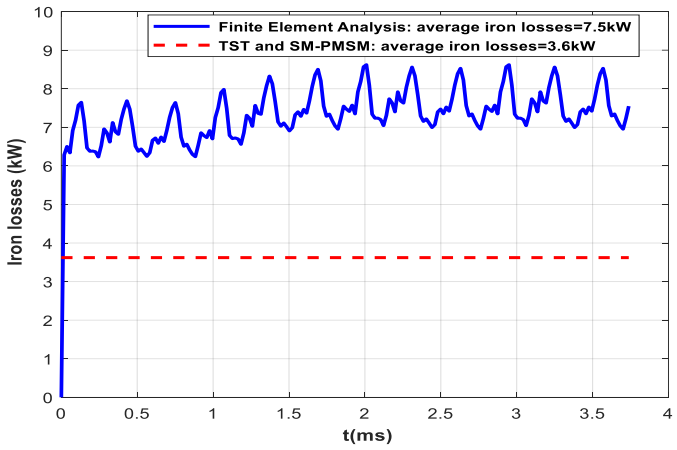

Figure IV. 22. Slotted model: Iron losses

To conclude the comparison, Table IV.7 summarizes the deviations of electric motor 2025 performances between TST and SM-PMSM with finite element analysis. Deviations between these tools is less than 4% for no-load magnetic flux, for back-electromotive force and for electromagnetic torque. In contrast, deviations between these tools is 32% for self-inductance, 21% for mutual and cyclic inductance. These deviations are significant by reason of ignoring the leakage flux in inductance calculations in TST and SM-PMSM. In contrast, deviations of slotless model of TST and SM-PMSM with slotless model of finite element analysis are negligible.

Table IV. 7: Electric motor of medium term target 2025: summary comparison of performances between analytical tools and finite element analysis

Performances	TST	SM-PMSM	Finite Element Analysis		Slotless model deviation	Slotted model deviation
			Slotless model	Slotted model		
Max. No-load magnetic flux "Φ_{vm}[Wb]"	-	0.102	0.10	0.10	**2%**	**2%**
Rms Back-Electromotive Force "E_i[V]"	-	241	238	236	**1%**	**2%**
Electromagnetic torque "T_{em}PU]"	1	1	0.98	0.97	**2%**	**3%**
Self-inductance "L_s[µH]"	-	14.89	15.7	22.03	**5%**	**32%**
Mutual inductance "M[µH]"	-	-7.44	-6.20	-6.20	**20%**	**20%**
Cyclic inductance "L_{cs}[µH]"	-	22.34	21.91	28.24	**2%**	**21%**

IV.3.6 Thermal behaviour and cooling system design

Cooling system proposed by WP3 is mainly based on: *ambient air cooling* and *cooling primary circuit*. Ambient air cooling consists of taking the outside ambient air as cold source considering that its maximum temperature at cruise is -12°C and at ground is 38°C [All_18].

Cooling primary circuit is composed of a heat exchanger placed near to the cold source, a hydraulic circuit and a pump. Heat exchanger allows the evacuation of heat generated by electric motor to the outside air through plate embedded around the nacelle. It is composed of pipes and a cold plate. The heat evacuation is carried out mainly by conduction heat transfer between the pipes and cold plate (i.e. nacelle) and then by convection heat transfer between the nacelle and the air as presented in Figure IV.23.

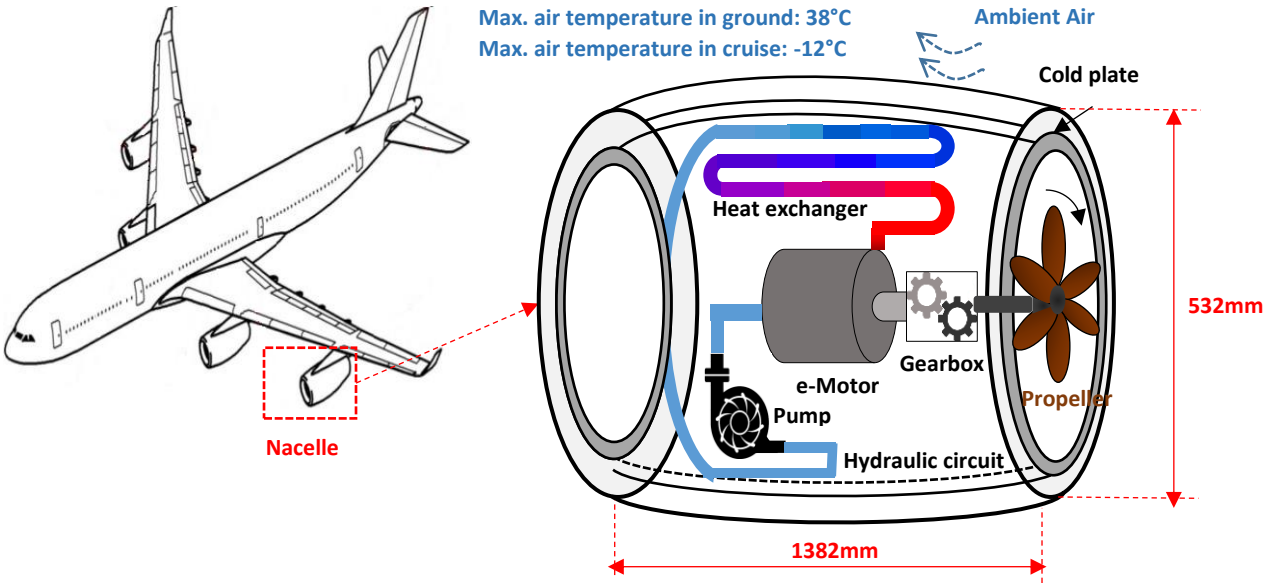

Figure IV. 23. Nacelle architecture: electric motor with its cooling circuit

Hydraulic circuit is used to extract the heat flux generated by electric motor losses to the heat exchanger. Hydraulic circuit is composed of pipes which coolant as Ethylene Glycol Water 50/50 (cf. Table IV.8) circulates inside them using a hydraulic pump.

Table IV. 8. Characteristics of Ethylene Water-Glycol 50/50 [Ton_14]

Characteristics	Water-Glycol 50/50
Density [kg.m^{-3}]	1065
Thermal conductivity [W.m^{-1}.K^{-1}]	0.3937
Specific heat [J.kg^{-1}.K^{-1}]	3361
Dynamic viscosity [kg.m^{-1}.s^{-1}]	2.2564×10^{-3}
Freezing temperature	-37°C
Boiling temperature	107.2°C

This coolant extracts and evacuates the heat flux by circulating inside cooling channels performed in frame and inside cooling channel performed in shaft as shown in Figure IV.24. This cooling method aims to cool stator through the frame, and rotor through the shaft.

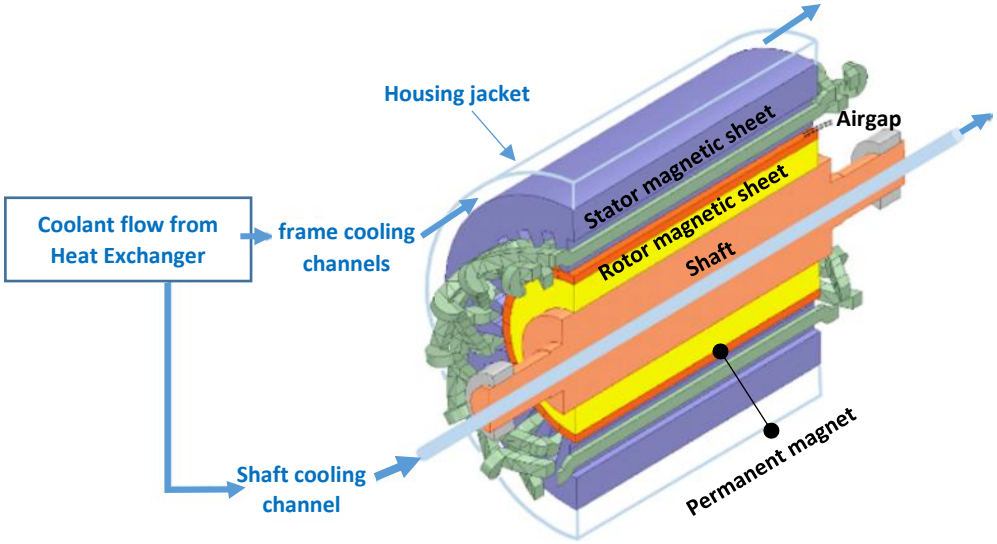

Figure IV. 24. Medium term target 2025: Electric motor with its cooling channels

WP3 sizes cooling system and takes as thermal limits the maximum allowed winding and permanent magnet temperatures (220°C for winding and 150°C for permanent magnet). For the purpose, WP1 gives to WP3 the losses profiles function of time flying (cf. Figure IV.25, maximum total losses which WP3 should be evacuated are 16.8kW) for sizing cooling system and to take into account its transient thermal behaviour. In these loss profiles, iron losses are assessed using finite element analysis whereas Joule and mechanical losses are assessed using analytical models established in TST and SM-PMSM. The characteristics of cooling system sized by WP3 are summarized in Table IV.9. Indeed, as cooling in frame and shaft are designed, assessment of electric motor weight is recalculated. Cooling system weight includes pipes of heat exchanger, coolant and hydraulic pump. Total weight of cooling system is 32kg, therefore, the specific power of the electric motor with its cooling system is almost 5kW/kg. This achieved target can be improved with more optimized cooling system.

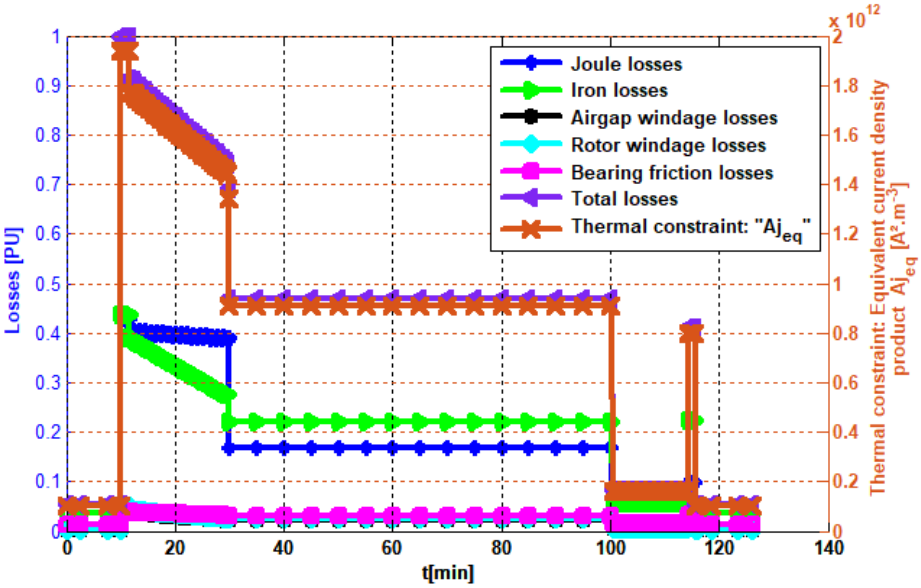

Figure IV. 25. Medium term target 2025: Losses profiles and equivalent current density product function of time flying

Table IV. 9: Medium term target 2025: Cooling system characteristics given by WP3

Cooling channels inside housing jacket and shaft		
Parameters of cooling channels	Housing jacket	Shaft
Hydraulic diameter [mm]	45	14
Flow rate [$m^3.s^{-1}$]	4.2×10^{-3}	10^{-4}
Heat transfer coefficient [$W.m^{-2}.K^{-1}$]	3900	1000
Heat exchanger		
Parameters	Pipes	Cold plate
Material	"Aluminium"	
Thickness[mm]	1	3
Flow rate [$m^3.s^{-1}$]	4.3×10^{-3}	-
Hydraulic diameter [mm]	45	-
Hydraulic Pump		
Normal operating pressure [bars]	206	
Maximum speed [rpm]	3646	
Length [cm]	26.16	
Height [cm]	21.84	
Width [cm]	17.27	
Weight [kg]	14	
Coolant	**"Ethylene Glycol Water 50/50"**	

The thermal electric motor behaviour is given using the Lumped Parameter Thermal Model [Zea_18] developed by WP3 as shown in Figure IV.26.a. The resulting thermal behaviour according to the mission profile is given in Figure IV.26.b. Within, temperatures in most critical zones are given as temperature in winding (node 34 for slot and 13 for end winding), permanent magnet (node 14), magnetic sheets (nodes 12 and 35 for stator and 14 for rotor) and in the outlet coolant on the electric motor side (node 53). Temperature in end-winding is the hotspot zone in electric motor, however, its temperature remains below the winding thermal class.
To exceed the first targeted specific power (i.e. 5kW/kg), loads should be more increased. Consequently, it is important to further improve cooling by adding, for instance, another cooling inside or near to the winding.

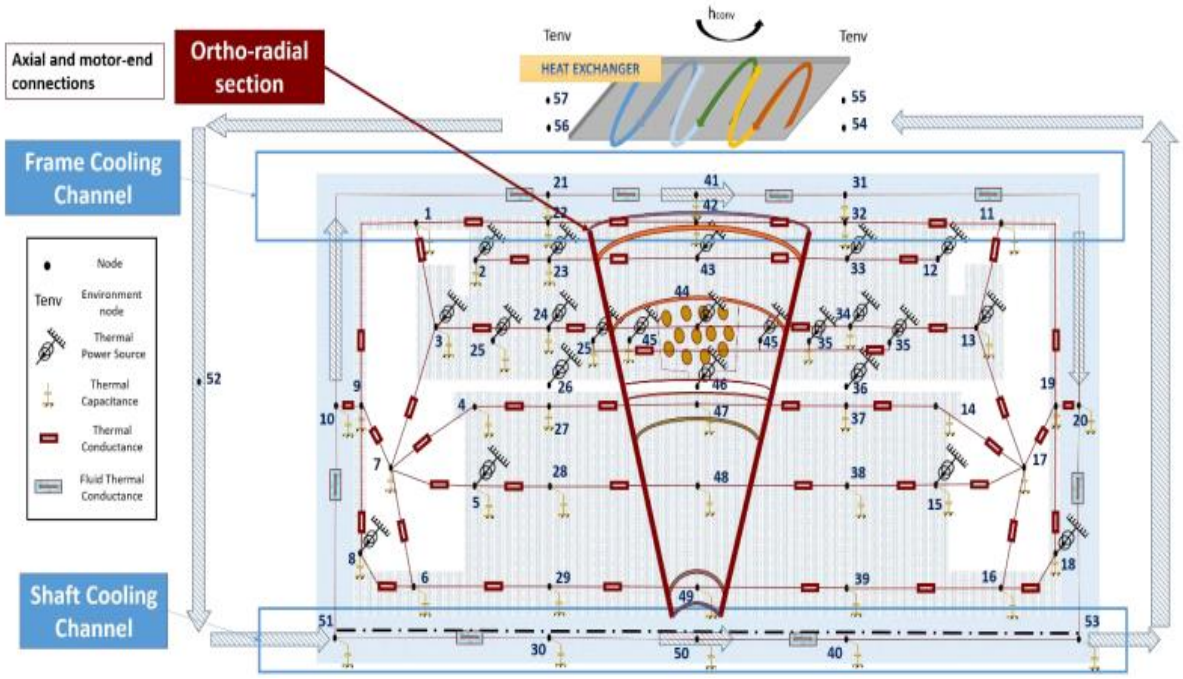

(a)

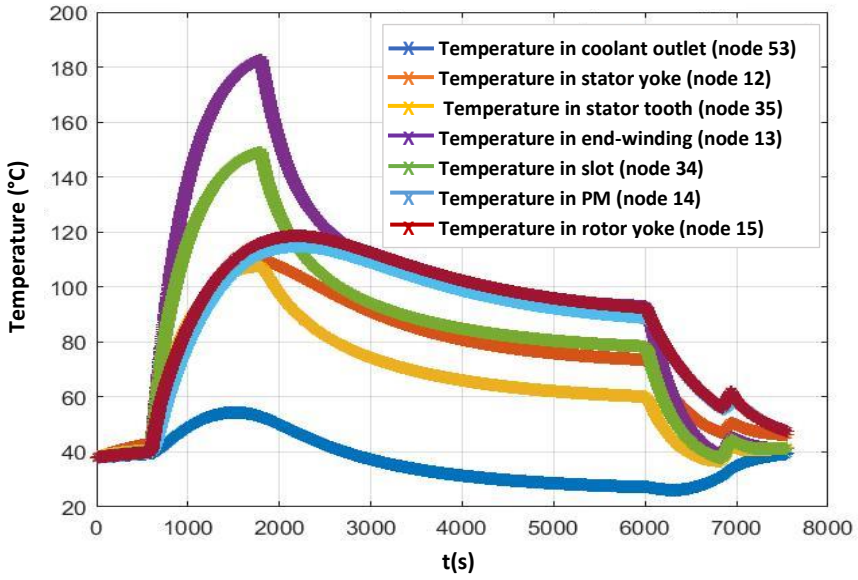

(b)

Figure IV. 26. Medium term target 2025: (a) Axial and ortho-radial section of SM-PMSM including its cooling system with Lumped Parameter Thermal Model LPTM nodes location, and axial and motor-end connections, (b) Temperature evolution during flying mission in the sized electric motor [Zea_18][Tou_20]

IV.4 Sizing of electric motor for long term target 2035

IV.4.1 Issues, limitations and strategy to achieve target 2035

As well as for the medium term target 2025, issues for long term target 2035 are the same. Besides, limitations for long term target 2035 are huger than those medium term target 2025. To achieve long term target 2035: specific power of 10kW/kg and efficiency at sizing point greater than 97%, loads, speed, number of pole pair, copper fill factor, thermal class should be further increased. Considering the thermal limitations, new cooling methods are mainly the key solution for exceeding, for instance, the chosen loads for medium term target. These new cooling methods will involve new thermal limit. The latter will hence be higher than the thermal limit of medium term target. Table IV.10 reminds chosen loads, speed, number of pole pairs, thermal class and technological solutions carried out for medium term target 2025. Therefore, for reaching long term target 2035, technological choices will be improved compared to those given in Table IV.10.

Table IV. 10: Technological choices performed for medium term target 2025

Loads, speed, number of pole pair and slot fill factor	Technological solutions
- Tangential stress "σ=50000Pa" - Current density "j_{rms}=8.1A/mm²" - Max surface current density "K_m=111.1kA/m" - RMS linear current density "A_{rms}=81.4kA/m" - Current density product "$A_{rms}j_{rms}$=6.5948×10^{11} A²/m^3" - Max airgap flux density "B_m=0.9T" - Flux density in teeth "B_{st}=1.3T" - Flux density in yoke "B_{sy}=1.2T" - Rotational speed "Ω=15970rpm" - Number of pole pairs "p=2" - Slot fill factor is 0.5%	- Stranded and twisted conductors - Magnetic sheet: "Vacoflux 48- 0.35mm" - Halbach permanent magnet with radial and axial segmentation to ensure sinewave airgap flux density to reduce eddy current losses - Carbon Fiber Sleeve

By following the same sizing approach, technologies will be firstly selected and assessed for reaching the targeted specific power and efficiency (i.e. 10kW/kg and 97%) using TST. By choosing the same electric motor structure, the sizing will be performed using SM-PMSM and validated by Finite Element Analysis. With WP3 interaction, the sizing will be finished by the sizing of cooling system.

IV.4.2 Choice of technological levels

We define another range values of loads for this 2nd Hastecs target as presented in Table IV.11. Mainly, flux density in stator tooth and yoke and current density are expanded respectively to 2.35T (cf. Appendix A) and to 25A/mm² corresponding to the high saturation flux density level and to achieved current density for inner cooling method (cf. Chapter I, Table I. 16).

Table IV. 11:Range values of electric, magnetic and thermal loads for long term target 2035

Loads	Range values
Airgap flux density B_m[T]	0.8-1.05
Stator yoke flux density B_{sy}[T]	1.2-2.35
Stator tooth flux density B_{st}[T]	1.2-2.35
Current density j_{rms} [A.mm^{-2}]	8-25
Linear current density A_{rms}[A.mm^{-1}]	80-200
Max tangential stress σ [Pa]	50000-148500
Current density product $A_{rms} \times j_{rms}$ [A².m^{-3}]	0.64×10^{12}-5×10^{12}

Therefore, according to range values of loads, some technological levels are kept same as those used in 1st Hastecs target such as:

→ cooling methods in shaft and in frame,
→ material choices of magnetic sheets, permanent magnet and sleeve,

and some technological solutions are added as:

→ direct inner cooling method for stator winding cooling,
→ potting materials around end-windings for improving their cooling (cf. Chapter I),
→ insulation materials with 240°C thermal class by using inorganic insulation materials. It allows increasing of current density and frequency levels;
→ Litz wires to reduce winding losses at very high frequency (i.e. $R_{AC}/R_{DC} \approx 1$ for very high frequency 400Hz to 5kHz) unlike to the stranded conductors where R_{AC}/R_{DC} can be greater than 1 at frequency > 1kHz. Compacted Litz wire conductor illustrated in Appendix C is used as conductor reference for this motor.

IV.4.3 Assessment of electric motor technologies: Target Setting Tool

In the same way, we apply at the beginning the limited values of loads (cf. Table. IV.11), high rotational speed (Ω >16000rpm), high number of pole pairs (p >2) and high copper fill factor in order to assess the maximum reached specific power regardless of resulting losses. If the achieved specific power is not enough greater than the target, we increase again the speed and the number of pole pairs until to exceed 10kW/kg. Once it is done, we adjust these loads, speed, the number of pole pairs and the copper fill factor in order to decrease the losses while controlling the specific power and efficiency.
Table IV.12 shows the adjusted loads, rotational speed, number of poles pairs, copper fill factor and others adjusted parameters which allow achieving targets (i.e. specific power >10kW/kg and efficiency >97%). The main sizes, weights of electric motor and further intrinsic parameters are also summarized in Table IV.12.

By comparison between the 1st and 2nd Hastecs targets, we notice significant increasing of:

- Current density from 8A/mm² to 20A/mm²,
- Linear current density from 80kA/m to 110kA/m,
- Tangential stress from 50000Pa to 70000Pa,
- Rotational speed increases from 15970rpm to 20000rpm,
- Number of pole pairs from 2 to 4. They therefore allow duplicating specific power of electric motors.

However, although the partial discharges are allowed for 2nd Hastecs target, the fill factor is eventually adjusted to equal to 1st Hastecs target since cooling is chosen inside slots.

Table IV. 12: Target Setting Tool inputs/outputs for long term target 2035

Target Setting Tool inputs	Target Setting Tool outputs
Mechanical specifications - Electromagnetic power "P_{em}= 1PU" - Rotational speed "Ω=20000rpm" **Thermal specifications** - winding temperature "T_{win}=180°C" **Magnetic and electric loads** - Tangential stress "σ=70000Pa" - Current density "j_{rms}=20A/mm²" - Max surface current density "K_m=155.5kA/m" - RMS linear current density: "A_{rms}=110kA/m" - Current density product "$A_{rms}j_{rms}$=2.199×10^{12} A²/m^3" - Max airgap flux density "B_m=0.9T" - Flux density in teeth "B_{st}=1.25T" - Flux density in yoke "B_{sy}=1.25T" **Geometrical choice** - Shape coefficient "λ=0.5" - Slot copper fill factor "50%" - End-winding coefficient "k_{tb}=1.4" - Number of pole pairs "p=4" Material of stator electrical sheet: "Vacoflux 48- 0.35mm"	**Main sizes** - Frame external stator radius "R_{fr}=123.6mm" - External stator radius "R_{out}=111.9mm" - Stator bore radius "R=72.9mm" - Active length "L_m=292m" - Stator yoke height "h_y=14.1mm" - Tooth (or slot) height "h_s=25mm" - Airgap thickness "e_g=3.06mm" **Weights** - Stator magnetic core weight "$W_{stat-core}$=39.9kg" - Winding stator weight "$W_{stat-wind}$=14.22kg" - Rotor weight "W_{rot} =27.7kg" - Frame weight "W_{fra}=12.53kg" **Specific power and torque of electric motor** - Specific power "S_p=15.121kW/kg" - Specific torque "S_T=7.22Nm/kg" **Further intrinsic parameters** - Peripheral speed "V_p=146.3m/s" - Joule losses "P_{js}=13.293kW" - Iron losses "P_{fs}=6.468kW" - Mechanical losses "$P_{mech-loss}$=1.086kW" - Efficiency "η=98%" **Equivalent current density product "Aj_{eq}= 3.978×10^{12} A²/m^3"** Electromagnetic torque "T_{em}=1PU" Synchronous frequency "f_s=1.333kHz"

In the sizing of electric motor for 2nd Hastecs target, we deliberately place our target above 10kW/kg considering that cooling system is not taken into account in TST. Moreover, electric motor weight is approximately calculated in TST (electric motor structure is not defined) as it has been shown in the electric motor of 2025.

IV.4.4 Size electric motor: Surface Mounted Permanent Magnet Synchronous Motor

Using the main sizes given by TST, the further sizes are given by choosing the stator and rotor configurations as summarized in Table IV.13. Since that cooling is inner, the number of slots is chosen similar to the previous electric motor (i.e. 24 slots). For the purpose, the number of slots per pole and per phase is 1. For the rotor, configuration is kept similar to the one chosen for medium term target. Table IV.14 presents the outputs as further sizes, recalculated weight and recalculated losses of surface mounted permanent magnet synchronous motor. Deviations between TST and SM-PMSM on weights, specific power and torque are less than 14%.

Table IV. 13: SM-PMSM Tool Inputs for long term target 2035

Stator configuration	Rotor configuration
- Full pitch winding "τ=1" - Number of layers "n_l=1" - Number of phases "q=3" - Number of slots per pole and per phase "m=1"	- Flux density in rotor yoke "B_{ry}=1.4T" - Polarization of permanent magnet "J=1.16T"

Table IV. 14: SM-PMSM Tool Outputs for long term target 2035

Further sizes	Electric parameters for "N_{cs}=1"
- Permanent magnet thickness "e_{pm}=7.84mm" - Rotor yoke thickness "h_{ry}=16.66mm" - Rotor shaft radius "R_{sh}=45.36mm" - Stator slot width "l_s=9.71mm" - Stator tooth width "l_t=9.38mm"	- Resistance "R_s=1.01mΩ" - Self-inductance "L_s=3.12µH" - Mutual inductance "M=-1.56µH" - Rms back electromotive force "E_i=226.77V" - No-load magnetic flux "φ_{vm}=0.0383Wb"
Recalculated winding parameters	**Recalculated equivalent current density product**
- Winding coefficient "k_w=1" - End winding coefficient "k_{tb}=1.402"	- Equivalent current density product "Aj_{eq}=4.065×10^{12}A²/m^3"

Recalculated weights	Recalculated specific power and specific torque (without cooling system)
- Stator magnetic core weight "$W_{stat-core}$=39.9kg" - Winding stator weight "$W_{stat-wind}$=14.24kg" - Rotor weight "W_{rot} =42.58kg" - Frame weight "W_{fra}=12.6kg"	- Specific power "S_p=13kW/kg" - Specific torque "S_T=6.25Nm/kg"
Recalculated performances:	
- Joule losses "=13.312kW" - Iron losses "=6.468kW" - Mechanical losses "=1.557kW" - Efficiency "η=98%"	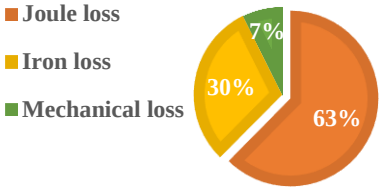

By comparison to the medium term target, we notice that resulting mechanical losses of long term target are less than those resulting of medium term target although speed is increased. It may be explained by the rotor size which is reduced. It may then lead to decrease mechanical losses as indicated in equations (II-70, II-75 and II-78).
Efficiency at sizing point is greater than the targeted efficiency at sizing point. Performances such as electric parameters and losses will be validated by Finite Element Analysis as will be given in the next paragraph.

IV.4.5 Validation with Finite Element Analysis

For the 2nd Hastecs target, validation with finite element analysis is essential for quantifying the sizing validation range of TST and SM-PMSM. In fact, this validation will mainly allow us to check on one hand the performances such as losses, torque and inductances. On the other hand, validation allow us to check the saturation risk in stator magnetic sheet given that loads are significant. For the purpose, the slotless and slotted models will be used.

VI.4.5.1. Slotless model

Slotless model conditions for simulations of the 2nd Hastecs targeted electric motor are the same as conditions (cf. Figure IV.27) taken for slotless model of the 1st Hastecs targeted electric motor.

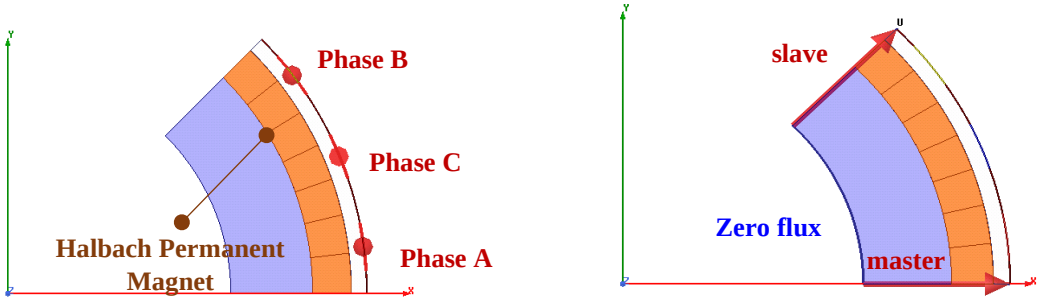

(a) (b)

Figure IV. 27. Slotless model electric motor of long term target 2035: (a) Slotless model structure on one pole, (b) boundary conditions applied on one pole structure

a. <u>No-load simulation</u>

Structure of segmented Halbach permanent magnet obtained by optimization is summarized in Table IV.15. Its polarization is shown in Figure IV.28.a. Validation of airgap flux density, no-load magnetic flux and back-emf are illustrated respectively in Figure IV.28.b, Figure IV.29.a and b. Total harmonic distortion calculated on the airgap flux density confirms that the latter are closer to sinewaves.

Table IV. 15: Electric motor of long term target 2035: seven segment Halbach PMs

Segment	1	2	3	4	5	6	7
Orientation γ(°)	76.13	48.56	22.77	0	22.77	48.56	76.13
Angular width: $\frac{\beta}{\pi/p}$ (%)	15.00	14.449	13.781	13.538	13.781	14.449	15.00

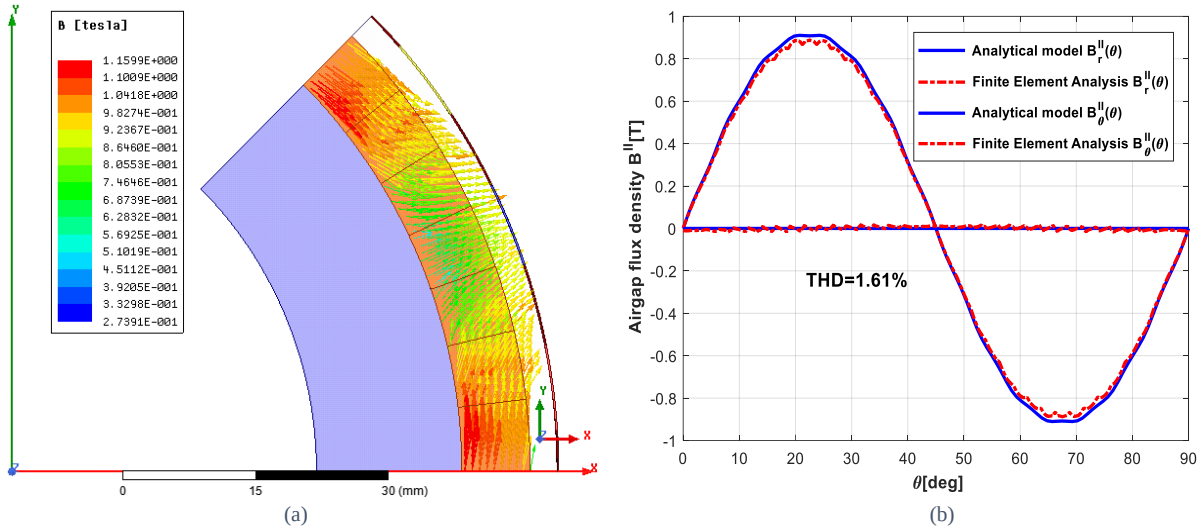

(a) (b)

Figure IV. 28 Electric motor of long term target 2035 (a) Halbach array 7 segment PMs, (b) Airgap flux density

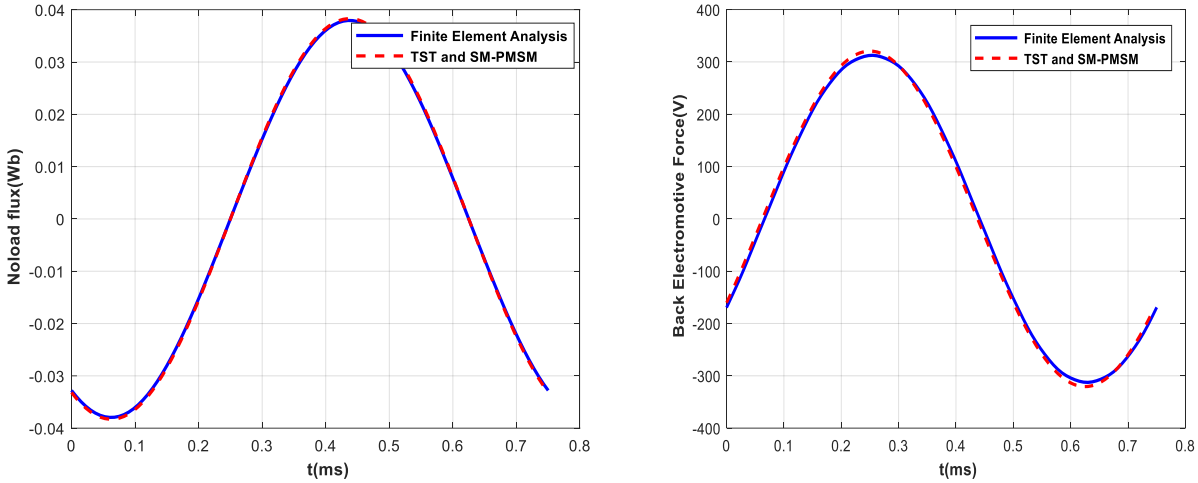

(a) (b)

Figure IV. 29. Slotless model: (a) No-load magnetic flux, (b) Back electromotive force

b. <u>Load simulation</u>

Airgap flux density resulting of the stator current and the rotor permanent magnets is represented in Figure IV.30. Through comparison between models and at the fundament component, we validate again the airgap flux density analytically calculated. Figure IV.31 shows the comparison between inductances analytically calculated and inductances calculated by finite element analysis. The last ones have values of 4.034µH on self-inductance, -1.211µH on mutual inductance and 5.245µH on cyclic inductance. Hence, we notice a deviation of 23% on self-inductance, deviation of 29% on mutual inductance and a deviation of 11% on cyclic inductance. Figure IV.32 shows the simulated electromagnetic torque. Its mean value is about 0.988PU which is close to 1PU, the value calculated using the surface current density and airgap flux density waves. Therefore, deviation on electromagnetic torque is 1.2%.

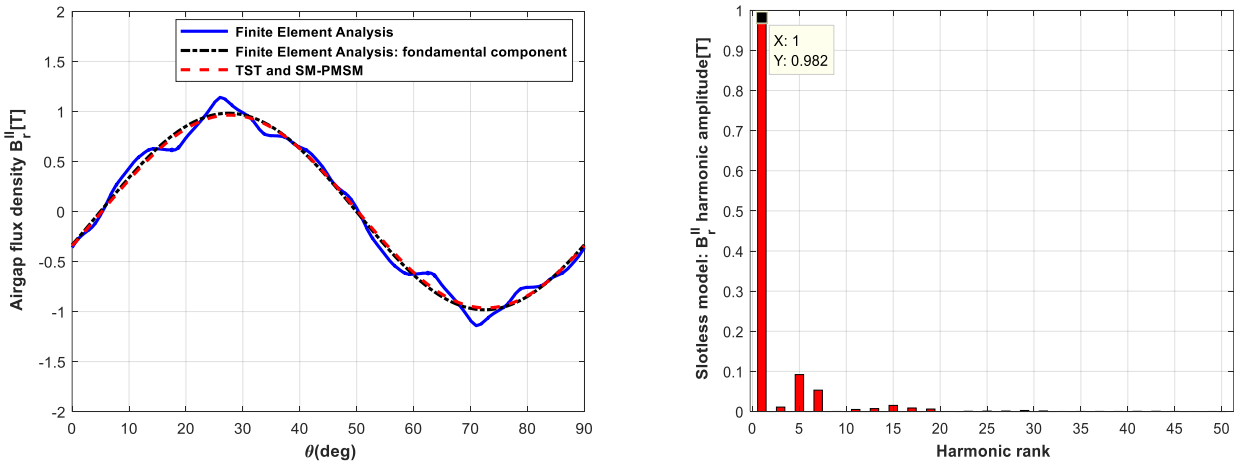

(a) (b)

Figure IV. 30. Slotless model: (a) Airgap flux density, (b) harmonic analysis of airgap flux density given by Finite Element Analysis

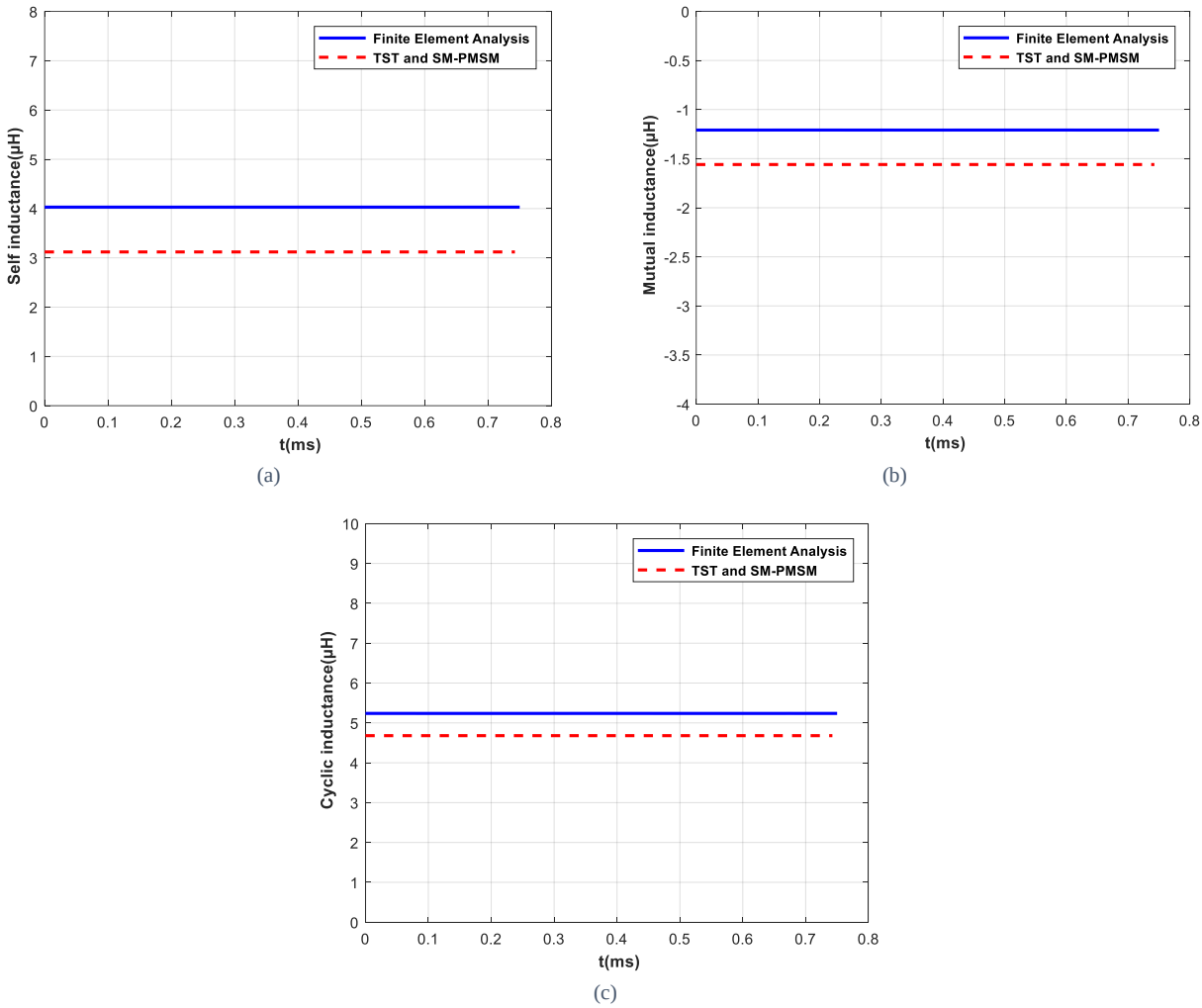

(a) (b) (c)

Figure IV. 31. Slotless model: (a) Self-inductance, (b) Mutual inductance, (c) Cyclic inductance

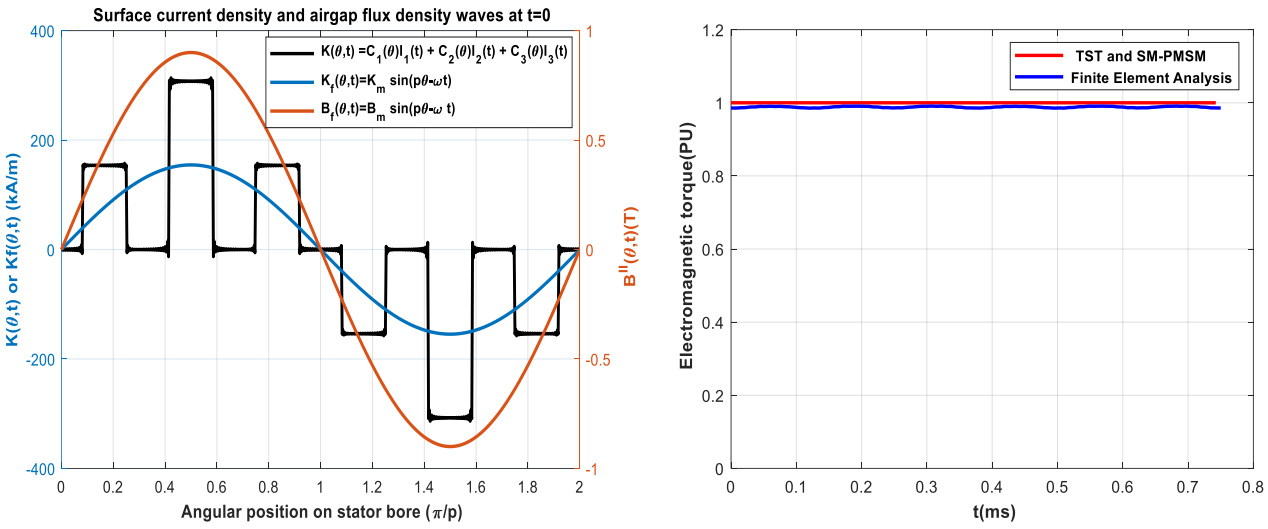

(a) (b)

Figure IV. 32. Slotless model: (a) Surface current density and airgap flux density waves, (b)The electromagnetic torque

VI.4.5.2. Slotted model

Slotted structure of electric motor is represented on one pole as shown in Figure IV.33. Performances will be calculated for one conductor per slot and will be compared to those given by TST and SM-PMSM.

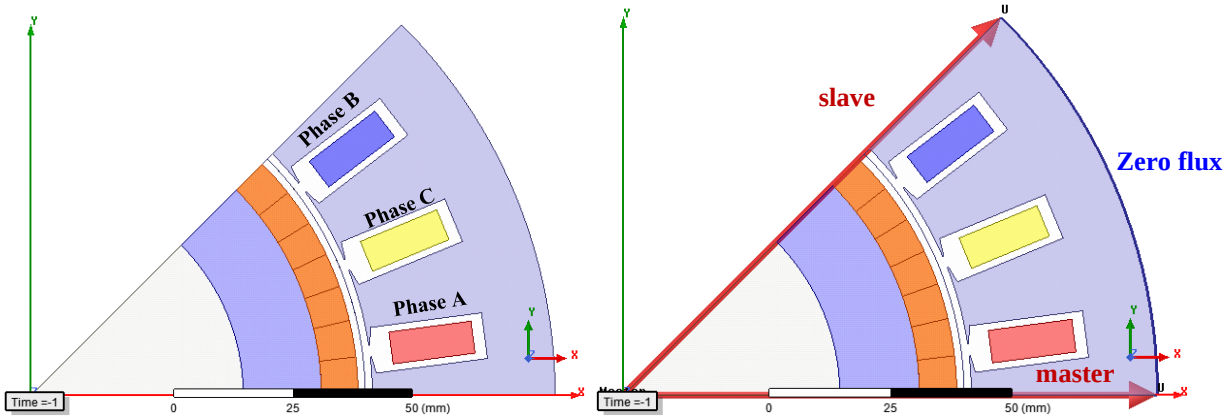

(a) (b)

Figure IV. 33. Slotted model electric motor of long term target 2035: (a) Slotted model structure on one pole, (b) boundary conditions applied on one pole structure

a. <u>No-load simulation</u>

Figure IV.34.a presents the airgap flux density resulting from permanent magnet with and without slot effect. The harmonic analysis of airgap flux density (cf. Figure IV.34.b) obtained by slotted model indicates that it remains close to the sinusoidal waveform. Moreover, the amplitude of fundamental component is 0.9T. Therefore, slot effect on airgap flux density is negligible.

Flux densities in tooth and stator yoke resulting from rotation of permanent magnet at rated speed are illustrated in Figure IV.35. Their maximum respective values are 1.256T and 1.159T. No-load magnetic flux and back-electromotive force are shown in Figure IV.36. They are very close to those calculated using TST and SM-PMSM. Cogging torque resulting from magnetic interaction of permanent magnets and slotted stator is shown in Figure IV.37. Its peak to peak value is 9.08Nm about 1.3% of rated electromagnetic torque.

Figure IV.38.a shows the magnetic flux density distribution and Figure IV.38.b the flux lines at no-load. Slight saturation in the tooth bottom can be observed. The maximum local magnetic flux density in tooth is about 0.9T to 2.35T. In rotor yoke, the mean flux density is about 0.8T.

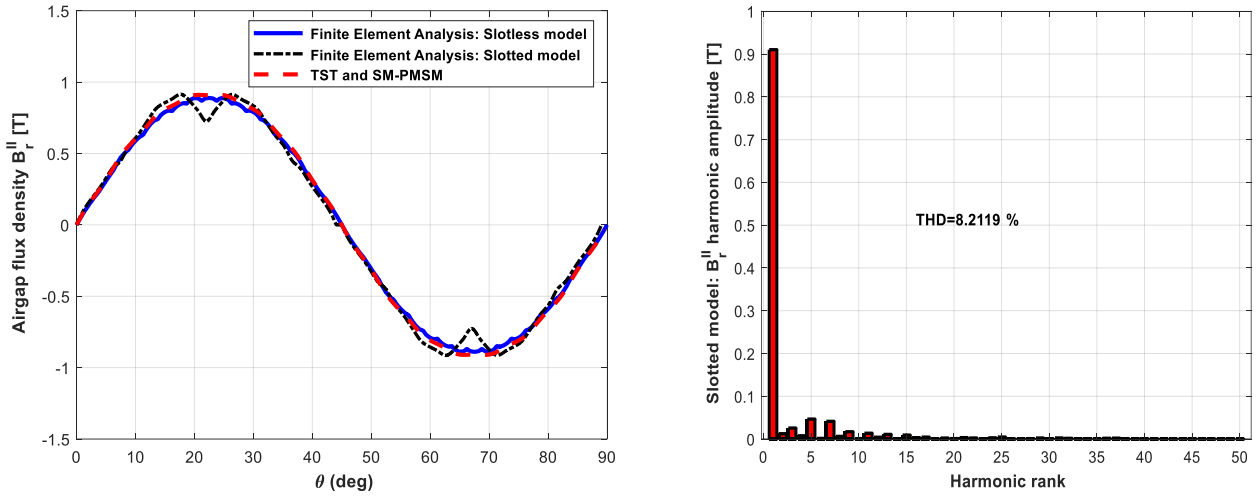

(a) (b)

Figure IV. 34. Airgap flux density at noload: (a) slotless and slotted models, (b) harmonic analysis

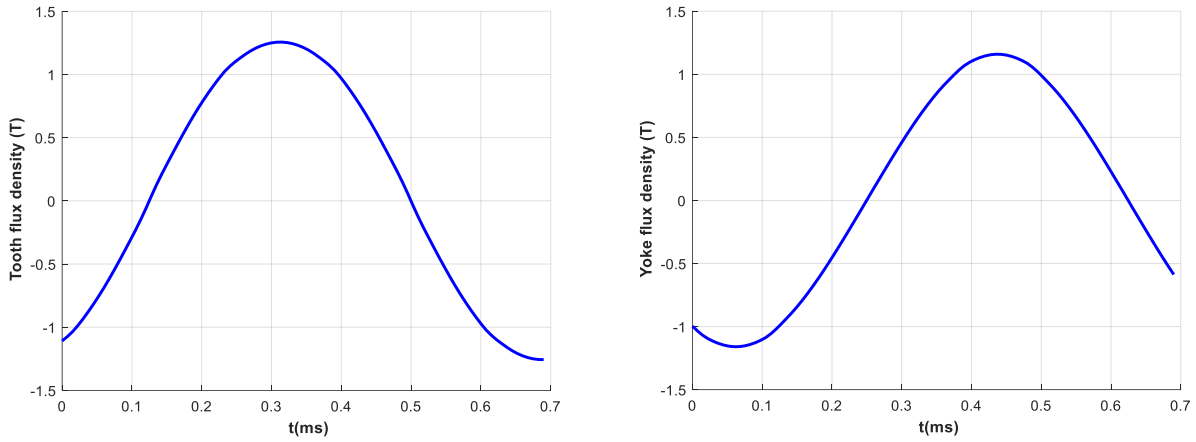

(a) (b)

Figure IV. 35. Slotted model at no-load: (a) tooth flux density, (b) stator yoke flux density

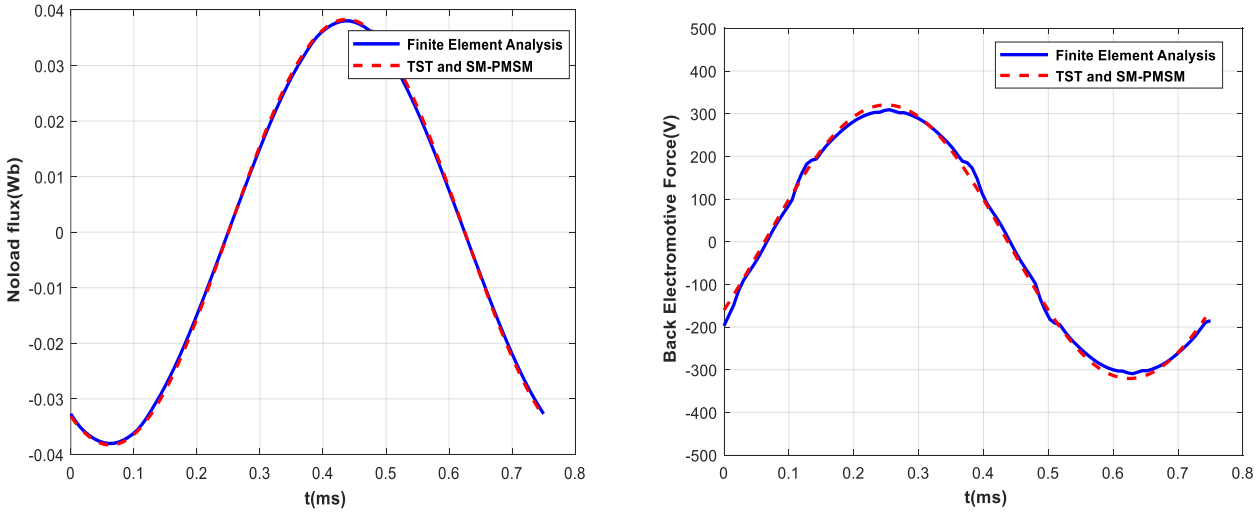

(a) (b)

Figure IV. 36. Slotted model: (a) Noload magnetic flux, (b) Back electromotive force

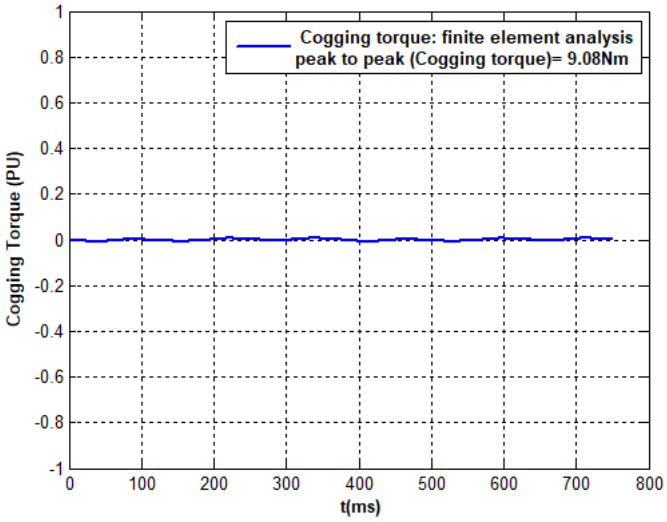

Figure IV. 37. No-load simulation: cogging torque

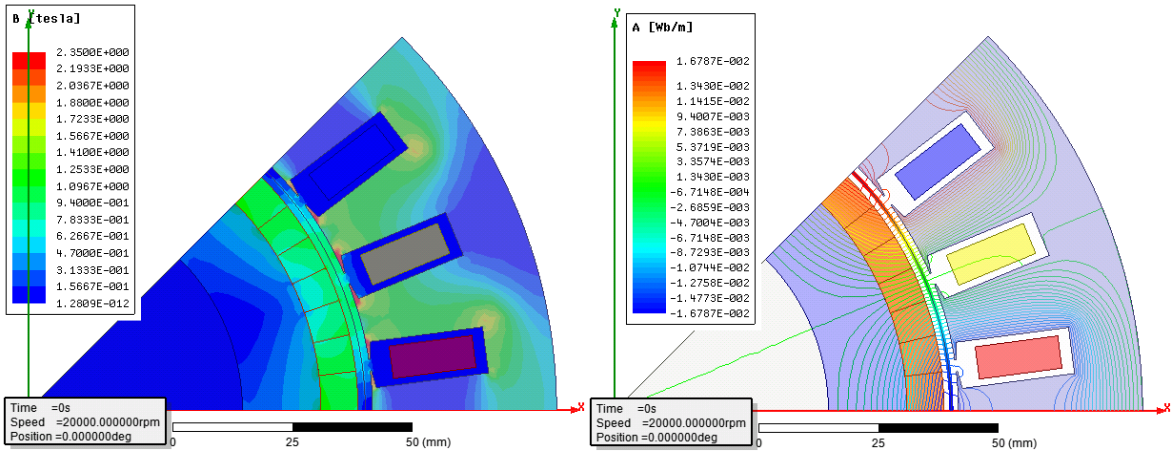

(a) (b)

Figure IV. 38. Slotted model at noload simulation: (a)Magnetic flux density distribution, (b) Flux line distribution

b. Load simulation

In load simulation, the airgap flux density and its harmonic analysis are given in Figure IV.39. Fundamental component obtained by FEA is aligned to the one calculated analytically in TST and SM-PMSM. According to its amplitude, the airgap flux density due to armature reaction is less than 0.06T. Increasing of flux densities in stator tooth and yoke due to the armature reaction is about 0.27T and 0.31T respectively (cf. Figure IV.40).

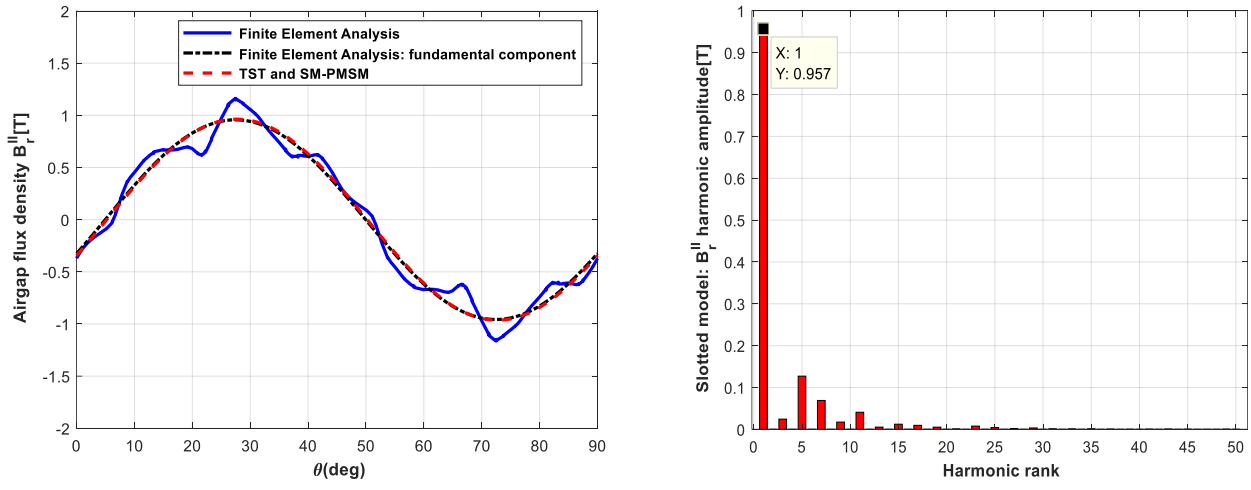

(a) (b)

Figure IV. 39. Slotted model at load: (a) airgap flux density, (b) harmonic analysis

Magnetic flux density distribution and flux lines are presented in Figure IV.41. In teeth, the maximum local magnetic flux density is about 1.4T to 2.35T. In yoke, the maximum local magnetic flux density is about 1.25T to 1.88T for stator and 0.7T to 1.25T for rotor.
Self, mutual and cyclic inductances obtained by finite element analysis are illustrated in Figure IV.42. Their respective mean values are 7.9µH, -1.2µH and 9.2µH. They have ripples which can be due to the magnetic saturation. We notice deviations around 30% between inductances calculated in SM-PMSM and those obtained by finite element analysis. These deviations are mainly due to the ignoring flux leakages.

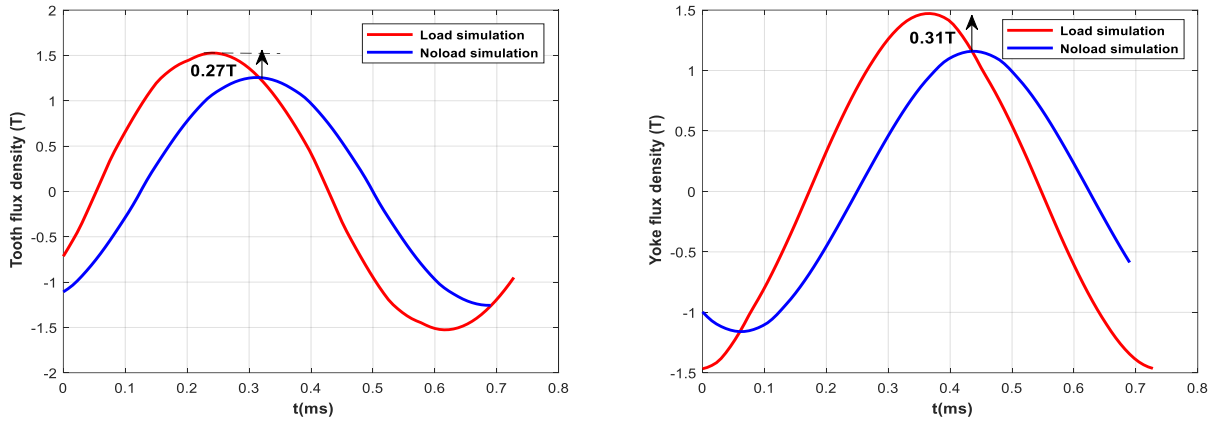

(a) (b)

Figure IV. 40. Slotted model at load: (a) tooth flux density, (b) stator yoke flux density

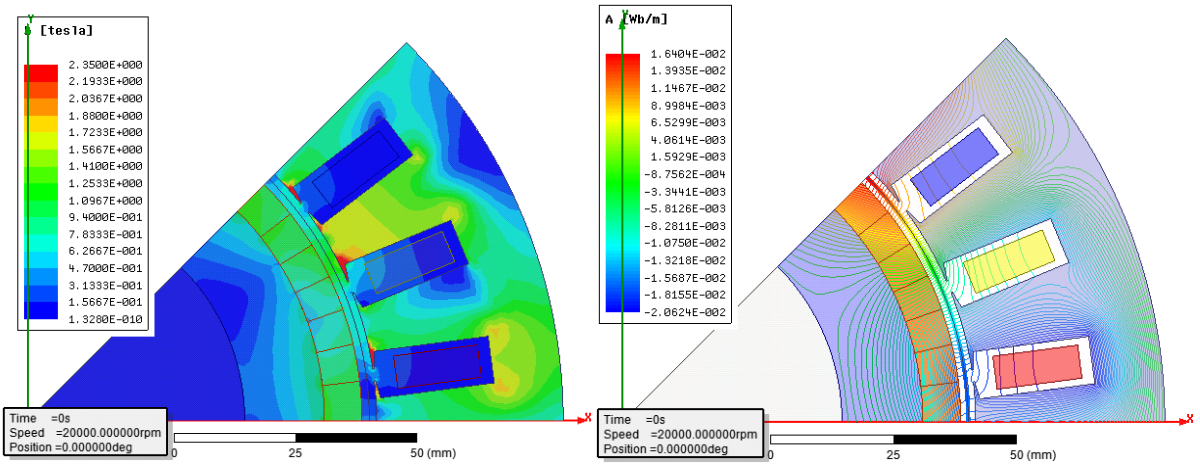

(a) (b)

Figure IV. 41. Slotted model at load simulation: (a)Magnetic flux density distribution, (b) Flux line distribution

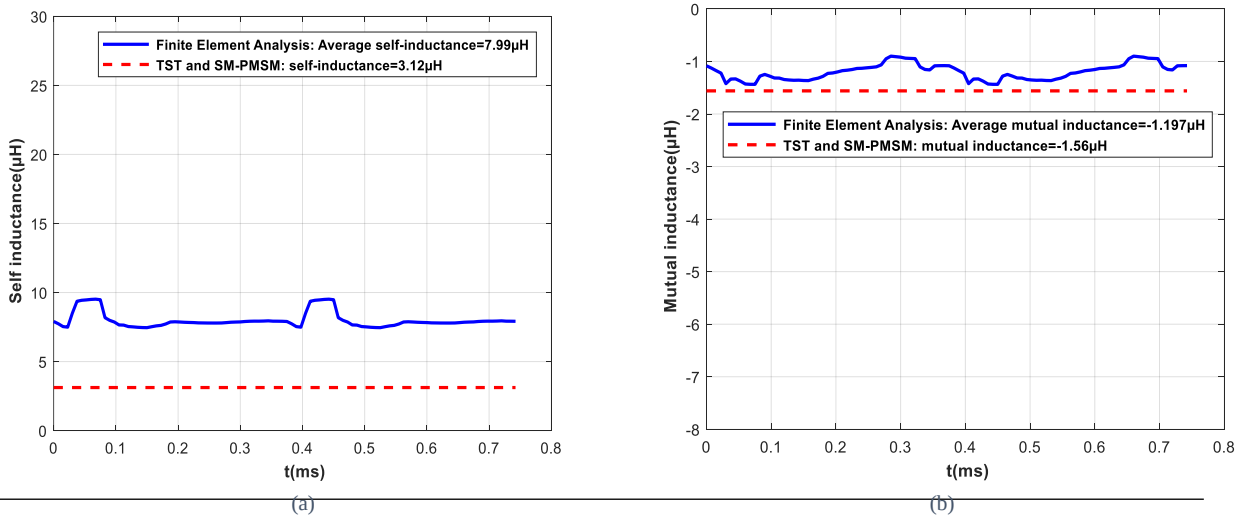

(a) (b)

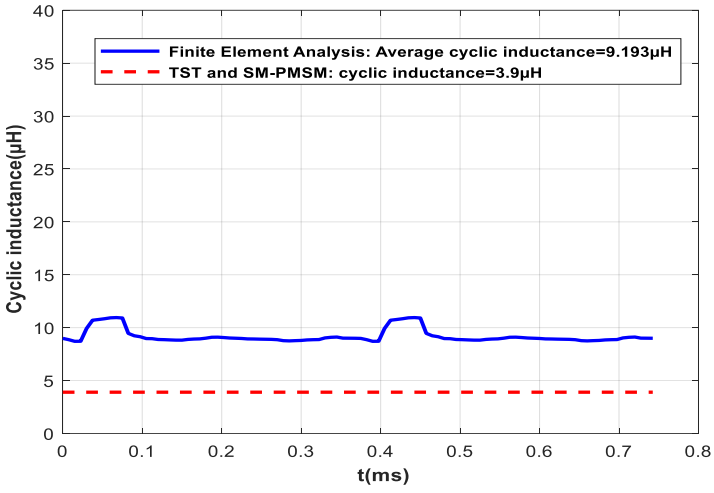

(c)

Figure IV. 42. Slotted model: (a) Self-inductance, (b)Mutual inductance, (c) Cyclic inductance

Figure IV.43 shows the rated electromagnetic torque. The mean value is 0.99PU which is close to the rated value calculated in TST and in SM-PMSM. Thus, deviation is 1%.

The iron losses in electric motor are shown in Figure IV.44. The mean value of these losses is 13.45kW. It is twice greater than the losses calculated in TST and in SM-PMSM. Likewise, for the 1st electric motor, the analytical model of iron losses remains imprecise mainly due to the nonlinear behaviour of magnetic stator and rotor sheets.

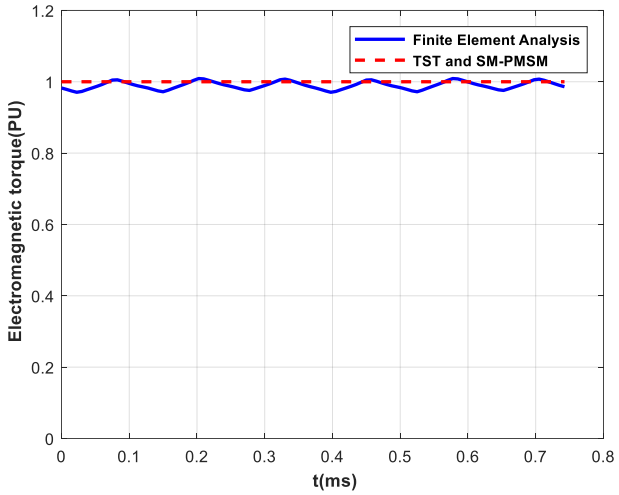

Figure IV. 43. Slotted model: The electromagnetic torque

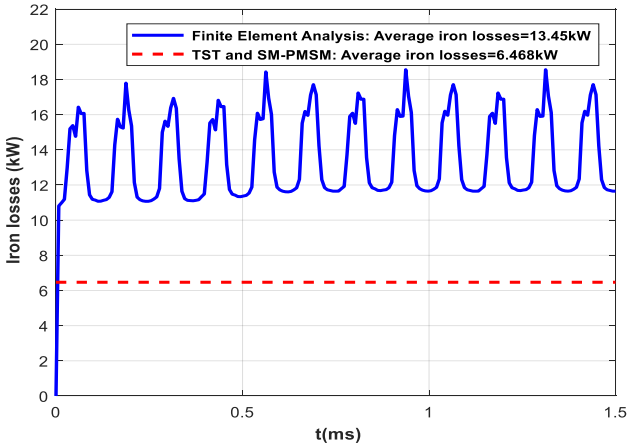

Figure IV. 44. Slotted model: Iron losses

In summary of these comparisons, performances as electromagnetic torque, no-load flux and back electromotive force are well validated as shown in Table IV.16. In contrast, analytical inductances are relatively validated only with slotless model. Due to the neglecting of flux leakages and the nonlinear behaviour of magnetic material, calculation of inductances and iron losses in TST and SM-PMSM remain relatively imprecise. From the electromagnetic torque and the iron losses analysed using FEA, efficiency is recalculated. Its value is closer to 98%, it remains higher than targeted efficiency at sizing point. Deviation on efficiency is quasi-zero.

Table IV. 16: Electric motor of long term target 2035: summary comparison of performances between analytical tools and finite element analysis

Performances	TST	SM-PMSM	Finite Element Analysis		Slotless model deviation	Slotted model deviation
			Slotless model	Slotted model		
Max. Noload magnetic flux "Φ_{vm}[Wb]"	-	0.0383	0.0379	0.0381	**1%**	**0.5%**
Rms Back- electromotive force "E_i[V]"	-	226.77	224.13	223.5	**1.2%**	**1.4%**
Electromagnetic torque "T_{em}[PU]"	1	1	0.98	0.99	**2%**	**1%**
Self-inductance "L_s[µH]"	-	3.12	4.034	7.996	**23%**	**61%**
Mutual inductance "M[µH]"	-	-1.56	-1.211	-1.1972	**29%**	**30%**
Cyclic inductance "L_{cs}[µH]"	-	4.68	5.245	9.1933	**11%**	**49%**

IV.4.6 Thermal behaviour and cooling system design

As for electric motor of 1st target, cooling system of 2nd target is designed from heat flows generated by magnetic, electric and mechanical losses. Figure IV.45 illustrates losses profiles obtained for operating at maximum torque (Appendix D). In these loss profiles, iron losses are assessed using finite element analysis whereas Joule and mechanical losses are assessed using analytical models established in TST and SM-PMSM. Thermal constraint expressed by equivalent current density is also shown in Figure IV.45. Based on these losses, the maximum equivalent current density is equal to 5.10^{12} A²/m³. It indicates the required cooling effort. Maximum total losses which WP3 should be evacuated are 28kW.

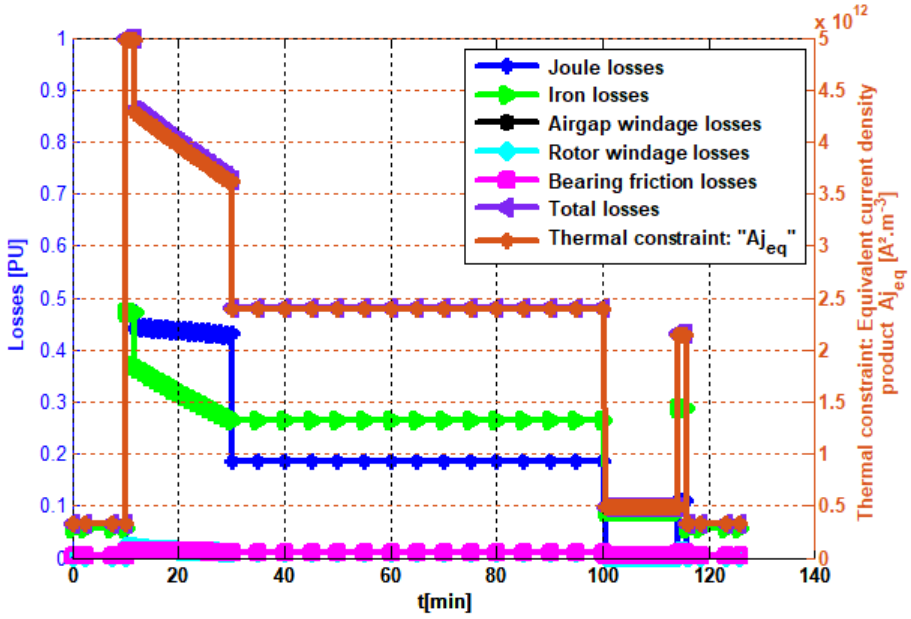

Figure IV. 45. Long term target 2035: Losses profiles and equivalent current density product function of time flying

As for 1st targeted electric motor, cooling circuit is composed of heat exchanger, hydraulic circuit and hydraulic pump for evacuating losses (cf. Figure IV.23). Joule losses are the highest losses compared to other losses, indeed their extraction and evacuation in small zones is a huge challenge. For the purpose, inner cooling method in winding is added to the cooling methods employed in 1st targeted electric motor. Inner cooling method is performed by two cooling channels embedded in slots as presented in Figure IV.46. These cooling channels are designed in order to respect copper fill factor of 50%.

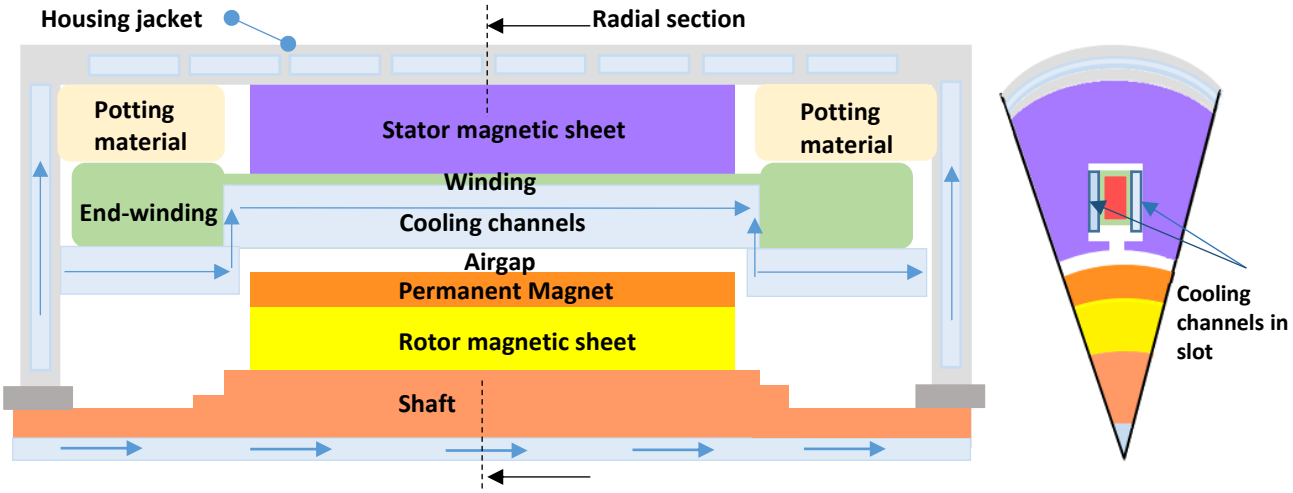

Figure IV. 46. Long term target 2035: axial and radial sections of electric motor and its cooling channels

Iron and mechanical losses are extracted using cooling housing jacket and using cooling channel implemented in rotor shaft. Therefore, to take into account the inner cooling method in winding, WP3 proposed another lumped parameter thermal model given in Figure IV.47.a. Lumped parameter thermal model associated to the cooling system design model allows to evaluate temperatures in electric motor with its cooling system during flying mission as shown in Figure IV.47.b. We notice that temperature in slot does not exceed 160°C due to the direct cooling effort performed in slot. In end-winding, temperature achieves maximum value of 190°C (in take-off flying phase). The latter is lower than to the thermal class chosen in §VI.4.1. Moreover, due to both cooling efforts in shaft and in slots, temperature in permanent magnet does not exceed 130°C which thus leads sustaining the electromagnetic performances of targeted electric motor. The cooling system weight given by WP3 is 33kg with 10kg for the pump weight and 23kg for the coolant, the pipes, the potting materials and the pipes of the heat exchanger. Then the motor with its cooling system reached almost 10kW/kg. Characteristics of cooling system designed by WP3 are summarized in Table IV.13. By comparison to the cooling system of targeted electric motor 2025, we notice that cooling effort performed in winding allows to reduce on one side the winding temperature especially in slot and on the other side reducing the cooling efforts performed in shaft and in frame as indicate the heat transfer convections (cf. Tables IV.7 and IV.13).

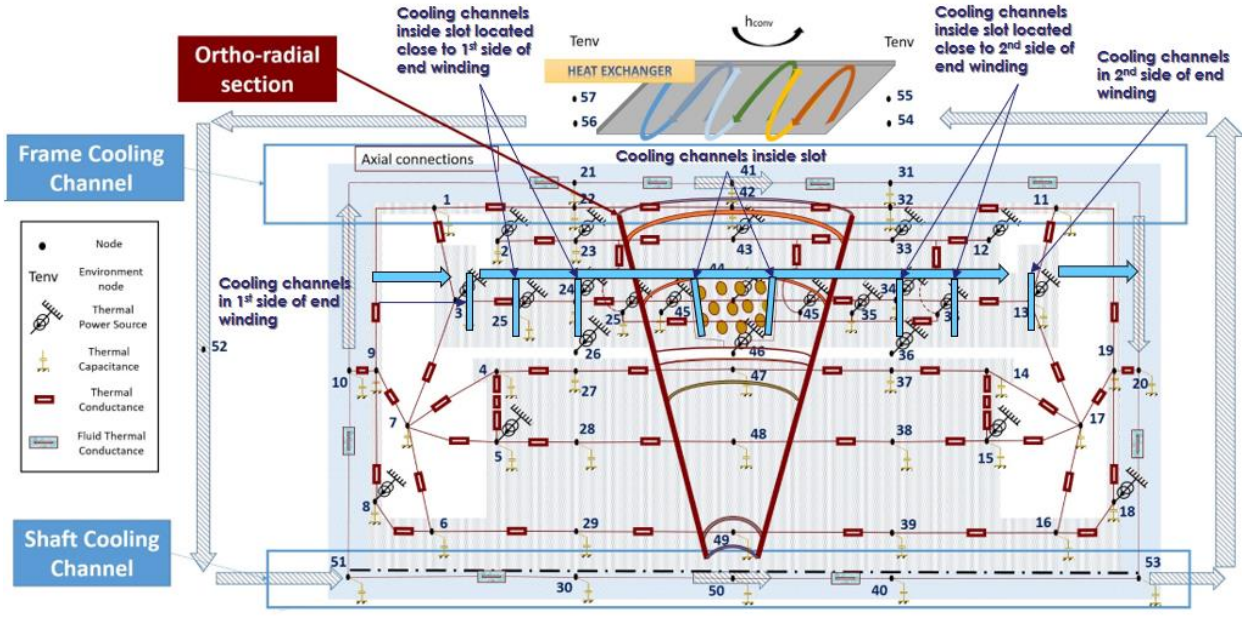

(a)

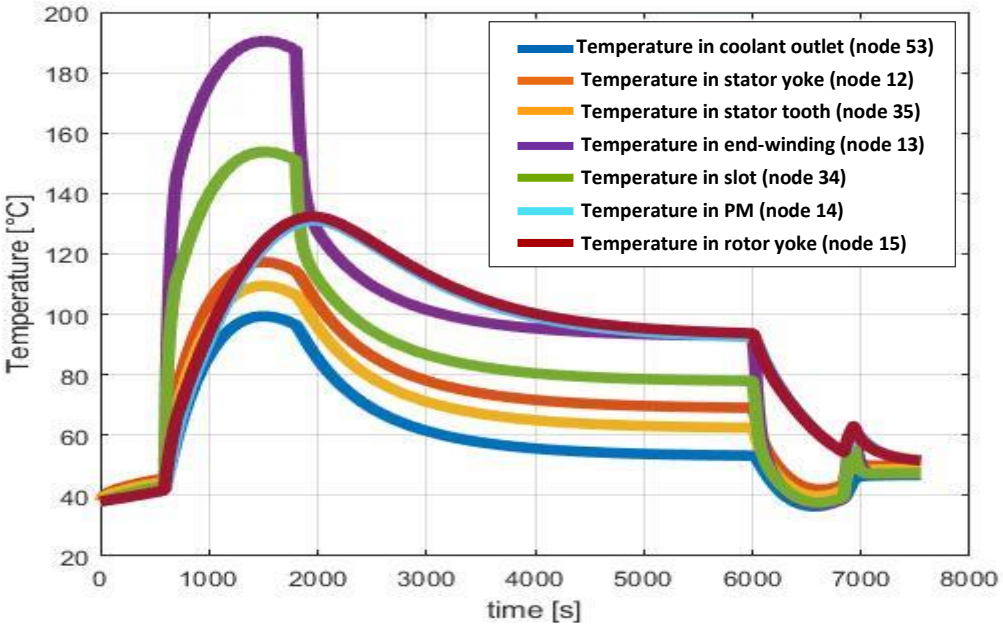

(b)

Figure IV. 47. Long term target 2035: (a) Axial and ortho-radial section of SM-PMSM including its cooling system with Lumped Parameter Thermal Model LPTM nodes location, and axial and motor-end connections, (b) Temperature evolution during flying mission in the sized electric motor

Table IV. 17: Long term target 2035: Cooling system characteristics given by WP3

Cooling channels inside housing jacket and shaft		
Parameters of cooling channels	Housing jacket	Shaft
Hydraulic diameter [mm]	7.1	9.1
Flow rate [$m^3.s^{-1}$]	1×10^{-4}	5×10^{-5}
Heat transfer coefficient [$W.m^{-2}.K^{-1}$]	250	1600
Heat exchanger		
Parameters	Pipes	Cold plate
Material	"Aluminium"	
Thickness[mm]	1	3
Hydraulic diameter [mm]	42	-
Flow rate [$m^3.s^{-1}$]	2.55×10^{-3}	-
Heat transfer coefficient [$W.m^{-2}.K^{-1}$]	3300	-
Cooling channels inside slots: inside winding		
Material	"Silicone rubber"	
Section [mm^2]	2.415	
Thickness [mm]	0.2	
Flow rate [$m^3.s^{-1}$]	5×10^{-5}	
Heat transfer coefficient [$W.m^{-2}.K^{-1}$]	4700	
Coolant	**"Ethylene Glycol Water 50/50"**	
Potting material	**"CoolThermTM EP - 3500"**	
Thermal conductivity [$W.m^{-1}.K^{-1}$]	3.3	
Hydraulic Pump		
Normal operating pressure [bars]	206	
Maximum speed [rpm]	4420	
Length [cm]	26.42	
Height [cm]	19.05	
Width [cm]	17.78	
Cooling total weight[kg]	**33**	

Conclusion

This chapter aims to identify the most promising electric motor technologies for achieving medium and long term targets using Target Setting Tool developed in Chapter II. It aims also to size the electric motors with their cooling systems using Surface Mounted Permanent Magnet Synchronous Motor Tool developed in Chapter III and cooling design models performed by WP3. For sizing electric motors taking into account interactions with WP3 and WP5, we have slightly overrated the targeted specific power and slightly underrated the fill factor in TST and SM-PMSM for including subsequently the cooling system and the insulation respectively.

This chapter provides the following conclusions:

a. Increasing specific power of electric motor is mainly based on the improving material properties and cooling effort, as it is illustrated in the summary table given below.
b. Using external cooling method carried through the frame, using ambient external air as cooled source and with stranded and twisted conductors and high performance materials, the medium term target of 5kW/kg is achieved.
c. Using inner cooling method in winding in electric motor, thermal limit set for medium term target is exceeded. Therefore, long term target of 10kW/kg is achieved
d. Thermal limit expressed as equivalent current density product represents a good indicator to design high specific power electric motors.
e. Thermal limit expressed by the equivalent current density does not exceed $2.10^{12}A^2/m^3$ and $5.10^{12}A^2/m^3$ for respectively medium term target and long term target. These given values can be taken as good hybrid propulsion chain optimization constraints for the two targets.
f. For medium term target winding insulation materials should be 220°C thermal class and for long term target winding insulation materials should be 240°C thermal class.
g. Although for a given specific power, there are sizing solutions at low speed with high pole pairs, these solutions are similar in terms of electric frequency to sizing solutions at high speed and low number of pole pairs.

Medium term target 2025	Long term target 2035
Loads, speed, number of pole pair and slot fill factor	
- Tangential stress "σ =50000Pa" - Current density "j_{rms}=8.1A/mm²" - Max surface current density "K_m=111.1kA/m" - RMS linear current density: "A_{rms}=81.4kA/m" - Current density product "$A_{rms}j_{rms}$=6.5948×10^{11} A²/m^3" - Max airgap flux density "B_m=0.9T" - Flux density in teeth "B_{st}=1.3T" - Flux density in yoke "B_{sy}=1.2T" - Rotational speed "Ω=15970rpm" - Number of pole pairs "p=2" - Slot fill factor is 0.5	- Tangential stress "σ=70000Pa" - Current density "j_{rms}=20A/mm²" - Max surface current density "K_m=155kA/m" - RMS linear current density:"A_{rms}=110kA/m" - Current density product "$A_{rms}j_{rms}$=2.199×10^{12} A²/m^3" - Max airgap flux density "B_m=0.9T" - Flux density in teeth "B_{st}=1.25T" - Flux density in yoke "B_{sy}=1.25T" - Rotational speed "Ω=20000rpm" - Number of pole pairs "p=4" - Slot fill factor is 0.5
Technological solutions	
- Stranded and twisted conductors (frequency <1kHz) - Magnetic sheet: "Vacoflux 48- 0.35mm" - Halbach permanent magnet with radial and axial segmentation to ensure sinewave airgap flux density to reduce eddy current losses - Carbon Fiber Sleeve - Thermal winding class 220°C	- Compacted rectangular litz wires conductors (frequency >1kHz) - Magnetic sheet: "Vacoflux 48- 0.35mm" - Halbach permanent magnet with radial and axial segmentation to ensure sinewave airgap flux density to reduce eddy current losses - Carbon Fiber Sleeve - Thermal winding class 240°C
Cooling methods	
- Conventional direct cooling method performed in the frame and shaft - Thermal limit: equivalent current density product is 2 $10^{12}A^2/m^3$	- Conventional direct cooling method performed in the frame and shaft - direct inner cooling method for stator winding cooling, - potting materials around end-windings for improving their cooling - Thermal limit: equivalent current density product is 5 $10^{12}A^2/m^3$
→ Speed: 15970rpm → Cooling system weight: 32kg	→ Speed: 20000rpm → Cooling system weight: 33kg

→ Specific power: 5kW/kg → Efficiency >97%	→ Specific power: 10kW/kg → Efficiency >97%

Despite of tools developed in Chapters II and III are based on huge assumptions, they are suitable for sizing electric motors with tolerable deviations. They are developed in Matlab for becoming useful for hybrid propulsion chain optimization (WP6) given that they need very few input data. Therefore, they provide results in a short time.

Appendices

- **Appendix A: Magnetic sheet Iron Cobalt "FeCo: Vacoflux 48-0.35mm"**

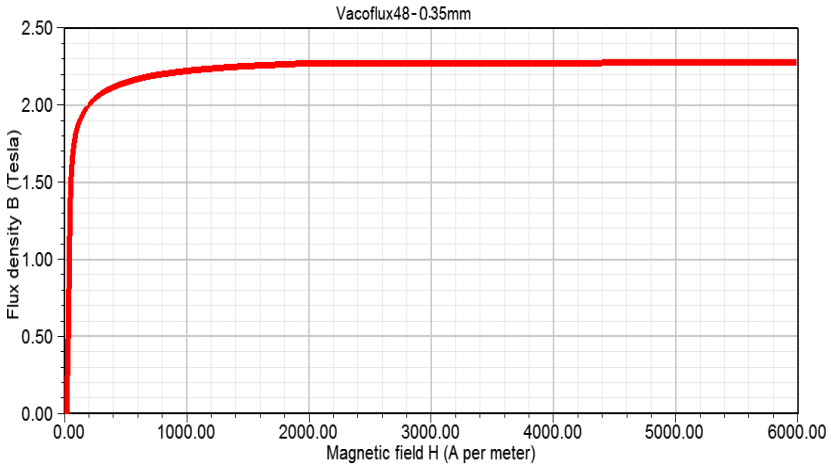

Figure IV. 48: B(H) characteristic of iron cobalt magnetic sheet: Vacoflux 48-0.35mm

Table IV. 18: Bertotti model of iron loss for Vacoflux 48-0.35mm : equation (II-66)

Iron loss coefficients	Hysteresis loss coefficient "k_h" [W.s.T^{-2}.kg^{-1}]	Eddy loss coefficient "k_c" [W. s^2. T^{-2}kg^{-1}]	Excess loss coefficient "k_e" [W.(s/T)$^{3/2}$.kg^{-1}]
	0.049058	4.44997.10^{-5}	0

Table IV. 19: New formulation of iron loss for Vacoflux 48-0.35mm : equation (II-67)

Iron loss coefficients	"a_{11}"	"a_{12}"	"a_{13}"	"a_{14}"	"a_{21}"	"a_{22}"	"a_{23}"	"a_{24}"
	4.369	-13.65	13.66	-4.33	-0.705	2.193	-2.17	0.688
	"a_{31}"	"a_{32}"	"a_{33}"	"a_{34}"	"a_{41}"	"a_{42}"	"a_{43}"	"a_{44}"
	0.0308	-0.0966	0.098	-0.0317	-0.0006	0.001985	-0.002217	0.00085743

- **Appendix B: Permanent Magnet Samarium Cobalt (SmCo) "Recoma33E"**

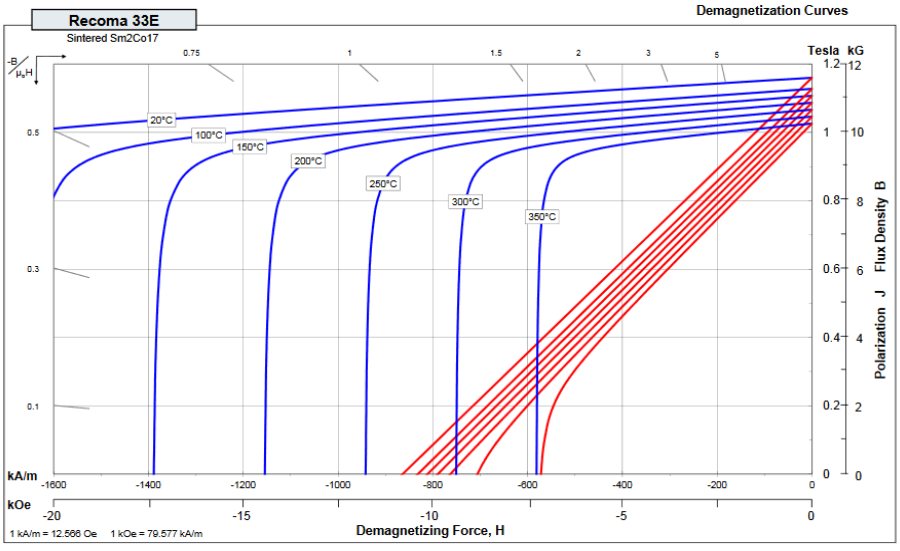

Figure IV. 49 Demagnetization curves of Samarium Cobalt (Sm_2Co_{17}): "Recoma 33E [ArnCat]

Table IV. 20: Magnetic properties of Samarium Cobalt (Sm_2Co_{17}): "Recoma 33E" [ArnCat]

Properties	Minimum	Nominal
Residual induction "B_r"	1.14 T	1.16 T
Coercivity "H_{Cb}"	845kA/m	865kA/m
Intrinsic coercivity "H_{cj}"	1750kA/m	2100kA/m
Maximum energy product "BH_{max}"	238kJ/m^3	251kJ/m^3

Table IV. 21: Physical properties of Samarium Cobalt (Sm_2Co_{17}):"Recoma 33E" [ArnCat]

Thermal properties	Value
Reversible temperature coefficient induction "α_B"	-0.035
Reversible temperature coefficient coercivity "α_H"	-0.25
Thermal conductivity	10W.m^{-1}. K^{-1}
Specific heat	350J.kg^{-1}. K^{-1}
Max. recommended use temperature	350°C
Curie temperature	825°C
Density	8300kg/m^3
Electrical resistivity	90μΩ.cm

- **Appendix C: "Rectangular compacted litz wires"**

- *Rectangular compacted litz wires "New England Wire Technologies Catalogue"*

According to New England Wire Technologies Catalogue, rectangular compacted Litz wire type 8 (cf. Figure IV.50) is the particular suitable conductor for high frequency electric machines. Rectangular compacted litz conductor is designed with 60 to 75 of copper filling. Table IV.22 presents some characteristics of rectangular compacted litz wires.

Table IV. 22. Rectangular compacted litz wire type 8 [NewCat]

Equivalent AWG	Circular Mil Area	Number of wires	AWG of wire	Film coating	Nominal width	Nominal thickness	Nominal linear inductance	Direct Current Resistance	Construction
Unit	Cmils	-	-	-	inch	inch	Lbs/1000ft	Ohms/1000ft	-
Recommended operating frequency- 400Hz to 5kHz									
4	46403	7	12	H*	0.327	0.152	140.0	0.262	7×12
2	79548	12	12	H	0.533	0.152	240.0	0.153	12×12
1	106064	16	12	H	0.704	0.152	320.0	0.115	16×12
1/0	**119322**	**18**	**12**	**H**	**0.789**	**0.152**	**361.0**	**0.102**	**18×12**
6	28763	7	14	H	0.262	0.121	88.0	0.416	7×14
4	41090	10	14	H	0.374	0.121	126.0	0.291	10×14
1	82180	20	14	H	0.700	0.121	251.0	0.146	20×14

(*) Heavy film coating insulation, cmils=6.4516 10^{-4}mm², inch=2.54 10^{-2}m, lbs=0.4536kg, ft=304.8mm

Figure IV. 50. Rectangular compacted litz-wire type 8 [NewCat]

- *Chosen conductor for long term target: "Compacted rectangular compacted Litz wires: 18×AWG12"*

Characteristics of chosen conductor for long term target are shown in bold in Table IV.22. This conductor is composed of 18 wires of AWG 12. Characteristics of AWG 12 wire is given in Table IV.23. Rectangular compacted litz has nominal width of 20mm for 9 wires in one row and nominal thickness of 3.86mm with two rows of nine wires (i.e. 9×2 arrangement) as shown in Figure IV.51.

Table IV. 23. Copper whole AWG12 of Essex Magnet Wire Catalogue [EssCat]

Round wire data		Bar wire	Single Build Film-Insulated wire	Heavy Build Film-Insulated Wire	Triple Build Film-Insulated Wire
Bar wire diameter	[mm]	2.052	2.052	2.052	2.052
Bar wire cross section	[mm²]	3.3081	3.3081	3.3081	3.3081
Bar wire weight	[kg/m]	29.44	29.44	29.44	29.44
Bar wire resistance	[Ω/m]	0.005212	0.005212	0.005212	0.005212
Insulated thickness	[μm]	-	21.590	43.18	60.959
Insulated wire weight	[kg/km]	-	0.18	0.380	0.550
Insulated material density	[kg/m^3]	-	1279	1337	1359
Overall wire diameter	[mm]	-	2.0955	2.138	2.174
Overall wire cross section	[mm²]	-	3.4488	3.592	3.7128
Film-insulated wire weight	[kg/km]	-	29.589	29.789	29.959
Film-insulated wire resistance	[Ω/m]	-	0.005216	0.005216	0.005218

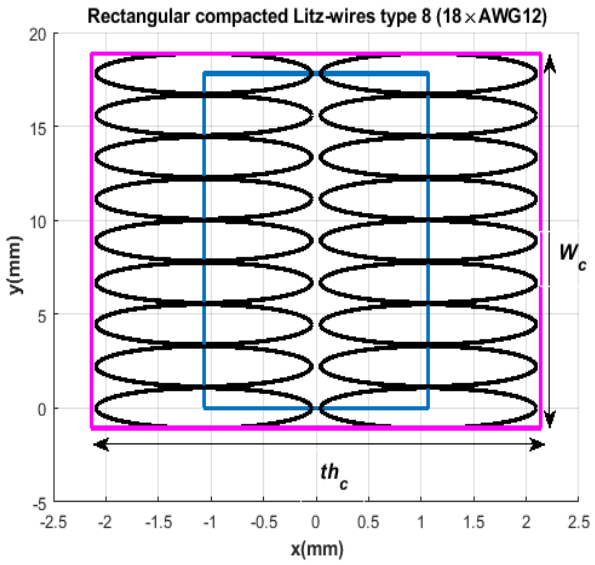

Figure IV. 51. Arrangement of rectangular compacted Litz wires type 8 [NewCat]

- Calculation of "k_{lc} " taking into account the twisting effect

In rectangular compacted Litz wires, wires are twisted with an angle β_e on the lay length as illustrated in Figure IV. 52. Indeed, wires have circular cross-section in perpendicular plan of twisting direction which leads elliptical cross-section as shown in Figure IV.53. Therefore, the angle between circular and elliptical cross-sections is none other than the β_e angle. It can be calculated by the following equation:

$$\cos(\beta_e) = \frac{D_{iw}}{W_c/n_{w1}} \quad \text{(IV- 1)}$$

With:

$$n_{w1} = \frac{n_w}{n_{w2}} \quad \text{(IV- 2)}$$

Where: D_{iw} is the insulated wire diameter (cf. Table IV.23), W_c is the width of rectangular compacted Litz wire (cf. Table IV.22), n_w is the total number of wires (for chosen rectangular compacted Litz wire $n_w = 18$), n_{w1} is the number of wires in *y* direction (for chosen conductor $n_{w1} = 9$), n_{w2} is the number of wires in the *x* direction (for chosen conductor $n_{w2} = 2$).

Then the lay length shown in Figure IV.52.b can be given by:

$$\text{lay length} = 2 \times \frac{\left(\frac{n_{w1}-1}{n_{w1}}\right) W_c}{\tan(\beta_e)} \quad \text{(IV- 3)}$$

Thus, the length of a wire can be deduced by:

$$l_w = 2 \times \left(\frac{0.5 \text{ lay length}}{\cos(\beta_e)} + D_{wi}\right) \quad \text{(IV- 4)}$$

The coefficient taking into account the twisting effect is governed by:

$$k_{lc} = \frac{l_w}{\text{lay length}} \quad \text{(IV- 5)}$$

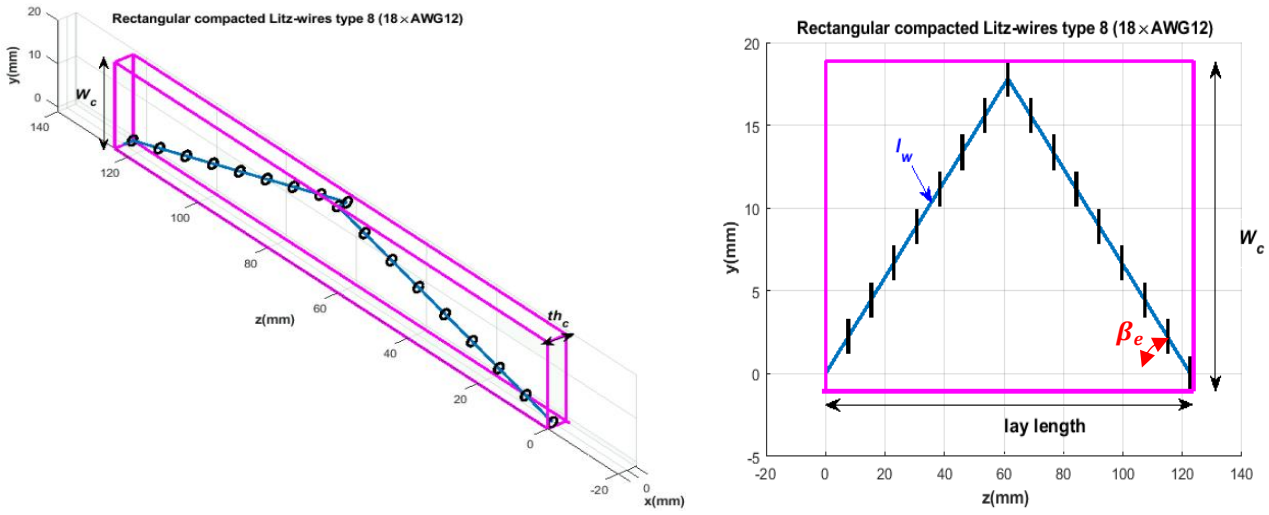

(a) (b)

Figure IV. 52. Rectangular compacted Litz wires type 8: (a) 3D view, (b) YZ view

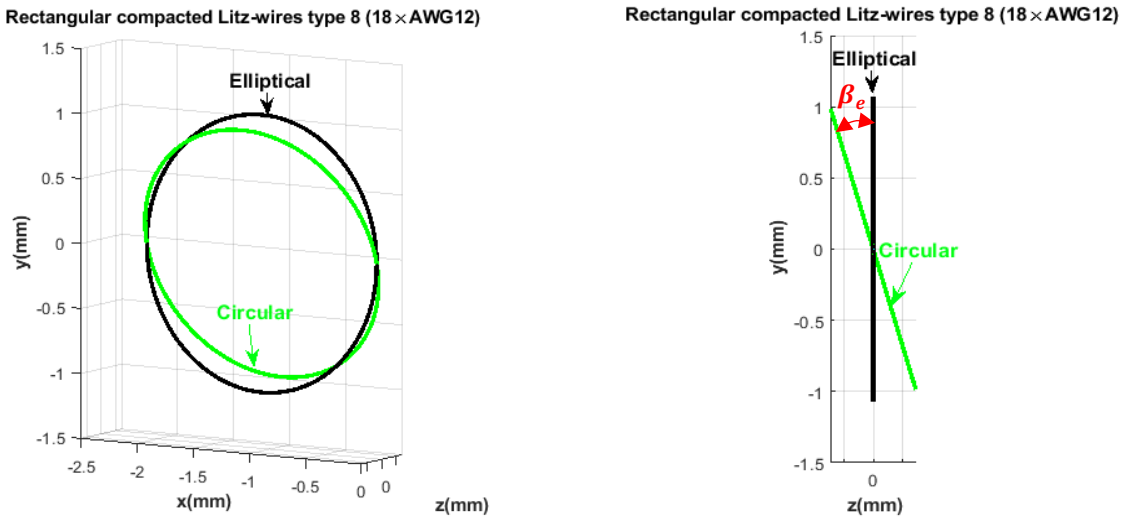

(a) (b)

Figure IV. 53. Circular and elliptical cross sections: (3D) view, YZ view

- Calculation of "k_{sc}" which takes into account the elliptical cross section of conductors

Coefficient "k_{sc}" is governed by:

$$k_{sc} = \frac{S_w}{S_{elliptical}} \quad \text{(IV- 6)}$$

With: $S_{elliptical}$ is the elliptical cross-section of wire:

$$S_{elliptical} = \frac{S_w}{\cos(\beta_e)} \quad \text{(IV- 7)}$$

Where: S_w is the circular cross section of wire ($S_w = \frac{\pi}{4} D_{wi}^2$).

- Calculation of fill factor of conductor "$k_{fillcond}$"

Copper filling of conductor is given by:

$$k_{fillcond} = \frac{n_w S_{elliptical}}{W_c th_c} \quad \text{(IV- 8)}$$

Eventually, rectangular compacted Litz wire 18×12AWG are characterized by:

$$\begin{cases} \beta_e = 29.89° \\ k_{sc} = 86.69\% \\ k_{lc} = 1.153 \\ k_{fillcond} = 71.67\% \end{cases} \quad \text{(IV- 9)}$$

- **Appendix D: "Control strategy of permanent magnet synchronous motor"**

For controlling electric machines, model using Park transformation is often employed. Park transformation aims to transform three phase model of electric machines into two phases in quadratic reference noted by *dq* (*d* is the direct axis; *q* is the quadratic axis) [Kim_17] [Oun_16]. Park model of permanent magnet synchronous motor expresses the voltage equations given in direct axis (d) and quadrature axis (q) by:

$$\begin{cases} V_d = R_s I_d + L_{cs}\frac{dI_d}{dt} - L_{cs} I_q \omega \\ V_q = R_s I_q + L_{cs}\frac{dI_q}{dt} + L_{cs} I_d \omega + E \end{cases} \quad \text{(IV- 10)}$$

Where: V_d, V_q are respectively direct and quadratic voltages, I_d and I_q are respectively the direct and quadratic currents, ω is the electric pulsation, L_{cs} is the cyclic inductance and R_s is the resistance.

In steady state, equation (IV-10) can be written by:

$$\begin{cases} V_d = R_s I_d - L_{cs} I_q \omega \\ V_q = R_s I_q + L_{cs} I_d \omega + E \end{cases} \quad \text{(IV- 11)}$$

Permanent magnet synchronous motor can operate at either constant torque mode or at constant power mode according to control strategies applied to the inverter. Figure IV.54 illustrates the torque-speed characteristic and the two operation modes of permanent magnet synchronous motor.

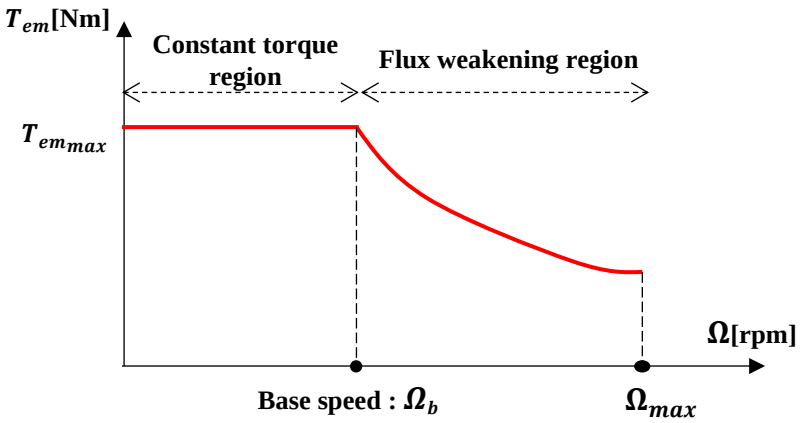

Figure IV. 54. Torque-speed characteristic of SM-PMSM

Electric power using dq voltages and currents is given by:

$$P_{ele} = V_q I_q + V_d I_d \quad \text{(IV- 12)}$$

By using equation (IV-10), equation (IV-11) can be written by:

$$P_{ele} = R_s\left(I_d^2 + I_q^2\right) + E I_q \quad \text{(IV- 13)}$$

Knowing that:

$$P_{ele} = P_j + P_{em} \quad \text{(IV- 14)}$$

And

$$E = \omega \phi_{vm} \quad \text{(IV- 15)}$$

By identification:

$$P_{em} = E I_q \quad \text{(IV- 16)}$$

Therefore, the electromagnetic torque using quadratic current is:

$$T_{em} = \frac{P_{em}}{\Omega} = p \phi_{vm} I_q \quad \text{(IV- 17)}$$

References

[Pyr_14] J. Pyrhönen, T. Jokinen, V. Hrbovcovà, "Design of rotating electrical machines," 2nd Edition, John Wiley & Sons, 2014.

[All_18] Jean-François Allias, AIRBUS HASTECS deliverable 2018, July 2018.

[Tou_20] S. Touhami, A. Zeaiter, M. Fénot, Y. Lefevre, J. F. Llibre, E. Videcoq," Electrothermal Models and Design Approach for High Specific Power Electric Motor for Hybrid Aircraft", 1st Edition of the Aerospace Europe Conference AEC 2020, Bordeaux, France, 25th-28th February 2020.

[Zea_18] A. Zeaiter, M. Fénot, "Thermal sensitivity analysis of a high power density electric motor for aeronautical application", 2018 IEEE International Conference on Electrical Systems for Aircraft Railway, Ship Propulsion and Road Vehicles and International Transportation Electrification Conference (ESARS-IETC), Nottingham, United Kingdom, 7-9 Nov 2018.

[Ton_14] Wei Tong, "Mechanical Design of Electric Motors", CRC Press, Taylor and Francis Group, LLC, 2014.

[ArnCat] "Arnold Magnetic Technologies' Catalogue", https://www.arnoldmagnetics.com

[NewCat]"New England Wire Technologies",http://www.litzwire.com/nepdfs/Rectangular_Compacted_Litz_Catalog.pdf

[EssCat]"Essex Magnet Wire Catalogue", https://prod.essexwire.com/sites/essexwire.com/files/2017-08/Essex-Wire-Engineering-Data-Handbook-EN.pdf

[Oun_16] H. Ounis, "Conception intégrée par optimisation multicritère multi-niveau d'un système d'actionnement haute vitesse pour l'avion plus électrique", PhD thesis, Toulouse University, November 2016.

[Kim_17] Sang-Hoon Kim, "Electric Motor Control: DC, AC and BLDC Motor", Elsevier Science, 2017, https://books.google.fr/books?id=ewKqDQAAQBAJ

General conclusion and perspectives

In this manuscript, we were interested in the development of models and tools allowing to identify the most promising actual and future technologies and breakthroughs which need to be overcome for increasing specific power of electric motors dedicated to serial hybrid aircraft propulsion. These models and tools are carried out as part of the HASTECS project which set two high specific power targets for H2020 Horizon (i.e. 5kW/kg for 2025 and 10kW/kg for 2035). They have been carried out, on the one hand, to be integrated in global optimization study of hybrid propulsion chain and on the other hand for supplying details required for sizing the further components and for studying partial discharges.

To satisfy our thesis goal, we have drafted, in the first Chapter, a wide panorama on the electric motor current and future technologies in order to situate the actual specific power and to identify used technologies. Several materials, electric motor topologies and cooling technologies have been studied and compared to emphasize on their advantages and disadvantages in terms of weights, loads and limits. It results that is difficult, in this phase, to identify the most promising materials, the most cooling technology and the best electric motor topology. Considering the strengths and weaknesses of each technology, establishing trade-offs on the wide technology panorama is essential. It results also that thermal constraints are the major limitations for reaching the HASTECS targets.

In the second chapter, we have focused on the development of model and tool for the assessment electric motor technologies. For the purposes, we firstly reminded the loadability concepts which characterize the technological levels. Afterward, we have introduced loadability concepts on the analytical model of non-salient sinewave electric machines for carrying out tool for assessing performances without describing the topology. Indeed, this presents the strong and original features. To consider limits, two constraints have been introduced the first one is thermal expressed from the concept of current density product and the second one is mechanical expressed from rotor shape factor. We have developed this tools in Matlab software as a tool called **T**arget **S**etting **T**ool "TST". It takes as inputs: the specifications, loads and materials library and gives as outputs set of data such as main sizes, weights, losses, efficiency, specific power and torque. Developed model of TST is in fact an inverse model.

Surface Mounted Permanent Magnet Synchronous Motor "SM-PMSM" is one of the topology satisfying TST assumptions. In Chapter II, a sizing tool based on this topology provides additional data for the other packages. It is most accurate than TST Tool while remaining an uncomplicated analytical model. As well as for TST, we have programmed SM-PMSM in Matlab software. To ensure sinewave airgap flux density we have chosen Halbach structure for permanent magnets. Therefore, we have established analytical model for determining the polarization and additional rotor sizes using direct design and using an optimization. By choosing distributed winding configurations we have determined the additional stator sizes and the electric circuit parameters by means of established conductor distribution functions. Moreover, as structure is defined, we have updated some data mainly weights and performances (i.e. losses, specific power and specific torque).

In the last Chapter, we have sized through interaction with WP3, two electric motors including their cooling systems for HASTECS targets. This sizing allowed us on the one hand to identify for each target the most promising technologies and on the other hand to validate the assessment tool "TST" and sizing tool "SM-PMSM". From flying mission profiles (i.e. mechanical power and speed) given by AIRBUS, we have firstly discussed on the choice of sizing point given that electric motors should be satisfying specifications (mainly mechanical power between kW to MW). As a result, choice was made on the take-off phase given that is the most critical flying phase for electric motors. Thereafter, as sizing cooling systems strongly depends on the sizing of electric motor, we have proposed a sizing procedure which involves all tools and models performed in Chapters II and III and in those developed by WP3. For each target, we reminded the issues and limitations in order to define the strategies to be followed before starting the sizing. We have therefore proposed two strategies: the first one consists to define the involved cooling methods according to the actual/future cooling technologies. The second one consists to define the involved materials according to the chosen cooling methods. For the 1st target (2025), sizing was based on the actual technological levels whereas for 2nd target (2035) sizing was based on the actual and future technological levels. For reaching high specific power for the two targets, we have increased

loads while making sure we don't exceed thermal limits (i.e. expressed by the equivalent current density product). We have decreased losses by using high performance materials and using design technology solutions that allow it.

According to actual technology, we have introduced in TST and SM-PMSM a set of loads and parameters which allowing to reach 5kW/kg, namely:

- Tangential stress "σ =50000Pa"
- Current density "j_{rms}=8.1A/mm²"
- Max surface current density "K_m=111.1kA/m"
- RMS linear current density: "A_{rms}=81.4kA/m"
- Current density product "$A_{rms}j_{rms}$=6.6×10^{11} A²/m^3"
- Max airgap flux density "B_m=0.9T"
- Flux density in teeth "B_{st}=1.3T"
- Flux density in yoke "B_{sy}=1.2T"
- Rotational speed "Ω=15970rpm"
- Number of pole pairs "p=2"
- Slot fill factor is 0.5,

and this is for the following technological choices:

- Using external cooling method carried out frame for cooling stator
- Using ambient external air as cooled source
- Using inner cooling method in rotor shaft for cooling rotor
- Using stranded and twisted conductors to limit AC joule losses at high frequency
- Using Halbach PM radially and axially segmented for decreasing eddy current losses and to ensure sinewave airgap flux density.
- Using high thermal classes in insulation winding: 220°C
- Using high performance materials: Vacoflux 48, Samarium Cobalt SmCo, Carbon fiber sleeve...etc.

Through interaction with WP3, the thermal limit obtained for the specific power 5kW/kg with the used cooling methods is 2.10^{12}A²/m^3. Using finite element analysis, we have validated with tolerable deviations the assessment tool TST and the sizing tool SM-PMSM even they are based on huge assumptions especially TST.

Based on the sizing electric motor of the 1st target, we have increased some loads in TST and SM-PMSM and we have kept the others in order to double the achieved specific power (i.e. for reaching 10kW/kg):

- Tangential stress "σ=70000Pa"
- Current density "j_{rms}=20A/mm²"
- Max surface current density "K_m=155kA/m"
- RMS linear current density:"A_{rms}=110kA/m"
- Current density product "$A_{rms}j_{rms}$=2.2×10^{12} A²/m^3"
- Flux density in yoke "B_{sy}=1.25T"
- Rotational speed "Ω=20000rpm"
- Number of pole pairs "p=4",

this is for the following new technological choices specially in winding, insulation and stator cooling:

- Adding inner cooling method in winding to improve cooling stator because thermal limit set for 1st target is exceeded
- Using litz-wires to limit AC joule losses at very high frequency (>1kHz)
- Using very high thermal classes in insulation winding: 240°C, the technologies of the other electric machine parts remain same.

Always with WP3 interaction on this target 10kW/kg, thermal limit should be not exceeding 5.10^{12}A²/m^3.

Once again, we have validated with tolerable deviations the assessment tool TST and the sizing tool SM-PMSM. In conclusion of these two sizing electric motors, reaching 2nd Hastecs target strongly relies on the using cooling method (in our studied motor winding should be directly cooled).

After sizing electric motors with their cooling systems and validation of tools, it would be interesting for future works to carry out an optimization using developed tools (i.e. using only TST or using both

TST and SM-PMSM) in order to determine the most critical points for increasing the specific power given that for instance, these two motors have been sized for high speed rotation.

List of publications

Conferences with HASTECS Project Acknowledgement

- Yvan Lefèvre, Sami El Aabid, Jean-François Llibre, Carole Henaux, **Sarah Touhami**, Performance assessment tool based on loadability concepts, the 18th International Symposium on Applied Electromagnetics and Mechanics, France September 2017.
- **Sarah Touhami**, Yves Bertin, Yvan Lefèvre, Jean-François Llibre, Carole Henaux, Matthieu Fénot, Lumped Parameter Thermal Model of Permanent Magnet Synchronous Machines, International Conference Electrimacs, Transactions of IMACS Mathematics and Computers in Simulation (special issue), Toulouse July 2017.
- **Sarah Touhami**, Yvan Lefèvre, Jean François Llibre. Joint Design of Halbach Segmented Array and Distributed Stator Winding. IEEE Proceedings of the XXIII International Conference on Electrical Machines (ICEM'18), Alexandroupoli, Greece September 2018.
- Philippe Colin, **Sarah Touhami**, David Malec, Yvan Lefèvre, Jean-François Llibre, Design of Electric Machine Taking into Account the Partial Discharges Phenomena for Future Hybrid Propelled Aircrafts, More Electric Aircraft (MEA 2019) Conference, Toulouse February 2019.
- **Sarah Touhami**, Yvan Lefèvre, Jean François Llibre, Original Optimization Procedures of Halbach Permanent Magnet Segmented Array, 19th International Symposium on Electromagnetic Fields in Mechatronics Electrical and Electronic Engineering, 29-31 August 2019, Nancy-France.
- **Sarah Touhami**, Amal Zeaiter, Matthieu Fenot, Yvan Lefèvre, Jean-François Llibre, Electro-thermal Models and Design Approach for High Specific Power Electric Motor for Hybrid Aircraft, Aerospace Europe Conference 2020, 25-28 February 2020, Bordeaux, France.
- Matthieu Pettes-Duler, Xavier Roboam, Bruno Sareni, **Sarah Touhami**, Yvan Lefèvre, Jean François Llibre, Sensitivity Analysis of a Hybrid-Electric Aircraft Powertrain Based on Sobol Indices, Aerospace Europe Conference 2020, 25-28 February 2020, Bordeaux, France.
- **Submitted and accepted conference abstract: Sarah Touhami**, Yvan Lefèvre, Jean François Llibre, Effects of Splitting and Twisting Conductor on the AC Joule losses, 19th IEEE Conference on Electromagnetic Field Computation, CEFC 2020, November 16-19, Pisa Italy.

Journal

Yvan Lefèvre, Sami El Aabid, Jean-François Llibre, Carole Henaux, **Sarah Touhami**, Performance assessment tool based on loadability concepts, International Journal of Applied Electromagnetics and Mechanics, IOS Press, vo. Pre-press, no. Pre-press, December 2018.

Other submitted journal papers

- **Sarah Touhami**, Amal Zeaiter, Matthieu Fenot, Yvan Lefevre, Jean-François Llibre, Etienne Videcoq, Electrothermal models and Design Approach for High Specific Power Electric Motor for Hybrid Aircraft Propulsion, **Submitted to CEAS Aeronautical Journal Springer.**
- **Sarah Touhami**, Yvan Lefevre, Jean-François Llibre, Direct and Optimisation Based Designs of an Halbach Permanent Magnet Segmented Array, **Submitted to the International Journal for Computation and Mathematics in Electrical and Electronic Engineering**.
- **Sarah Touhami,** Yvan Lefevre, Jean-François Llibre, Pré-dimensionnement d'un Moteur Electrique de Très Forte Puissance Spécifique pour Avion Hybride**, Submitted to Revue de l'Electricité et de l'Electronique (REE).**

HASTECS Acknowledgement

This project has received funding from the CleanSky2 Joint Undertaking under the European Union's Horizon 2020 research and innovation program under grant agreement No 715483.

List of publications

Other conference paper

- Theo Capri, Maxime Bonnet, **Sarah Touhami**, Yvan Lefevre, Jean-François Llibre, Unified Sizing Model Approach for Radial and Axial Flux Permanent Magnet Machines, IEEE Proceedings of the XXIV International Conference on Electrical Machines (ICEM'20), Gothenburg, Sweden, 23rd-26th August 2020.